Selective contacts
for crystalline silicon solar cells

Thomas Tom

Doctoral Thesis

Selective contacts for crystalline silicon solar cells

Thomas Tom

Directors: Dr. Joan Bertomeu i Balagueró,

Dr. Julià Vidrier López

UNIVERSITAT DE BARCELONA

Selective contacts for crystalline silicon solar cells

Memòria presentada per optar al grau de doctor per la

Universitat de Barcelona

Programa de doctorat en Enginyeria i Ciències Aplicades

Thomas Tom

Directors: Dr. Joan Bertomeu i Balagueró
Dr. Julià Vidrier López

Tutor: Dr. Joan Bertomeu i Balagueró

Departament de Física Aplicada, Facultat de Física

UNIVERSITAT DE BARCELONA

A mi Appa, Amma, Marti y mi amor...

Table of Contents

Abstract

Global energy use has increased, causing a rapid shift in the climate. Renewable energy sources such as solar energy must replace fossil fuels to slow down this trend. In order to achieve this, the amount of power generated by solar energy must increase by a factor of 40 by 2050. As silicon solar cells account for 90% of the global photovoltaic industry, addressing their existing limiting factors such as efficiency and production cost can help to make a big difference. Therefore, the primary objectives of this thesis are to minimize or replace indium (In) in transparent conducting layers (due to rising In costs) and to develop efficient hole and electron transport layers utilizing more industrial and less expensive ways for silicon heterojunction (SHJ) solar cells.

To enhance the efficiency of SHJ solar cells the transparent conducting oxides used must exhibit high mobility and high infrared transparency. Here, fluorine-doped indium oxide (IFO) films were developed with DC sputtering. Highest mobility of 93 $cm^2V^{-1}s^{-1}$ was achieved, the films showing an efficiency of 22.6% when used in SHJ solar cells. To reduce the usage of In, these IFO films were thinned down to few tens of nm keeping their high mobility. Therefore, the idea of growing transparent conducting aluminum-doped zinc oxide (AZO) on top of the seed layer of IFO resulted in achieving high mobility, high conductivity, and better antireflection properties.

In addition, In-free transparent conducting layers were developed using dielectric-metal-dielectric (DMD) structures based on AZO as the dielectric with an ultra-thin silver aluminum metallic interlayer. The optimized DMD structures were used as a front contact for n-type silicon solar cells by introducing a hole-selective vanadium pentoxide (V_2O_5) dielectric layer.

Moreover, hole transport layers (HTL) for SHJ solar cells were fabricated using the industrially scalable technique of sputtering. First, molybdenum oxide (MoO_x) films were fabricated employing reactive sputtering using a metallic target. Structural, compositional, electrical, and optical properties of these

films are studied and, as a proof of concept, these films were tested as HTL on SHJ solar cells, achieving a power conversion efficiency (*PCE*) of 8.8%. Next, the MoO_x films were sputtered from a ceramic target in different oxygen and hydrogen atmospheres. X-ray photoelectron spectroscopy revealed that working in reducing atmosphere of hydrogen, while applying additional temperature to the substrates, lead sub-stochiometric MoO_x films.

Finally, studies were carried out to develop organic dipole interlayer as electron transport layer (ETL) in dopant-free SHJ solar cells. The three types of organic layers used were polyethylenimine (PEI), Poly(amidoamine) (PAMAM) dendrimer, and Deoxyribonucleic Acid (DNA), and the spin coating technique was adopted to fabricate these films. The use of PEI as interface modification of electron-selective contacts clearly enhanced electrical transport with lower contact resistance and significant surface passivation. This modification was able to eliminate completely Fermi-level pinning at the metal/semiconductor interface, while shifting the work function of the metallic electrode by more than 1 eV. Proof-of-concept SHJ solar cells were fabricated with *PCE* of 13.8% this demonstrated the beneficial effect of PEI dipolar interlayers. The interface modification by the PAMAM dendrimer was due to the large number of protonated amines that contributed to the formation of a dipole layer. This was supported by the observation of a low contact resistivity of 4.5 mΩ cm^2, the shift in work function, and the *n*-type behavior of PAMAM dendrimer films on the surface of crystalline silicon. A SHJ solar cell containing the PAMAM dendrimer interlayer is presented, achieving a PCE of 14.5%. Finally, a SHJ solar cell was fabricated using DNA as the electron ETL, with a PCE of 15.5%. The deposition and characterization of the DNA films on crystalline silicon showed an *n*-type behavior with a work function of 3.42 eV and a contact resistance of 28 mΩ cm^2.

In sum, high-efficiency SHJ solar cells with high-mobility transparent conductors were achieved, and the electron selective contacts were successfully replaced by organic molecules. Furthermore, the potential to utilize these transparent layers and organic compounds in various electronic devices extends far beyond solar cell applications and should be seen as an attractive trend.

Resum

El consum d'energia global ha augmentat, provocant un ràpid canvi en el clima. Les fonts d'energia renovables com l'energia solar han de substituir els combustibles fòssils per frenar aquesta tendència. Per aconseguir-ho, la quantitat d'energia generada per l'energia solar ha d'augmentar en un factor 40 de cara l'any 2050. Com que les cèl·lules solars de silici representen el 90% de la indústria fotovoltaica mundial, abordar els seus factors limitants existents, com ara l'eficiència i el cost de producció, pot marcar una gran diferència. Per tant, els objectius principals d'aquesta tesi són minimitzar o substituir l'indi (In) en capes conductores transparents, a causa de l'augment del cost de l'In, i desenvolupar capes eficients de transport d'electrons i forats utilitzant maneres mètodes més industrials i menys costosos per a les cèl·lules solars d'heterojunció de silici (SHJ).

Per millorar l'eficiència de les cèl·lules solars SHJ, els òxids conductors transparents utilitzats han de ser d'alta mobilitat i amb alta transparència en l'infraroig proper. Aquí les pel·lícules d'òxid d'indi dopat amb fluor (IFO) s'han desenvolupat amb polvorització catòdica (*sputtering*) DC. S'ha aconseguit una la mobilitat més alta de 93 $cm^2V^{-1}s^{-1}$, tot demostrant una eficiència del 22,6% en cèl·lules solars SHJ. Per reduir l'ús d'In, aquestes pel·lícules IFO s'han reduït a poques desenes de nm, tot mantenint la seva alta mobilitat. Per tant, la idea de fer créixer òxid de zinc dopat amb alumini (AZO) conductor transparent sobre una capa d'IFO ha comportat una alta mobilitat, una alta conductivitat i millors propietats antireflectants. També s'han desenvolupat capes conductores transparents basades en estructures dielèctric-metall-dielèctric (DMD), amb AZO com a dielèctric i una capa intermèdia metàl·lica ultrafina de plata dopada amb alumini. Les estructures DMD optimitzades s'han utilitzat com a contacte frontal per a cèl·lules solars de silici de tipus *n* mitjançant la introducció d'una capa dielèctrica de pentaòxid de vanadi (V_2O_5) selectiva per forats.

S'han desenvolupat capes de transport de forats (HTL) per a cèl·lules solars SHJ mitjançant una tècnica industrialment escalable com ho és la polvorització catòdica. En primer lloc, es van fabricar pel·lícules d'òxid de molibdè (MoO$_x$) utilitzant polvorització reactiva mitjançant un blanc metàl·lic. S'han estudiat les propietats estructurals, composicionals, elèctriques i òptiques d'aquestes pel·lícules i, com a prova de concepte, s'han provat com a HTL en cèl·lules solars SHJ, tot aconseguint una eficiència de conversió d'energia (PCE) del 8,8%. Tot seguit, es van dipositar pel·lícules de MoO$_x$ a partir d'un blanc ceràmic utilitzant diferents atmosferes que implicaven oxigen i hidrogen. L'espectroscòpia de fotoelectrons de raigs X va revelar que treballar en una atmosfera reductora d'hidrogen i amb temperatura addicional al substrat dóna lloc a MoO$_x$ sub-estoquiomètric.

Finalment, s'han desenvolupat capes intermèdies de dipols orgànics com a capa de transport d'electrons (ETL) en cèl·lules solars SHJ lliures de dopants. Els tres tipus de capes orgàniques que s'utilitzen són la polietilenimina (PEI), el dendrímer de poli (amidoamina) (PAMAM), i l'àcid desoxiribonucleic (ADN), i s'ha adoptat la tècnica de recobriment giratori (*spin coating*) per fabricar aquestes pel·lícules. L'ús de PEI per millorar la interfície de contactes selectius d'electrons ha potenciat el transport elèctric, tot disminuint la resistència de contacte i passivant la superfície significativament. Aquesta modificació ha estat capaç d'eliminar completament la fixació del nivell de Fermi a la interfície metall/semiconductor, i ha canviat la funció de treball de l'elèctrode metàl·lic en més d'1 eV. Les cèl·lules solars SHJ de prova de concepte fabricades han assolit una PCE del 13,8%, tot demostrant l'efecte beneficiós d'intercalar les capes dipolars de PEI. La modificació de la interfície per part del dendrímer PAMAM es deu a un gran nombre d'amines protonades que contribueixen a la formació d'una capa dipolar. Això es recolza en l'observació d'una baixa resistivitat de contacte de 4,5 mΩ cm^2, el canvi en la funció de treball i el comportament de tipus *n* de les pel·lícules de dendrímers PAMAM a la superfície del silici cristal·lí. Es presenta una cèl·lula solar SHJ que conté la capa intermèdia de dendrímer PAMAM, amb una PCE del 14.5%. Finalment, s'ha fabricat una cèl·lula solar SHJ amb ADN com a ETL, tot obtenint una PCE del 15,5%. El dipòsit i la caracterització de les pel·lícules d'ADN sobre silici cristal·lí mostren un comportament de tipus *n* amb una funció de treball de 3,42 eV i una resistència de contacte de 28 mΩ cm^2.

En resum, s'han aconseguit cèl·lules solars SHJ d'alta eficiència amb conductors transparents d'alta mobilitat, i s'han substituït amb èxit els contactes selectius d'electrons per molècules orgàniques. A més, el potencial d'utilitzar aquestes capes transparents i compostos orgànics en diversos dispositius electrònics s'estén molt més enllà de les aplicacions solars i s'ha de veure com una tendència atractiva.

Chapter 1: Introduction

This chapter explains the framework, objectives, and structure of the thesis in order to reduce or replace the Indium usage and also to replace the conventional doped contacts used in SHJ solar cells.

1.1 Framework

The climate change is currently the most important global issue right now. Its rapid acceleration endangers the existence of all living things on the planet. Comparing the preindustrial average temperature between 1850–1900 with the current average global surface temperature, the latter has already increased by about 1.1 °C. Due to this rise in surface temperature, it is anticipated that the risk of extreme weather conditions, such as heat waves, wildfires, droughts, flooding, and severe storms, will grow [1][2].

The amount of the most significant greenhouse gases in air, CO_2 amongst them, is frequently employed as an indicator of the climate crisis. They stay as an indirect indication because these gases do not directly heat the planet surface. Instead, these greenhouse gases strongly scatter the infrared radiation that is reflected or emitted from the surface of the Earth, as well as trapping it within the atmosphere.

CO_2 concentrations are rising due to burning of fossil fuels like coal and oil for the generation of electricity, heat, and other forms of energy. The main issue is the rhythm at which CO_2 emission takes place. Indeed, that carbon, extracted from the atmosphere by plants via photosynthesis over many millions of years, is being reintroduced by us to the atmosphere in only a few hundred years by burning. The concentrations of CO_2 have risen to a very alarming scenario, from 11 billion tons a year in the 1960s to 35 billion tons a year in 2010s, according to the Global Carbon Update 2021 [3]. Therefore, and unfortunately, it is irrelevant to ask whether we can stop global warming. Instead, we are confronted with the dilemma of how to reduce it.

The majority of the scientific community now recognizes and concurs that renewable energy sources are the primary tool for addressing the climate crisis. For this, solar energy, together with wind energy, is expected to be the major player, taking into account that the amount of solar energy reaching the Earth surface is about 1000 times the yearly global energy consumption [4]. The amount of power generated from solar energy must rise by a factor of 40 in 2050 in order to achieve the goal of less than 1.5 °C global warming as shown in Fig. 1.1. In rough numbers, this means that the 600 TWh generated in 2018 must increase up to 25000 TWh in 2050 [5].
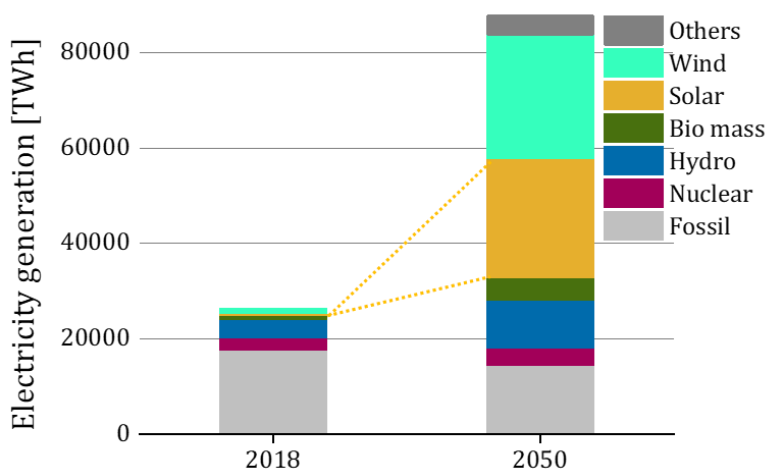
Figure 1.1: Electricity generation, in 2018 and 2050 (in TWh), in the 1.5 °C scenario. Data adapted from world energy transitions outlook [5].

Currently, more than 90% of the photovoltaics (PV) market is dominated by silicon solar cells [6]. However, traditional technologies like back surface field (BSF), and passivated emitter rear cell (PERC) solar cells, are challenging and expensive to scale up to industrial levels due to their multilayered structures and sub-millimeter intra-contact patterning. However, the heterojunction with intrinsic thin layer (HIT), employs a semi-

insulating material to provide full-area passivation of the rear and front surfaces while allowing carrier transport, thus overcoming these drawbacks.

HIT solar cells have achieved power conversion efficiency (*PCE*) of 27.6% by LONGi [7]. Nevertheless, these HIT cells have to overcome various technological challenges to improve the efficiency and to decline the cost per kWh of installed capacity. Some of the main drawbacks of HIT cells are: (i) they suffer from high-temperature processing and often require complex deposition techniques like plasma-enhanced chemical-vapor deposition (PECVD) involving the use of hazardous gases in the fabrication process; (ii) they employ a higher wafer thickness that increases the production cost; (iii) the material costs for silver contacts and indium (In)-based transparent conducting oxides (TCOs) are ever increasing; and (iv) the doping process usually produces defects which cause parasitic absorption and recombination in the cells [8][9][10][11][12].

The main motivation behind this thesis is overcoming some of these challenges by reducing or replacing indium and replacing the doped layers by a carrier selective contact layer, for which a broad variety of techniques have been used.

1.2 Objective and outline of the thesis

The main part of the thesis work had been carried out at Solar Energy Group at the Universitat de Barcelona (UB) and in collaboration with Micro and Nanotechnology Group at the Universitat Politècnica de Catalunya (UPC). Also, a part of the work was carried out at Fraunhofer Institute for Solar Energy Systems (ISE) during the research stay. The work involves the research projects from Selective Contacts and Active Layers for Energy Devices (SCALED) consortium which involves the participation of Micro and Nanotechnology Group at the UPC, Solar Energy Group at the UB, Photovoltaic Solar Energy Group at the Centro de Investigaciones Energéticas Medioambientales y Tecnológicas (CIEMAT), and Centro Láser at the Universidad Politécnica de Madrid.

The initial part of the thesis is focused in developing the high-mobility TCO layers to reduce the near-infrared (NIR) free-carrier absorption (FCA) and evaluating the possibility of thinning down these high mobility TCO to a few tens of nm to reduce the usage of indium, while keeping their high mobility and high lateral conductivity. Later, dielectric-metal-dielectric (DMD) structures have been fabricated to replace the indium in silicon solar cells.

In the second part of the thesis, transition metal oxides (TMOs) are explored as hole selective contacts in silicon solar cells. Different deposition techniques such as sputtering and thermal evaporation were used for this purpose. These contacts were dopant free, which reduces the carrier recombination and band gap narrowing, highly transparent with wide band gap, non-hazardous, and deposited at low temperature.

The final part of the thesis is dedicated to develop spin coating-deposited organic dipole interlayers acting as electron selective contacts for silicon solar cells. The dipole interlayers help tuning the Fermi level in the devices, thus achieving either ohmic or rectifying contacts. The incorporation of dipole interlayers has proved to induce abrupt changes in the electronic band structure across interfaces, hence modifying the work function of the metal electrode.

The thesis structure is as follows:

Chapter 2: Fundamentals This chapter deals with the fundamentals of the solar cell operation, crystalline silicon technology, transparent conductors, hole selective contacts, and electron selective contacts.

Chapter 3: Experimental This chapter describes the experimental techniques for the thin films' fabrication and their characterization. It also describes the steps for solar cell fabrication and characterization.

Chapter 4: Transparent conductors High mobility fluorine-doped indium oxide (IFO) was explored using an industrial sputtering unit. To reduce the usage of indium, aluminum-doped zinc oxide (AZO) was grown on top of the seed layer of IFO. Furthermore, to replace the indium from TCOs, ultra-thin metallic films were implemented in DMD structures based on AZO (as the dielectric) and an ultra-thin silver aluminum (Ag:Al) metallic interlayer.

Chapter 5: Hole transport layers Sputtering was employed to obtain MoO_x films with better control and reliability. The MoOx films were obtained by reactive sputtering of Mo and also by sputtering from a ceramic target of MoO_3 with a reactive atmosphere that could tune the metal oxide properties. As a proof-of-concept, c-Si solar cells were fabricated using MoO_x as hole transport layer (HTL) and compared to the thermally evaporated ones.

Chapter 6: Electron transport layers Organic molecules were explored as the electron transport layer (ETL) in silicon solar cells. Branched polyethylenimine(b-PEI), poly(amidoamine) (PAMAM) dendrimers, and deoxyribonucleic acid (DNA) were explored as dipoles that could modify the interface of metal-semiconductor junctions.

Chapter 7: Conclusions In this chapter, a short summary of the main findings of this thesis is presented.

References

[1]   S. Cevik, Climate Change and Energy Security: The Dilemma or Opportunity of the Century?, IMF Work. Pap. 2022 (2022) 1. https://doi.org/10.5089/9798400218347.001.

[2]   B.R. H.-O. Pörtner, D.C. Roberts, M. Tignor, E.S. Poloczanska, K. Mintenbeck, A. Alegría, M. Craig, S. Langsdorf, S. Löschke, V. Möller, A. Okem, IPCC, 2022: Climate Change 2022: Impacts, Adaptation, and Vulnerability. Contribution of Working Group II to the Sixth Assessment Report of the Intergovernmental Panel on Climate Change, 2021. https://doi.org/10.1017/9781009325844.Front.

[3]   P. Friedlingstein, M.W. Jones, M. O'Sullivan, R.M. Andrew, D.C.E. Bakker, Global Carbon Budget 2021, raport Earth System Science Data, Earth Syst. Sci. Data. 14 (2022) 1917–2005. http://www.globalcarbonatlas.org/en/content/global-carbon budget.

[4]   REN21, Renewables 2020 Global Status Report, 2020. http://www.ren21.net/resources/publications/%0Ahttps://www.ren21.net/wp-content/uploads/2019/05/gsr_2020_full_report_en.pdf.

[5]   IRENA, World energy transitions outlook: 1.5 degrees pathway, 2021. https://irena.org/publications/2021/March/World-Energy-Transitions-

Outlook.

[6]   T.G. Allen, J. Bullock, X. Yang, A. Javey, S. De Wolf, Passivating contacts for crystalline silicon solar cells, Nat. Energy. 4 (2019) 914–928. https://doi.org/10.1038/s41560-019-0463-6.

[7]   National Renewable Energy Laboratory (NREL), Best Research-Cell Efficiencies, Accessed January 2023. (2023). https://doi.org/https://www.nrel.gov/pv/assets/pdfs/best-research-cell-efficiencies.pdf.

[8]   M.J. De Wild-Scholten, Energy payback time and carbon footprint of commercial photovoltaic systems, Sol. Energy Mater. Sol. Cells. 119 (2013) 296–305. https://doi.org/10.1016/j.solmat.2013.08.037.

[9]   J. Geissbuhler, S. De Wolf, A. Faes, N. Badel, Q. Jeangros, A. Tomasi, L. Barraud, A. Descoeudres, M. Despeisse, C. Ballif, Silicon heterojunction solar cells with copper-plated grid electrodes: Status and comparison with silver thick-film techniques, IEEE J. Photovoltaics. 4 (2014) 1055–1062. https://doi.org/10.1109/JPHOTOV.2014.2321663.

[10]   L. Ciacci, T.T. Werner, I. Vassura, F. Passarini, Backlighting the European Indium Recycling Potentials, J. Ind. Ecol. 23 (2019) 426–437. https://doi.org/10.1111/jiec.12744.

[11]   C. Battaglia, A. Cuevas, S. De Wolf, High-efficiency crystalline silicon solar cells: Status and perspectives, Energy Environ. Sci. 9 (2016) 1552–1576. https://doi.org/10.1039/c5ee03380b.

[12]   D. Adachi, J.L. Hernández, K. Yamamoto, Impact of carrier recombination on fill factor for large area heterojunction crystalline silicon solar cell with 25.1% efficiency, Appl. Phys. Lett. 107 (2015) 22–25. https://doi.org/10.1063/1.4937224.

Chapter 2: Fundamentals

This chapter deals with the basics of crystalline silicon solar cells, c-Si heterojunction technology, transparent conductors, electron, and hole selective contacts. In transparent conductors, the basics of transparent conducting oxides and dielectric metal dielectric structures are described. In addition, transition metal oxides to form hole selective contacts and organic molecules to form electron selective contacts, are seen in detail.

2.1 Basics of crystalline silicon solar cells

Solar cells operate based on the photovoltaic effect, which is the formation of a potential difference at the junction of two distinct materials in response to electromagnetic radiation. The solar cells mainly consist of an *absorber* region, semipermeable membranes and metallic contacts [1][2]. The schematic of a solar cell with crystalline silicon (c-Si) as absorber region, heavily doped p^+ and n^+ regions, respectively acting as *hole selective contact* (or *hole transport layer*, HTL) and *electron selective contact* (or *electron transport layer*, ETL), and with metallic contacts is shown in Fig. 2.1.
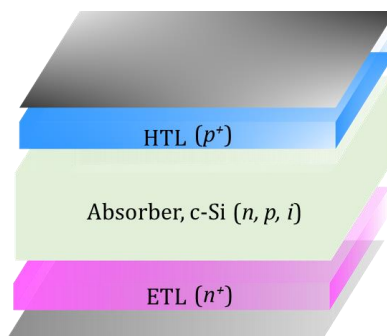
Figure 2.1: Illustration of a silicon solar cell, which is essentially made of absorber, electron transport (ETL) and hole transport (HTL) layers.

The basic working principle of a solar cell can be divided into three basic processes:

(i) Generation of charge carriers due to the absorption of photons in the absorber region made of a semiconductor material. Here the light is absorbed and then transformed into electrical energy via photogeneration of electron-hole pairs.

(ii) Separate extraction of electrons and holes from the absorber region utilizing the junctions. They are the semipermeable membranes present on both sides of the absorber, such that holes can flow out through one layer and electrons through the other. These membranes are called HTL and ETL, respectively. The term energy barriers can be used to explain the selectivity of these layers from an energy perspective [3]. The energy-band diagram of a solar cell with the previously specified construction is shown in Fig. 2.2. The photogenerated electrons are able to flow to the right, through the ETL, whereas the high energy barrier prevents electrons from moving to the left, through the HTL. This is the reason this layer is often called *electron-blocking layer* in the literature. Similar to but oppositely, photogenerated holes can flow to the left through the HTL but are rejected by the high energy barrier at the ETL, often referred as *hole-blocking layer* in the literature.

(iii) Finally, collection of the photogenerated charge carriers via the metallic contacts and their transfer to the external circuits.
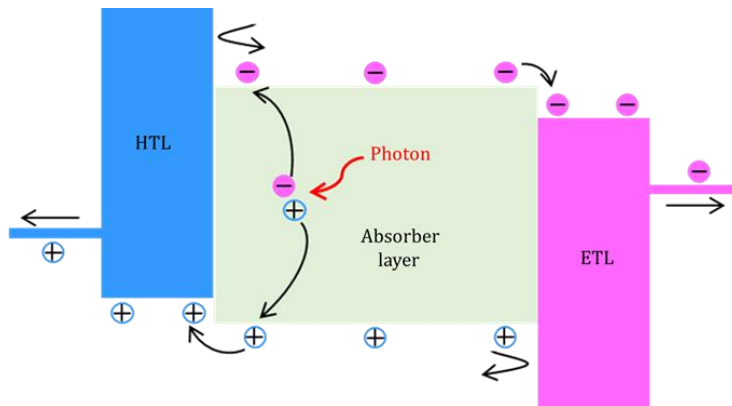
Figure 2.2: The energy-band diagram of the solar cell where the photogenerated electrons flow to the ETL and holes are collected by the HTL.

In the following, the different involved parts in a solar cell, as well as the fundamentals their operation obey, will be described in detail.

2.1.1 The absorber

In a semiconductor, electrons can occupy energy levels below the *valence band* (VB) edge (E_v) and above the *conduction band* (CB) edge (E_c). The energy difference between these two levels is known as the *band gap energy*, denoted by $E_g = E_c - E_v$. The most general energy band diagram of a semiconductor is shown in Fig. 2.3.
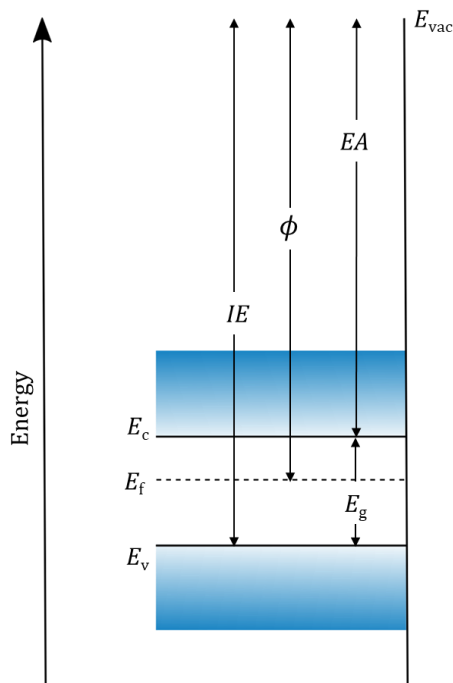
Figure 2.3: The energy diagram of a semiconductor showing the valence band energy (E_v), the conduction band energy (E_c), the Fermi level energy (E_f), the energy gap (E_g), the work function (ϕ), the ionization energy (IE) and the electron affinity (EA).

When a photon is absorbed by a semiconductor material, its energy is used to excite an electron from its initial energy level within the valence band to a higher energy level in the conduction band. For this to occur, the minimum required photon energy is that of the band gap [2]. In semiconductors, the absence of energy levels and electrons within the band gap energy (E_g) causes them to behave differently than other classes of materials. If a photon with higher energy than E_g strikes a semiconducting material, it will be absorbed, whereas a photon with energy lower energy than E_g will pass unaffected through the material.

The next parameter that must be understood from the energy band diagram is the Fermi level energy. The Fermi level may be thought of as a hypothetical energy level of an electron, with a 50% probability of being occupied at any given time under thermodynamic equilibrium. The distribution that describes the occupation states in a semiconductor is given by Fermi-Dirac distribution function, *f(E)*, expressed as

$$f(E) = \frac{1}{e^{(E-E_f)/kT} + 1} \tag{2.1}$$

where E is the energy of the state or level, which could be located everywhere within the band diagram (even within the band gap). The energy E_f is called the *Fermi level energy*. The energy position of the Fermi level is determined by the doping level. In *n*-type semiconductors the Fermi level is close to the conduction band, whereas and in *p*-type semiconductors it is found close to the valence band [4].

Electrons are bound to the solid by nature. At the surface of the material, an energy barrier stops them from escaping into the vacuum. This barrier ends at the *vacuum level* (E_{vac}). E_{vac} is usually defined as the energy level of an electron that is at rest a few nanometres outside of a solid, meaning that it has no kinetic energy with respect to the surface of the sample. Neglecting the few electrons that might be at the CB because of doping or thermal excitation, the electrons at the E_v have the closest energy to E_{vac}. The difference in energy between E_{vac} and this level is the minimum energy needed to remove an electron from the system. This energy difference is called the *ionization energy* (*IE*). On the other hand, neglecting the few holes

that might be at the VB, the energy gained by dropping an electron from the vacuum level to the lowest empty level, the E_c, is the *electron affinity* (*EA*) of the solid. The *work function* (ϕ) is defined as the energy necessary to remove an electron originally at the Fermi level (E_f) deep inside the material and place it at rest at a point in free space just outside the surface, i.e., at least at E_{vac} [5].

In a semiconducting material, the valence and conduction bands vary based on the *k*-vector, which defines the crystal momentum. If the VB maximum and CB minimum are at the same *k*-vector, upon adequate photoexcitation an electron can be excited from E_v to E_c without changing the crystal momentum; these are called *direct band gap* semiconductors. Instead, if the excitation of electron affects the crystal momentum, they are classified as *indirect band gap* semiconductors. Absorbers consisting of direct band gap semiconductors, such as Cadmium Telluride (CdTe) or chalcogenides, have a high absorption coefficient in the usable portion of the solar spectrum. In this instance, solar cells can be made with a typical absorber thickness of 1-2 µm. In contrast, indirect band gap semiconductors such as silicon (Si) and germanium (Ge) require thicker substrates due to the deep absorption of photons. Therefore, solar cells typically have substrates more than 100-µm-thick for adequate light absorption [4].

When light strikes a surface between two media with different refractive indices, a portion of the light will be reflected while the rest will be transmitted. In order to increase the photon absorption, the reflection losses from the absorber layer must be reduced. Different approaches to address this issue are: (i) usage of anti-reflective coatings (ARC) on the absorber surface; (ii) absorber-front surface texturization. Compared to a flat surface, a tilted interface between two media gives rise to deviation of the photon via the Snell law, so that the light path length through the absorber is increased, and inner reflections are hindered; and (iii) utilization of back-reflectors. This minimizes the photon escape on the rear surface, thereby increasing light trapping inside the absorber [3].

The Fig. 2.4 shows the schematic representation of the methods to reduce the reflection losses.
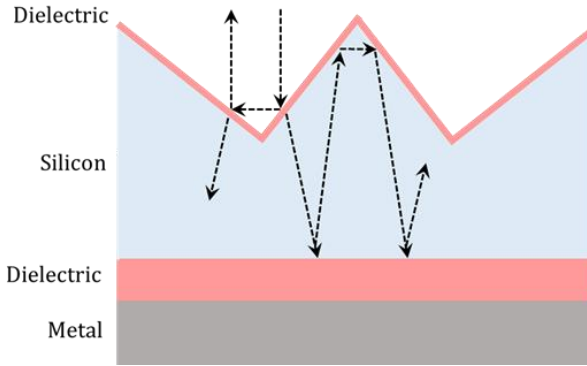
Figure 2.4: Methods to reduce reflection losses by texturing the front surface with an ARC, also with a back-reflector of dielectric and metal. Arrows indicate possible reflections in the system.

When the semiconducting absorber layer is illuminated by light, the generation of electron-hole pairs takes place. When the illumination stops, the electrons will recombine with the holes after a characteristic time known as the *recombination lifetime* (τ), until the equilibrium (all electrons VB-bound) is reached. There are mainly three different types of recombination in the bulk (Shockley-Read-Hall, –SRH– recombination, radiative recombination and Auger recombination), as well as surface recombination (front and rear), which is shown in Fig. 2.5. Therefore, the total recombination time can be characterized by the effective lifetime (τ_{eff}), which can be expressed as,

$$\frac{1}{\tau_{\text{eff}}} = \sum_j \frac{1}{\tau_j} = \left(\frac{1}{\tau_{\text{Rad}}} + \frac{1}{\tau_{\text{Auger}}} + \frac{1}{\tau_{\text{SRH}}} \right)_{\text{bulk}} + \frac{S_{\text{front}}}{W} + \frac{S_{\text{rear}}}{W} \qquad (2.2)$$

where the terms in parenthesis can be grouped as an effective bulk lifetime $1/\tau_{\text{bulk}}$, S_{front} and S_{rear} are the front and rear surface recombination velocities, respectively, and W is the absorber layer thickness.
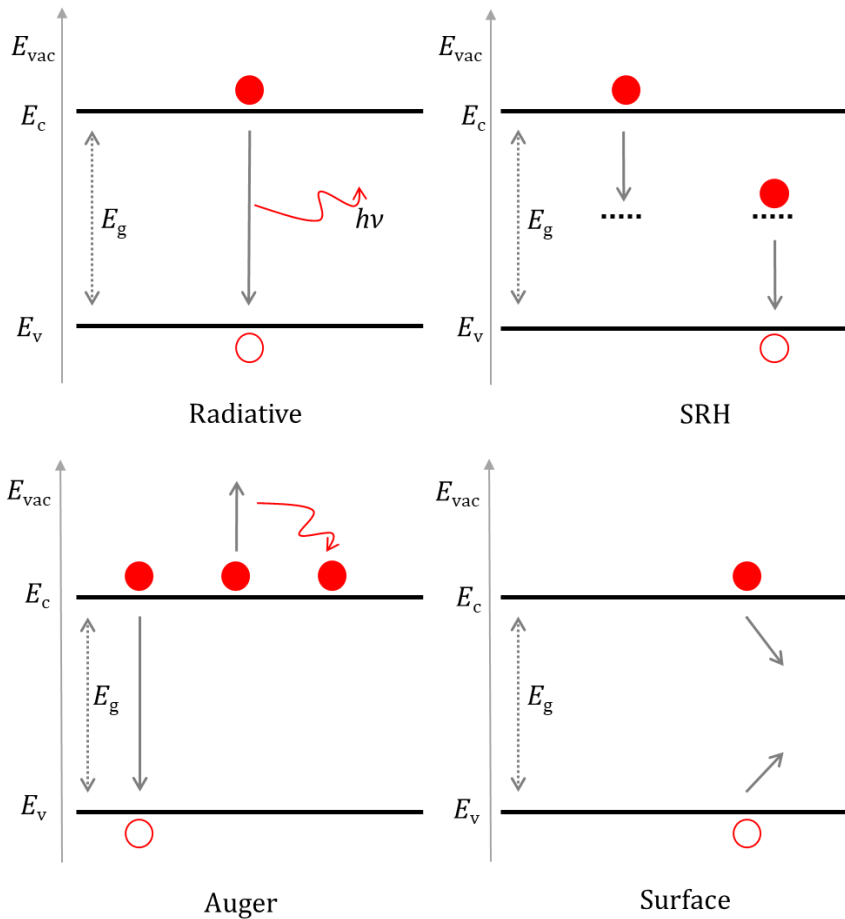
Figure 2.5: Different types of recombination mechanisms in a semiconductor material. Full and open circles respectively represent electrons and holes.

The bulk recombination mechanisms are defined as follows:

(i) Radiative recombination is a direct recombination mechanism in which the electrons in the CB recombine with the holes in the VB, which releases energy in the form of photon.

(ii) In the SRH mechanism, the recombination occurs via traps or impurities in the band gap, and therefore it is not a band-to-band process such as (i).

This recombination process is non-radiative in nature and the resulting energy is liberated into absorber layer in the form of heat.

 (iii) Auger recombination is a three-particle process in which the energy from the recombination is transferred to another charge carrier. When this excited charge carrier relaxes, the energy dissipated in the lattice as heat. Auger recombination and radiative recombination are intrinsic to the material and cannot be avoided. SRH, on the other hand, can be kept to a minimum in high-quality c-Si wafers with a mono-crystalline structure.

The surface recombination arises due to the defects on the surface of the bare c-Si. These are defects at the valence orbitals on the surface containing one electron. These are called as the dangling bonds on the surface of the lattice and the recombination here is by the SRH mechanism. The recombination speed of the electrons and holes on the surface is typically characterized by surface recombination velocity. The lifetime of the high-quality c-Si wafers is mostly limited by the surface recombination due to defect rich boundaries in the bulk. To reduce the surface recombination surface passivation techniques are used for the highly efficient devices [6].

2.1.2 Collection of the charge carriers

The charge carriers must be spatially separated to transfer the chemical energy into electrical energy, which can then be extracted from the electrodes of the cell. The electrons and holes are guided by mainly two forces acting on them, the electrical and chemical forces. Whereas the electrical force is caused by the drift, the chemical force results from the carrier diffusion produced by spatial gradients in the electron and hole concentrations. The resultant force is the sum of the gradient of electrical and chemical forces, and the resultant current is the product of conductivity and the sum of these forces [2][7]. The total current density is then given by:

$$j_Q = \frac{\sigma_\mathrm{n}}{q}\,\mathrm{grad}\ E_\mathrm{FC} + \frac{\sigma_\mathrm{p}}{q}\,\mathrm{grad}\ E_\mathrm{FV} \qquad (2.3)$$

Here, q states for the elementary charge, σ_n and σ_p are the electron and hole conductivities, respectively, and E_FC and E_FV are, respectively, the quasi-

Fermi energy levels within the CB and the VB. According to this relationship, to force the electrons toward one of the two contacts and the holes towards the other, an imbalance in the conductivities and/or the quasi-Fermi level gradients must be generated. Indeed, the necessary selectivity must be entirely provided by the electron and hole conductivities because the quasi-Fermi level gradients cannot be implemented in a solar cell device to serve this function. In addition, since the product of charge carrier density and mobility is defined as the conductivity, varying the any of both variables (carrier density and/or mobility) will improve the conductivity and thus enhance the device operation.

In practice, adjusting the local concentrations of electrons and holes near the silicon surface is the primary mechanism by which electron and hole selective contacts function. Common methods for achieving this goal include doping, the deposition of materials with a notably high or low work function (relative to the Si absorber), and the introduction of fixed charges. Thus, the electrons and holes move specifically to the ETL and HTL layers, respectively, giving a net current density to the load. In addition, the recombination rate of electrons and holes at the Si surface is reduced thanks to this regulation of the carrier concentration, which is a crucial component for solar cell performance [8].

Two key factors are frequently utilized in the literature to characterize the selective behavior of a contact. The first one is its conductivity; it is measured by the specific contact resistance (ρ_c), which is expressed in units of Ω cm^2. The second parameter is the recombination current density (J_{0c}), expressed in fA cm^{-2}. Low values for ρ_c and J_{0c} are indicative of good selective contacts [3].

2.1.3 Equivalent circuit and solar cell parameters

The current-voltage (*J-V*) characteristics of a solar cell can be described by the equivalent circuit, the two-diode model as depicted in Fig. 2.6 [2].
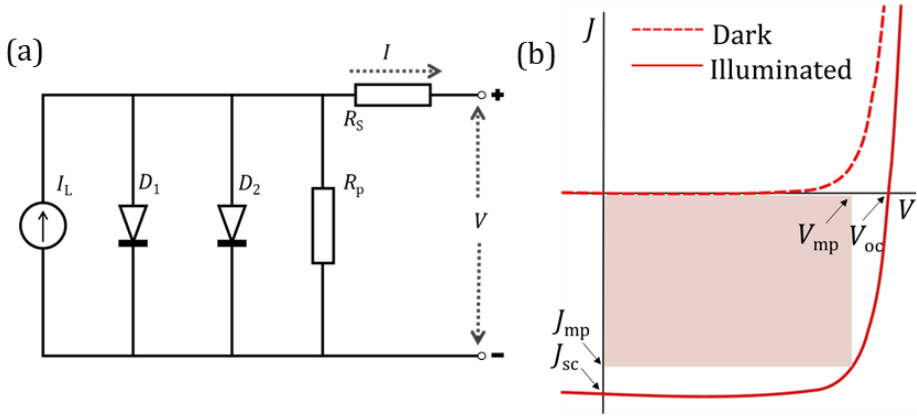
Figure 2.6: (a) Equivalent circuit of the solar cell as a two-diode model. (b) J- V curves of the solar cell in dark and under illumination.

The recombination losses are represented by the diodes D_1 and D_2. D_1 is the ideal diode, corresponding to the direct recombination with ideality factor $g = 1$. The diode D_2 is associated to the impurity recombination or device edge recombination with an ideality factor of $g = 2$. In parallel with the two diodes of the two-diode model, the resistance R_p represents the shunts that occur at the surfaces, at the pin holes between the metal contact and the absorber, or at the grain boundaries. The voltage drop across the transport resistance of the solar cell and connections to the external circuit is accounted by the series resistance R_s in the two-diode model. The working point of the diodes is represented by the external voltage V. The current leaving out of the solar cell from the two-diode model is adequately defined by Eq. 2.4.

$$J(V) = \frac{J_{0,1}\left\{\exp\frac{q[V-J(V)R_s]}{g_1 k_B T} - 1\right\} + J_{0,2}\left\{\exp\frac{q[V-J(V)R_s]}{g_2 k_B T} - 1\right\}}{+\frac{V-J(V)R_s}{R_p} - J_{ph}} \quad (2.4)$$

where $J_{0,1}$ and $J_{0,2}$ are the recombination currents to the diodes D_1 and D_2 reflected in the first two terms of the Eq. 2.4. The term J_{ph} represents the voltage-independent photogenerated current, the parameter which differentiates a diode in dark and a solar cell.

For simplicity, the two-diode equation can be expressed as the single-diode equation with the series R_s and parallel resistance R_p as,

$$J = J_0 \left\{ \exp \left(\frac{q[V - J(V)R_s]}{g k_B T} \right) - 1 \right\} - \frac{V - J(V)R_s}{R_p} - J_{ph} \qquad (2.5)$$

where g is the ideality factor, J_0 is the recombination prefactor, k_B is the Boltzmann constant and T is the temperature.

The evaluation of the solar cell performance involves three parameters, the the open-circuit voltage, the short-circuit current density and the fill factor.

The **open-circuit voltage (V_{oc})** is the voltage extracted when $J = 0$, and that is the maximum volatge a solar cell can generate. According to Eq. 2.5, when there is no current flowing through the circuit R_s does not infuence the V_{oc}. In the limit of a high R_p and with fixed photo-generated current J_{ph}, the V_{oc} is limited by the recombination process, which can be used as a figure of merit to quantify the passivation quality of the devices.

The **short-circuit current density (J_{sc})** is the current when $V = 0$, and that is the maximum current that can be extracted from the solar cell. $J_{sc} = J_{ph}$ in the ideal conditions of high R_p and no recombination ($J_0 = 0$). Actually, at zero external voltage, J_{sc} is lowered by the recombination current, but it remains strongly reliant on photogeneration and is thus frequently employed as a figure of merit for the optical features of the solar cell.

The **fill factor (*FF*)** is defined as the ratio between the maximum power density (mp) delivered by the cell, i.e., $V_{mp} \cdot J_{mp}$, and the $V_{oc} \cdot J_{sc}$ product (maximum ideal power density delivered by the cell), see Eq. 2.6. The *FF* specifies the "squareness" of the light *J-V* curve shown in Fig. 2.6. The fill factor depends on the carrier transport and recombination in the solar cells.

$$FF = \frac{J_{mp}V_{mp}}{J_{sc}V_{oc}} \qquad (2.6)$$

The **power conversion efficiency (*PCE*)** can be expressed by combining the aforementioned parameters as:

$$PCE = \frac{P_{\text{out}}}{P_{\text{in}}} = \frac{J_{\text{sc}} V_{\text{oc}} FF}{P_{\text{in}}} \qquad (2.7)$$

where P_{out} is the maximum output power at the maximum-power point and P_{in} is the total incident power on the solar cell. P_{in} is calibrated to 1000 W m^{-2}, spectrally weighted according to the AM1.5 spectrum.

The **external quantum efficiency (*EQE*)** is another essential parameter that quantifies the number of incoming photons incident on the solar cell converted to electron-hole pairs in the absorber layer, which are successfully collected. The *EQE* is wavelength dependent and is obtained by step-by-step illuminating the device at each spectrum wavelength (λ) while measuring the resulting photocurrent, $I(\lambda)$. The *EQE* is determined as

$$EQE(\lambda) = \frac{I(\lambda)}{q \, \Phi(\lambda)} \qquad (2.8)$$

where $\Phi(\lambda)$ is the spectral photon flow and q is the elementary charge.

2.2 c-Si heterojunction solar cells

The heterojunction approach is a promising innovation in the field of photovoltaics that has already demonstrated high efficiency solar cells on industrial scale. In heterojunction technology two distinct types of semiconductor materials are combined in the same device. The first heterojunction solar cell was developed in 1983 as the bottom cell of a tandem junction solar array [9]. The so-called heterojunction intrinsic thin-layer (HIT) solar cell concept was introduced by Sanyo (now Panasonic), and it features a thin buffer layer of undoped hydrogenated amorphous silicon (a-Si:H, $E_g \sim 1.7$ eV) between the c-Si wafer ($E_g \sim 1.1$ eV) and a doped a-Si:H layer [10]. The schematic representation of the HIT structure is shown in Fig. 2.7.

Chemical surface passivation of the c-Si absorber is provided by the a-Si:H; specifically, a 5-10-nm-thick layer of intrinsic a-Si:H. The carrier-selective contacts are formed by *p*- or *n*-type doped a-Si:H, both on a scale of

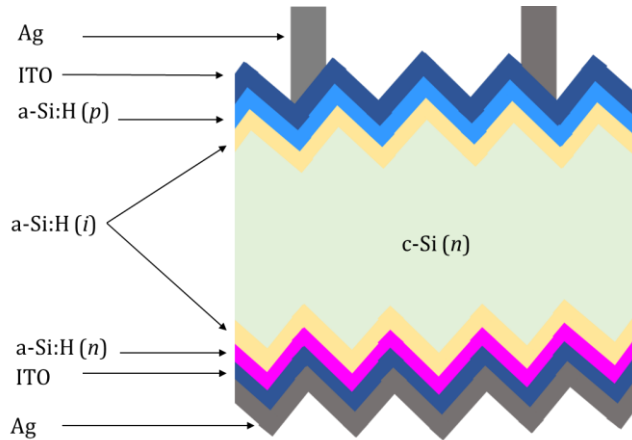5-15 nm. The thickness of these layers must be as thin as possible to prevent the parasitic absorption.

Figure 2.7: Schematic illustration of a crystalline silicon heterojunction solar cell.

Plasma-enhanced chemical vapor deposition (PECVD) is typically used for the a-Si:H deposition. The absorber layer is typically made of *n*-type c-Si wafers of thickness around 130 μm. To improve light coupling into the absorber, a TCO layer, usually indium tin oxide, is required as a third layer between the metal contacts and the doped a-Si:H layers. TCO as the front contact, it decreases series resistance and as back contact it avoids metal diffusion and enhances reflectance. Magnetron sputtering is widely utilized as a reliable, large-scale technique for TCO deposition. For the metal contacts, silver (Ag) paste is screen-printed onto the TCO, and then cured at a low temperature (200 °C).

The advantages of the HIT technology are its simple structure, low-temperature processing, high stability and improved high-temperature efficiency. Fig. 2.8 shows the band diagram of the standard *n*-type heterojunction silicon solar cell. The heterojunction of a-Si:H/c-Si is formed by two materials of different band gaps (E_g) (c-Si = 1.12 eV, a-Si:H = 1.75 eV) and with difference in the electron affinities (EA) (c-Si = 3.9 eV, a-Si:H = 4.05 eV). The band offsets formed at the conduction and valence band edges (ΔE_c and ΔE_v) are due to the differences in band gaps and electron affinities

[11]. The difference in electron affinities equals the ΔE_c in the conduction-band edge and the difference both electron affinities and band gaps equal ΔE_v in the valence band edge.
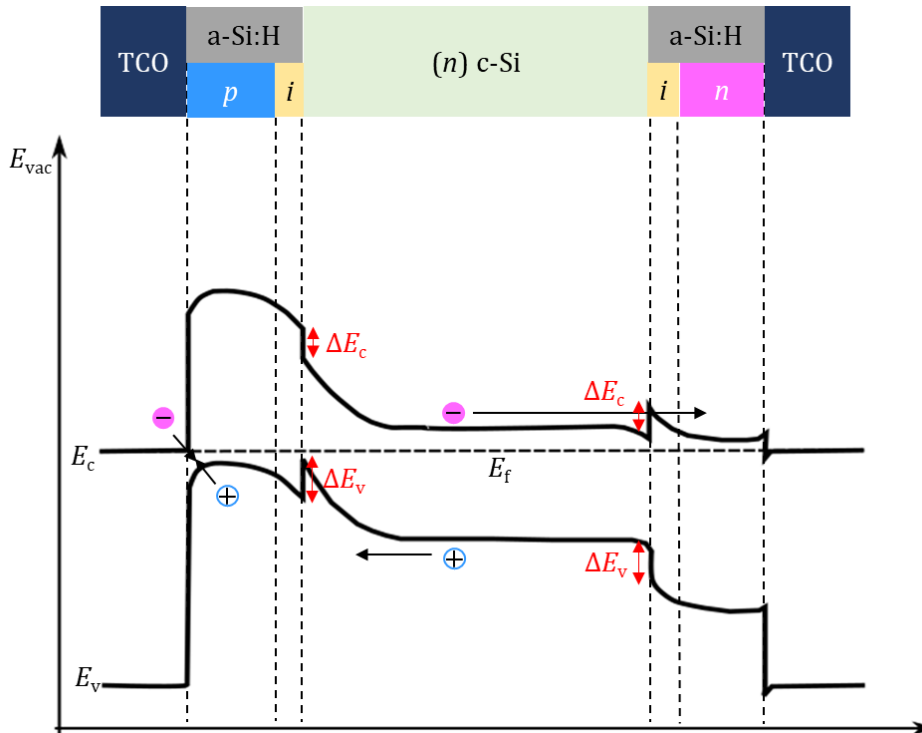

Figure 2.8: Band diagram of the *n*-type heterojunction silicon solar cell. The front is a-Si:H(*i/p*) stack and rear side with the a-Si:H(*i/n*) stack, respectively.

As a result, in a-Si:H/c-Si the valence band offset is greater than in the conduction band offset [12]. Such that the minority carrier holes may become stuck in the potential well caused by the significant valence band offset at the front junction, therefore efficient transport of photo-generated carriers is hindered. However, it is possible for the trapped holes to tunnel through the extremely thin a-Si:H(*i*) layer and into the a-Si:H(*p*) emitter. The broad valence band offset on the rear creates a "mirror" for holes. With such

a little offset at the conduction band, electron collection at the rear contact is highly effective by a-Si:H(i/n) stack [13].

The dangling bonds are the primary source of defect on the crystalline silicon surface: their presence at the contact produce recombination losses, which reduce solar cell performance. Field-effect passivation minimizes excess carrier concentration establishing an electric field. It is achieved by inserting a highly doped a-Si:H(n) on c-Si. Chemical passivation uses a thin coating of a-Si:H(i) at the surface of c-Si contact therefore hydrogen atoms link to the surfaces, thus minimizing the dangling bonds.

To summarise, the standard heterojunction devices are typically obtained by depositing amorphous silicon films on crystalline substrates as the carrier selective contacts. However, hydrogenated amorphous silicon solar cells have a few drawbacks. These include parasitic absorption, use of expensive PECVD systems, and use of hazardous gas precursors to grow the doped layers. Moreover, the TCO layer is typically tin doped indium oxide (ITO). Therefore, due to the scarcity of indium sources, which has resulted in an ever-increasing indium price, there is an urgent need to reduce the use of indium or to identify new materials that might act as transparent conductors. Recently, the concept of charge-carrier selective contacts using materials other than doped a-Si:H has emerged in the field of semiconductor devices. Typically, the transition metal oxides and organic selective contacts are attracting interest as a possible replacement for the doped amorphous silicon layer because of its excellent optoelectronic properties and as well due to its associated simple deposition techniques and supplies.

2.3 Transparent conductors

Transparent conductors are materials that simultaneously possess high electrical conductivity and high transparency. Due to this unique trade-off, transparent conductors are of great interest for a broad range of applications, such as photovoltaic devices, light emitting diodes (LEDs), flat panel displays, smart windows and optical coatings. The most employed transparent conductors are TCOs consisting of wide band gap semiconductors (E_g > 3 eV) [14][15]. Typically, n-type semiconducting

materials such as ITO and aluminum-doped zinc oxide (AZO) are used as TCOs. Other alternatives to the TCOs are dielectric-metal-dielectric (DMD) structures, metallic nanowire networks, carbon nanotubes, conductive polymers, graphene, and ultra-thin metallic films [16][17][18][19][20].

2.3.1 Electrical conductivity

The high electrical conductivity of *n*-type TCOs is due to the degenerate doping and shifting of the Fermi level into the CB. Their electrical conductivity is dominated by the flow of free carriers, which behave as an electron gas [21][22]. The electrical conductivity (σ) is expressed as

$$\sigma = q\mu N_e \tag{2.9}$$

where q is the elementary charge, μ is the electron mobility ($cm^2\,V^{-1}\,s^{-1}$) and N_e is the free-carrier concentration (cm^{-3}). The conductivity is expressed in the unit of $S\,cm^{-1}$. The resistivity is expressed as the inverse of the conductivity. Commonly, sheet resistance (R_{sh}) of the films is calculated as the average of resistivity (ρ) over the thickness of the film (t), by means of the following expression:

$$R_{sh} = \frac{\rho}{d} = \frac{1}{\sigma t} \tag{2.10}$$

Therefore, the sheet resistance depends on N_e, μ and thickness of the films, where N_e depends in turn on the doping concentration of the films and the mobility is related to the electron transport in the films. Mobility can be understood as the ease with which an electron can move through the lattice of a material in response to an external electric field.

2.3.1.1 Doping mechanisms

Low resistivity in *n*-type doped degenerate TCOs could be accomplished by various doping mechanisms:

(i) Intrinsic doping: Is the kind of doping in which the lack of oxygen during the deposition process (sub stoichiometry), causes donor-type vacancies in the films. The oxygen vacancies could act as doubly-charged donors

---

contributing with two electrons. This could achieve degeneracy, but not for boosting the mobility as observed mostly in In_2O_3 films [23].

(ii) Extrinsic doping: It consists in the introduction of foreign cation or anion dopants to replace metal or oxygen atoms from the TCOs. They act as single-charged donors. The proper dopant selection either lowers scattering caused by ionized or neutral impurities or improves film structure by decreasing the impact of grain boundaries, both effects maximizing the mobility of the films. The cation-doped (Ti, Cr, V, Zr, Mo, Ce, Hf, Ta, W, Zn, Zr) In_2O_3 films have attained a mobility greater than 60 cm^2 V^{-1} s^{-1}, better than the conventional Sn doping [24][25][26]. Nevertheless, anion doping in these films is much less explored. Among them, fluorine-doped indium oxide (IFO) is found to be a suitable candidate. Here, the substitutional replacement of F$^-$ with O^{2-} takes place because of the ion radius of F$^-$ being similar to that of O^{2-}, thus causing a minor distortion in the lattice and high mobilities above 90 cm^2 V^{-1} s^{-1} [27].

(iii) Hydrogen doping: In recent years, several studies have highlighted the positive effect of adding hydrogen to the reactive atmosphere for the deposition of both In_2O_3- and ZnO-based TCOs. The results show mobility and carrier concentration being successfully controlled by the amount of hydrogen (or water) input [28][29][30]. Hydrogen atoms were found to contribute to the high electron mobility of hydrogen-containing indium oxide-based TCOs by, (i) acting as singly-charged donors [31], (ii) passivating cation vacancies as well as defects at the grain boundaries [32], and (iii) playing a critical role in the crystallization process of amorphously grown, and subsequently solid phase crystallized, TCOs [33].

2.3.1.1 Transport mechanisms

The high carrier concentrations and high mobilities in the TCO films contribute to their low resistivities. Heavy doping in the films could lead to (i) reduced electron mobility due to the higher presence of scattering centers such as ionized dopant atoms, (ii) free-carrier absorption at longer wavelengths due to high concentration of charge carriers, and (iii) phase separation, in case that impurity concentration is high enough. Increasing

electron mobility is one way to counteract these effects. However, there are several phenomena that can restrict electron mobility [34][35][36]:

(i) Ionized impurity scattering (μ_i): Ionized impurities such oxygen vacancies, dopants, or excess metal atoms are common in heavily-doped TCOs. In degenerated semiconductors, such impurities serve as powerful electron scattering centers, where scattering typically increases at higher charge carrier density.

(ii) Neutral impurity scattering (μ_n): It is the scattering induced by the neutral impurities such as atoms. This scattering plays a minor role in heavily-doped TCOs.

(iii) Scattering at grain boundaries (μ_g): It is the scattering caused by disordered atoms present at the boundaries of regions with differing lattice orientations. This results in incomplete atomic bonding and, as a result, a significant defect density. The electron current through the TCO is disrupted when electrons become trapped at these defects, thus creating a potential barrier. The electron transport through these potential barriers can be caused by three distinct mechanisms: field emission (tunneling), thermionic emission and thermionic field emission (a combination of field emission and thermionic emission).

(iv) Lattice vibration scattering (μ_l): At increasing temperatures, there is a general rise in the lattice vibration scattering. As the lattice vibration increases, the lattice may deform. This gives rise to acoustic phonon generation, in turn inducing scattering that limits the mobility of electrons.

(v) Other scattering mechanisms (μ_x): There are also other mechanisms that cause electron scattering, such as piezoelectric scattering, dislocation scattering, etc.

The scattering effects on the electron mobility can be described by the equation:

$$\frac{1}{\mu} = \frac{1}{\mu_i} + \frac{1}{\mu_l} + \frac{1}{\mu_g} + \frac{1}{\mu_n} + \frac{1}{\mu_x} \tag{2.11}$$

2.3.2 Optical properties

Total Transmittance (TT), Total reflectance (TR), and absorptance (A) are three primary wavelength-dependent phenomena that can result from the interaction of light with a material. These phenomena often occur simultaneously, obeying the following relation:

$$1 = A(\lambda) + TT(\lambda) + TR(\lambda) \tag{2.12}$$

where the sum accounts for the total amount of incident radiation. For solar cell applications, the electromagnetic spectrum of interest can be divided into three main regions:

(i) Ultraviolet region (300–400 nm): Here, fundamental absorption dominates, caused by the transition of electrons from the valence to the conduction band, which is sensitive to the optical band gap. The absorption coefficient (α), which could be determined from the transmittance and reflectance, is given by [37],

$$TT \approx (1 - TR)^2 \exp{(-\alpha t)} \tag{2.13}$$

where, TT and TR are the total transmittance and reflectance, respectively, and t is the thickness of the film. For direct transitions, the band gap determined from the absorption coefficient follows the expression:

$$\alpha h\nu = B\big(h\nu - E_{\mathrm{g}}\big)^{1/2} \tag{2.14}$$

where $h\nu$ is the incident photon energy, E_{g} is the band gap energy and B is a constant parameter.

(ii) Visible region (400–1000 nm): This is known as the *optical window* of TCOs, where the absorption is typically very low (less than 10%). This transparent window makes the TCOs appropriate for their use as electrodes in silicon solar cells and other optoelectronic applications.

(iii) Infrared region (1000–2500 nm): In this region free-carrier absorption takes place, due to the collective oscillations of the free carriers.

The increased charge carrier density or heavy doping results in an increased free-carrier absorption in in this region.

2.3.3 Fluorine-doped indium oxide films

Several cation doping in In_2O_3 films have been recently explored but anion doping in In_2O_3 is much less explored. Different deposition techniques have been adopted to fabricate conductive IFO films. Such as ion plating, spray pyrolysis, chemical vapor deposition, and RF sputtering.

Avaritsiotis *et al*. fabricated IFO films by reactive ion plating. The fluorine doping in In_2O_3 films were done by introducing the CH_4 as the gaseous fluorine dopant during the rf discharge. These films showed a sheet resistance of 40 Ω/Sq and achieved a mobility of 13 $cm^2V^{-1}s^{-1}$ [38].

The IFO films were prepared by spray pyrolysis by Singh *et al*. The IFO films were prepared using the aqueous solution of NH_4F as the fluorine dopant, these films had a sheet resistance of 10 Ω/Sq and achieved a mobility of 48 $cm^2V^{-1}s^{-1}$ [39]. Untila *et al.* have used the ultrasonic spray pyrolysis to fabricate the IFO films and have shown an efficiency of 18% in silicon solar cells [40].

IFO films were also prepared by chemical vapor deposition using indium 2- ethylhexanoate and indium fluoride as the raw materials by Maruyama *et al.* These films were obtained at a temperature of 330 - 430 °C and showed a resistivity of 2.89×10^{-4} Ω cm [41].

The RF magnetron sputtering is the most promising techniques that uses the low temperature process and that could be easily commercialized. But only few works were reported in for IFO films using this technique. Shigesato *et al*. have prepared the IFO films by two methods using the InF_3 pellets and by introducing CF_4 gas to the chamber. They have obtained films with mobility of 40 $cm^2V^{-1}s^{-1}$ and a carrier density around 2×10^{20} cm^{-3} [42]. Recently Han *et al*. demonstrated high mobility IFO films by RF sputtering with mobility of 87 $cm^2V^{-1}s^{-1}$, a carrier density of 1.2×10^{20} cm^{-3}. These films were prepared using an IFO target and the fabricated silicon solar cells showed an efficiency of 21.1% [27].

2.3.4 Alternatives to TCOs

Ultra-thin metal films and dielectric-metal-dielectric structures

Ultra-thin metal films are films of atomic layer thickness that act as a transparent electrode alternative to the TCOs. Examples of this films can be found in Ag-coated waveguides, vanadium thin films for optical switches, etc. For those applications the most important characteristics of the films are related to the film thickness, in order to minimize detrimental optical losses [38]. Therefore, it is very interesting to study an effective method such as sputtering or thermal evaporation to develop these very thin layers with thicknesses under 10 nm. However, the main disadvantage of this method is the agglomeration of the metal atoms, which related to the lack of uniformity of the ultra-thin films. The uniformity and roughness of the deposited layer may be affected by factors such as the surface topography and the rate of deposition, as well as the presence of interatomic or intermolecular cohesive forces, which are unique to each material. For the ultra-thin films, mostly three growth mechanisms are encountered (see Fig. 2.9): the Frank–van der Merwe growth, the Volmer–Weber growth, and the Stranski–Krastanov growth [39].

(i) Frank–van der Merwe growth: In this mechanism, the growth occurs as sequential occupation of layers. It is also known as the *layer-by-layer growth*, because the formation of a new layer starts only after the growth of the previous layer is complete. This is shown in Fig. 2.9(a). In most of the cases this growth is preferable to produce smooth films thanks to the high wettability of the deposited materials.

(ii) Volmer–Weber growth: Here, the growth is defined by the formation of three-dimensional islands on the substrate, also called *island growth*. It can occur when the deposited atoms coalesce to create individual islands in materials with low wettability. This is shown in Fig. 2.9(b). Typically, soft metals exhibit this growth mechanism when deposited on insulators.

(iii) Stranski–Krastanov growth: In this growth mechanism, the growth happens initially layer-by-layer but eventually produces three-dimensional islands over a particular thickness. Typically, it is the Frank-Van der Merwe

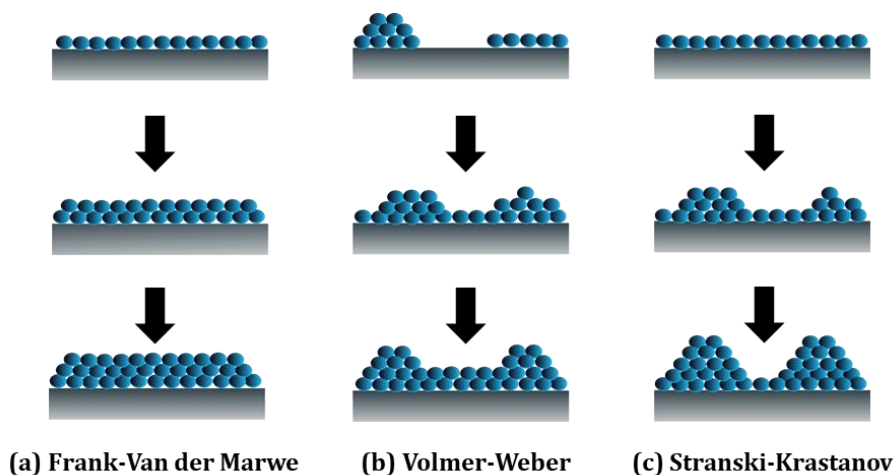nucleation phase followed by a Volmer-Webber growth phase. This is shown in Fig. 2.9(c).

Figure 2.9: Growth mode of thin films: (a) Frank–van der Merwe growth, (b) Volmer–Weber growth and (c) Stranski–Krastanov growth.

As it will be described in chapter 4 of this thesis, the fundamental difficulty encountered in the growth of ultra-thin films of Ag is the coalescence threshold. Usually, strategies such as depositing a seed (wetting) layer and co-sputtering of metals have been employed to lessen these phenomena and to increase the smoothness while reducing the thickness of the films.

An example of utilisation of ultra-thin metallic films are DMD structures, which consist of an ultra-thin metal film sandwiched between two dielectric films. The metallic film enhances the conductivity of the structure, whereas the two dielectric films improve the optical transparency of the structure by combined light interference effect. The low resistivity metals such as Ag, Au and Cu (ρ_{Ag} = 1.6 µΩ cm, ρ_{Cu} = 1.7 µΩ cm, and ρ_{Au} = 2.4 µΩ cm at 20 °C) are the most employed metallic layers. The equivalent circuit can be understood from Fig. 2.10, where three parallel resistances (R_0 for the dielectric –TCO in this case– films and R_M for the metal layer) are considered, the total resistance (R_T) being defined as [40]:

$$1/R_\mathrm{T} = 1/R_\mathrm{M} + 2/R_\mathrm{O} \qquad\qquad (2.15)$$

Since the resistivity of these metals is more than an order of magnitude smaller than that of TCOs, the resistance of DMD structures is mostly related to that of the metal film. Even though the metallic layer provides high conductivity to the DMD layers, the optical transmittance of the films is limited by the thickness of both the metallic layer and dielectric films.
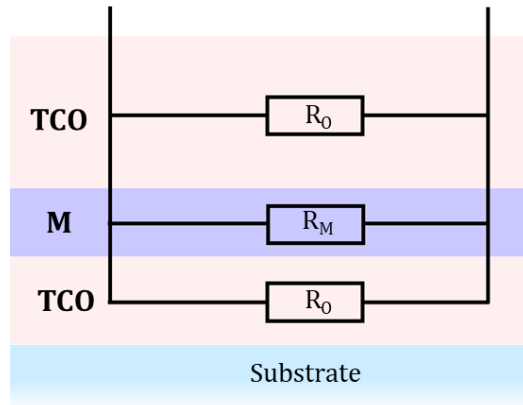

Figure 2.10: Equivalent scheme of the TCO/Metal/TCO (DMD) structures.

The usage of a metal layer in the DMD approach poses an evident drawback as a consequence of the metal own nature: the metallic layer prevents achieving high transmittance because of the huge amount of mobile charge carriers, which causes high reflectance. The density of charge carriers (electrons) in metals like Al or Ag is roughly 10^{23} cm^{-3}. Because of this, metals reflect visible light very well, giving them their dazzling appearance. To overcome this disadvantage, the reflectance of the metal must be reduced, which can be done by modifying the refractive index along the path of light. When a metal is placed between two dielectrics, the overall reflectance can destructively interfere if the dielectric refractive indices and layer thicknesses are selected accordingly. Therefore, the own DMD structure acts against the reflectance limitation of the metal layer.

Besides the thickness, choosing the proper dielectric is crucial for the final optoelectronic properties of the multi-layered stack. In this sense, transition metal oxides (TMOs) such as vanadium, tungsten, and molybdenum oxides, are very interesting dielectrics for DMD structures. Some of the interesting features of TMOs are their high refractive index, their large work function that ranges from 2 to 7 eV, and their wide band gap (> 3 eV) [41]. These materials possess an extraordinary transparency to visible light, and they can be used as the ARC layers on silicon due to their band gap and refractive index. Furthermore, their deep work function allows TMOs to actively participate in the band structure of the device, selectively collecting holes over electrons.

2.3.5 AZO/Ag:Al/AZO multilayer structures

Recently, dielectric-metal-dielectric (DMD) structures have emerged as valid candidates to substitute the ITO electrode in silicon solar cells. But these DMD structures were fabricated using the thermal evaporation technique. The main disadvantage of this method is the agglomeration of the metal, related to the particular growth mode (i.e., Volmer-Webber type) of the deposited film. In order to overcome these disadvantages several AZO/Ag/AZO DMDs were fabricated using sputtering.

Sutthana *et al*. fabricated AZO/Ag/AZO multilayer structures using DC magnetron sputtering yielding a sheet resistance of 19.8 Ω/Sq and an average transmittance in the visible region of 61%. The dye-sensitized solar cell fabricated using this DMD structure showed a PCE of 0.61% [47]. Later Park *et al* showed that AZO/Ag/AZO transparent multilayered electrodes fabricated by RF magnetron sputtering on perovskite solar cells yielded an efficiency of 18.3% [48]. Finally, Al doping effects on a thin Ag layer and AZO/Ag/AZO multilayers were investigated by Sugimoto *et al*. These films were fabricated by ion beam sputtering showed an average transmittance of 66.8 % and a sheet resistance of 3.6 Ω/Sq [49].

2.4 Transition metal oxides as hole transport layers

A breakthrough in crystalline silicon solar cells in the past decades is the development of passivating selective contacts. Thin films of intrinsic and doped a-Si:H emerged as the most promising materials for this application. However, the a-Si:H layers suffer from high temperature and complex deposition techniques involving the use of hazardous gases in the fabrication process. Moreover, defects created in the doping process are a cause for parasitic absorption and recombination in the films. To minimize these losses, doped layers could be replaced with materials of wide band gap and appropriate work function. A prime example for these materials is TMOs due to its combination of large band gap (E_g > 3 eV) and wide range of work function (from 3 to 7 eV). The large band gap offers higher optical transparency while the wide work function offers hole and electron collection from c-Si, which improves the J_{sc} in silicon heterojunction (SHJ) [50].

The preferred HTLs are TMOs with high work-function (ϕ > 7 eV), such as molybdenum oxide (MoO$_x$), tungsten oxide (WO$_x$) and vanadium oxide (V$_2$O$_x$); whereas the preferred ETLs are low work-function (Φ < 4 eV) TMOs such as magnesium oxide (MgO$_x$) and titanium oxide (TiO$_x$). The energy diagram of different HTL materials indicating different band energies are shown in Fig. 2.11 [51]. In addition, they could be deposited by a broad variety of techniques (e.g., thermal evaporation, sputtering, spin-coating, atomic layer deposition, etc.), this idea can help to eliminate high temperature diffusion processes and lead to simple, cleaner, and cheaper fabrication processes in silicon solar cells.

The working principle of TMO-based HTLs relies on the *n*-type doping and the extremely high work function of TMO materials that induces a strong hole inversion layer or band bending at the *n*-type c-Si. Typically, an interfacial dipole is present at the inverted *n*-Si interface. The resulting band structure is shown in Fig. 2.12, where electrons are blocked due to the build-in energy barrier like that of p^+n junctions. On the other hand, the photogenerated holes collected from the c-Si, following a multi-tunneling

capture and emission (MTCE) mechanism, recombine with the electrons from conduction band of TMO [52].
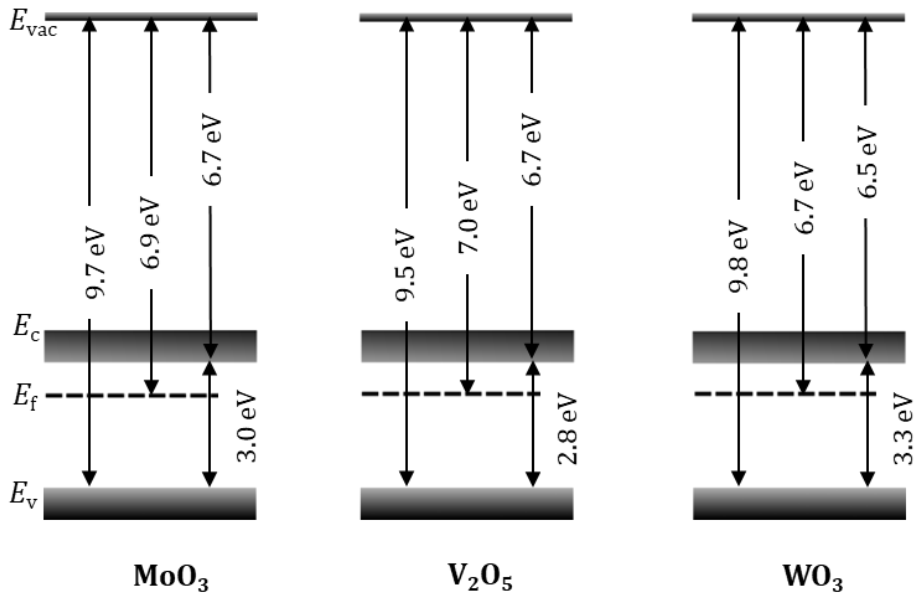

Figure 2.11: Energy band diagram of different TMO materials indicating different band energies with respect to vacuum level.

Finally, for the TMO layers to work as an excellent HTL, in addition they need an increased density of defects or oxygen deficient sites such that they could sustain the charge-carrier transport by the MTCE. For that reason, the TMOs must be sub-stoichiometric (oxygen deficient), which accounts for their *n*-type behaviour. Therefore, the hole collection efficiency of the TMO devices depend on the degree of surface inversion and defect density of the films [52].

In conclusion, in order for TMOs to behave as an excellent hole contact, they must have (i) oxygen vacancies, making it an *n*-type semiconductor, (ii) higher work function (although large number of oxygen vacancies decreases their work function), and (iii) positive band bending by the higher work function of TMOs which can be observed by measuring the difference

between the implied and the external open circuit voltage ($\Delta V = iV_{oc} - V_{oc}$) [53][54].
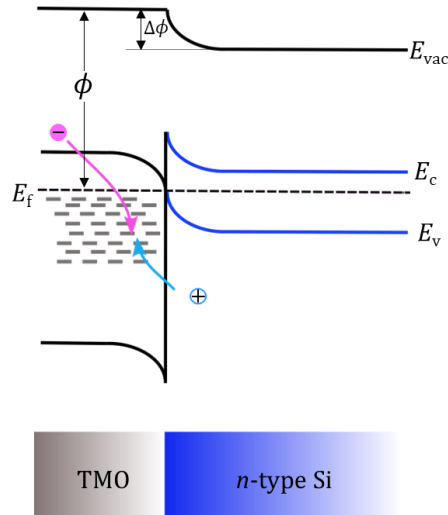
Figure 2.12: Band diagram of TMO layer deposited on *n*-type Si. The high work function of TMO induces a strong band bending at the interface.

2.4.1 Molybdenum trioxide

MoO_3 in its sub-stoichiometric form is the one most promising HTL that has been well studied due to its high stability. The *n*-type behaviour of the MoO_x films is due to the oxygen vacancies that influence its optical and electrical properties. Therefore, many processing techniques have been studied to fully realize the potential of MoO_x films. MoO_x-based HTL layers were manufactured by a variety of methods such as solution process using organic precursors, atomic layer deposition (ALD), thermal evaporation, electron beam evaporation and sputtering.

Tong *et al.* have demonstrated that the solution-processed molybdenum oxide films on c-Si shows a low contact resistivity and a high passivation quality [55]. But the first solution-processed MoO_x as HTL for silicon solar cells was reported by Lu *et al.*, showing a *PCE* of 8.22%, V_{oc} of 463 mV, J_{sc} of

31.16 mA cm^{-2}, and *FF* of 56.87% [56]. The best *PCE* of 11.8% for solution processed MoO$_3$ was reported by Wang *et al.* [57].

Macco *et al*. have shown the preparation of sub-stoichiometric MoO$_x$ with high passivation quality [implied open circuit voltage(*iV*$_{oc}$) of 717 mV] by plasma-enhanced ALD [58]. Low contact resistivity of 4.59 mΩ cm^2 for MoO$_x$/SiO$_x$ stack on *p*-type c-Si was reported by Gregory *et al*. [59]. In this case, the MoO$_x$ was deposited by ALD and a thin tunnelling SiO$_x$ layer was grown after a short ultraviolet (UV)-ozone treatment.

Yu *et al.* demonstrated a *PCE* of 14% on crystalline silicon solar cells with electron-beam-evaporated molybdenum oxide and magnesium oxide as deposited as HTL (front) and ETL (rear) contacts, respectively [60]. Sen *et al.* have shown a *PCE* of 16.1%, *V*$_{oc}$ of 696 mV, *J*$_{sc}$ of 37.5 mA cm^{-2}, FF of 61.5% for crystalline silicon solar cells with electron-beam-evaporated MoO$_x$ as HTL [61].

Bivour *et al*. have demonstrated passivation and clear correlation between the induced c-Si band bending and the hole selectivity of annealed sputtered MoO$_x$ on c-Si [62]. Parashar *et al*. have investigated sputtered sub-stoichiometric molybdenum oxide on c-Si. For c-Si/MoO$_x$ cell, the *PCE* was enhanced from ~3.0% to ~4.3% after including a SiO$_x$ passivating layer between the c-Si and MoO$_x$ [63].

The first conjunction of transition metal oxides with *n*-type silicon absorber was demonstrated by Battaglia *et al.* [64], by employing an ultrathin (~15 nm in thickness) thermally-evaporated sub-stoichiometric molybdenum oxide layer as a transparent HTL. These solar cells achieved a *PCE* of 14.3%. The work from Gerling *et al*. achieved a *PCE* of 13.6% with a *V*$_{oc}$ of 581 mV for vacuum thermal-evaporated of MoO$_x$ as HTL in silicon heterojunction solar cells [65]. A significant *PCE* of 20% was achieved by Mallem *et al.*, showing the superior hole extraction of thermally-evaporated MoO$_x$ in silicon heterojunctions [66]. Later, Dreon *et al.* have demonstrated an increased *PCE* of 23.5% with a FF of 81.8% for thermally-evaporated MoO$_x$ [67]. The highest efficiency achieved for solar cells with ultra-thin hole collector up to date is from Cao *et al.*, showing a *PCE* of 23.83%. The cells

were fabricated with 1.7-nm-thick MoO_x with a demonstrated J_{sc} well above 40 mA cm^{-2} [68].

2.5 Electron transport layers – Organic molecules as dipoles

Carrier selective contacts based on organic molecules as ETL and HTL for silicon heterojunctions have attracted research interest due to their highly adjustable electronic and chemical properties and cheaper fabrication process. Interfacial layers based on organic molecules have been shown to modify the apparent work function (ϕ') of metallic electrodes. In this sense, the electric dipole moment of these interlayers has been proven to be capable of shifting the electronic band alignment across the interface and therefore the properties of the metal/semiconductor junction. Thus, these interfacial layer helps attaining a better selective carrier transport, reduced recombination by effective passivation, improved physical contact, and avoiding the Fermi level pinning (FLP) [69][70], which will be described later in this chapter. Various organic molecules investigated for ETL layers such as conjugated polyelectrolyte (CP), poly [(9,9-bis(3′-(N,N-dimethylamino)propyl)-2,7-fluorene)-alt-2,7-(9,9-dioctylfluorene), amino acids such as glycine, histidine, phenylalanine, and HTLs such as poly(3,4-ethylene dioxythiophene):poly-(styrenesulfonate), fluorescent polymer poly(9,9-dioctylfluor- enyl-2,7-diyl), and Lissamine Green B, have reported good efficiencies beyond 14% [71][72][73][74].

2.5.1 Electric dipole films

An electric dipole consists of two point charges, $+q$ and $-q$, separated by a distance $\vec{d}$. The electric dipole moment is defined as the magnitude of charge times the distance, $\vec{p} = q\vec{d}$. The direction of the dipole moment is from $-q$ to $+q$. Electric dipoles can be found in every chemical system. The presence of an electric dipole is a characteristic of any asymmetric chemical bond or asymmetric molecule made up of atoms with different electronegativity. However, in most bulk materials, the tiny dipole moments cancel out, because of the random orientation in a gas, liquid, or amorphous solid. But

in the case of interfaces the intrinsic asymmetry of the interface aligns chemical bonds or causes orientation of tiny dipole moments in its proximity. A sharp potential drop occurs from the positive charge side to the negative charge side when large amounts of positive and negative charges are distributed asymmetrically in a thin layer, forming an electric dipole layer that can be approximated as a large number of single electric dipole moments arranged abreast [75]. Fig. 2.13 shows the potential distribution of an electrical dipole in a thin layer, where potential (φ) slowly decays with distance (x).
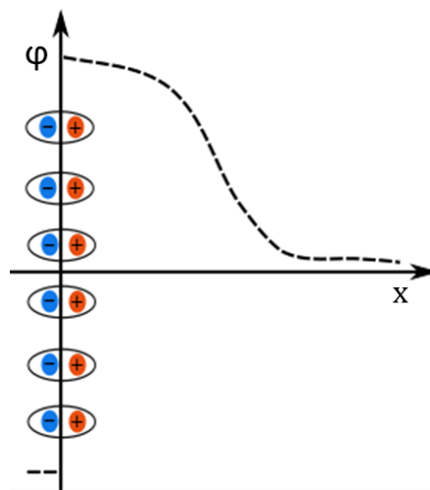
Figure 2.13: Potential distribution of an electric dipole layer as a function of the distance the dipole layer. As x increases, the potential is reduced.

2.5.2 Dipole interfaces

One of the main factors that influence the transport properties of a metal/semiconductor junction is the work function difference. In the case of *n*-type silicon, if the work function of the metal is lower than that of silicon, it produces a downward band bending that enhances the electron collection. But if the work function of the metal is greater than that of silicon, it induces an upwards band bending at the interface enhancing hole collection. This leads to the formation of a Schottky barrier at the metal/silicon interface, because the charge carriers move due to different Fermi levels until these

are equal at thermal equilibrium. The barrier height is determined by the Schottky–Mott rule, but sometimes the height of the barrier is poorly estimated by this rule due to the phenomenon known as Fermi level pinning (FLP) [6].

The FLP phenomenon arises due to the interface states located inside the semiconductor band gap. These states can be either due to the incomplete surface bonds on the surface of c-Si or due to chemical bonding between the metal and the semiconductor [shown in Fig. 2.14(a)]. Under metal-semiconductor contact the charge transfers from the metal to these interface states, which can act as donor-like or acceptor-like. This way, band bending or barrier height becomes independent of the work function but totally depends on the interface states [6][76].

The FLP can be reduced by inserting an interlayer of dipoles in between metal and semiconductor. This dipole thin layer modifies the interface and reduces the ϕ' of the metal electrode. It also protects the semiconductor from the reactive metal. The shift ($\Delta\phi$) in the apparent work function is determined by the direction in which the dipoles are arranged. If the interfacial dipole is arranged in such a way that positive charge ends pointing towards the c-Si and negative charge ends pointing towards the metal electrode, ϕ' is decreased ($\phi' = \phi - \Delta\phi$); thus, there is charge transfer from metal to semiconductor inducing a downward band bending enhancing the electron collection [see Fig. 2.14(b)]. However, if the interfacial dipole is arranged in such a way that negative charge ends pointing towards the c-Si and positive charge ends pointing towards the metal electrode, ϕ' is increased ($\phi' = \phi + \Delta\phi$); this causes the charge transfer from the semiconductor to the metal, inducing as upward band bending enhancing the hole collection [see Fig. 2.14(c)] [52].

The main conduction mechanism through the dipole layer is direct tunnelling. But if the thickness of the films is lower than a certain limit, ~1 nm, then charge transport is mainly dominated by thermionic emission partially injecting the carriers over the pinned surface. These mechanisms are proved from the contact resistivity measurements of dipoles on c-Si [77].
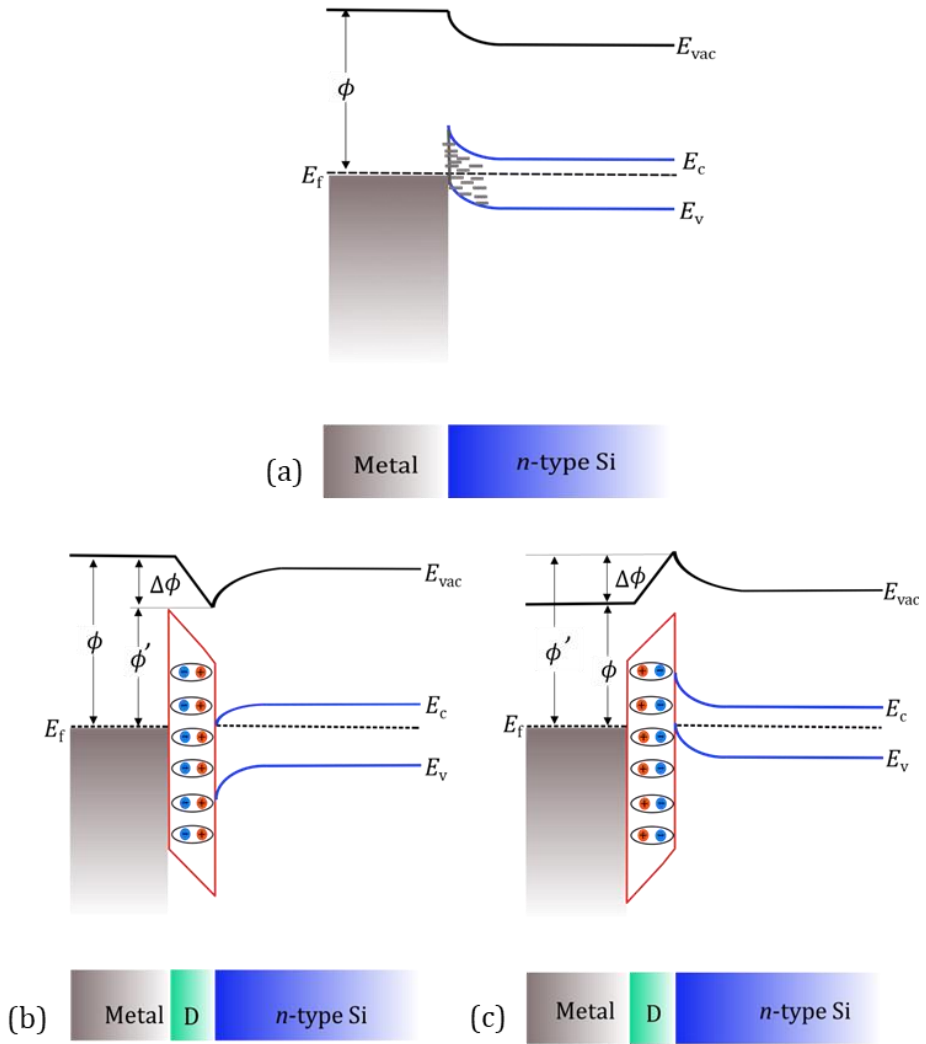
Figure 2.14: (a) Energy band diagram of a metal/Si junction with pinned Si surface. The effect of a dipole layer at the metal/silicon interface is shown in (b), where the accumulation of electrons at the interface causes downward band bending; and (c) where the depletion of electrons at the interface causes upward band bending.

2.5.3 Organic molecules used as ETLs

Branched polyethylenimine (b-PEI) is a cationic polyelectrolyte with a large number of amines. The lone pair of electrons in these amines is reactive enough to modify the interface. PEI was reported as an effective ETL for different types of solar cells.

Courtright *et al.* demonstrated PEI could be used as an ETL buffer layer for inverted organic photovoltaic devices. PEI coated on ITO/ZnO substrate provided a better photovoltaic performance with a *PCE* of 8.22% and without PEI showed a *PCE* of 6.06% [78]. High-performance inverted organic solar cells with low-temperature solution-processed ETL consisting of 10 at. % antimony-doped tin oxide (ATO) and the neutral polymer polyethylenimine (PEI) was reported by Georgiou *et al.* [79]. Polymer solar cells with a room-temperature TiO_x/PEI ETL achieving an average power conversion efficiency of 8.72% was demonstrated by Yang *et al.* [80]. Yan *et al.* investigated the effect of PEI ETL interlayer on the work function and the interface resistance of ITO electrode in inverted polymer solar cells; they have shown that champion *PCE* of the devices with the PEI cathode interlayer is 7.84%, more than doubled of that without the interlayer [81]. The use of PEI as buffer layer for ETL was also extended to perovskite solar cells by Kang *et al.* [82]. They observed that interfacial dipole and change in Fermi energy can be explained by either *n*-type doping at the interface or a reduction of the electrode work function, with a *PCE* of 15.47% in devices. The idea of PEI to be used as ETL in silicon solar cells was first demonstrated by Javey *et al.*; their silicon heterojunction solar cell integrated with b-PEI achieved a power conversion efficiency of 19.4% [83]. Yang *et al.* have reported a light-promoted adsorption method to establish high-density Lewis base PEI monolayers as ETL in SHJ achieving a *PCE* of 19.5% [84].

Polyamidoamine (PAMAM) dendrimers are regularly and hyperbranched monodisperse macromolecules that have a single core, an inner shell, and an outer shell [85][86][87][88]. The structure is typically tree-like with arms or branches representing the numerous chain ends, all emanating from a single core [89][90][91].

The potential of the dendrimers is already proven in the literature for the photovoltaic devices. Mozer *et al.* investigated the charge transfer properties of different thiophene dendrimers in a fullerene bulk heterojunction, achieving a *PCE* of 0.72% [92]. In another work, Wong *et al.* showed the performance of Self-Assembling Thiophene Dendrimers as an electron donor in bulk heterojunction with a power conversion efficiency of 2.5% [93]. In dye-sensitized solar cells, phenothiazine dendrimers were used as additives to enhance the performance of the cell to achieve an efficiency of 8.6% [94]. Recently, hole-transporting Poly(dendrimer)s were used in bulk heterojunction organic solar cells, exhibiting a fill factor of 65% and a *PCE* of 2.1% [95]. A recent study by Du *et al.* used different generations of dendrimers to regulate the perovskite intergranular interactions, finally achieving an efficiency of 14.6% in perovskite solar cells [96].

Deoxyribonucleic acid (DNA) is the most important naturally-driven biomolecule that carries genetic code in all living organisms [97][98]. DNA-composed layers exhibit unique electrochemical and optical properties with an advantageous biocompatibility and capacity to store information in nucleic acid sequences.

Recently, the use of DNA has been reported both as electron and hole transport layers in photovoltaic devices [99][100]. Yosoff *et al.* incorporated DNA-hexadecyl trimethyl ammonium chloride (CTMA) as the HTL in solution-processed low-temperature perovskite solar cells, which resulted in a *PCE* of 15.86% [101]. In another work, DNA-based hybrid materials were used for interface engineering of polymer solar cells and have achieved an efficiency of 7.6% [102]. A recent study by Hou *et al.* demonstrated the extraction and transport of holes in perovskite heterostructure-based solar cells [103]. In their work, instead of incorporating DNA as a separate layer under the perovskite, they used the idea of wrapping the core-shell heterostructure of the perovskite by DNA-CTMA through a self-assembling process, which yielded a *PCE* of 20.63%. The electron transport capacity of DNA has been also studied in recent years by Dajar *et al.* as the ETL in an organic solar cell, with a reported photovoltaic efficiency of 4.88% [104]. In another investigation, in which DNA-coated ZnO nanoparticles were used as

ETL for polymer solar cells, the authors were able to achieve an efficiency of 8.5% [105].

References

[1]   A. Cuevas, D. Yan, Misconceptions and misnomers in solar cells, IEEE J. Photovoltaics. 3 (2013) 916–923. https://doi.org/10.1109/JPHOTOV.2013.2238289.

[2]   P. Würfel and U. Würfel, Physics of Solar Cells: From Principles to New Concepts, Second, Up, Wiley-VCH Verlag GmbH & Co., Weinheim, Germany, 2009.

[3]   G. Masmitjà Rusiñol, Design, fabrication and characterisation of interdigitated back-contacted c-Si solar cells based on transition metal oxides. PhD Thesis, Universitat Politècnica de Catalunya (2019). https://upcommons.upc.edu/handle/2117/172050.

[4]   P. Bhattacharya, Semiconductor Optoelectronic Devices, 2nd ed., Prentice Hall, Hoboken, New Jersey, U.S., 2011.

[5]   A. Kahn, Fermi level, work function and vacuum level, Mater. Horizons. 3 (2016) 7–10. https://doi.org/10.1039/c5mh00160a.

[6]   K.K.N. S.M. Sze, Physics of Semiconductor Devices, 3rd ed., John Wiley & Sons, Inc., Hoboken, New Jersey, U.S., 2006.

[7]   U. Wurfel, A. Cuevas, P. Wurfel, Charge carrier separation in solar cells, IEEE J. Photovoltaics. 5 (2015) 461–469. https://doi.org/10.1109/JPHOTOV.2014.2363550.

[8]   L. Tutsch, Implementing Sputter-deposited Transparent Conductive Metal Oxides Into Passivating Contacts for Silicon Solar Cells. PhD Thesis, Fraunhofer-Institut für Solare Energiesysteme (2020).

[9]   K. Okuda, H. Okamoto, Y. Hamakawa, Amorphous Si/Polycrystalline Si Stacked Solar Cell Having More Than 12% Conversion Efficiency, Japanese J. Appl. Physics, Part 2 Lett. 22 (1983) 605–607. https://doi.org/10.1143/jjap.22.l605.

[10]   M. Tanaka, M. Taguchi, T. Matsuyama, T. Sawada, S. Tsuda, S. Nakano, H. Hanafusa, Y. Kumano, Development of new a-Si/c-Si heterojunction solar

cells: Acj-hit (artificially constructed junction- heterojunction with intrinsic thin-layer), Jpn. J. Appl. Phys. 31 (1992) 3518–3522. https://doi.org/10.1143/JJAP.31.3518.

[11]   R.L. Anderson, Experiments on Ge-GaAs heterojunctions, Solid. State. Electron. 5 (1962) 341–351. https://doi.org/10.1016/0038-1101(62)90115-6.

[12]   R. Stangl, A. Froitzheim, M. Schmidt, W. Fuhs, Design criteria for amorphous/crystalline silicon heterojunction solar cells, - A simulation study, 17th Eur. Photovolt. Sol. Energy Conf. Munich. B (2001) 1387.

[13]   Delfina Muñoz Cervantes, Silicon heterojunction solar cells obtained by Hot-Wire CVD, PhD Thesis, Universitat Politècnica de Catalunya (2008). http://hdl.handle.net/2117/93666.

[14]   A.E. Delahoy, S. Guo, Transparent Conducting Oxides for Photovoltaics, Handb. Photovolt. Sci. Eng. 32 (2011) 716–796. https://doi.org/10.1002/9780470974704.ch17.

[15]   S.C. Dixon, D.O. Scanlon, C.J. Carmalt, I.P. Parkin, N-Type doped transparent conducting binary oxides: An overview, J. Mater. Chem. C. 4 (2016) 6946–6961. https://doi.org/10.1039/c6tc01881e.

[16]   T. Tom, E. Ros, N. López-Pintó, J. Miguel Asensi, J. Andreu, J. Bertomeu, J. Puigdollers, C. Voz, Influence of Co-Sputtered Ag:Al Ultra-Thin Layers in Transparent V_2O_5/Ag:Al/AZO Hole-Selective Electrodes for Silicon Solar Cells, Materials (Basel). 13 (2020) 4905. https://doi.org/10.3390/ma13214905.

[17]   J. Krantz, M. Richter, S. Spallek, E. Spiecker, C.J. Brabec, Solution-processed metallic nanowire electrodes as indium tin oxide replacement for thin-film solar cells, Adv. Funct. Mater. 21 (2011) 4784–4787. https://doi.org/10.1002/adfm.201100457.

[18]   X. Zheng, J. Deng, N. Wang, D. Deng, W.H. Zhang, X. Bao, C. Li, Podlike N-doped carbon nanotubes encapsulating FeNi alloy nanoparticles: High-performance counter electrode materials for dye-sensitized solar cells, Angew. Chemie - Int. Ed. 53 (2014) 7023–7027. https://doi.org/10.1002/anie.201400388.

[19]   S. James, R. Contractor, Study on Nature-inspired Fractal Design-based

Flexible Counter Electrodes for Dye-Sensitized Solar Cells Fabricated using Additive Manufacturing, Sci. Rep. 8 (2018) 1–12. https://doi.org/10.1038/s41598-018-35388-2.

[20]   M. Gautam, Z. Shi, A.H. Jayatissa, Graphene films as transparent electrodes for photovoltaic devices based on cadmium sulfide thin films, Sol. Energy Mater. Sol. Cells. 163 (2017) 1–8. https://doi.org/10.1016/j.solmat.2017.01.002.

[21]   P. Drude, Zur Elektronentheorie der Metalle, Ann. Phys. 306 (1900) 566–613. https://doi.org/10.1002/andp.19003060312.

[22]   T. Conductors, Handbook of Transparent Conductors, 2010. http://www.springer.com/gp/book/9781441916372.

[23]   R. Bel Hadj Tahar, T. Ban, Y. Ohya, Y. Takahashi, Tin doped indium oxide thin films: Electrical properties, J. Appl. Phys. 83 (1998) 2631–2645. https://doi.org/10.1063/1.367025.

[24]   M.F.A.M. Van Hest, M.S. Dabney, J.D. Perkins, D.S. Ginley, M.P. Taylor, Titanium-doped indium oxide: A high-mobility transparent conductor, Appl. Phys. Lett. 87 (2005) 10–13. https://doi.org/10.1063/1.1995957.

[25]   L. Tutsch, H. Sai, T. Matsui, M. Bivour, M. Hermle, T. Koida, The sputter deposition of broadband transparent and highly conductive cerium and hydrogen co-doped indium oxide and its transfer to silicon heterojunction solar cells, Prog. Photovoltaics Res. Appl. (2021) 835–845. https://doi.org/10.1002/pip.3388.

[26]   M. Morales-Masis, S. De Wolf, R. Woods-Robinson, J.W. Ager, C. Ballif, Transparent Electrodes for Efficient Optoelectronics, Adv. Electron. Mater. 3 (2017). https://doi.org/10.1002/aelm.201600529.

[27]   C. Han, L. Mazzarella, Y. Zhao, G. Yang, P. Procel, M. Tijssen, A. Montes, L. Spitaleri, A. Gulino, X. Zhang, O. Isabella, M. Zeman, High-Mobility Hydrogenated Fluorine-Doped Indium Oxide Film for Passivating Contacts c-Si Solar Cells, ACS Appl. Mater. Interfaces. 11 (2019) 45586–45595. https://doi.org/10.1021/acsami.9b14709.

[28]   B. Macco, H.C.M. Knoops, M.A. Verheijen, W. Beyer, M. Creatore, W.M.M. Kessels, Atomic layer deposition of high-mobility hydrogen-doped zinc oxide, Sol. Energy Mater. Sol. Cells. 173 (2017) 111–119.

https://doi.org/10.1016/j.solmat.2017.05.040.

[29]   R. Chierchia, E. Salza, A. Mittiga, Effect of Hydrogen gas dilution on sputtered Al:ZnO film, Energy Procedia. 60 (2014) 135–142. https://doi.org/10.1016/j.egypro.2014.12.355.

[30]   D. Gaspar, L. Pereira, K. Gehrke, B. Galler, E. Fortunato, R. Martins, High mobility hydrogenated zinc oxide thin films, Sol. Energy Mater. Sol. Cells. 163 (2017) 255–262. https://doi.org/10.1016/j.solmat.2017.01.030.

[31]   S. Limpijumnong, P. Reunchan, A. Janotti, C.G. Van De Walle, Hydrogen doping in indium oxide: An ab initio study, Phys. Rev. B - Condens. Matter Mater. Phys. 80 (2009) 1–4. https://doi.org/10.1103/PhysRevB.80.193202.

[32]   J.B. Varley, H. Peelaers, A. Janotti, C.G. Van De Walle, Hydrogenated cation vacancies in semiconducting oxides, J. Phys. Condens. Matter. 23 (2011). https://doi.org/10.1088/0953-8984/23/33/334212.

[33]   B. MacCo, M.A. Verheijen, L.E. Black, B. Barcones, J. Melskens, W.M.M. Kessels, On the solid phase crystallization of In_2O_3:H transparent conductive oxide films prepared by atomic layer deposition, J. Appl. Phys. 120 (2016) Art. no. 85314. https://doi.org/10.1063/1.4962008.

[34]   A. Luque, S. Hegedus, Handbook of Photovoltaic Science and Engineering, 2nd ed., John Wiley & Sons, Ltd., UK, 2011.

[35]   P. Carreras, Transparent Conducting Oxides for silicon thin film solar cells: Doped and multi-compound ZnO-based transparent conducting oxides for silicon thin film solar cells. PhD Thesis, Universitat de Barcelona (2012). https://diposit.ub.edu/dspace/handle/2445/41811.

[36]   D. Erfurt, New TCO for Use as Transparent Front Contact in Chalcopyrite Thin Film Solar Cells. PhD Thesis, Technical University Berlin (2019) https://depositonce.tu-berlin.de/items/2a6dec96-a089-491f-bffa-13a02bda568c.

[37]   J.I. Pankove, Optical process in semiconductors, J. Electrochem. Soc. 119 (1975) 450.

[38]   J.N. Avaritsiotis, R.P. Howson, Fluorine doping of In_2O_3 films employing ion-plating techniques, Thin Solid Films. 80 (1981) 63–66. https://doi.org/10.1016/0040-6090(81)90207-8.

[39]   S.P. Singh, A. Raza, A.K. Sharma, O.P. Agnihotri, L.M. Tewari, Characterization of fluorine-doped In_2O_3 films synthesized by spray pyrolysis, Thin Solid Films. 105 (1983) 131–138. https://doi.org/10.1016/0040-6090(83)90201-8.

[40]   G.G. Untila, T.N. Kost, A.B. Chebotareva, E.D. Kireeva, Contact resistance of indium tin oxide and fluorine-doped indium oxide films grown by ultrasonic spray pyrolysis to diffusion layers in silicon solar cells, Sol. Energy Mater. Sol. Cells. 137 (2015) 26–33. https://doi.org/10.1016/j.solmat.2015.01.018.

[41]   T. Maruyama, K. Fukui, Indium-tin oxide thin films prepared by chemical vapor deposition, J. Appl. Phys. 70 (1991) 3848–3851. https://doi.org/10.1063/1.349189.

[42]   Y. Shigesato, N. Shin, M. Kamei, P.K. Song, I. Yasui, Study on fluorine-doped indium oxide films deposited by rf magnetron sputtering, Japanese J. Appl. Physics, Part 1 Regul. Pap. Short Notes Rev. Pap. 39 (2000) 6422–6426. https://doi.org/10.1143/jjap.39.6422.

[43]   P.J.D. Whiteside, J.A. Chininis, H.K. Hunt, Techniques and challenges for characterizing metal thin films with applications in photonics, Coatings. 6 (2016) 1–26. https://doi.org/10.3390/coatings6030035.

[44]   M. Wuttig, X. Liu, Ultrathin Metal Films, Springer, Berlin Heidelberg, 2004.

[45]   L. Cattin, J.C. Bernède, M. Morsli, Toward indium-free optoelectronic devices: Dielectric/metal/dielectric alternative transparent conductive electrode in organic photovoltaic cells, Phys. Status Solidi Appl. Mater. Sci. 210 (2013) 1047–1061. https://doi.org/10.1002/pssa.201228089.

[46]   M.T. Greiner, L. Chai, M.G. Helander, W.M. Tang, Z.H. Lu, Transition metal oxide work functions: The influence of cation oxidation state and oxygen vacancies, Adv. Funct. Mater. 22 (2012) 4557–4568. https://doi.org/10.1002/adfm.201200615.

[47]   S. Sutthana, N. Hongsith, S. Choopun, AZO/Ag/AZO multilayer films prepared by DC magnetron sputtering for dye-sensitized solar cell application, Curr. Appl. Phys. 10 (2010) 813–816. https://doi.org/10.1016/j.cap.2009.09.020.

[48]   C. Park, J.W. Lim, J.H. Heo, S.H. Im, Color Implementation of High-Efficiency Perovskite Solar Cells by Using Transparent Multilayered Electrodes, ACS

Appl.   Energy   Mater.   5   (2022)   12151–12157.
https://doi.org/10.1021/acsaem.2c01658.

[49]   Y. Sugimoto, K. Igarashi, S. Shirasaki, A. Kikuchi, Thermal durability of
        AZO/Ag(Al)/AZO transparent conductive films, Jpn. J. Appl. Phys. 55 (2016).
        https://doi.org/10.7567/JJAP.55.04EJ15.

[50]   R.A. Vijayan, S. Essig, S. De Wolf, B.G. Ramanathan, P. Loper, C. Ballif, M.
        Varadharajaperumal, Hole-Collection Mechanism in Passivating Metal-Oxide
        Contacts on Si Solar Cells: Insights from Numerical Simulations, IEEE J.
        Photovoltaics.   8   (2018)   473–482.
        https://doi.org/10.1109/JPHOTOV.2018.2796131.

[51]   J. Meyer, S. Hamwi, M. Kröger, W. Kowalsky, T. Riedl, A. Kahn, Transition
        metal oxides for organic electronics: Energetics, device physics and
        applications,   Adv.   Mater.   24   (2012)   5408–5427.
        https://doi.org/10.1002/adma.201201630.

[52]   E. Puigdollers, J., Voz, C., Ros, Physics and Technology of Carrier Selective
        Contact Based Heterojunction Silicon Solar Cells, Springer, Singapore, 2022.
        https://doi.org/10.1007/978-981-19-4526-7_2.

[53]   C. Messmer, M. Bivour, J. Schon, S.W. Glunz, M. Hermle, Numerical Simulation
        of Silicon Heterojunction Solar Cells Featuring Metal Oxides as Carrier-
        Selective   Contacts,   IEEE   J.   Photovoltaics.   8   (2018)   456–464.
        https://doi.org/10.1109/JPHOTOV.2018.2793762.

[54]   G. Gregory, M. Wilson, H. Ali, K.O. Davis, Thermally Stable Molybdenum Oxide
        Hole-Selective Contacts Deposited using Spatial Atomic Layer Deposition,
        2018 IEEE 7th World Conf. Photovolt. Energy Conversion, WCPEC 2018 - A
        Jt. Conf. 45th IEEE PVSC, 28th PVSEC 34th EU PVSEC. (2018) 2006–2009.
        https://doi.org/10.1109/PVSC.2018.8547343.

[55]   J. Tong, Y. Wan, J. Cui, S. Lim, N. Song, A. Lennon, Solution-processed
        molybdenum oxide for hole-selective contacts on crystalline silicon solar
        cells,   Appl.   Surf.   Sci.   423   (2017)   139–146.
        https://doi.org/10.1016/j.apsusc.2017.06.011.

[56]   C. Lu, Rusli, A.B. Prakoso, Z. Li, Investigation of solution processed
        molybdenum oxide as selective contacts for silicon solar cells application,
        Mater.   Chem.   Phys.   236   (2019)   121779.
        https://doi.org/10.1016/j.matchemphys.2019.121779.

[57] L.Y. Wang, T.Y. Yang, C.C. Huang, Y.C. Chao, H.F. Meng, P. Yu, Solution-Processed Molybdenum Trioxide as Hole Selective Contact for Crystalline Silicon Solar Cells, Conf. Rec. IEEE Photovolt. Spec. Conf. (2021) 1062–1064. https://doi.org/10.1109/PVSC43889.2021.9518970.

[58] B. Macco, M.F.J. Vos, N.F.W. Thissen, A.A. Bol, W.M.M. Kessels, Low-temperature atomic layer deposition of MoO_x for silicon heterojunction solar cells, Phys. Status Solidi - Rapid Res. Lett. 9 (2015) 393–396. https://doi.org/10.1002/pssr.201510117.

[59] G. Gregory, C. Luderer, H. Ali, T.S. Sakthivel, T. Jurca, M. Bivour, S. Seal, K.O. Davis, Spatial Atomic Layer Deposition of Molybdenum Oxide for Industrial Solar Cells, Adv. Mater. Interfaces. 7 (2020) 1–9. https://doi.org/10.1002/admi.202000895.

[60] J. Yu, Y. Fu, L. Zhu, Z. Yang, X. Yang, L. Ding, Y. Zeng, B. Yan, J. Tang, P. Gao, J. Ye, Heterojunction solar cells with asymmetrically carrier-selective contact structure of molybdenum-oxide/silicon/magnesium-oxide, Sol. Energy. 159 (2018) 704–709. https://doi.org/10.1016/j.solener.2017.11.047.

[61] M.A. Sen, P. Spinelli, B. Kikkert, E. Hoek, B. Macco, A. Weeber, P. Bronsveld, Electron beam evaporated molybdenum oxide as hole-selective contact in 6-inch c-Si heterojunction solar cells, AIP Conf. Proc. 1999 (2018) 1–6. https://doi.org/10.1063/1.5049264.

[62] M. Bivour, F. Zähringer, P. Ndione, M. Hermle, Sputter-deposited WOx and MoOx for hole selective contacts, Energy Procedia. 124 (2017) 400–405. https://doi.org/10.1016/j.egypro.2017.09.259.

[63] P.K. Parashar, V.K. Komarala, Sputter deposited sub-stochiometric MoOx thin film as hole-selective contact layer for silicon based heterojunction devices, Thin Solid Films. 682 (2019) 76–81. https://doi.org/10.1016/j.tsf.2019.05.004.

[64] C. Battaglia, X. Yin, M. Zheng, I.D. Sharp, T. Chen, S. Mcdonnell, A. Azcatl, C. Carraro, B. Ma, R. Maboudian, R.M. Wallace, A. Javey, Hole Selective MoO, NanoLett. 14 (2014) 967–971.

[65] L.G. Gerling, S. Mahato, A. Morales-Vilches, G. Masmitja, P. Ortega, C. Voz, R. Alcubilla, J. Puigdollers, Transition metal oxides as hole-selective contacts in silicon heterojunctions solar cells, Sol. Energy Mater. Sol. Cells. 145 (2016) 109–115. https://doi.org/10.1016/j.solmat.2015.08.028.

[66]   K. Mallem, Y.J. Kim, S.Q. Hussain, S. Dutta, A.H.T. Le, M. Ju, J. Park, Y.H. Cho, Y. Kim, E.C. Cho, J. Yi, Molybdenum oxide: A superior hole extraction layer for replacing p-type hydrogenated amorphous silicon with high efficiency heterojunction Si solar cells, Mater. Res. Bull. 110 (2019) 90–96. https://doi.org/10.1016/j.materresbull.2018.10.018.

[67]   J. Dréon, Q. Jeangros, J. Cattin, J. Haschke, L. Antognini, C. Ballif, M. Boccard, 23.5%-Efficient Silicon Heterojunction Silicon Solar Cell Using Molybdenum Oxide As Hole-Selective Contact, Nano Energy. 70 (2020). https://doi.org/10.1016/j.nanoen.2020.104495.

[68]   L. Cao, P. Procel, A. Alcañiz, J. Yan, F. Tichelaar, E. Özkol, Y. Zhao, C. Han, G. Yang, Z. Yao, M. Zeman, R. Santbergen, L. Mazzarella, O. Isabella, Achieving 23.83% conversion efficiency in silicon heterojunction solar cell with ultra-thin MoO_x hole collector layer via tailoring (i)a-Si:H/MoO_x interface, Prog. Photovoltaics Res. Appl. (2022) 1–10. https://doi.org/10.1002/pip.3638.

[69]   D. Wang, J. Sheng, S. Wu, J. Zhu, S. Chen, P. Gao, J. Ye, Tuning back contact property via artificial interface dipoles in Si/organic hybrid solar cells, Appl. Phys. Lett. 109 (2016). https://doi.org/10.1063/1.4959839.

[70]   J. Liu, Y. Ji, Y. Liu, Z. Xia, Y. Han, Y. Li, B. Sun, Doping-Free Asymmetrical Silicon Heterocontact Achieved by Integrating Conjugated Molecules for High Efficient Solar Cell, Adv. Energy Mater. 7 (2017) 1–7. https://doi.org/10.1002/aenm.201700311.

[71]   E. Ros, Z. Barquera, P.R. Ortega, L.G. Gerling, G. Masmitjà, I. Martín, R. Alcubilla, J. Puigdollers, C. Voz, Improved Electron Selectivity in Silicon Solar Cells by Cathode Modification with a Dipolar Conjugated Polyelectrolyte Interlayer, ACS Appl. Energy Mater. 2 (2019) 5954–5959. https://doi.org/10.1021/acsaem.9b01055.

[72]   C. Reichel, U. Würfel, K. Winkler, H.F. Schleiermacher, M. Kohlstädt, M. Unmüssig, C.A. Messmer, M. Hermle, S.W. Glunz, Electron-selective contacts via ultra-thin organic interface dipoles for silicon organic heterojunction solar cells, J. Appl. Phys. 123 (2018). https://doi.org/10.1063/1.5010937.

[73]   N. Ikeda, T. Koganezawa, D. Kajiya, K.I. Saitow, Performance of Si/PEDOT:PSS Hybrid Solar Cell Controlled by PEDOT:PSS Film Nanostructure, J. Phys. Chem. C. 120 (2016) 19043–19048. https://doi.org/10.1021/acs.jpcc.6b07101.

[74]   L.Y. Li, C.H. Chen, C.L. Chiu, Y.L. Li, H.F. Meng, P. Yu, Diffusion-Free Organic Hole Selective Contacts for Silicon Solar Cells, Conf. Rec. IEEE Photovolt. Spec. Conf. (2019) 2299–2302. https://doi.org/10.1109/PVSC40753.2019.8981369.

[75]   L. Chen, Q. Chen, C. Wang, Y. Li, Interfacial dipole in organic and perovskite solar cells, J. Am. Chem. Soc. 142 (2020) 18281–18292. https://doi.org/10.1021/jacs.0c07439.

[76]   R. Islam, G. Shine, K.C. Saraswat, Schottky barrier height reduction for holes by Fermi level depinning using metal/nickel oxide/silicon contacts, Appl. Phys. Lett. 105 (2014). https://doi.org/10.1063/1.4901193.

[77]   E. Ros, T. Tom, D. Rovira, J. Lopez, G. Masmitja, B. Pusay, E. Almache, I. Martin, M. Jimenez, E. Saucedo, E. Tormos, J.M. Asensi, P. Ortega, J. Bertomeu, J. Puigdollers, C. Voz, Expanding the Perspective of Polymeric Selective Contacts in Photovoltaic Devices Using Branched Polyethylenimine, ACS Appl. Energy Mater. 5 (2022) 10702–10709. https://doi.org/10.1021/acsaem.2c01422.

[78]   B.A.E. Courtright, S.A. Jenekhe, Polyethylenimine Interfacial Layers in Inverted Organic Photovoltaic Devices: Effects of Ethoxylation and Molecular Weight on Efficiency and Temporal Stability, ACS Appl. Mater. Interfaces. 7 (2015) 26167–26175. https://doi.org/10.1021/acsami.5b08147.

[79]   E. Georgiou, I.T. Papadas, I. Antoniou, M.F. Oszajca, B. Hartmeier, M. Rossier, N.A. Luechinger, S.A. Choulis, Antimony doped tin oxide/polyethylenimine electron selective contact for reliable and light soaking-free high performance inverted organic solar cells, APL Mater. 7 (2019). https://doi.org/10.1063/1.5115260.

[80]   D. Yang, P. Fu, F. Zhang, N. Wang, J. Zhang, C. Li, High efficiency inverted polymer solar cells with room-temperature titanium oxide/polyethylenimine films as electron transport layers, J. Mater. Chem. A. 2 (2014) 17281–17285. https://doi.org/10.1039/c4ta03838j.

[81]   L. Yan, Y. Song, Y. Zhou, B. Song, Y. Li, Effect of PEI cathode interlayer on work function and interface resistance of ITO electrode in the inverted polymer solar cells, Org. Electron. 17 (2015) 94–101. https://doi.org/10.1016/j.orgel.2014.11.023.

[82]   J.H. Kang, Y.J. Park, Y. Khan, Y. Ahn, J.H. Seo, B. Walker, Cationic polyelectrolytes as convenient electron extraction layers in perovskite solar cells, Dye. Pigment. 182 (2020) 108634. https://doi.org/10.1016/j.dyepig.2020.108634.

[83]   W. Ji, T. Allen, X. Yang, G. Zeng, S. De Wolf, A. Javey, Polymeric Electron-Selective Contact for Crystalline Silicon Solar Cells with an Efficiency Exceeding 19%, ACS Energy Lett. 5 (2020) 897–902. https://doi.org/10.1021/acsenergylett.0c00110.

[84]   X. Yang, Z. Ying, Z. Yang, J.R. Xu, W. Wang, J. Wang, Z. Wang, L. Yao, B. Yan, J. Ye, Light-Promoted Electrostatic Adsorption of High-Density Lewis Base Monolayers as Passivating Electron-Selective Contacts, Adv. Sci. 2003245 (2021) 1–13. https://doi.org/10.1002/advs.202003245.

[85]   D.A. Tomalia, H. Baker, J. Dewald, M. Hall, G. Kallos, S. Martin, J. Roeck, J. Ryder, P. Smith, A New Class of Polymers : Starburst-Dendritic, Polym. J. 17 (1985) 117–132.

[86]   D. Astruc, E. Boisselier, C. Ornelas, Dendrimers designed for functions: From physical, photophysical, and supramolecular properties to applications in sensing, catalysis, molecular electronics, photonics, and nanomedicine, Chem. Rev. 110 (2010) 1857–1959. https://doi.org/10.1021/cr900327d.

[87]   E. Abbasi, S.F. Aval, A. Akbarzadeh, M. Milani, H.T. Nasrabadi, S.W. Joo, Y. Hanifehpour, K. Nejati-Koshki, R. Pashaei-Asl, Dendrimers: Synthesis, applications, and properties, Nanoscale Res. Lett. 9 (2014) 1–10. https://doi.org/10.1186/1556-276X-9-247.

[88]   D.K. Smith, A.R. Hirst, C.S. Love, J.G. Hardy, S. V. Brignell, B. Huang, Self-assembly using dendritic building blocks - Towards controllable nanomaterials, Prog. Polym. Sci. 30 (2005) 220–293. https://doi.org/10.1016/j.progpolymsci.2005.01.006.

[89]   M.. Malkoch, M; Walter, and Other Dendritic Polymers, Introd. to Dendrimers Other Dendritic Polym. (2020) 1–20. http://dx.doi.org/10.1039/9781788011327-00001.

[90]   Y. Zeng, Y.Y. Li, J. Chen, G. Yang, Y. Li, Dendrimers: A mimic natural light-harvesting system, Chem. - An Asian J. 5 (2010) 992–1005. https://doi.org/10.1002/asia.200900653.

[91] P.K. Maiti, T. Çağin, G. Wang, W.A. Goddard, Structure of PAMAM dendrimers: Generations 1 through 11, Macromolecules. 37 (2004) 6236–6254. https://doi.org/10.1021/ma035629b.

[92] A.J. Mozer, C.Q. Ma, W.W.H. Wong, D.J. Jones, P. Bäuerle, G.G. Wallace, The effect of molecule size and shape on free charge generation, transport and recombination in all-thiophene dendrimer:fullerene bulk heterojunctions, Org. Electron. 11 (2010) 573–582. https://doi.org/10.1016/j.orgel.2009.12.016.

[93] W.W.H. Wong, C.Q. Ma, W. Pisula, C. Yan, X. Feng, D.J. Jones, K. Müllen, R.A.J. Janssen, P. Bäuerle, A.B. Holmes, Self-assembling thiophene dendrimers with a hexa-peri-hexabenzocoronene core-synthesis, characterization and performance in bulk heterojunction solar cells, Chem. Mater. 22 (2010) 457–466. https://doi.org/10.1021/cm903272y.

[94] P. Rajakumar, C. Satheeshkumar, M. Ravivarma, S. Ganesan, P. Maruthamuthu, Enhanced performance of dye-sensitized solar cell using triazole based phenothiazine dendrimers as additives, J. Mater. Chem. A. 1 (2013) 13941–13948. https://doi.org/10.1039/c3ta13159a.

[95] W. Jiang, M. Stolterfoht, H. Jin, P.L. Burn, Hole-Transporting Poly(dendrimer)s as Electron Donors for Low Donor Organic Solar Cells with Efficient Charge Transport, Macromolecules. (2020). https://doi.org/10.1021/acs.macromol.0c00520.

[96] Y. Du, X. Wang, D. Lian, Y. Liu, L. Zhang, S. Xu, S. Cao, Dendritic PAMAM polymers for strong perovskite intergranular interaction enhancing power conversion efficiency and stability of perovskite solar cells, Electrochim. Acta. 349 (2020) 136387. https://doi.org/10.1016/j.electacta.2020.136387.

[97] R.G. Endres, D.L. Cox, R.R.P. Singh, Colloquium: The quest for high-conductance DNA, Rev. Mod. Phys. 76 (2004) 195–214. https://doi.org/10.1103/RevModPhys.76.195.

[98] G.J.V. Nossal, The double helix and immunology, Nature. 421 (2003) 440–444. https://doi.org/10.1038/nature01409.

[99] P. Ensslen, S. Gärtner, K. Glaser, A. Colsmann, H.A. Wagenknecht, A DNA-Fullerene Conjugate as a Template for Supramolecular Chromophore Assemblies: Towards DNA-Based Solar Cells, Angew. Chemie - Int. Ed. 55

(2016) 1904–1908. https://doi.org/10.1002/anie.201509332.

[100] Ö. Ateş Sönmezoğlu, S. Akın, B. Terzi, S. Mutlu, S. Sönmezoğlu, An Effective Approach for High-Efficiency Photoelectrochemical Solar Cells by Using Bifunctional DNA Molecules Modified Photoanode, Adv. Funct. Mater. 26 (2016) 8776–8783. https://doi.org/10.1002/adfm.201603454.

[101] A.R. bin M. Yusoff, J. Kim, J. Jang, M.K. Nazeeruddin, New Horizons for Perovskite Solar Cells Employing DNA-CTMA as the Hole-Transporting Material, 9 (2016) 1736–1742. https://doi.org/10.1002/cssc.201600288.

[102] A. Elfwing, W. Cai, L. Ouyang, X. Liu, Y. Xia, Z. Tang, O. Inganäs, DNA Based Hybrid Material for Interface Engineering in Polymer Solar Cells, ACS Appl. Mater. Interfaces. 10 (2018) 9579–9586. https://doi.org/10.1021/acsami.7b17807.

[103] Y. Hou, K. Wang, D. Yang, Y. Jiang, N. Yennawar, K. Wang, M. Sanghadasa, C. Wu, S. Priya, Enhanced performance and stability in DNA-perovskite heterostructure-based solar cells, ACS Energy Lett. 4 (2019) 2646–2655. https://doi.org/10.1021/acsenergylett.9b01894.

[104] J. Dagar, M. Scarselli, M. De Crescenzi, T.M. Brown, Solar Cells incorporating water/alcohol- Soluble electron-extracting DNA nanolayers, ACS Energy Lett. 1 (2016) 510–515. https://doi.org/10.1021/acsenergylett.6b00192.

[105] J. Dagar, G. Scavia, M. Scarselli, S. Destri, M. De Crescenzi, T.M. Brown, Coating ZnO nanoparticle films with DNA nanolayers for enhancing the electron extracting properties and performance of polymer solar cells, Nanoscale. 9 (2017) 19031–19038. https://doi.org/10.1039/c7nr06982k.

Chapter 3: Experimental

This chapter explains the various deposition techniques and structural, morphological, electrical, and optical characterization of thin films used in this thesis. This chapter also describes the fabrication of heterojunction silicon solar cells and its characterization.

3.1 Deposition techniques and pre- and post-deposition treatments

The thin films in this thesis were mainly fabricated using physical and chemical vapor deposition (PVD and CVD, respectively) techniques. Magnetron sputtering and thermal evaporation were the PVD techniques used for deposition of metallic and oxide films. Plasma enhanced chemical vapor deposition (PECVD) is the CVD technique used for deposition of a-Si:H films. The technique of spin coating was also used for deposition of organic molecules films.

3.1.1 Magnetron sputtering

Sputtering is the process by which atoms or molecules of a solid material are removed or ejected by bombardment with high kinetic energy ions. The ions then transfer their momentum to the surface atoms of the solid material (target), thus creating a cascade of atomic collisions. As a result, a stream of particles is emitted onto the substrate at a certain distance from the target, where they condense to form a film [1].

3.1.1.1 Working principle

The schematic representation of sputtering deposition is showed in Fig 3.1. The sputtering process begins when a glow discharge is produced by applying a voltage between the target (cathode) and the substrate (anode) in a vacuum chamber, where an inert gas, usually argon (Ar), is flowed into it. The electron collision causes the ionization of Ar atoms (Ar$^+$), by expelling

an electron from its outer shell. These ionized particles form a luminous plasma near the surface of the target. The Ar$^+$ ions accelerate to the target, which is negatively biased. If this bombardment energy of Ar$^+$ is greater than the binding energy of the target atom in the crystalline network, it results in sputtering of atoms from the target's surface, which eventually get deposited on the substrate surface forming thin films. The secondary electrons emitted from the target surface sustain the glow discharge. Moreover, in the particular case of magnetron sputtering deposition, magnets are used in the cathode to trap electrons near the target surface, enhancing argon ionization and therefore deposition rate.
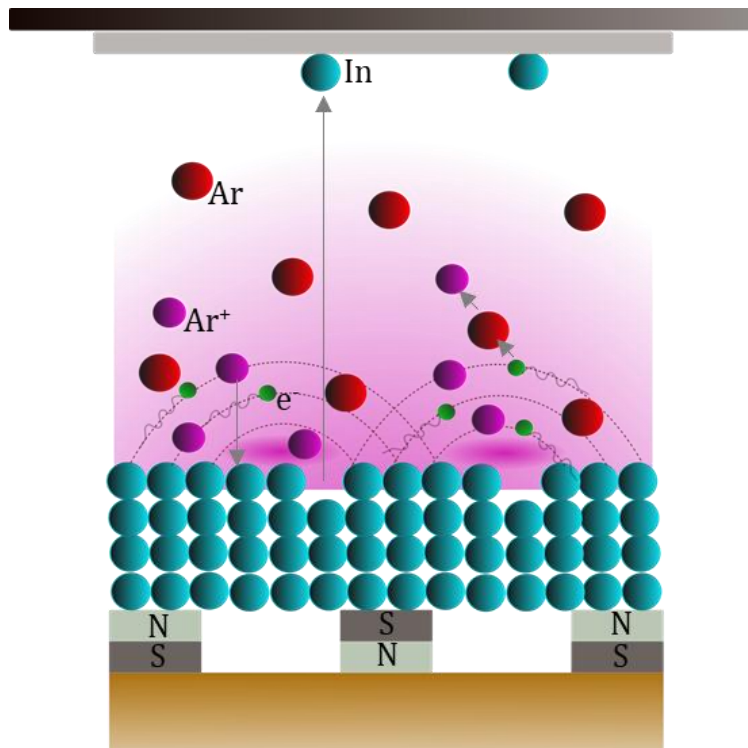
Figure 3.1: Schematic representation of the magnetron sputtering process.

3.1.1.2 Reactive sputtering

It is possible to employ non-inert gases like oxygen (O_2), hydrogen (H_2) or nitrogen (N_2) during sputtering procedures. These gases can be used instead of, or in addition to, Ar. By introducing a non-inert gas that gets ionized, one can trigger chemical interactions with the target material vapour cloud and can form new molecular compounds that will be deposited on the substrate. This variation of the sputtering technique is known as reactive sputtering. The stoichiometry and other properties of thus deposited films can be tuned by changing the partial pressure of the non-inert gas. However, caution must be taken in this case because of the target´s surface poisoning: these reactive gas ions can chemically react with the atoms on the target surface, changing the elemental concentration, conductivity, and sputtering ability of the target. If the target surface is poisoned, it can be cleaned by sputtering the top layer with an inert gas like Ar.

3.1.1.3 Power sources

Different types of power sources, such as direct current (DC) and radio frequency (RF), can be used for sputtering. In the former case, a constant potential difference in time is provided by DC power sources. It is typically employed with electrically-conductive target materials, and it is distinguished by its ease of control and cheap energy cost. However, when dealing with dielectric materials, DC sputtering has some restrictions, arisen from the fact that the surface of these insulating materials becomes charged when bombarded by positively-charged ions. These positive charges cannot be compensated due its insulating nature. As a consequence, excessive charge accumulation can cancel out the applied potential difference and therefore extinguish the plasma. This charge accumulation can potentially bring about film quality concerns caused by electric arc discharge in the plasma. This problem can be solved by using a time-varying voltage signal with changing polarization. With the RF power source, while the sinusoidal cycle is in the negative voltage region, positively-charged ions are driven towards the target and charge accumulation occurs. When the cycle is at positive voltage, the plasma electrons are propelled towards the material and neutralize the previously accumulated positive charge.

3.1.1.4 Description of the equipment

The magnetron sputtering was performed using two different systems: a lab-scale tool at Universitat de Barcelona and an industrial scale tool at Fraunhofer ISE Freiburg im Breisgau (Germany).

Lab-scale tool: The confocal balanced-magnetron sputtering lab-scale tool was used for sputtered depositions at Universitat de Barcelona. It is a commercially-available ATC-ORION 8 HV system from AJA International, Inc., which handles samples up to 10×10 cm^2. The instrument is shown in Fig. 3.2(a). It consists of a dry primary pump and a high-vacuum turbomolecular pump which can pump down to a base pressure of 7×10^{-4} mTorr. The chamber is provided with four sputter guns that can host targets of 7.62 cm in diameter and with a 3° tilt. The substrate holder can rotate between 0 and 20 rpm and the distance from substrate to targets can be varied between 11.7 and 18 cm. RF (300 or 600 W) or DC (750 W) adjustable power sources can be used simultaneously. Substrates can be heated from the backside using three halogen lamps which can reach a maximum temperature of 800 °C. The gases Ar, O_2 and Ar:H_2 can be adjusted by three different mass flow controllers. The targets can be protected by metallic chimneys and shutters to avoid cross contamination.

Industrial-scale tool: In-line magnetron sputtering industrial-scale tool was used for depositions at Fraunhofer ISE, Freiburg im Breisgau (Germany). It is a commercially-available *Vistaris 600* system from *Singulus technologies AG* that can handle six M2 (156.75 mm × 156.75 mm) wafer samples. This instrument is shown in Fig. 3.2(b). The tool could be divided into three main regions. The first region consists of three chambers called load/unlock (LL1), extension buffer (EB1), and extension chambers (EC1). Samples can be loaded into the unit through LL1, which is separated from EC chambers using a high vacuum gate. The EC chambers are used mainly for heating and rotating the sample holder. The next region comprised of a process chamber which consists of three cathode units called PM1, PM2 and PM3. PM1 contains two rotatable cylindrical targets of 1 m in length. PM2 is prepared for the low damage sputtering and PM3 for the planer target. The final region consists of EB2, EC2 and LL2. The final part helps in the rotation and movement of the substrate holder. The tool is connected to dry pumps

and five high-vacuum turbomolecular pumps which pump the chamber down to a base pressure of 3.9×10^{-7} mTorr. The substrate holder can be moved in-line with the targets and can be rotated for multiple depositions on both sides of the wafers. DC, pulsed DC or RF sources can be used for the depositions. Substrates can be heated using resistive heating that can reach a maximum temperature of 600 °C. Different gases like Ar, O_2 H_2, and N_2 can be used for the depositions. The targets in PM1 were covered using metallic slides to avoid cross contamination.
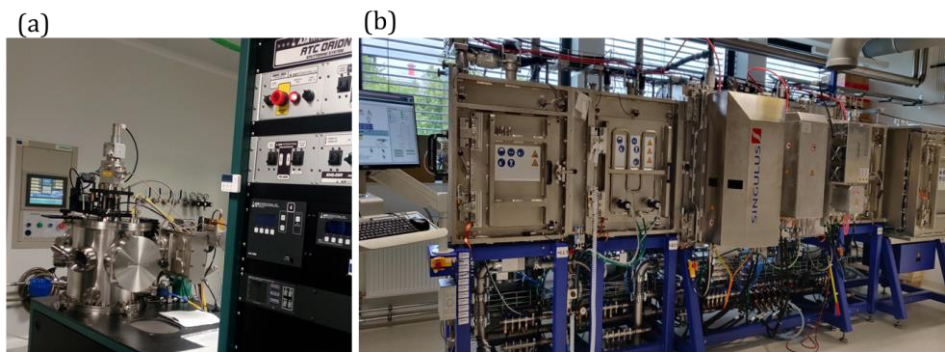
Figure 3.2: (a) Lab-scale sputtering tool ATC-ORION 8 HV at UB. (b) Industrial-scale sputtering tool Vistaris 600 at ISE Fraunhofer.

3.1.2 Plasma-enhanced chemical-vapour deposition (PECVD)

Chemical-vapour deposition (CVD) is a subset of chemical deposition techniques where atoms from different precursor gases form a solid thin film on substrates. To do this, the precursor gases are introduced into a vacuum chamber and energy is supplied to dissociate the molecules and trigger chemical reactions. The radicals then diffuse to the surface, where they eventually deposit. In the case of plasma-enhanced CVD (PECVD), a plasma source provides the energy for dissociation [2].

The equipment mainly consists of a load-lock chamber and a process chamber separated by a high vacuum gate. The pressure of each chamber is maintained by a vacuum pump. After evacuating the load lock-chamber, the substrate is transferred to the process chamber. Here, the precursor gases

are introduced via mass flow controllers and a constant pressure is maintained in the chamber by pumping out the gases during deposition. An RF generator then ignites plasma between the top and lower electrodes, and the process gas is dissociated into ions and radicals that react on the sample producing thin coatings.

The precursor gases used for intrinsic a-Si:H deposition are silane (SiH_4) and H_2. The sources for the boron and phosphorus doping are diborane (B_2H_6) or trimethylborane (TMB), and phosphine (PH_3) diluted in hydrogen, respectively. For the research work performed at Fraunhofer ISE, depositions of a-Si:H were carried out at a substrate temperature of 200 °C in an *Octopus II* PECVD tool from *INDEOtec*. For the works carried out at Universitat Politècnica de Catalunya (UPC), a substrate temperature of 250 °C was used with an RF PECVD tool from *Elettrorava S.p.A.*

3.1.3 Thermal evaporation

Thermal evaporation is a thin-film coating technique in which the source material evaporates in vacuum due to high temperature heating, and it gets deposited on the substrates. The main components in the evaporator chamber are materials that are used as the source, a rotating substrate holder for the uniformity of the films, vacuum pumps, adjustable DC high current supply, deposition controller and quartz crystal for thickness determination.

In this research work, the TMOs as carrier selective contacts were evaporated in a chamber located inside a N_2 atmosphere glovebox (*MB200B, MBraun*, Germany). This was meant to avoid sample degradation by exposure to ambient conditions. The powdered TMOs (purchased from *Sigma Aldrich*) were placed on a tantalum boat for evaporation. After reaching a vacuum of 7.5×10^{-3} mTorr the power is supplied until vapor pressure of a solid or liquid is overcome (sublimation or evaporation, respectively). The molecules are then expelled ballistically in the direction of the substrate surface. The deposition rate was kept at 0.1 nm/s for the films. The Au, Ag and Al metallic contacts were evaporated in the evaporator chambers located in the clean rooms of UB and UPC. For this, Al rods were

placed into tungsten helical filaments, whereas for Au and Ag tantalum or molybdenum boats were used.

3.1.4 Spin coating

Spin coating is a popular and simple technique widely used to get uniform thin films on flat surfaces. It is mostly used due to its low cost and ease of use. The material used for coating is dissolved in a solvent and afterwards dispensed over the substrate surface. Then the substrate is allowed to rotate at a specific velocity. As the solvent evaporates, the thin film of the coating is deposited on the substrate. The different stages of spin coating are schematically represented in Fig. 3.3.
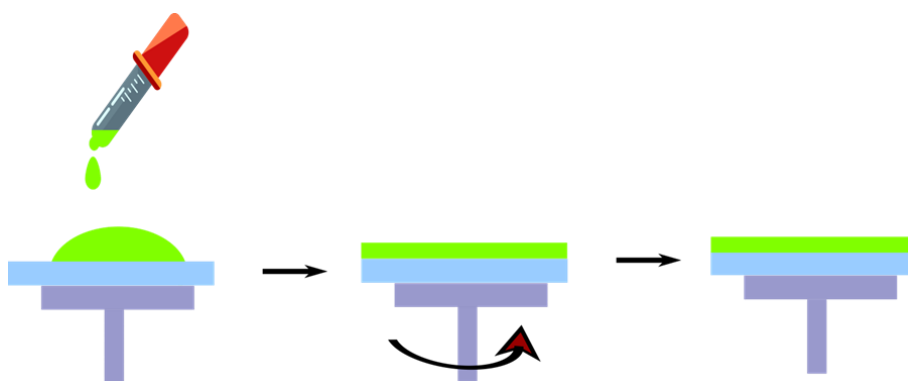
Figure 3.3: Schematic sketch of the spin-coating process.

In the research work conducted for the development of the organic molecular films, they were either dried again using a hot plate in ambient atmosphere, or kept in N_2 atmosphere overnight. In this work, the spin coating equipment at UPC (*Laurell Technologies Corporation, WS-650-23 model*) was employed.

3.1.5 Pre- and post- deposition treatments

For the research works described in the following chapters, the substrates used for deposition were on i) Si wafers [non-textured, flat zone, *n*-type c-silicon (100) wafers with a thickness of 280 μm and resistivity of 2 Ω cm], ii) Corning glass (1730F), iii) glass slides, and iv) sapphire substrates for the

transmittance measurements, because of the high transmittance of these substrates in near UV range (190 nm - 400 nm). The silicon substrates were dipped in 1% HF solution before deposition to remove the oxide layer on it. The Corning glass, glass slides and sapphire substrates were cleaned using soap and rinsed in ultrapure water (18 MΩ cm) to remove the dirt. Then, the glass was cleaned using isopropanol to remove all the organic impurities on it, and dried using the nitrogen gun.

After deposition, the samples were annealed either in a forming gas (mixture of H_2:N_2) atmosphere using a furnace at UPC or in ambient air using the hot plate.

3.2   Characterization techniques

In this section the equipment and techniques used to evaluate the thickness, the structural, the morphological, the composition, the optical and electrical properties of the films are explained. Also, the fabrication and characterization of the SHJ solar cells are explained in detail.

3.2.1 Thickness determination

3.2.1.1 Surface profilometer

The surface profilometer is a contact-type instrument that measures the surface morphology of the sample. It is equipped with a stylus of contacting diamond tip that moves vertically and laterally to scan over the sample surface. Then the position transducer converts the movements into height values creating surface profiles. To measure the thickness of a deposited film, a step was created on the film using the simple lift off -technique with ink and acetone. The equipment used was *Alpha-Step D-120 profilometer*, at UPC.

3.2.1.2 Spectroscopic ellipsometer

Spectroscopic ellipsometry is a non-destructive way of analyzing the thickness and optical properties of the thin films without the requirement of complex sample preparation. The basic principle of ellipsometry is based on the fact that, when the polarized light impinges onto the sample, some part

gets transmitted, and another gets reflected. In this method, the changes in the polarization of the reflected light from the samples are measured.

The complex reflectance ratio, (ρ), between the initially linearly polarized light and the reflected light from the sample surface is determined by the analyzer. The measured parameters ψ and Δ respectively denote the amplitude ratio and the phase difference induced by the reflection.

$$\rho = \tan(\psi)\,e^{i\Delta} \qquad (3.1)$$

To obtain the thickness and desired optical properties these measured values are then compared to an optical model, usually the Tauc-Lorenz model. In this work, three types of ellipsometers were used for the thickness measurements. At UB, a self-built ellipsometer with a deuterium halogen lamp as light source, and with a spectral region from 240 nm to 1150 nm, was employed. At UPC, a *Plasmos SD2300 Ellipsometer* at a wavelength of 632.8 nm, and at Fraunhofer ISE, an *M-2000 Ellipsometer* from J.A. Woollam, with a spectral range from 250 nm to 1000 nm, were used for the measurements.

3.2.2 Structural, morphology and composition

3.2.2.1 X-Ray diffraction (XRD)

The X-Ray Diffraction technique was used for the evaluation of the crystalline structure of the films. The principle of this technique is based on exposing the samples to the monochromatic X-rays with an angle (θ). After interaction with the sample, the rays are scattered from a number of lattice planes. Then, these diffraction angles from the scattered beam are measured. Constructive interference occurs whenever the Bragg law is satisfied: [3].

$$m\lambda = 2d_{\mathrm{hkl}}\sin\theta \qquad (3.2)$$

where m is an integer, λ is the characteristic wavelength of the X-rays to which to the crystallite are exposed [Cu Kα (λ = 0.154 nm) radiation was used as the X-ray source], d_{hkl} is the interplanar spacing between lattice planes and θ is the angle of the X-ray beam with respect to the planes.

The *PANalytical X'pert PRO MRD Alpha 1* diffractor at Centres Científics i Tecnològics de la Universitat de Barcelona (CCiT-UB) was used for the measurements. Peaks in the diffraction pattern appear whenever the Bragg condition is satisfied while scanning through different angles. The diffraction pattern gives a wide range of details from the intensity, position, and widths of these peaks. The structure, orientation and crystallinity can be inferred from them. The diffraction data are subsequently compared with the powder diffraction patterns from the International Centre for Diffraction Data (ICDD). The width of the peaks is characterized by the full-width at half-maximum (FWHM). The crystalline size (*D*) was determined from the peaks fitting by using a single line approach method. The diffraction line is conceived as a convolution of a Lorentzian profile, i.e., a Voigt function.

The average crystallite size is calculated via the Debye–Scherer's equation [4]:

$$D = \frac{k\lambda}{\beta \cos(\theta)} \qquad (3.3)$$

where β is the FWHM and *k* is the shape factor.

3.2.2.2 Transmission electron microscopy (TEM)

TEM electron microscopy uses a high-energy electron beam, with an energy equal to or greater than 200 keV, to analyse the microstructure of materials. Here the electron beam is accelerated by a voltage source (60–300 kV) and then focused via electromagnetic lenses onto an ultrathin layer of the sample with a resolution proportional to the electron wavelength [5]. The scanning transmission electron microscope (STEM) used was a *FEI Titan* with high-angle annular dark-field imaging (HAADF) at Laboratorio de Microscopias Avanzadas (LMA-INA) of Zaragoza was used measurement. The chemical composition was analysed by energy-dispersive X-ray spectroscopy (EDS) and electron energy loss spectroscopy (EELS) with sub nanometer spatial resolution.

3.2.2.3 Atomic force microscopy (AFM)

The surface morphology of the films was investigated by an *AFM Bruker Multimode 8* instrument at CCiT-UB. The sample surface is scanned using a

nano-sized tip attached to the cantilever. In accordance with the surface features, the laser light reflecting from the cantilever changes. This reflected light is measured using a photodiode and is recorded as a signal. The surface information, such as vertical and lateral sizes of the grains or structures, can be interpreted to obtain the topographical map of the samples. This gives information to compare different sample surfaces. One of the most useful parameters that is used throughout this thesis is the comparison of root mean square roughness (R_q) of the films, that provides information of the vertical features [6]. The measurement results were evaluated using the *Nanoscope* analysis software.

3.2.2.4 Scanning electron microscopy (SEM)

Scanning electron microscopy is a type of electron microscopy in which an electron beam is focused to scan over the sample surface and to form an image [5]. When an electron beam hits the sample both electrons and photons are produced, and the image is formed from the detected scattered electrons. Depending on the depth from which the electrons escape, various signals can be produced such as X-rays, cathodoluminescence and secondary backscattered electrons. These signals carry information on the composition, topography and morphology of the sample. The secondary backscattered electrons result from the inelastic collision between the beam electrons and the sample. They are usually low-energy electrons with less than 50 eV and escaping from a surface of 2-5 nm depth, which are useful for topographically and morphologically imaging.

The SEM instrument used for characterization, at CCiT-UB, is a *FESEM JEDL J-7100 Microscope* with *GATAN MONO-CL4* Cathodoluminescence Spectrometer, EDS Detector, Rear Scattered Electron Detector, and with a resolution of 1.2 nm.

3.2.2.5 X-Ray photoelectron spectroscopy (XPS)

XPS is a surface-sensitive technique employed to determine the chemical composition of a material's surface, including the elemental composition and electronic states. This technique works by irradiating the outer sample surface (1-10 nm) by monochromatic X-ray photons and measuring the

characteristic kinetic energy (*KE*) of the resulting emitted photons. This can be obtained using:

$$KE = h\nu - BE - \phi \qquad (3.4)$$

where the *KE* provided to the photoelectron depends upon the incident photon energy (*hν*) and the binding energy (*BE*) of the core level electrons in a chemical element, and ϕ is the work function of the material [7].

The XPS analyses were performed with a *Phoibos 150 analyzer, SPECS* in ultra-high vacuum conditions at CCiT-UB. XPS measurements were carried out with a monochromatic Al K_α X-ray source (1486.74 eV). The energy resolution, as measured by the FWHM of the Ag3d$_{5/2}$ peak for a sputtered silver foil, was 0.62 eV. Each peak in an XPS spectrum represents the orbital of the particular element in the sample, and the area under each peak is proportional to the atomic concentration of each present element. The XPS survey spectra were analysed using the *CASA XPS* software, after considering the adventitious carbon contamination present in the samples.

3.2.3 Optical and electrical characterization

3.2.3.1 UV-VIS-NIR spectroscopy

Optical characterization of the thin-film layers and other multi-structured layers were studied using the UV-VIS-NIR spectroscopy technique. These measurements were performed using the *PerkinElmer Lambda 950* and *PerkinElmer Lambda 1050* instruments available respectively at UB and at Fraunhofer ISE, both equipped with an integrating sphere. These instruments were used to measure the total transmittance (*TT*) and total reflectance (*TR*) of the films, and were hence effectively used to calculate the absorptance (*A*), the absorption coefficient (α) and the optical band gap (E_g), as explained in chapter 2, section 2.3.2.

To accurately determine E_g, linear regressions were evaluated at every point of the Tauc Plot, and the optical bandgap value was taken from the fitting where the linear regression coefficient (ρ^2) was maximized, as further described in [8].

We utilized the absorptance value to compare the quantity of light parasitically absorbed by an electrode irrespective of substrate and surface roughness. Then, absorptance was spectrally weighted to the 1 Sun air mass 1.5 global (AM 1.5G) spectrum, expressed as [9]:

$$A_{\text{weighted}} = \frac{\int_{\lambda_1}^{\lambda_2} I_{\text{light}}(\lambda)\, A(\lambda)\, d\lambda}{\int_{\lambda_1}^{\lambda_2} I_{\text{light}}\, d\lambda} \tag{3.5}$$

were A_{weighted} is the weighted absorptance, $A(\lambda)$ is the absorptance of the transparent electrode as a function of wavelength, I_{light} is the intensity of AM 1.5G radiation, and λ_1 and λ_2 are 300 and 1200 nm, respectively. The 300–1200 nm wavelength range was chosen because it encompasses the optimum operation wavelength range for SHJ solar cells.

To quantify the electro-optical performance of the films, the figure of merit (*FOM*), can be calculated from the inverse product of *A* and the sheet resistance (R_{sh}). The *FOM* is expressed as [9]:

$$FOM = \frac{1}{A_{\text{weighted}} * R_{\text{sh}}} \tag{3.6}$$

In both spectrometers used, two separate lamps a deuterium lamp that emits light in the ultraviolet region and a halogen lamp that emits light in the visible and infrared regions were used to provide illumination. Therefore, a total spectral range from 180 nm to 2500 nm could be scanned for *T* and *R* measurements. It should be mentioned that, for wavelengths below 250 nm, N_2 was pumped to the lamp chamber in order avoid the moisture. To collect and quantify the amount of transmitted or reflected light, a photomultiplier tube detector was used for wavelengths above 856 nm in both spectrophotometers, whereas below this wavelength a PbS detector was used at UB and an InGaAs detector at Fraunhofer ISE.

3.2.3.2 Four-point probe:

A *JANDEL RM3* four-point probe station was used to measure the sheet resistance (R_{sh}) of the thin films. This measurement system consists of four in-line probes of tungsten carbide that are spaced 1 mm apart. The

measurements were done by laying the probes on the surface of the samples, passing current through the two outer probes while measuring the voltage through the inner ones. The applied current can be modulated between 10 mA and 1 µA, which allows measuring sheet resistance values between 1 to $10^7 \, \Omega/\text{Sq}$, respectively.

The sheet resistance can be calculated according to:

$$R_{\text{sh}} = \frac{V}{I} \frac{\pi}{\ln 2} \tag{3.7}$$

The equation is valid only if the film measured is no thicker than 40% of the probe spacing and the films lateral size is sufficiently large [10]. In addition, the resistivity of the films can be obtained from the product of sheet resistance and film thickness (t).

$$\rho = R_{\text{sh}} \, t \tag{3.8}$$

3.2.3.3 Hall effect measurement

The Hall effect is a phenomenon in which a voltage develops across a material when it is placed in a magnetic field. Efforts made by Edwin Hall in 1879, made it possible to measure the voltage transverse to the direction of current on a current-carrying wire in a magnetic field. The voltage measured is known as Hall voltage. The schematic of the Hall effect is shown in Fig. 3.4.
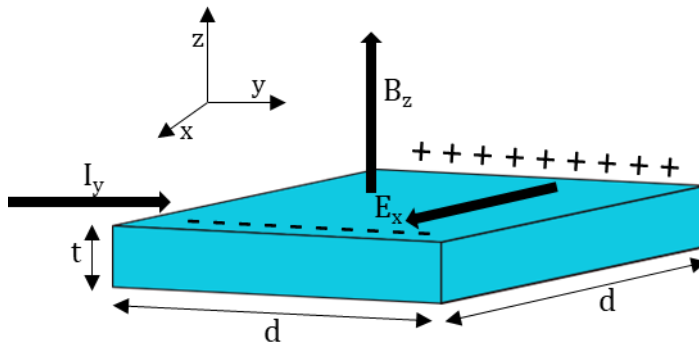
Figure 3.4: Schematics of the Hall effect.

An electrical current (I_y) is applied in y-direction, laterally through a conducting film of area (d^2) and thickness t. A magnetic field (B_z) is applied in z axis, direction perpendicular to the films surface. Because of the magnetic field the electrons will be driven in the x-direction. However, as soon as the electrons come into contact with the film's edge, they begin to accumulate, building up charge and creating an electric field E_x. This causes a potential difference between the edges of the film. This Hall voltage can be expressed as:

$$V_\mathrm{H} = \frac{I_y B_z}{N_\mathrm{e} q t} \tag{3.9}$$

Here, I_y represents the applied current, B_z denotes the magnetic field strength, N_e the free carrier concentration, q the elementary charge and t the thickness of the layer.

The Van der Pauw configuration allows us to determine mobility (μ), free carrier concentration (N_e) and resistivity (ρ) of the films, by means of the following relations:

$$N_\mathrm{e} = \frac{I_y B_z}{V_\mathrm{H} q t} \tag{3.10}$$

$$\mu = \frac{1}{N_\mathrm{e} q \rho} \tag{3.11}$$

Then using the thickness, the resistivity can be calculated using the Van der Pauw method as described in [11]. All the measurements were done using the Hall set up at Fraunhofer ISE, with an applied magnetic field of 0.4 T.

3.2.3.4 Transfer length method (TLM)

Transfer length method (TLM) consists of measuring the resistance between two metal coplanar contacts at different distances [12]. In order to determine the contact resistance between the metal and the substrate, the TLM structures were fabricated using a shadow mask and by thermal evaporation of metallic contacts of Au/Ag or Al on the films. The contact separation distances were 0.15, 0.25, 0.35, 0.45 and 0.55 mm. The fabricated

structures and the masks used are shown in Fig. 3.5. Thickness of Au/Ag or Al contacts was selected around 300 nm.
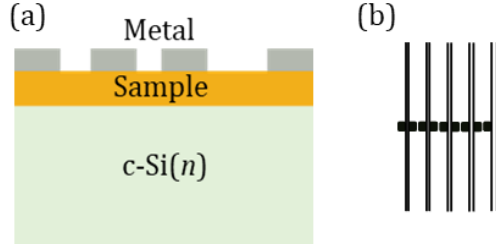
Figure 3.5: (a) Design of the fabricated structures. (b) Evaporation masks used for contact resistance measurements. The contact separation distances were 0.15, 0.25, 0.35, 0.45 and 0.55 mm.

The total resistance R_T measured between different contacts follows a linear trend with the contact separation (L) as follows:

$$R_T = \frac{R_{sh}}{W_c} \times (L + 2L_T)$$

(3.12)

where R_{sh} the sheet resistance of the films, W_C is the width of the contact, and L_T is the transfer length, which indicates the average distance that a carrier travels beneath the contact before it flows up into the contact. Then, the effective contact area (A_c) can be determined as:

$$A_c = L_T W_c$$

(3.13)

Consequently, the contact resistance R_c is calculated as twice the y-axis intercept and the specific contact resistance (ρ_c) is determined by applying the effective contact area as in Eq. 3.13.

$$\rho_c = R_c L_T W_c$$

(3.14)

3.2.3.5 Electronic band measurements via UPS

Ultraviolet photoelectron spectroscopy (UPS) is a non-destructive measurement technique that uses photons with energy ranging from 10 to 150 eV as the excitation source, and it measures the kinetic energy of the

photoelectron emitted from the surface. UPS is a technique employed to investigate the work function and the valence band of a material. The UPS measurements of the films were performed using a *Phoibos 150 analyzer* in ultra-high vacuum conditions (base pressure of 3.7×10^{-7} mTorr) from Institut Català de Nanociència i Nanotecnologia (ICN2). The UPS measurements were carried out with a monochromatic He I UV source (21.2 eV). The energy resolution, as measured by the FWHM of the Ag $3d_{5/2}$ peak for a sputtered silver foil, is 0.11 eV.

The work function of the material was determined using the following equation from the UPS spectrum:

$$\phi = h\nu - E_0 - E_{\mathrm{f}} \qquad (3.15)$$

where ϕ is the work function, $h\nu$ is the source energy (21.22 eV for He I UV source), E_0 is the secondary electron cut-off and E_{f} is the Fermi energy.

On the other hand, UPS allows determining the valence band edge of the material from the cut-off of the lowest binding energy, which represents the difference between the Fermi level and the maximum of the valence band [13].

3.3 Solar cell fabrication

The main objective of this thesis was the development of alternative transparent conductors and dopant-free carrier-selective contacts for *n*-type c-Si (*n*-Si) heterojunction solar cells. First, high mobility fluorine-doped indium oxide films and DMD structures were developed that act as front TCO and anti-reflection coating (ARC). Second, TMOs and organic molecules were explored as hole and electron selective contacts. They were explored in a front-side full-area configuration, similar to a HIT solar cell architecture. In this section, the solar cell fabrication procedures employed to achieve such structures will be described.

3.3.1 Cleaning and texturing

Cleaning of the wafer surface is an essential and critical process before the fabrication of heterojunction silicon solar cells. Most commonly, the contaminants are organic and inorganic molecular-scale contamination, ions and dust particles. They can act as thin film imperfections, shunts or highly-active recombination centers. The other drawbacks of these contaminants are the negative effects they cause on the deposition systems. For this reason, the procedure for cleaning was developed by the Radio Cooperation of America (RCA) which consists of two oxidizing steps [14]. The first step (RCA 1) is devoted to remove the organic and metal contaminants with $H_2O:H_2O_2:NH_3$ alkaline solution at 70 °C, whereas the second step (RCA 2) is meant to remove the alkali ions, heavy metals and metal hydroxides with $H_2O:H_2O_2:HCl$ acidic solution at 70 °C. Between the steps RCA 1 and RCA 2, a layer of silicon oxide (SiO_2) forms when the peroxide oxygen reacts with the wafer surface. To remove this oxide layer, 1% hydrofluoric acid (HF) attack is performed after each steps, leaving behind an H-terminated surface-passivated silicon surface [15]. In order to obtain high-efficiency devices, substrate texturization is an essential step, following the substrate cleaning. Single-crystalline silicon wafers, with (100) crystal orientation, were textured by anisotropic chemical attacks; this allowed effectively reducing the reflection loss from 30% on flat silicon substrates to 10% on textured ones. As a consequence, increased photon absorption and conversion efficiency were achieved. Random pyramidal texturing is usually obtained by chemical anisotropic etching using a tetramethyl ammonium hydroxide (TMAH) and isopropyl alcohol solution at 80 °C along the (111) crystal planes [16].

3.3.2 Deposition of passivating and selective contacts

The intrinsic and doped layers of amorphous silicon were deposited via PECVD. The cells fabricated at Fraunhofer ISE had a rear emitter design with the hole-contact [a-Si:H (*i/p*)] at the rear and the electron contact [a-Si:H (*i/n*)] at the front. In contrast, the a-Si:H (*i/n*) layers were used only in the rear side as the electron contact in the cells fabricated at UPC. The hole contact for the cells at UPC consists of sputtered or thermally-evaporated

TMOs, whereas the organic layers for the electron contact were spin coated. Then, TCO was applied on both sides via sputtering for cells at ISE Fraunhofer, and only on the front side for cells at UPC as the transparent front electrode.

3.3.3 Active area definition

In order to accurately measure the efficiency of the solar cells fabricated, the devices must be in well-defined size. Defining the active area of the cells also helps avoiding edge effects such as current leakage or shunts. For the cells fabricated at Fraunhofer ISE, the active areas were defined using a 2.1×2.1 cm^2 shadow mask during the sputtering of the TCO. In the case of the cells fabricated at UPC, delimiting the active area of the cells to 1×1 cm^2 and 2×2 cm^2 sizes was carried out using photolithography [*SUSS* MicroTec, MJB4 (UV4)]. For this purpose, the positive photoresist was spin coated on both sides of the device. Then, the resist was UV-exposed to imprint squared patterns on the front side of the device. A developer solution was used to remove the UV-exposed resin, and then both the ITO and TMO layers were removed via wet etching in a 1% HF solution to define the accurate active area.

3.3.4 Front-rear electrodes

To extract the current with minimal series resistance from the solar cell, the metallic contact must be deposited on the TCO. To allow as much as light through the device, the front electrode, i.e., the metallic grid, must be carefully designed. The grid must be designed such that the device exhibits low electrical losses (resistivity of the metal, contact resistance between metal and TCO) and optical losses (shaded area by the grid).

For the cells fabricated at Fraunhofer ISE, the grid on the front was achieved via screen printing (SP) of an Ag paste cured at 200 °C for 10 min in a belt furnace. The rear electrode of Ag was deposited via SP or by sputtering with masks. For the cells fabricated at UPC, an Ag grid was deposited by thermal evaporation using a shadow mask. The thickness of the Ag grid was kept at about 3 μm, presenting a shadow loss of 4.2%. For the full-area rear electrodes, a 1-μm-thick Al layer was deposited by thermal evaporation.

3.4 Solar cell characterization

3.4.1 Carrier lifetime

Recombination in volume and on wafer surfaces affects the effective lifetime of photogenerated carriers, which is a critical parameter in determining the quality of crystalline silicon-based solar cells. As a result, the assessment of lifetime is extremely beneficial for the control of manufacturing processes and the optimization of solar cells. The most widely used technique to determine the lifetime of wafers is the analysis of photoconductance transients, which was originally proposed by R. A. Sinton and A. Cuevas [17]. Measuring the effective carrier lifetime at different fabrication stages of devices helps evaluating their passivation properties. In this work, a commercial *WTC-120* instrument from *Sinton instruments* was employed; it is based on the contactless measurement of photoconductance induced on a Si wafer by a flash lamp, as shown in Fig. 3.6. A coil acting as an eddy current sensor measures the photoconductance, which is linked to the excess carrier density through:

$$\Delta\sigma = qt(\mu + \mu')\Delta n \qquad (3.16)$$

Here, $\Delta\sigma$ is the change in photoconductance, t is the thickness of the sample, μ and μ' are the mobilities of electron and holes, respectively, and Δn is the photogenerated excess electrons.

In the measurement equipment used, two illumination regimes are possible: transitory state photo conductance decay (PCD), with a short illumination flash of $\sim$15 μs, and quasi-steady state photo conductance decay (QSS-PCD), with a monotonous intensity decay of $\sim$2.3 ms. The effective lifetime can be calculated through the use of excess charge carrier density as:

$$\tau_{\text{eff}} = \Delta n / d(\Delta n) / dt \qquad (3.17)$$

Eq. 3.17 is related to transient measurements (PCD). The PCD regime is used to assess the effective absorption inside the wafer, which could be smaller than the reference sensor due to optical effects (texturization, ARC layer, etc.).

The generation and recombination of the electron-hole pairs must be in balance in the case of QSSPC. Also, the photogeneration rate of excess carriers must be considered in this case, so that the equation for effective lifetime becomes, in the case of QSSPC:

$$\tau_{\text{eff}} = \frac{\Delta n}{G - \dfrac{\partial n}{\partial t}}$$

(3.18)

where G is the photogeneration rate of the excess carriers. The QSSPC is mostly used for instantly evaluating τ_{eff} at different injection levels. The experimental approach to measure the effective lifetime is determined by the total recombination in the bulk and on the wafer surfaces as explained in chapter 2, section 2.2. Consequently, lifetime measurements contain explicit information of the implied open circuit voltage (iV_{oc}), which is the maximum open-circuit voltage (V_{oc}) value that could be achievable in current state of the sample:

$$iV_{\text{oc}} = \frac{nk_{\text{B}}T}{q}\ln\left(\frac{np}{n_{\text{i}}^2}\right)$$

(3.19)

where n and p are the total electron and hole concentrations, respectively, n_{i} is the intrinsic carrier density, q is the elementary charge, k_{B} is the Boltzmann constant and T is the absolute temperature of the sample.
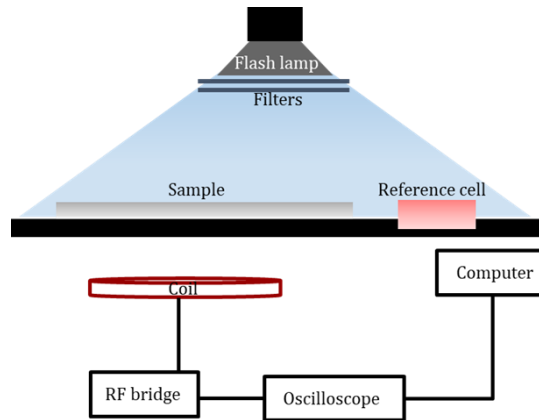
Figure 3.6*: Schematic diagram of the contactless photoconductance technique.*

3.4.2 Current density-voltage measurements

The operation of the solar cells was assessed by means of their current density (J)-voltage (V) response. The current density was measured as a function of applied voltage while the cell was in dark or under standard illumination, at controlled ambient temperature of 25 °C.

The measurements were done at UPC under AM1.5G illumination, as provided by a solar simulator equipped with a xenon lamp (450 W, ABB-class, *Oriel 94041A*). The source meter used was a *2601B Keithley* instrument, and data were collected using an in-house MATLAB routine. The measurements were also done at UB and Fraunhofer ISE under standard conditions.

3.4.3 Quantum efficiency

The external quantum efficiency (*EQE*) was defined in chapter 2, section 2.1.3. The *EQE* is determined by measuring the photocurrent generated by the solar cell when it is illuminated by a monochromatic light. A calibrated photodiode is used to measure the photon flux of the incoming light at each wavelength, in order to record an *EQE* spectrum. The generated current is determined using a lock-in amplifier and is compared to the incident power. Thus, the short-circuit current (J_{sc}) can be calculated by integrating over the wavelength range used for conversion. The complete optical and electrical characterization of solar cells offers information about the different involved layers, and it reveals the possible current loss mechanisms. The quality of the front electrode and emitter could be appreciated in the shorter wavelengths, whereas for the longer wavelengths the effect of the rear contact is dominant.

The front reflection of the solar cell is measured using a *PerkinElmer Lambda 950* spectrometer with a 150 mm integrating sphere, which determines the fraction of incident radiation that is reflected (R), i.e., without entering the solar cell. The *EQE* measurements were performed using the *QEX10 PV measurements* setup. Finally, once R of the cell is known, the internal quantum efficiency (*IQE*) can be determined, which indicates the ratio

between the collected electron-hole pairs per absorbed photon by the solar cell, following the expression [18]:

$$IQE\ (\lambda) = \frac{EQE\ (\lambda)}{1 - R(\lambda)} \qquad (3.20)$$

References

[1]   K. Seshan, Handbook of thin-film deposition processes and techniques, 2nd ed., Noyes Publications, Norwich, New York, 2002. https://doi.org/10.1201/9781482269680-18.

[2]   A. Luque, S. Hegedus, Handbook of Photovoltaic Science and Engineering, 2nd ed., John Wiley & Sons, Ltd., UK, 2011.

[3]   C. Richard Brundle, Charles A. Evans, Jr., Shaun Wilson, Encyclopedia of materials characterization: surfaces, interfaces, thin flms, USA, 1992.

[4]   E. Parsianpour, D. Raoufi, M. Roostaei, B. Sohrabi, F. Samavat, Characterization and Structural Property of Indium Tin Oxide Thin Films, Adv. Mater. Phys. Chem. 07 (2017) 42–57. https://doi.org/10.4236/ampc.2017.72005.

[5]   R.F. Egerton, Physical principles of electron microscopy, Springer, New York, USA, 2005.

[6]   P. Eaton, P. West, Atomic Force Microscopy, UK, 2010. https://doi.org/10.1093/acprof:oso/9780199570454.001.0001.

[7]   J.F.M. C.D Wagner, W.M. Riggs, L.E Davis, Handbook of X-ray photoelectron spectroscopy, Perkin-Elmer Corporation, USA, 1979.

[8]   B.D. Viezbicke, S. Patel, B.E. Davis, D.P. Birnie, Evaluation of the Tauc method for optical absorption edge determination: ZnO thin films as a model system, Phys. Status Solidi Basic Res. 252 (2015) 1700–1710. https://doi.org/10.1002/pssb.201552007.

[9]   M. Morales-Masis, S. De Wolf, R. Woods-Robinson, J.W. Ager, C. Ballif, Transparent Electrodes for Efficient Optoelectronics, Adv. Electron. Mater. 3 (2017). https://doi.org/10.1002/aelm.201600529.

[10] I. Miccoli, F. Edler, H. Pfnür, C. Tegenkamp, The 100th anniversary of the four-point probe technique: The role of probe geometries in isotropic and anisotropic systems, J. Phys. Condens. Matter. 27 (2015). https://doi.org/10.1088/0953-8984/27/22/223201.

[11] I.J. van Der Pauw, A method of measuring the resistivity and Hall coefficient on lamellae of arbitrary shape, Philips Tech. Rev. 20 (1958) 220–224.

[12] D.K. Schroder, Semiconductor material and device characterization, Third, John Wiley & Sons, Inc., Hoboken, New Jersey, USA., 2006.

[13] R. Schlaf, Tutorial on work function, (2012). https://www.ptonline.com/articles/how-to-get-better-mfi-results.

[14] W. Kern, Evolution of silicon wafer cleaning technology, Proc. - Electrochem. Soc. 90 (1990) 3–19. https://doi.org/10.1149/1.2086825.

[15] J.T.Y. H. Neergaard, Surface chemistry of silicon, Chem. Rev. 95 (1995) 1589–1673. https://doi.org/10.1201/9781420028706-28.

[16] P. Papet, O. Nichiporuk, A. Kaminski, Y. Rozier, J. Kraiem, J.F. Lelievre, A. Chaumartin, A. Fave, M. Lemiti, Pyramidal texturing of silicon solar cell with TMAH chemical anisotropic etching, Sol. Energy Mater. Sol. Cells. 90 (2006) 2319–2328. https://doi.org/10.1016/j.solmat.2006.03.005.

[17] R.A. Sinton, A. Cuevas, Contactless determination of current-voltage characteristics and minority-carrier lifetimes in semiconductors from quasi-steady-state photoconductance data, Appl. Phys. Lett. 69 (1996) 2510–2512. https://doi.org/10.1063/1.117723.

[18] W.J. Yang, Z.Q. Ma, X. Tang, C.B. Feng, W.G. Zhao, P.P. Shi, Internal quantum efficiency for solar cells, Sol. Energy. 82 (2008) 106–110. https://doi.org/10.1016/j.solener.2007.07.010.

Chapter 4: Transparent conducting layers

This chapter explores the development of high mobility fluorine doped indium oxide films. Also, investigates the reduction of indium usage in TCOs by employing a seed layer and ways to completely avoid indium by dielectric-metal-dielectric structures.

4.1 High mobility transparent layers and ways to reduce indium usage

Transparent electrodes with the remarkable combination of high electrical conductivity and low optical absorptance are amongst the most important components of optoelectronic devices like flexible touchscreens, solar cells and light emitting diodes [1][2]. Doped metal oxides, such as ITO, have dominated the area of transparent conductors for about forty years now [3]. However, optoelectronic properties of ITO are limited due to its high carrier density and moderate electron mobility that can lead to significant FCA. This increase in FCA within transparent electrodes in high efficiency devices such as silicon, tandem or perovskite solar cells will cause the parasitic absorption in the infrared part of the spectrum, thus critically affecting the efficiency of these devices [4][5][6].

Aiming at reducing the FCA and having lower sheet resistance in the films, TCOs with high mobility and reduced carrier density are referred to combine both excellent optical and electrical properties [7][8]. In addition, due to the scarcity of indium sources, which has resulted in ever-increasing indium prices, there is an urgent need to reduce the use of indium or to identify new materials that might act as transparent conductors [9][10]. Recently, dielectric-metal-dielectric structures and reduced use of indium as seed layers have emerged as valid candidates to substitute the ITO electrode [11][12][13].

In this chapter, the development of high mobility fluorine-doped indium oxide (IFO) is initially investigated, followed by the possibility of reducing the In content utilizing a seed layer. Finally, structures to completely replace In, using the dielectric-metal-dielectric approach, are fabricated and tested on SHJ solar cells.

4.2 High-mobility sputtered fluorine-doped indium oxide

Here, the IFO films were investigated in depth using a more industrial approach. Highest mobility of 93 $cm^2V^{-1}s^{-1}$ at a carrier density of 2.2×10^{20} cm^{-3} was achieved for the films deposited at (3.1%) O_2 and (2.5%) H_2. As a proof-of-concept, monofacial SHJ cells demonstrated increase in efficiency and short-circuit current density (J_{sc}) values. The best films achieved the highest efficiency of 22.6%.

4.2.1 Experimental method

A large-scale in-line DC-magnetron sputtering system with rotary IFO targets was used for the depositions. During the film depositions in Ar atmosphere, varying percentages of O_2 and H_2 gas were introduced, ranging from 0 to 3.5% and from 0 to 2.5%, respectively. Throughout all sets of depositions, the power (3000 W) and deposition pressure (3 mTorr) were kept constant. Base pressure of 5.2×10^{-4} mTorr was achieved before every deposition. Planar test substrates (glass and Si) were used for all depositions. Typically, prior to a set of depositions, the target was pre-sputtered to eliminate impurities and thus avoid differential sputtering effects. All the depositions were done at a substrate temperature of 150 °C (as-deposited state) and thickness of the films was ~100 nm. In ambient air, post-deposition annealing was performed for 20 minutes at 220 °C.

To test the IFO performance at the device level, solar cells were fabricated on random-pyramid textured, 1 Ω cm resistivity, 180-µm-thick *n*-type float zone (FZ) silicon wafers. Monofacial SHJ cells were fabricated using the rear emitter design. An active cell area of ~4 cm² was defined using a shadow mask on front TCO and rear TCO + Ag sputtering.

4.2.2 Structure and composition

The structural, compositional, and morphological analysis of the IFO films were done under the sputtering conditions of fixed percentage (3.1%) of O_2 and varying percentages (0.0%, 1.0%, and 2.5%) of H_2.

The XRD patterns of the films in as-deposited and annealed state are shown in Fig. 4.1. Post-deposition annealing was carried out at 220 °C for 10 min in ambient air. In as-deposited state, Fig. 4.1(a), the films deposited in the absence of H_2 and at 1.0% of H_2 showed a polycrystalline behavior. But when the H_2 percentage rose to 2.5%, the polycrystalline nature was suppressed, leading to a partially amorphous state. This is due to a reduced number of nucleation centers during the growth by increased incorporation of H_2 in the films [14][15].

All the peaks matched with the ICDD database and corresponded to the cubic bixbyite structure of In_2O_3 [16]. The strongest diffraction peak (222) is prominent at 30.56°; other peaks were assigned correspondingly. Fig. 4.1(b) shows the XRD patterns of the annealed films that achieved solid phase crystallization [14][17]. After annealing, the film deposited in 2.5% of H_2 changed from amorphous to crystalline nature.

Interestingly, for the films without H_2 doping and 1% of H_2 doping nucleation occurs continuously during the entire annealing process, which has been determined after calculating the mean crystallite size of the films from the full-width at half-maximum (FWHM) of the X-ray peak of (222) following the Scherrer's formula [5] (see Fig. 4.2).

For films deposited in the absence of H_2 and 1% of H_2, crystalline size remained almost constant before and after annealing. However, for films deposited in the presence of 2.5% H_2, crystalline size increased from 19 nm to 45 nm. The increase in the crystalline size can be directly attributed to the higher H_2 doping that reduces further nucleation during the post-annealing process [18][19][20].
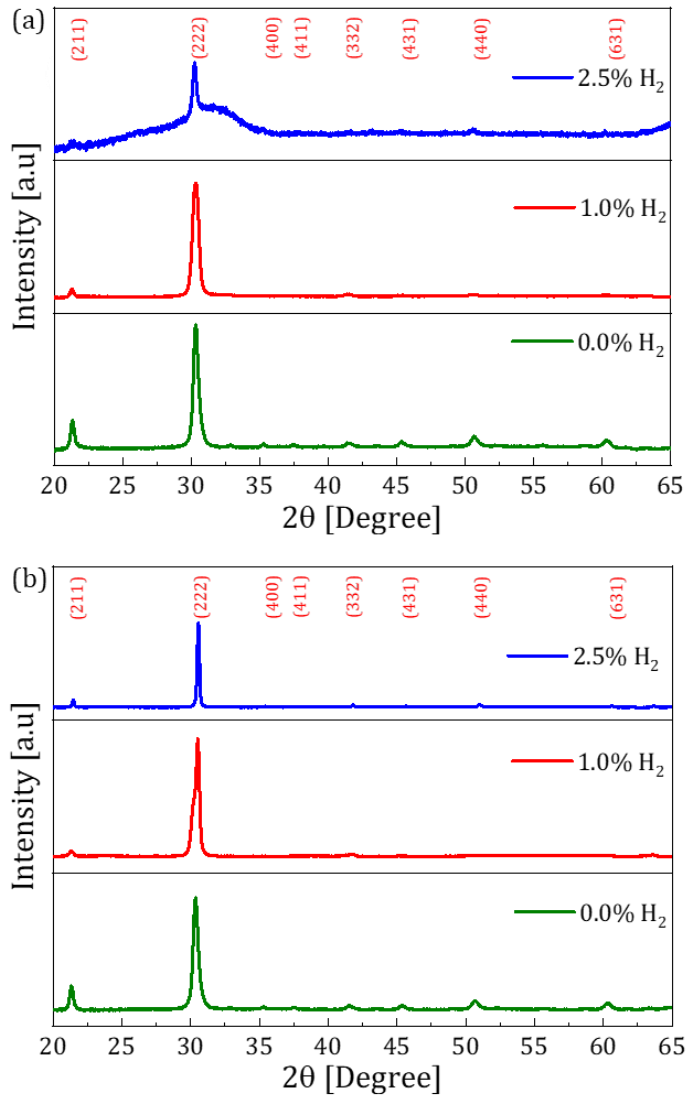
Figure 4.1: X-ray diffraction patterns of the IFO films doped with different percentages of H_2 and with a fixed 3.1% of O_2. (a) As-deposited state, and (b) annealed in ambient air at 220 °C for 10 min. All the XRD measurements were carried out on films deposited on silicon.
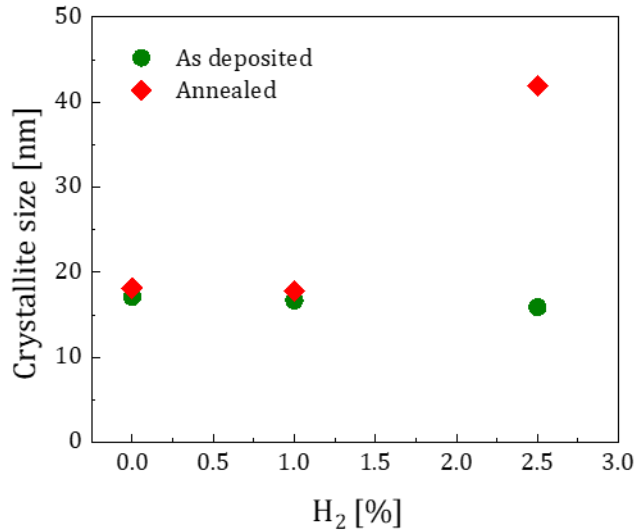
Figure 4.2: Crystalline size of the IFO films calculated using the Scherrer's formula as a function of different H_2 percentages in as-deposited and annealed states.

Fig. 4.3 shows the XPS general spectrum of the IFO films in as-deposited state grown in 2.5% H_2. This was carried out to understand the chemical structure and composition of the films. The scanning was performed in the binding energy range from 0 to 1300 eV, showing the main elements In3d, O1s, and F1s. The adventitious carbon signal (C1s) was detected at 284.8 eV, which was used as the reference peak [21]. Doped fluorine F1s peak at 684.9 eV indicates the presence of In-F bonds [22]. A fluorine doping percentage of 9.8% was calculated from the area of the F1s peak (F/(O+F)).

As discussed in the literature, due to the similar ionic radius of the fluorine and oxygen atoms, fluorine dopants can substitute the oxygen atoms or occupy the oxygen vacant sites. Thus, fluorine doping creates a free electron or eliminates the electron trap sites, which in turn increases the mobility of the films [23]. The inset of Fig. 4.3 shows the high-resolution spectrum of

In3d with two major peaks at 444.2 and 451.7 eV, respectively assigned to In3d$_{5/2}$ and In3d$_{3/2}$, thus confirming the In^{3+} state in IFO film [24].
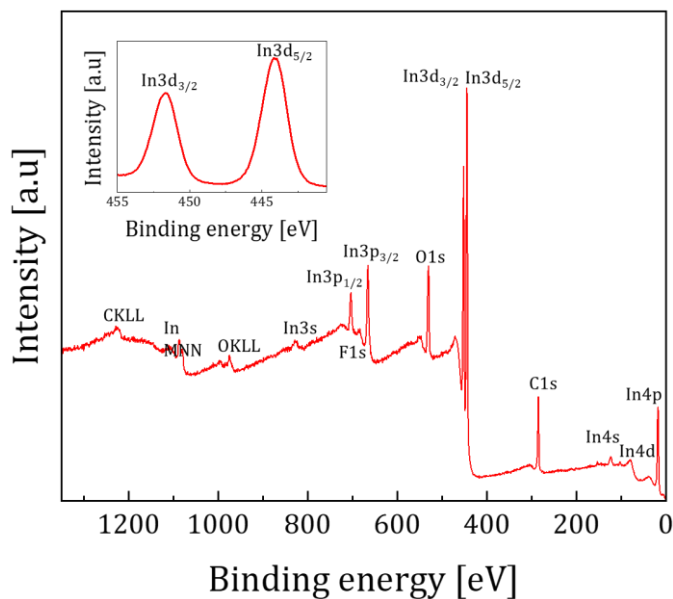
Figure 4.3: XPS general spectrum of the IFO film grown in H$_2$, indicating the In, O, F, and C peaks. The inset shows the In3d core-level spectrum. The XPS measurements were performed on films deposited on silicon substrates in the as-deposited state.

Fig. 4.4 shows the XPS spectra of O1s peaks of IFO films in as-deposited and annealed states. The O1s peaks were deconvoluted into three different oxygen peaks at 529.7, 531.2, and 532.0 eV, which were similar to the reported values [23][25]. The lowest energy peak at 529.7 eV (red) was assigned to the O^{2-} ions around In^{2+} in octahedral coordination, whereas the peak at 531.2 eV (blue) corresponds to the oxygen vacant sites, typically denoted as doubly-charged donors (V$_o^{++}$). The higher energy peak at 532.0 eV (cyan) was attributed to the hydroxyl group from the film, due to the exposure of the sample to air. Fig. 4.4(a) shows the deconvoluted O1s peaks in as-deposited state with an increasing percentage of H$_2$. The area percentage of the peak (obtained from Casa XPS) at 531.2 eV corresponds to the oxygen vacant sites, which is reduced when employing higher H$_2$

percentage [25]. For 0.0% H_2 in the films, the area of oxygen vacant peak is 40.3%. A further decrease to 37.2% and 28.4% is observed for 1.0% and 2.5% of H_2, respectively. At higher H_2 supply during deposition, the amount of substitutional and interstitial (H_o^+ and H_i^+, respectively) hydrogen rises. The H_o^+ atoms occupy the oxygen vacant sites, thereby passivating the doubly-charged oxygen vacancies (V_o^{++}) by substituting them with singly-charged H atoms. This is evident from the decrease in the oxygen vacant sites from the XPS [26]. Thus, H_2 doping could simultaneously provide passivation of doubly-charged defects while generating one free carrier per defect site, which contributes to the increase in mobility of the IFO films.
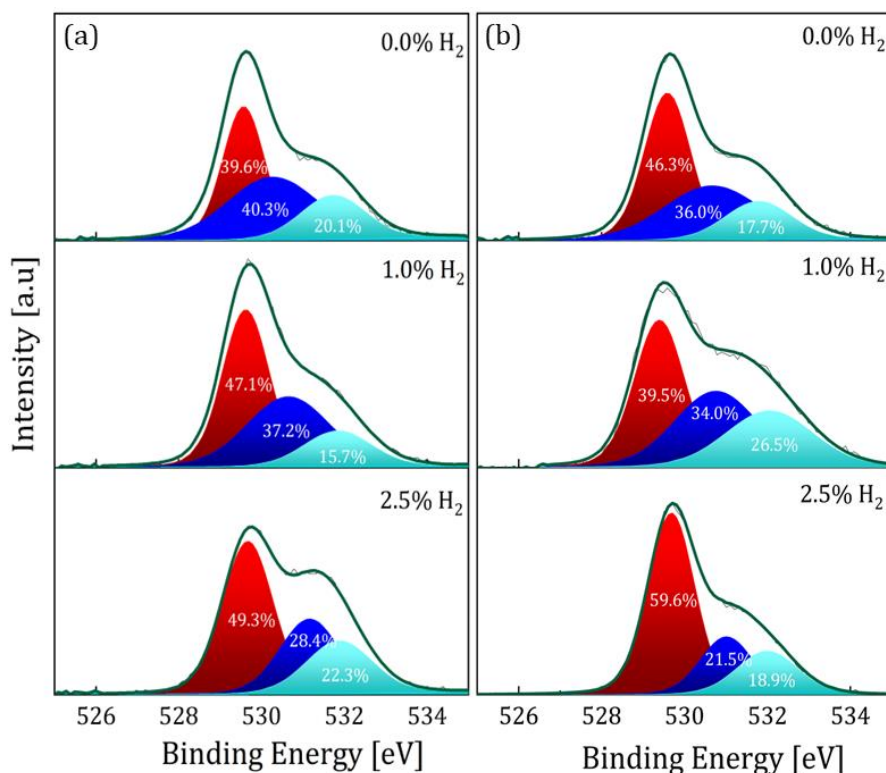
Figure 4.4: Deconvoluted O1s peaks from core-level XPS spectra of sputtered IFO films with increasing percentage of H_2. (a) Films in as-deposited state. (b) Films annealed at 220 °C for 10 min in ambient air.

Fig. 4.4(b) shows the deconvoluted O1s peaks after annealing at 220 °C for 10 min. A further reduction in the amount of oxygen-deficient sites was observed in the films after annealing. For films without H_2 doping, a decrease in oxygen vacancy peak from 40.3% to 36.0% was observed after annealing. For the highest doped films (2.5% of H_2), this area was reduced to almost half, down to 21.5%, compared to the films without H_2 doping. This was due to the defect passivation (oxygen deficiency sites) by deep intercalation of substitutional hydrogen atoms during the film crystallization, as observed from the XRD peaks. Therefore, the analysis of the O1s peaks revealed the key role of H_2 doping and effect of annealing in reducing the number of the defects in the IFO films.

4.2.3 Morphology

Fig. 4.5 displays the SEM micrographs of IFO films deposited in different percentages of H_2 doping in both as-deposited and annealed states. In general, the analysis of the SEM images showed that in the as-deposited state the crystallinity of the films decreases at higher H_2 content.

In particular, Fig. 4.5(e) shows that films deposited with the highest percentage of H_2 were essentially amorphous. This was attributed to the decrease in nucleation in the films caused by the addition of hydrogen during deposition [27]. After annealing at 220 °C, XRD already demonstrated that the crystallinity of all the films was enhanced [see Fig. 4.2(b)]. In the annealed films deposited with 2.5% H_2, Fig. 4.5(f), larger grains were observed due to the increase in H_2 doping, which reduces the further nucleation during the annealing process.

AFM measurements were performed to understand the morphology and surface roughness of the films grown in different H_2 atmospheres. Fig. 4.6 shows the AFM images of films deposited in different percentages of H_2 in both as-deposited and annealed states. The different growth mechanism is evident from the AFM micrographs at different growth conditions and after the post-deposition treatments.
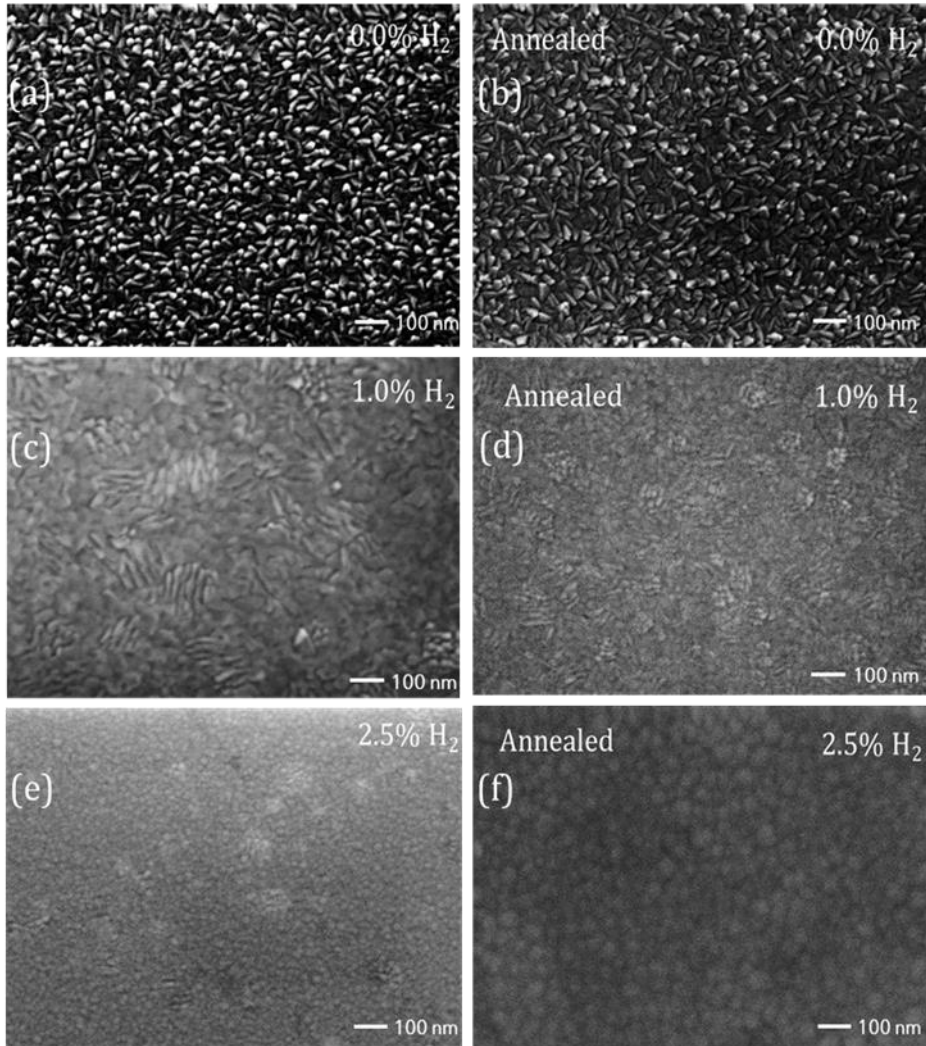
Figure 4.5: SEM micrographs of the sputtered IFO films: (a, b) 0.0% of H_2, (c, d) 1.0% of H_2, (e, f) 2.5% of H_2, respectively in as-deposited and annealed states. The SEM measurements were carried out on films deposited on Si substrates.
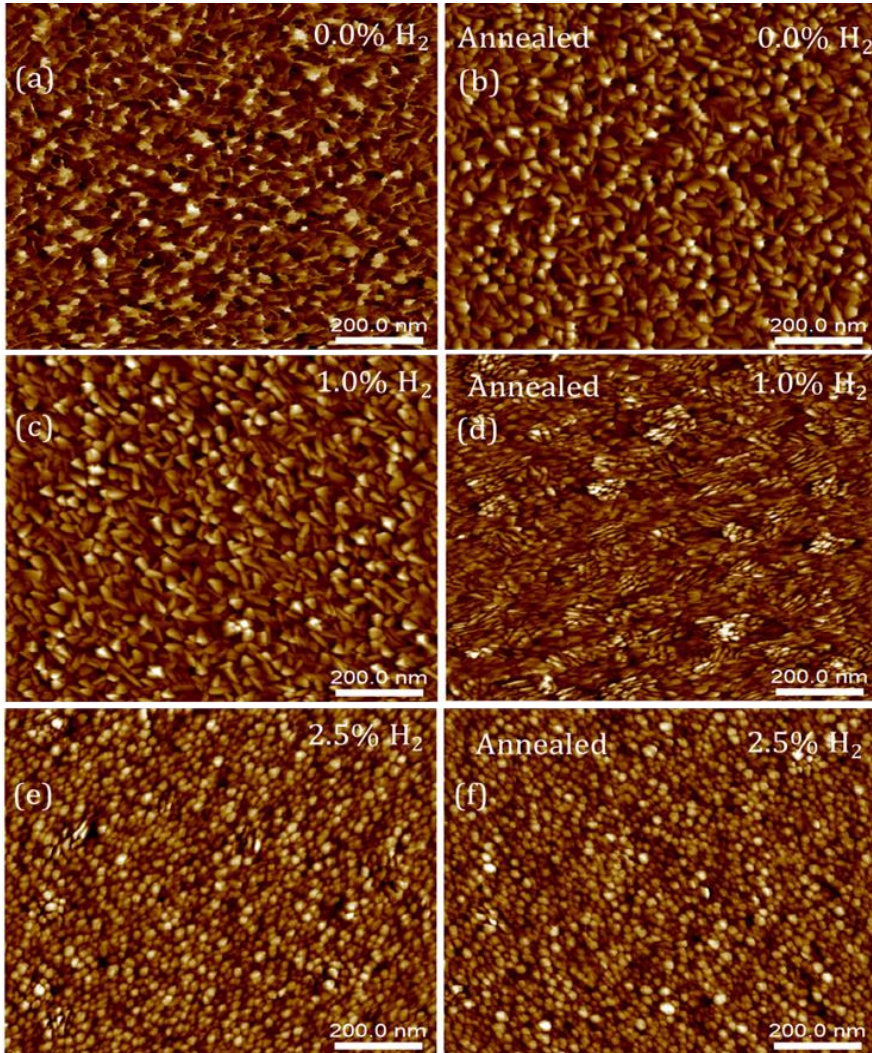
Figure 4.6: AFM micrographs of the sputtered IFO films: (a, b) 0.0% of H_2, (c, d) 1.0% of H_2, (e, f) 2.5% of H_2 in as-deposited and annealed states, respectively. The AFM measurements were performed on films deposited on Si substrates.

Fig. 4.7 shows the root mean square (RMS) roughness of the films with increasing H_2 concentration in as-deposited and annealed states. RMS

roughness of 4.1 nm was observed for films with 0.0% of H_2, and it reduced down to 3.8 nm for 1.0% H_2. The lowest value of 0.9 nm was observed for films grown with the highest H content, i.e., 2.5% of H_2 [28]. Annealing the films in ambient air again reduced the RMS roughness and the films became further smooth. The reduction in RMS roughness at higher H_2 percentage could be directly related to the increase in the crystallite size of the films as observed in XRD [29][30].
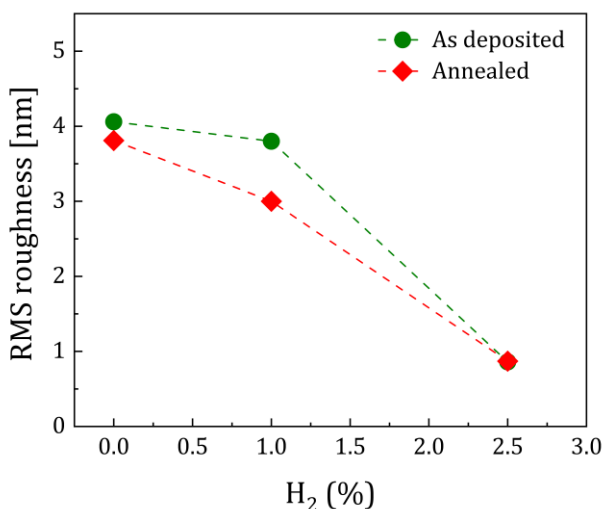
Figure 4.7: RMS roughness as a function of H_2 percentage. The RMS roughness of the films was obtained from the AFM measurements.

4.2.4 Electrical and optical

To determine the electrical properties of the layers, the electrical parameters of the as-deposited and annealed films were compared. All the films devoted to electrical characterization were deposited on glass substrates. Fig. 4.8 shows the Hall parameters of the IFO films in as-deposited and annealed states. The evolution of sheet resistance (R_{sh}), electron mobility (μ), and charge carrier density (N_e) in response to the atmospheric species during deposition is depicted in Fig. 4.8(a, b, c). After solid phase crystallization, the electrical characteristics of annealed films

were significantly impacted by the film structure, which can also be influenced by the deposition parameters as shown in Fig. 4.9(a, b, c). To gain a holistic understanding on the role of H_2 and O_2 we performed a very broad parameter variation and will first discuss the role of changing either O_2 or H_2. By doing so the heat map can be categorized into two regions:

Region 1 (R1): This region shows the influence of changing O_2 without H_2 being intentionally added during deposition. In the as-deposited state a huge drop in N_e, from 3.6×10^{20} cm^{-3} to 0.22×10^{20} cm^{-3}, was observed when adding O_2 in the films, and a corresponding increase in the sheet resistance, respectively from 94 Ω/sq to 699 Ω/sq, was also noted. An enhancement in mobility of the films from 17 cm^{2}V^{-1}s^{-1} to 40 cm^{2}V^{-1}s^{-1} at higher O_2 content was observed. As there was an increase in the oxygen supply, N_e decreased due to the reduction in the number of oxygen vacancies, typically doubly-charged donors (V_o^{++}) [31]. This, in turn, increased the mobility of the films due to reduced ionized impurity scattering by doubly-charged oxygen vacancies. A similar trend was seen in the films after annealing by further dropping the N_e and R_{sh} with an increase in mobility. N_e dropped from 2.7×10^{20} cm^{-3} to 0.37×10^{20} cm^{-3}, and mobility increased from 37 cm^{2}V^{-1}s^{-1} to 45 cm^{2}V^{-1}s^{-1}, with a rise in the sheet resistance from 59 Ω/sq to 523 Ω/sq, respectively; this is due to the additional decrease in the number of oxygen vacancies (V_o^{++}) caused by the solid phase crystallization of the films, as proved by XRD (see Fig. 4.1) and XPS (see Fig. 4.4) measurements.

Region 2 (R2): In this region, both O_2 and H_2 flows were introduced and varied independently. Here the N_e of the films decreased, and a huge increase in mobility was observed. These regions have the superposition of impact corresponding to the addition of both H_2 and O_2. Indeed, an increase in these two parameters (O_2, H_2) could have opposite impact on N_e and μ. For instance, it can be observed that the higher the percentage of H_2 supply during deposition, the higher the amount of substitutional and interstitial (H_o^+ and H_i^+) [7]. Mobility of films shoots up from 40 cm^{2}V^{-1}s^{-1} to 93 cm^{2}V^{-1}s^{-1} for the films sputtered at 2.5% of H_2 and 3.1% O_2 after annealing. The highest mobility of 93 cm^{2}V^{-1}s^{-1} with a N_e of 2.2×10^{20} cm^{-3} and sheet resistance of 31 Ω/sq was observed for best films with the highest hydrogen content (2.5%).
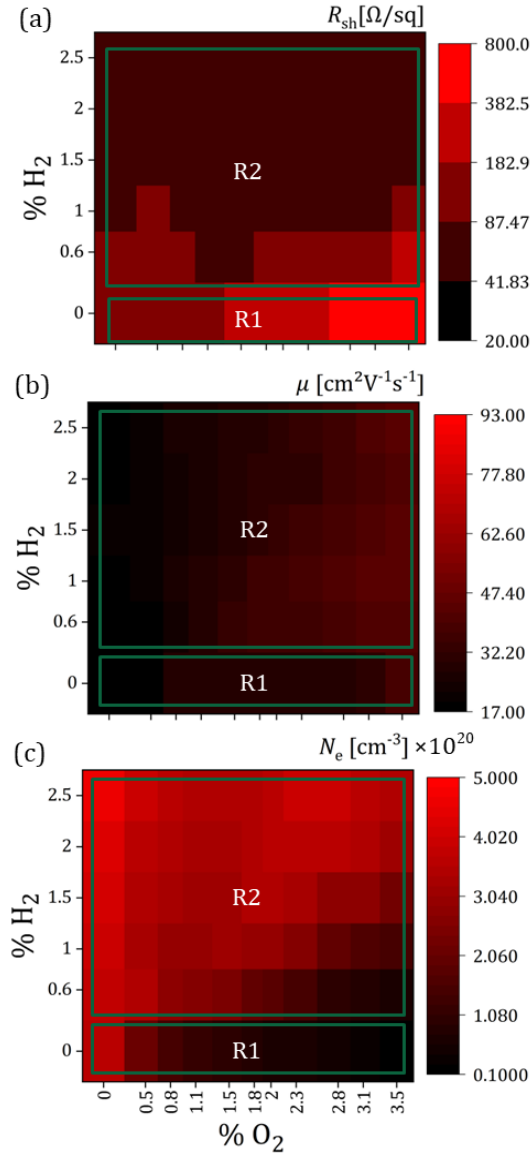
Figure 4.8: (a) Sheet resistance (R_{sh}), (b) electron mobility (μ), and (c) charge carrier density (N_e) of the IFO films, in as-deposited state, as a function of H_2 and O_2 content during deposition.
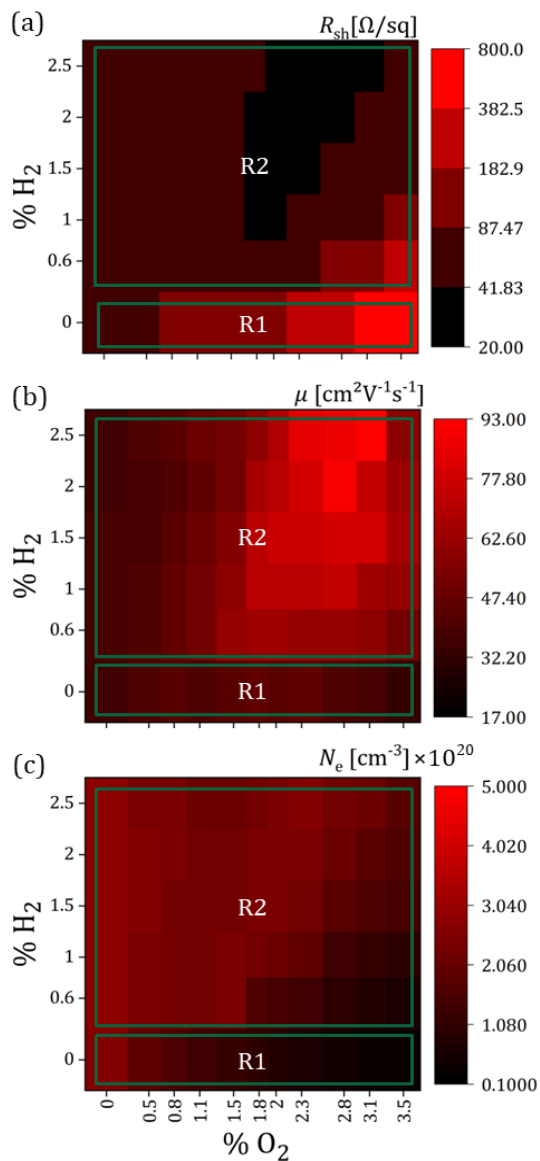
Figure 4.9: (a) Sheet resistance (R_{sh}), (b) electron mobility (μ), and (c) charge carrier density (N_e) of the IFO films, after annealing, as a function of H_2 and O_2 content during deposition.
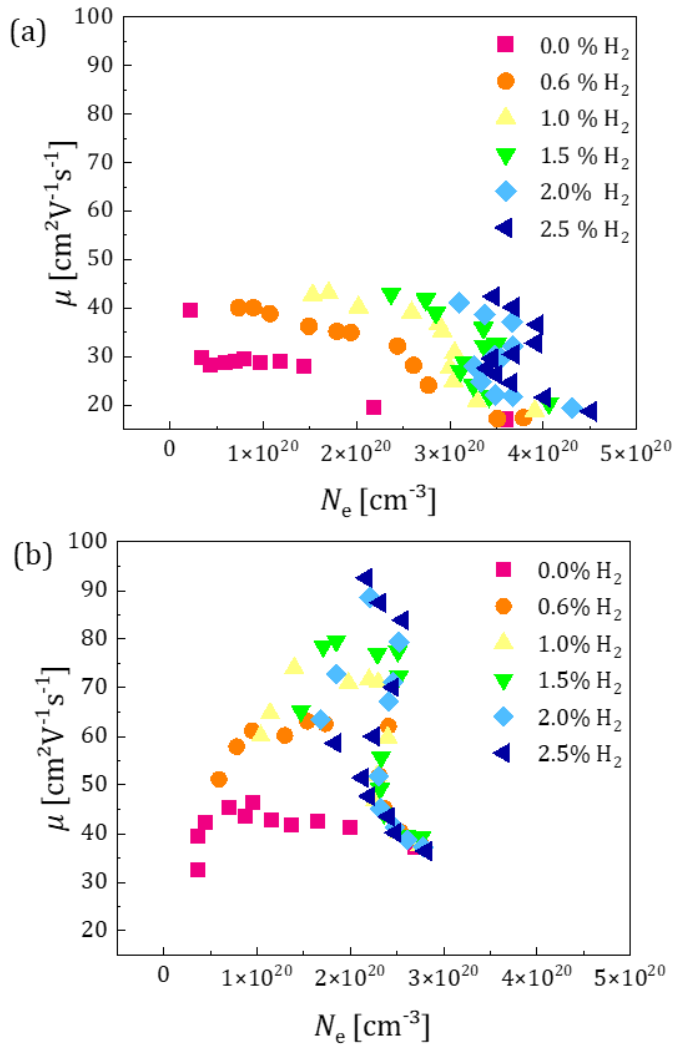
Figure 4.10: Mobility vs. charge carrier density at different H_2 percentage of films (a) in as-deposited state and (b) after annealing.

This could clearly explain the importance of O_2 and H_2 during the growth of films [evident in Fig. 4.9(b)]. Furthermore, the addition of H_2 could positively

impact the structural properties of the films, for instance inducing the formation of larger grain sizes (see Figs. 4.6 and 4.7) and the passivation of grain boundaries and defects (see Fig. 4.4). This could also act as a more efficient single-charged donor compared to the doubly-charged V_o^{++}. As a conclusion, the lower N_e and higher μ after solid phase crystallization can be presumably attributed to the interplay between these three possible dopants: O vacancies (V_o^{++}), fluorine dopants and atomic hydrogen (H_o^+ and H_i^+. Fluorine either substitutes the oxygen atoms or occupies the oxygen vacancy sites. H atoms will provide passivation to doubly-charged defects and thus generate a free carrier [16][32][33]. This is easily observable from Fig. 4.10, which shows the influence of N_e on mobility at higher percentage of H_2 during deposition.

To use IFO films as transparent conductors in SHJ, the films must not only have high mobility, but they must also have a low optical absorptance in the required wavelength range. The optical absorptance of the films was determined from the transmittance and reflectance measurements on the films deposited on the glass substrates. Then, we utilized the absorptance (*A*) value to compare the quantity of light parasitically absorbed by an electrode irrespective of substrate and surface roughness: *A* = 1 – *TT* – *TR*; where *TT* is the total transmittance and *TR* is the total reflectance. Then, absorptance was spectrally weighted to the 1 Sun air mass 1.5 global (AM 1.5G) spectrum expressed as in Eq. 3.5. The optical properties of the IFO film with different percentages of O_2 and H_2 in films are displayed in Fig. 4.11. Fig. 4.11(a) plots the weighted absorptance of the IFO films in as-deposited state with varying percentages of O_2 and H_2 during deposition. On one hand, in region R1 weighted absorptance of the films decreases at higher O_2 content during deposition. In particular, absorptance dropped from 30.2% to 0.9% as the percentage of O_2 increased from 0 to 3.5%, due to the reduced scattering by reduction of oxygen vacancies. On the other hand, in region R2, where both O_2 and H_2 flows were introduced and varied independently, a superposition of impact on the addition of H_2 and O_2 exists. Here, the absorptance of the films can be attributed to the passivation of defects and oxygen vacancies by the interplay of hydrogen and oxygen atoms that affects the scattering centers [34]. Absorptance of 3.9% was observed for films with mobility of 40 $cm^2V^{-1}s^{-1}$ at 3.1% O_2 and 2.5% H_2.
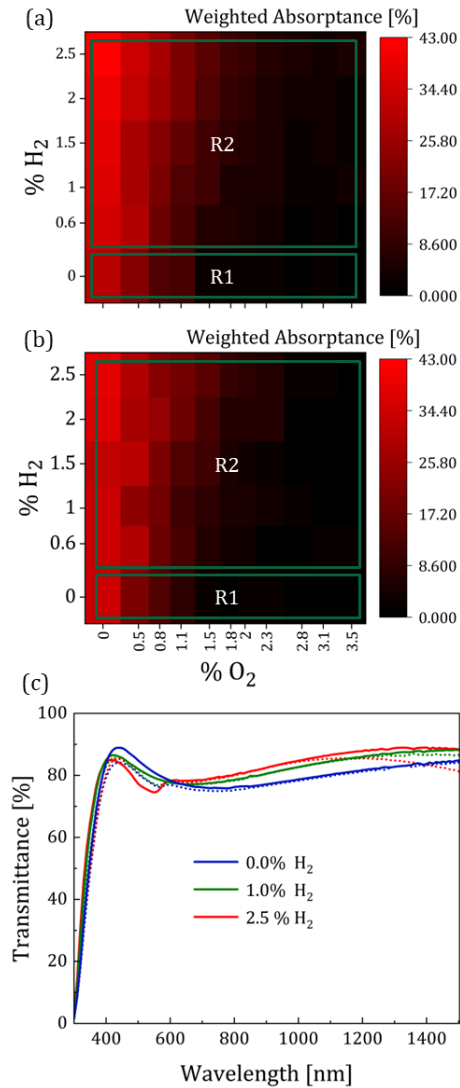
Figure 4.11: Optical properties of the IFO films with varying percentages of O_2 and H_2 during the deposition, in (a) weighted absorption in as-deposited and (b) annealed states. (c) shows the transmittance of the films at varying $H_2\%$ indicating the FCA (dashed lines showing the as-deposited states and solid lines indicating annealed states).

The weighted absorptance of the IFO films after annealing is shown in Fig. 4.11(b). The weighted absorbance was reduced after annealing due to solid phase crystallization in the films, which in turn led to increased grain size in the films and reduced amount of scattering centers [35][36]. The absorptance dropped from 33.0% to 0.4% as the percentage of O_2 increased from 0 to 3.5% in R1. In R2, films with the highest mobility of 93 cm²V⁻¹s⁻¹ at 3.1% O_2 and 2.5% H_2 showed an absorptance of 2.0%. The reduced FCA in the films at higher percentage H_2 films could be seen in near infrared part of the spectrum shown in Fig. 4.11(c). The dotted lines correspond to the transmittance in as-deposited state and solid lines indicates the transmittance after annealing. It is evident that the infrared transmittance improves after annealing due to the decreased carrier density and improved mobility of the films.

To highlight the high performance of the IFO films, the optical absorption of the films was compared with the sheet resistance of the films. In Fig. 4.12, the absorptance, which is weighted with the AM 1.5 solar spectrum according to Eq. 3.5, is plotted as a function of the sheet resistance for films sputtered in varying atmospheres. A *FOM*, quantifying the electro-optical performance of the films simply by calculating the inverse product of *A* and R_{sh}, and isolines thereof, are indicated by dashed lines in the figure. The *FOM* is expressed as in Eq. 3.6. The weighted absorbance in relation to the sheet resistance is shown in Fig. 4.12 for (a) as-deposited and (b) annealed films. As the films are annealed the sheet resistance and weighted absorbance of the films drop due to larger crystallite size via solid phase crystallization in the films (see Fig. 4.1). Therefore, annealing in the films is necessary to achieve higher *FOM* for IFO films. Fig. 4.13 displays μ vs. *FOM* of IFO films for different H_2 atmospheres after annealing, which clearly shows the importance of hydrogen in achieving a good optical-electrical trade-off. As the rise in H_2 doping in the films concurrently results in the passivation of doubly-charged defects and the generation of one free carrier per defect site, the mobility of the IFO films increases. This marks the significance of IFO films, which exhibit a high *FOM* with great mobility, in comparison to typical ITO films of 0.4 Ω^{-1} *FOM* and μ of 40 cm²V⁻¹s⁻¹ (marked as a black spot in Fig. 4.13), as Morales *et al.* reported [37].
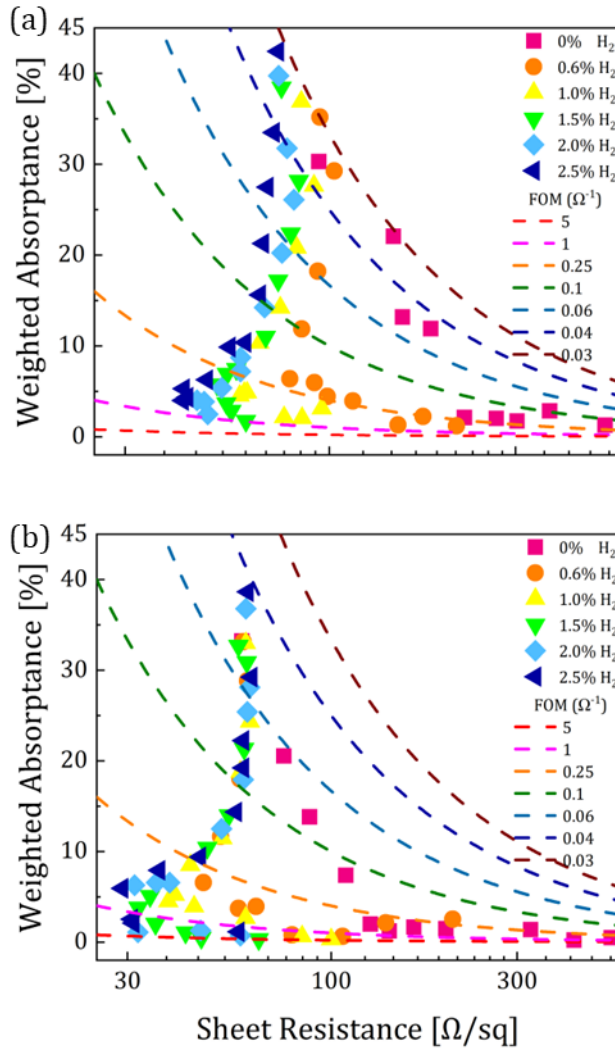
Figure 4.12: Weighted absorbance as a function of the sheet resistance for IFO films in (a) as-deposited and (b) annealed states. The dashed lines indicate curves of constant figure of merit (FOM).
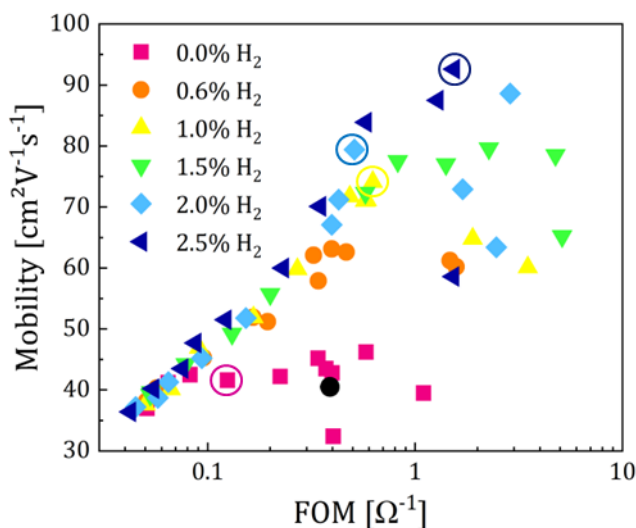
Figure 4.13: Mobility as a function of the figure of merit (FOM) of the films after annealing, in comparison to typical ITO films (marked as a black spot [37]).

4.2.5 Application to solar cells

To test the TCO films at device level, selected IFO films were applied on textured monofacial SHJ solar cells of an area of 3.84 cm^2. The schematic representation of the cell is shown in Fig. 4.14. A 130-nm-thick IFO layer on the rear side and a 75-nm-thick one on the front side were sputtered. This study aimed to observe how the trends of corresponding to the electro-optical properties of the IFO films are reflected in the short circuit current density in different test structures. The parameters under investigation were chosen with films deposited with different hydrogen percentages that modify the structure, composition and morphology of the films, and consequently their electrical and optical properties. The four different hydrogen percentages chosen were 0.0, 1.0, 2.0, and 2.5%, with mobilities of 41, 68, 78, and 93 cm^{2}V^{-1}s^{-1}, respectively. The mobility and *FOM* of these films are highlighted in Fig. 4.13 in coloured circles.

Table 4.1 shows the solar cell and electro-optical parameters for the different solar cells fabricated. As seen from the previous measurements on IFO films, an increase in the H_2 percentage in the films during deposition improves the crystallinity, grain size and, in turn, rises the mobility of the films. As the μ increases, there is a significant improvement in the J_{sc} of the cells from 36.8 mA cm^{-2} to 39.6 mA cm^{-2}. This is observed for cells fabricated with 0.0% H_2 (41 cm^{2}V^{-1}s^{-1}) and 2.5 % of H_2 (93 cm^{2}V^{-1}s^{-1}), respectively. An improvement in J_{sc} of 2.8 mA cm^{-2} is observed for cells fabricated with high mobility IFO. The clear correlation between the J_{sc} and the mobility of the films is shown in Fig. 4.15(a). The high mobility films with low sheet resistance and reduced carrier density reduce the near-IR FCA in films. The optical properties of the films (Fig. 4.11) is consistent with the observed FCA and the increase in J_{sc} of the cells. Also, the colored circles in Fig. 4.13 show the μ and *FOM* values of different solar cells, which clearly indicates the necessity of H_2 to have better J_{sc}. The open circuit voltage (V_{oc}) shows values between 727 and 729 mV for all the cells, without any dependence on the IFO film sputtering atmosphere. The fill factor of the cells also exhibits no dependence on the film composition, being around $\sim$78 % for all the cells.
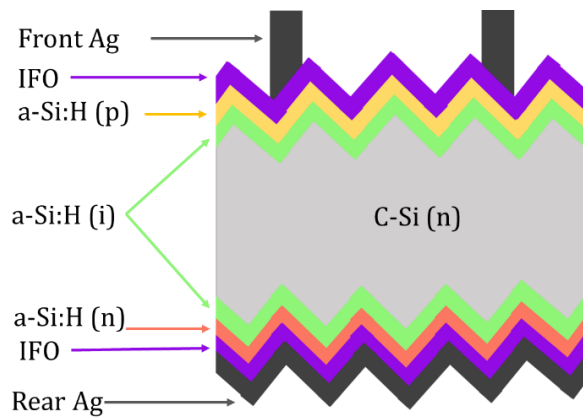
Figure 4.14: Schematic diagram of the textured monofacial SHJ solar cell fabricated with 75-nm-thick IFO films on front side and 130-nm-thick IFO films on the rear side.
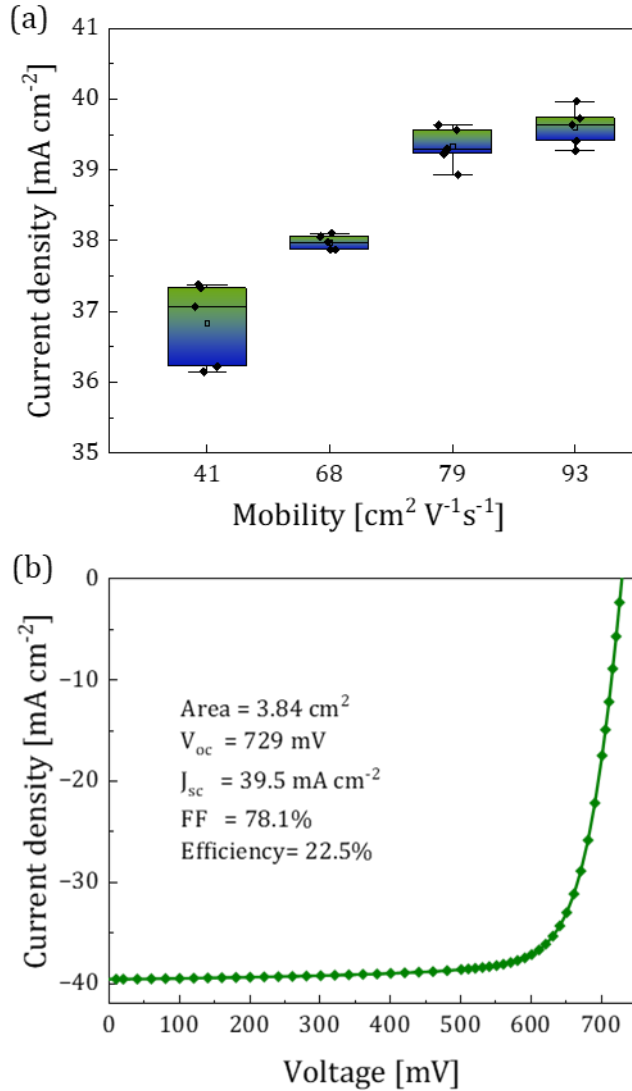
Figure 4.15: (a) Current density as a function of the mobility for different fabricated solar cells. (b) Current density-voltage characteristics corresponding to the best SHJ solar cell fabricated with the optimized IFO film, with a highest mobility of 93 cm^{2}V^{-1}s^{-1}.

The *PCE* of the cells was modified as the increase in H_2 % in the films during deposition. Films grown with 0.0% H_2 had a *PCE* of 20.9%, this value presenting an improvement of 1.7% for 2.5% H_2 films. The maximum power conversion efficiency of 22.6% was obtained for the cell containing the TCO with the highest mobility of 93 $cm^2V^{-1}s^{-1}$, fabricated with 3.1% O_2 and 2.5% H_2 [see Fig. 4.15(b)]. Overall, the hereby presented results prove the possibility of fabricating more transparent hydrogen-doped IFO films with high mobility, thus resulting in enhanced J_{sc}, and by means of an industry-compatible process. Therefore, our study confirms the versatility of IFO films as a suitable candidate for SHJ devices.

Table 4.1: Solar cell parameters of the SHJ solar cells fabricated. The optoelectronic properties of the films used for fabricating different devices are also written down.

SHJ H_2 %	V_{oc} (mV)	J_{sc} (mA cm^{-2})	FF (%)	PCE (%)	μ (cm^{2}V^{-1}s^{-1})	FOM (%)
0.0	727	36.8	78.1	20.9	41	0.1
1.0	727	38.0	77.1	21.3	68	0.6
2.0	728	39.3	78.3	22.4	79	0.5
2.5	729	39.6	78.5	22.6	93	1.5

To summarize, the structural, compositional, morphological, electrical, and optical properties of IFO films were investigated in depth using an industrial approach. DC-magnetron sputtering from a rotary target and H_2 diluted in Ar as hydrogen source were used to deposit IFO films. The highest mobility of 93 $cm^2V^{-1}s^{-1}$ at a carrier density of 2.2×10^{20} cm^{-3} was achieved for the films deposited at 3.1% O_2 and 2.5% H_2. The highest mobility film achieved the highest *PCE* of 22.65%, demonstrating IFO's versatility as a candidate for SHJ cells and other optoelectronic devices. As the next approach we have developed the idea to reduce the usage of In by using high mobility In with other TCOs as stacks.

4.3 Reducing the usage of indium by AZO films with high-mobility IFO as seed layers

In order to reduce the usage of In an alternative approach was adopted by reducing the thickness of IFO films. Here the thin films of IFO were used as seed layers on AZO films achieving high mobility. The high mobility IFO films deposited at 3.1% O_2 and 2.5% H_2 (previous section) were used as seed layers. Compared to the pure AZO films of low mobility the IFO/AZO films achieved a high mobilities.

4.3.1 Experimental method

The IFO and IFO/AZO films were grown on planar test substrates of glass and silicon. An in-line DC magnetron sputtering system using rotary target of IFO and planar target of AZO was used. A base pressure of 5.2×10^{-4} mTorr was achieved before each deposition, and substrate heating was kept at ~150 °C for both IFO and AZO films. During the IFO film deposition in Ar atmosphere, 3.1% of O_2 and 2.5% of H_2 were introduced. Throughout the whole set of IFO depositions, the power of 3000 W and deposition pressure of 3 mTorr were held constant. The AZO films of varying thickness were deposited on IFO films in Ar atmosphere with 1.2% of H_2 with a power of 1000 W and at a deposition pressure of 0.9 mTorr. For all the films in ambient air, post-deposition annealing was performed for 20 minutes at 220 °C.

4.3.2 Structure and morphology

Fig. 4.16 shows the XRD patterns of the of the IFO films, in as-deposited state and after annealing, as a function of the thickness. The peaks match with the cubic bixbyite structure of In_2O_3 according to the ICDD database [16]. The XRD patterns of the films grown in as-deposited state indicate the amorphous nature of the films, which is mainly due to the presence of H_2 during sputtering [14]. However, after annealing, the film achieves polycrystalline cubic In_2O_3 structure. This indicates the solid phase crystallization of the films after annealing at 220 °C [15]. The strongest diffraction peak (222) is prominent at 30.56°; other peaks were assigned correspondingly.
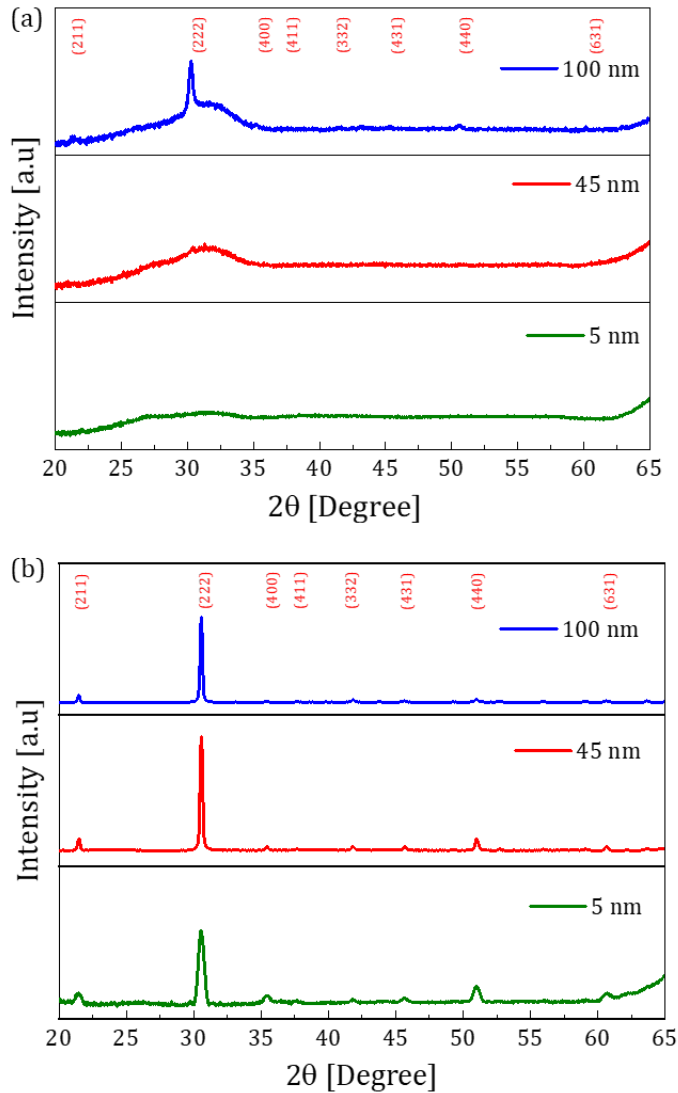
Figure 4.16: X-ray diffraction patterns of IFO samples deposited on silicon substrates with varying thickness in (a) as-deposited and (b) annealed states. The peaks match with the cubic bixbyite structure of In_2O_3 according to the ICDD database.

It was found that, as the thickness of the films increased, the intensity of the (222) reflections increased, whereas their width decreased. The mean crystallite size of the films was calculated from the FWHM of the X-ray (222) peak following the Scherrer's formula [5]. The 5 nm, 45 nm, and 100 nm films show a grain size of 19 nm, 39 nm, and 42 nm, respectively. This indicates that the grain size of the films increases at thicker films, which is generally observed in the growth of thin films [38].

Fig. 4.17 shows the SEM micrographs of 5-nm- and 100-nm-thick films before and after annealing. The clear formation of larger grains as thickness increases is observed, and increased grain size after annealing is visible.
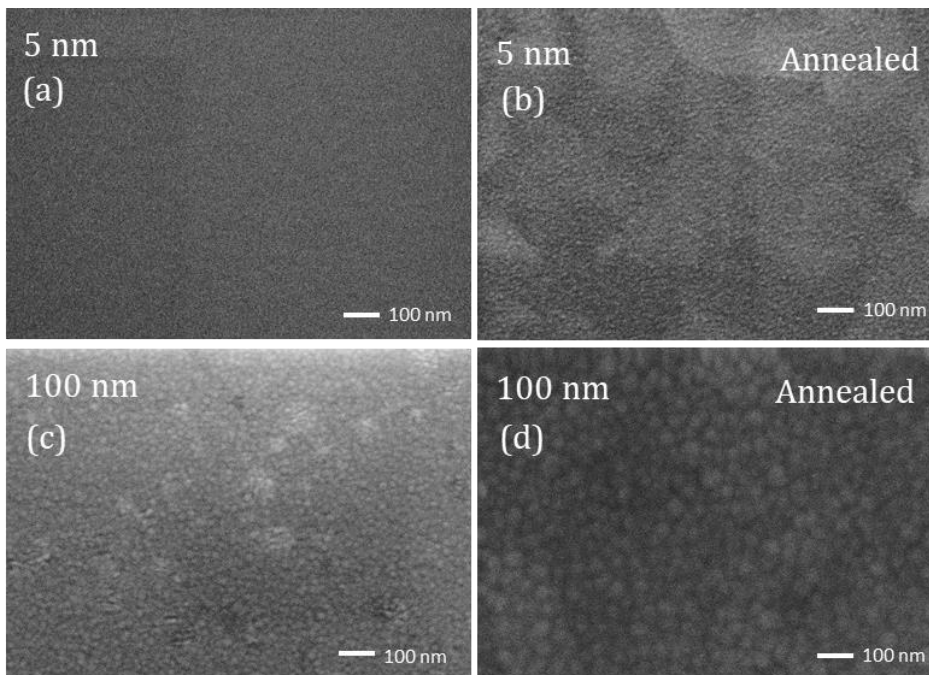
Figure 4.17: SEM micrographs corresponding to 5-nm- and 100-nm-thick IFO films, (a, b) in as-deposited state and (c, d) after annealing. All the SEM measurements were performed in samples grown on Si substrates.

Fig. 4.18 shows the AFM images corresponding to the same films (5 nm and 100 nm), before and after annealing. The measurements were performed on films grown on silicon substrates at 150 °C. It was observed that the root mean square (RMS) surface roughness of the films decreased as the thickness of the films increased, with values of 3.4 nm for 5-nm-thick films and 0.8 nm for 100-nm-thick films. A further decrease to 3.2 nm and 0.7 nm, respectively, was observed after annealing the films in ambient air. The higher RMS value on thin films indicates the formation of islands or clusters in the films [38]. As the thickness approaches 100 nm, the films show very smooth surface morphology, with an RMS value as low as 0.7 nm.
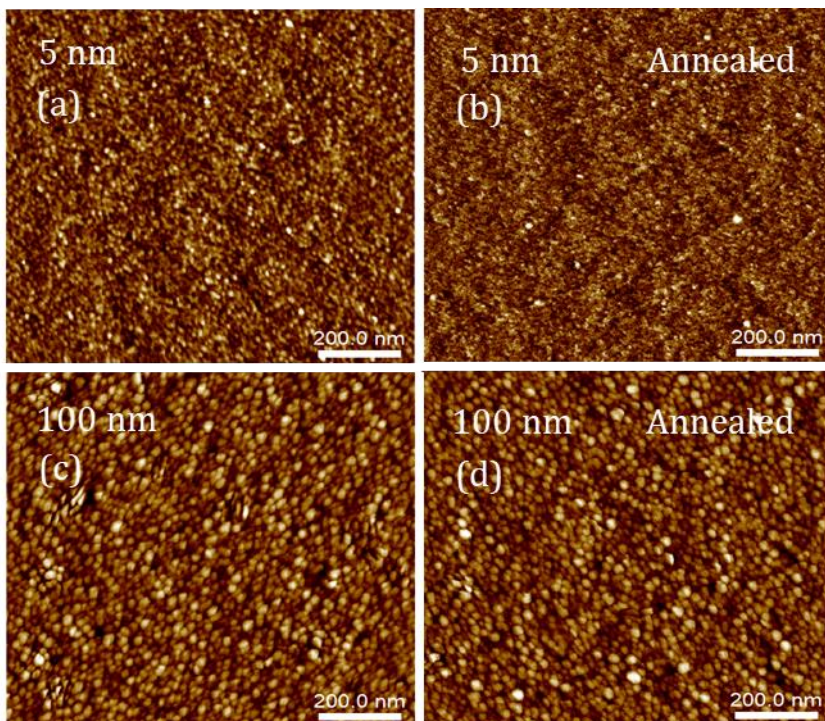
Figure 4.18: AFM images corresponding to 5-nm- and 100-nm-thick IFO films, (a, b) in as-deposited state (a, c) and (b, d) after annealing (c, d). All AFM measurements were carried out in samples grown on Si substrates.

4.3.3 Electrical and optical

The optimum deposition conditions for the best mobility IFO films were experimentally found to be at 3.1% of O_2 and 2.5% of H_2 (see section 4.2.2). Under this optimum deposition atmosphere, films with thicknesses ranging from 100 nm to 5 nm were studied. The Fig. 4.19 shows the resistivity, sheet resistance, mobility, and charge carrier density of the films as a function of the thickness, for as-deposited and annealed states.

As shown in Fig. 4.19(a), the resistivity of the films increased from 1.7×10^{-4} Ω cm to 5.0×10^{-4} Ω cm as the thickness of the film increased from 5 nm to 30 nm, and then remained almost constant until 100 nm. However, a decrease in resistivity is observed after annealing the films. The sheet resistance of the films dropped from 274 Ω/sq for 5 nm to 30 Ω/sq for 100 nm after annealing. Hall mobility slightly increased from 29.3 cm^2 V^{-1} s^{-1} to 31.3 cm^2 V^{-1} s^{-1} for films with thicknesses ranging from 5 nm to 31.3 nm, but for higher thicknesses (up to 100 nm) the mobility remained almost constant at around 40 cm^2 V^{-1} s^{-1}. After annealing the films, the mobility suddenly improved to 78.8 cm^2 V^{-1} s^{-1} for 5-nm-thick films and to 92.0 cm^2 V^{-1} s^{-1} for 100-nm-thick films. In addition, a drop in the carrier density from 1.2×10^{21} cm^{-3} to 3.9×10^{20} cm^{-3} was observed when increasing the thickness from 5 nm to 30 nm films, and it remained constant until 100 nm. Carrier concentration of the annealed films also showed the same trend.

According to the XRD measurements, the thickest film of 100 nm presents an average grain size of 42 nm, whereas in the thinnest film of 5 nm this value drops to 19 nm. The greater the grain size, the lower the density of grain boundaries, which act as traps for free carriers and barriers to carrier transport in the film. Therefore, an increase in grain size will reduce the scattering from the grain boundaries and, thus, increase the mobility and conductivity of the films [39]. This can also be noticed by the decrease in the sheet resistance at thicker films. The initial drop in resistivity is due to the high carrier density of the films. Then, the almost constant resistivity observed after 30 nm can be ascribed to the high mobility of the films that results from larger crystallite size. After annealing, the thinnest film of 5 nm

reaches a mobility around 78.8 cm^2 V^{-1} s^{-1}, which is remarkable for such thin film sputtered at low temperatures.
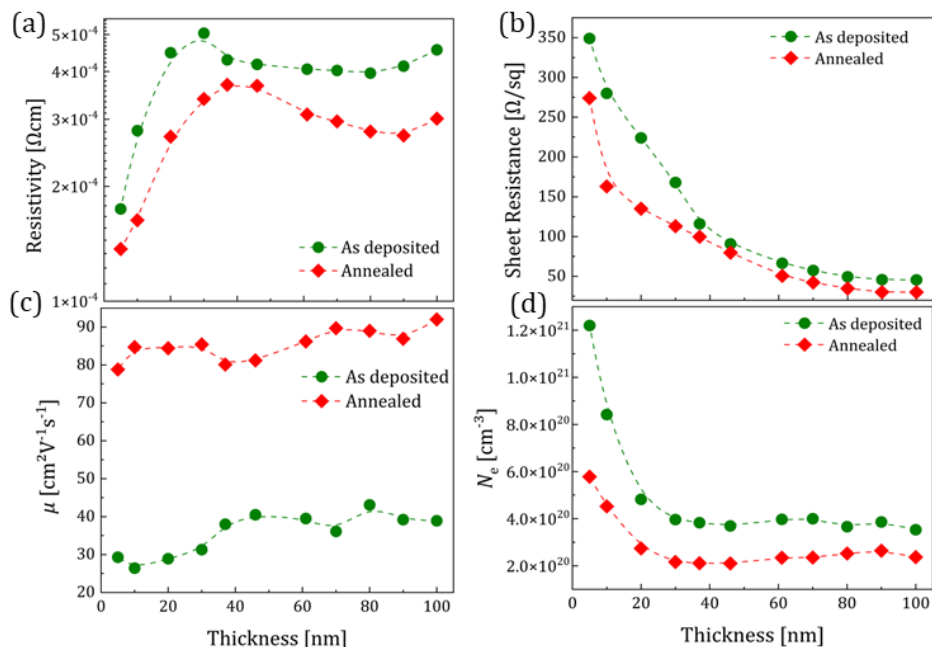
Figure 4.19: Electrical properties of as-deposited (green) and annealed (red) IFO films as a function of the thickness of the films. (a) Resistivity, (b) sheet resistance, (c) mobility, and (d) carrier density. The electrical properties of the films were measured in samples grown on glass substrates.

Finally, the increase in mobility after annealing, for films of different thicknesses, can be presumably attributed to solid phase crystallization, and to the interplay between these three possible dopants: oxygen vacancies (V_o^{++}), fluorine dopants and atomic hydrogen (H_o^+ and H_i^+) [39].

The optical properties of the IFO films as a function of the film thickness have been studied. All the measurements were conducted on films deposited on flat glass as substrate, and the properties were assessed before and after the annealing. Fig. 4.20 shows the weighted absorptance ($A_{weighted}$) of the films with different thickness ranging from 5 nm to 100 nm. As it can be seen in

Fig. 4.20, the absorption of the films increases as their thickness increases; as well, annealing results in an overall reduction in absorption. Under these conditions, a 100-nm-thick film annealed in air shows a weighted absorption of 2.1%, whereas the value decreases down to 0.1% in an annealed 5-nm-thick film. This observed trend with thickness could simply be explained by considering the Beer-Lambert law, i.e., $I(d) = I_0 \exp(-\alpha \cdot d)$, where I_0 is the intensity of the incident light, d is the thickness of the film, and α is the absorption coefficient [40].
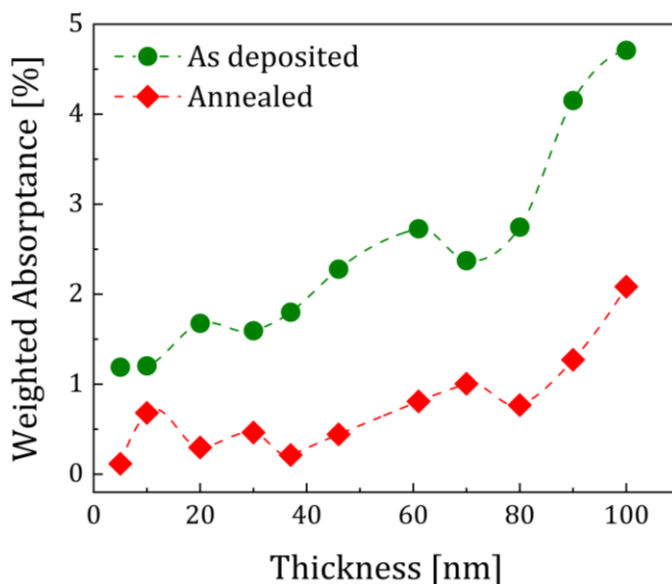
Figure 4.20: Weighted absorptance of the IFO films with varying thickness in as-deposited (green) and annealed (red) states. The weighted absorptance of the films were calculated from the total transmittance and total reflectance of the films measured on glass substrates.

4.3.4 Application of seed layers

The impact of AZO films on seed layers of IFO films has been studied. With this aim, a total thickness of 100 nm was maintained while varying the thicknesses of both AZO and IFO layers. Fig. 4.21(a), (b), and (c) show the sheet resistance, electron mobility and charge carrier density, respectively,

for the as-deposited and annealed films. The bottom x axis represents the thickness of IFO film, whereas the top x axis corresponds to the AZO thickness, complementary to that of IFO until reaching the total IFO/AZO stack thickness of 100 nm.
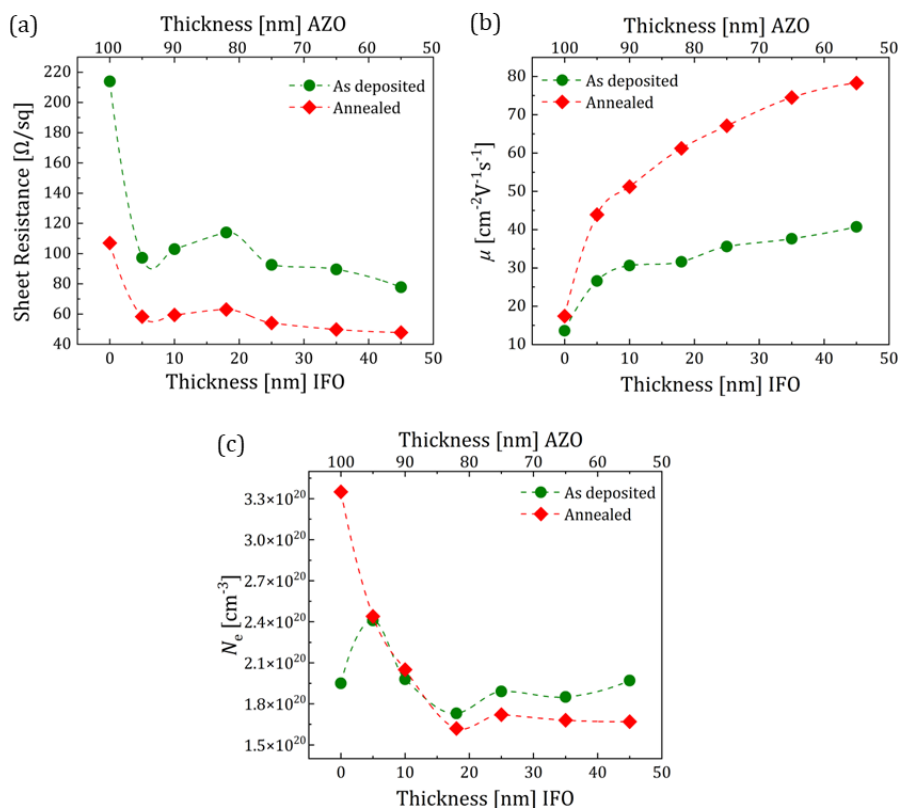
Figure 4.21: Electrical properties of as-deposited (green) and annealed (red) 100-nm-thick AZO/IFO stacks. The bottom x axis represents the thickness of IFO film, whereas the top x axis corresponds to the AZO thickness, complementary to that of IFO until reaching the total IFO/AZO stack thickness of 100 nm. (a) Sheet resistance, (b) mobility, and (c) carrier density of the films.

The sheet resistance [Fig. 4.21(a)] of the as-deposited films was found to decrease with increasing IFO films thickness, i.e., from 214 Ω/sq for pure

100-nm-thick AZO film to 78 Ω/sq for 45 nm/55 nm-IFO/AZO stack. After annealing, the sheet resistance of pure 100-nm-thick AZO films dropped from 214 to 107 Ω/sq. Likewise, after annealing the sheet resistance of 5 nm/95 nm IFO/AZO stack was reduced from 97 to 58 Ω/sq, and in 45 nm/55 nm IFO/AZO stack it decreased from 78 to 47 Ω/sq. Similarly, Hall mobility [Fig. 4.21(b)] was also found to increase with increasing IFO thickness, from a mobility of 13.6 cm^2 V^{-1} s^{-1} for pure 100-nm-thick AZO films to 41 cm^2 V^{-1} s^{-1} for 45 nm/55 nm IFO/AZO stack in as-deposited state. Here, as well, annealing improved the mobility of IFO/AZO stack. For 5 nm/95 nm IFO/AZO stack, mobility increased from 27 to 44 cm^2 V^{-1} s^{-1}, and from 40.7 to 78.3 cm^2 V^{-1} s^{-1} for the 45 nm/55 nm IFO/AZO stack. This shows the remarkable effect of even 5-nm-thick IFO seed layer in improving the mobility of the stack. It is also observed that annealing did not make any significant change in the mobility of pure 100-nm-thick AZO films.

The charge carrier density [Fig. 4.21(c)] of the as–deposited films initially increased when a 5-nm-thick IFO film was introduced instead of pure 100- nm-thick AZO film. Later, with further increase in IFO thickness the carrier density was reduced and remained almost constant. However, after annealing, the carrier density of the pure 100-nm-thick AZO film abruptly increased from 1.9×10^{20} to 3.4×10^{20} cm^{-3}. The charge carrier density of the IFO/AZO stack with 5 nm and 10 nm IFO thickness was not modified with annealing, but stacks with more than 18-nm-thick IFO films showed further reduced values than in the as-deposited ones. The improved conductivity and mobility of the IFO/AZO stack with respect to the pure AZO film was attributed to the increase in grain size of the AZO film during the growth owing to the presence of the IFO seed layer [8]. As the thickness of IFO films increases, the grain size became larger and thus enhanced mobility was observed. As a consequence, the increase in the grain size is expected to reduce the scattering from the grain boundaries, thus resulting in improved carrier mobility in the films. In addition, the solid-phase crystallization after annealing and the interplay of the dopants can also contribute to the increase in the mobility of films.

Fig. 4.22 shows the optoelectronic properties of the IFO/AZO stack with varying thicknesses of IFO and AZO layers in as-deposited and annealed

states. The weighted absorptance of the stack was calculated following Eq. 3.5.
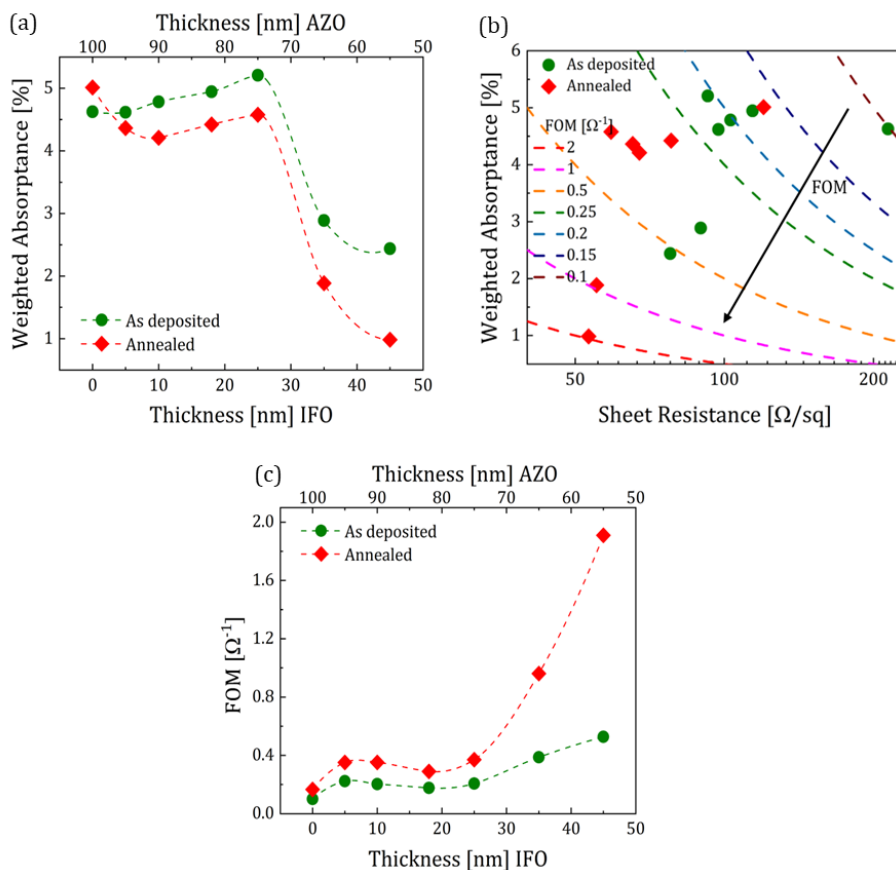
Figure 4.22: Optoelectronic properties of as-deposited (green) and annealed (red) 100-nm-thick AZO/IFO stacks. The bottom x axis represents the thickness of IFO film, whereas the top x axis corresponds to the AZO thickness, complementary to that of IFO until reaching the total IFO/AZO stack thickness of 100 nm. (a) Weighted absorptance of the films as a function of thickness, and (b) weighted absorptance as a function of the sheet resistance. The dashed lines in (b) indicate curves of constant FOM and the black straight line indicates the increase in FOM. (c) FOM of the IFO/AZO stack.

As indicated in Fig. 4.22(a), annealed IFO/AZO stack showed a reduced absorptance than in as-deposited state; nevertheless, in case of pure AZO film annealing increased absorptance due to enhanced carrier density in the films. Also, for both as-deposited and annealed IFO/AZO stack, weighted absorptance remained almost constant with the increment in IFO thickness until 25 nm. However, further increase in the IFO thickness dramatically decreased the absorptance value. This can be attributed to the lesser absorption in AZO layer owing to the decreased scattering from larger grain boundaries. The grain boundaries of AZO were found to increase with the increase in IFO seed layer thickness.

Fig. 4.22(b) shows the weighted absorptance (calculated for the 300–1200 nm wavelength range) as a function of the sheet resistance for IFO/AZO stacks. The dashed lines indicate a constant *FOM*, which can be calculated using Eq. 3.6. Annealed stacks showed reduced optical absorptance and low sheet resistance values that contributed to a high *FOM*.

In Fig. 4.22(c), the *FOM* of stacks are plotted as a function of IFO/AZO thickness for both as-deposited and annealed states. Stacks with IFO seed layer showed a clear improvement in the *FOM* than the pure 100-nm-thick AZO film. Moreover, annealing the stacks showed an enhancement in the *FOM* values. Therefore, making TCO stacks via the approach of using a high-mobility IFO seed layer proved as an effective method to enhance the electrical and optical properties of AZO films. This method can be applied to other TCO materials as well, while simultaneously reducing the usage of indium. As the next step, strategies were introduced to completely avoid In by employing dielectric metal dielectric structures.

4.4 Development of DMD structures as front contact for solar cells

Here, a completely sputtered, cost-effective and stable DMD layer of AZO/Ag:Al/AZO was fabricated to fully avoid the In usage. To avoid clustering of the metal nanostructures in the ultra-thin films the Ag was co-sputtered with Al. However, the AZO/Ag:Al/AZO layer does not promote a preferred hole-selectiveness. Later, it was accomplished by replacing the

bottom AZO layer with a high-quality hole-selective V_2O_5 layer. Silicon solar cells were then fabricated using a front V_2O_5/Ag:Al/AZO multilayer electrode, which was optimized for the thickness of the V_2O_5.

4.4.1 Experimental method

For examining and optimizing the properties of the DMD AZO/Ag:Al/AZO multilayers, these structures were deposited on Corning glass 1737F. All thin films were deposited by means of rf sputtering (ATC ORION 8 HV) using a 3-inch target. The vacuum chamber was pumped to a base pressure of 3×10^{-6} Torr prior to all the depositions. AZO films were deposited from ZnO/Al_2O_3 target (98/2 wt %) of 99.99% purity. The depositions were done at different pressures in the range between 1 and 8 mTorr with a constant power of 150 W. Reactive argon hydrogen (Ar:H_2) atmosphere (3.5% of H_2) was maintained in the vacuum chamber. The films were deposited at room temperature and at 100 °C with a deposition rate of 3.5 nm/min. The ultra-thin Ag:Al metallic films with sub-nanometer roughness were prepared by co-sputtering of Al and Ag at room temperature. The sputtering power of the Ag target (99.99% pure) was kept constant at 100 W whereas the power applied to Al target (99.99% pure) varied from 100 W to 175 W. The sputtering was performed in an atmosphere of argon and all the depositions were carried out at a base pressure of 1 mTorr. The thickness of the films was estimated from the deposition rates of 100-nm-thick films of Al and Ag deposited on glass substrate at similar conditions. Thus, the Al content in the Ag:Al films can be estimated between 16% to 20% in different samples.

N-type (100) c-Si wafers with a resistivity of 2 Ω cm, a thickness of 280 μm, one-side polished, and non-textured were used for the fabrication of solar cells. Four different solar cell architectures were developed with modifications in the hole-selective layer: one without sandwiching Ag:Al layer in AZO and V_2O_5, and the other three by incorporating Ag:Al layer with varied thickness of V_2O_5. Thermally-evaporated V_2O_5 was used as the dopant-free hole-selective contact. An intrinsic (*i*-type) a-Si:H and doped *n*-type a-Si:H layers were deposited on the rear side by PECVD to provide a reference electron selective contact. The lithographic patterning of 1 cm^2 was defined as the active area and a 2-μm-thick Ag grid (4.5% shadow) was

thermally evaporated as the front contact. Finally, the back-contact metallization was accomplished by thermally evaporating Al (1 μm thick).

4.4.2 Optimization of AZO films

Electrical and optical characterization of the sputtered AZO films was carried out. The total thickness of each film was kept around 75 nm, which provides a good antireflection property [41][42].Films were studied with varying pressure, keeping the temperature (100 °C) and power (150 W) as constant deposition parameters. As it can be seen in the inset of Fig. 4.23, a huge decrease in sheet resistance from about 1 kΩ/Sq to around 100 Ω/Sq was observed in the films by reducing the deposition pressure from 8 to 1 mTorr. This effect could be explained by either the formation of oxygen vacancies or a higher hydrogen reduction in the films. This agrees with the steady decrease in the infrared transmittance of the films (see Fig. 4.23) as the deposition pressure is reduced [43][44]. Transmittance measurements indicate that all the films grown at different pressures show an average transmittance of 80%. The transmittance of the films in the visible range was independent of the pressure as shown in Fig. 4.23, whereas the inset shows the drop in sheet resistance at lower deposition pressure.

4.4.3 Ultra-thin Ag:Al layers

To improve the electric properties of the AZO films, an ultra-thin Ag film was sandwiched between two AZO layers. The optical properties and sheet resistance of this intermediate ultra-thin Ag films for thickness ranging from 5 to 12 nm were studied. Results showed that the broad drop in transmittance within the visible region could be explained by the Volmer-Weber growth model [45], i.e., the tendency of silver atoms to form islands during the first few nanometers [see Fig. 4.24(a)]. The absorption caused by the formation of localized surface plasmons would explain the comparatively low optical transmittance and electrical discontinuity [46][47]. Therefore, the pure Ag films were highly resistive, reaching sheet resistances greater than 10^5 Ω/Sq until a threshold thickness of 10 nm, which leads to a sheet resistance of 2×10^3 Ω/Sq.

To obtain ultra-smooth Ag-based films with reduced RMS roughness, electrical continuity and higher transmittance, Ag:Al films were prepared by co-sputtering of Al with Ag. Al doping enhances the density of heterogeneous nucleation sites, thus achieving higher nuclei density and smaller particle size [48].
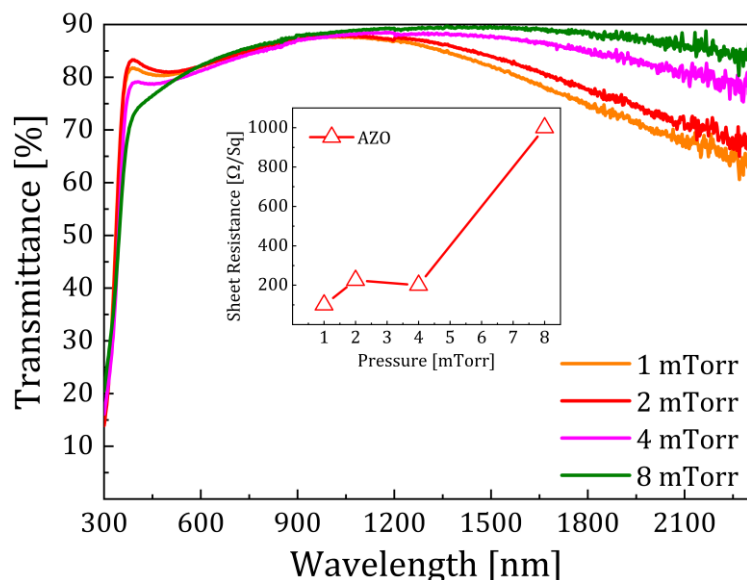
Figure 4.23: Optical transmittance of AZO films sputtered in Ar:H$_2$ atmosphere at varying pressure. Overall transmittance in the visible region was independent of the pressure. The inset shows the decrease in the sheet resistance of the films at lower pressures.

First, Ag:Al films were optimized for Al doping concentration with a constant power on the Ag target. Fig. 4.24(b) shows the transmittance of films deposited at varying powers of Al from 100 W to 175 W, while keeping constant the power of Ag at 100 W. It was found that the highest transmittance and lowest sheet resistance were obtained for the Ag:Al films sputtered at 138 W, with a transmittance of 75–80% in the visible region and a sheet resistance of 60 Ω/Sq. All other films exhibited higher sheet

resistance. Once optimized the plasma power during deposition, several Ag:Al films with varying thickness, co-sputtered with Al at 138 W, were studied. Fig. 4.25 shows the optical transmittance of the pure 6-nm-thick Ag film compared to that of different Ag:Al films with thickness ranging from 6 nm to 14 nm.
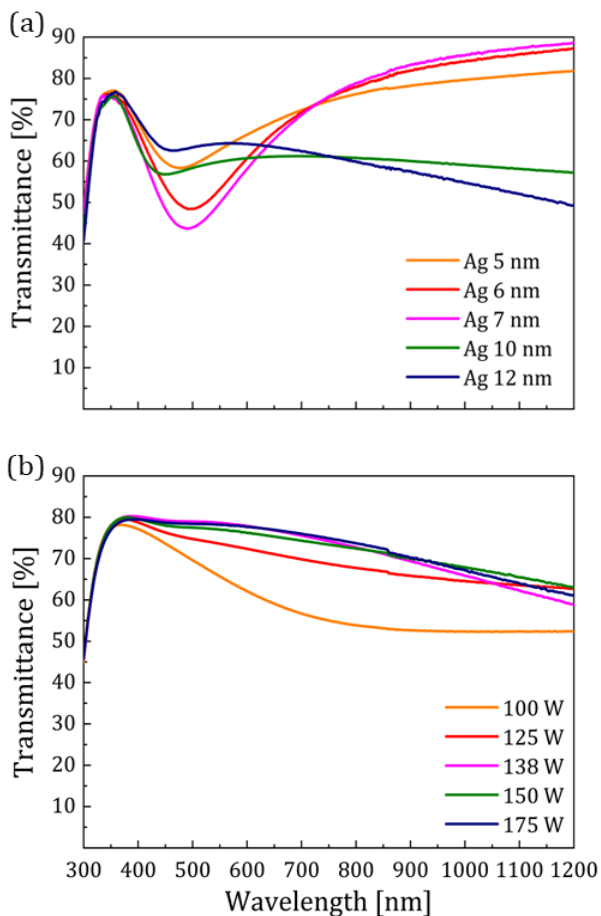
Figure 4.24: (a) Optical transmittance of Ag layers with varying thicknesses deposited on glass substrate. (b) Optical transmittance of Ag:Al films deposited on glass substrate.
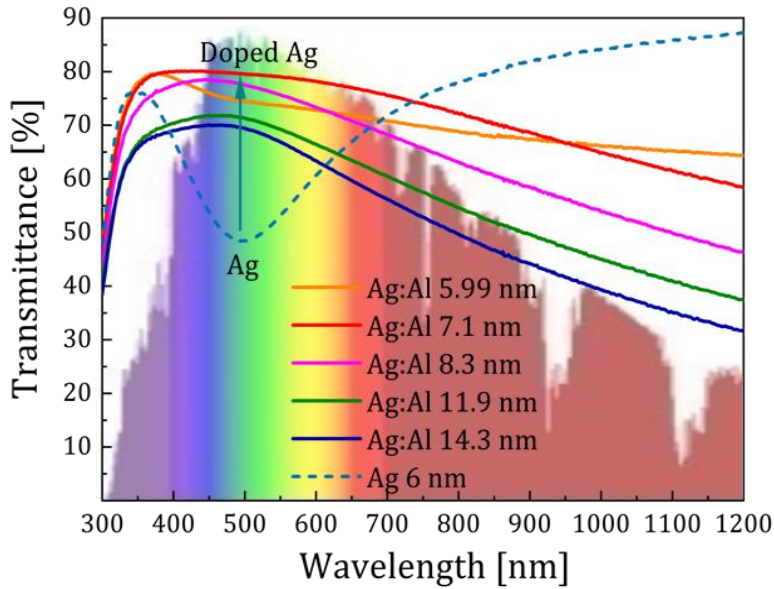
Figure 4.25: Optical transmittance of Ag:Al samples deposited on glass substrate. A sample with 6-nm-thick Ag layer without Al doping is also shown for the sake of comparison. A 30% increase in transmittance was observed due to doping.

For the same thickness of Ag and Ag:Al samples, an increase of 30% transmittance was obtained for the latter in the visible region. Thus, avoiding the surface plasmons absorption due to non-continuity of such ultra-thin films. The AFM images of the surface morphology of a 7-nm-thick pure Ag film, as well as 8.3-nm-thick and 7.1-nm-thick Ag:Al films, are shown in Fig. 4.26. The peak-to-valley height of pure Ag films, with a maximum value of 14.4 nm, and Ag:Al films with 1.8 nm, demonstrates the smoothness of the films. The RMS roughness value obtained for the 7- nm-thick pure Ag film was 3.99 nm, and 0.47 nm and 0.37 nm for the 8.3-nm-thick and 7.1-nm-thick Ag:Al films, respectively. This lower RMS value confirms again the ultra-smooth nature of the films. Fig. 4.27 shows the SEM micrographs of the above-mentioned samples. the easily observed clustering of pure Ag films

and the homogeneity in the Ag:Al films demonstrate the continuity in these layers.
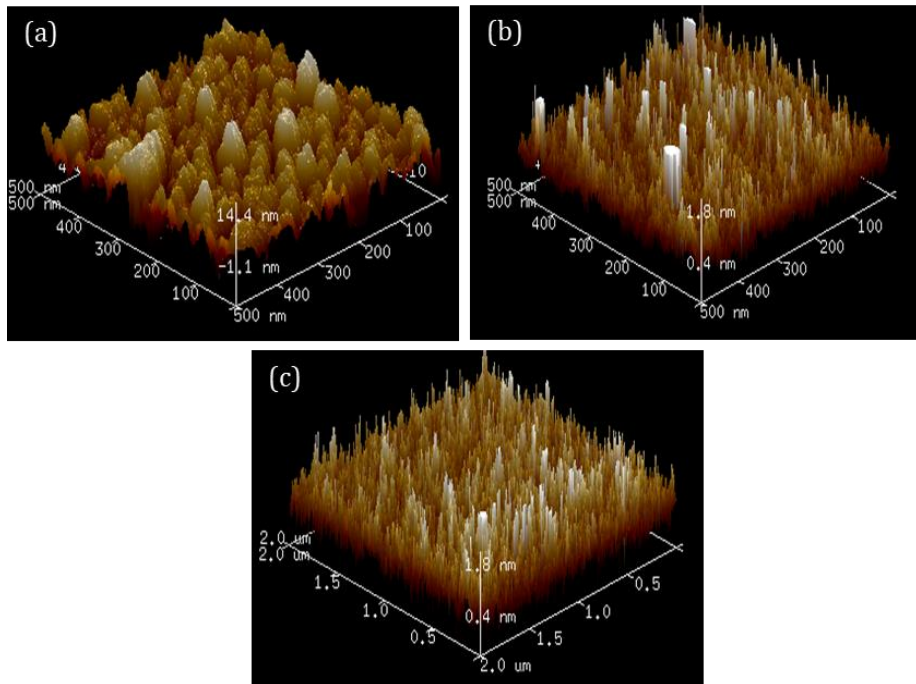
Figure 4.26: AFM images of (a) 6-nm-thick Ag film with an RMS roughness of 3.99 nm, (b) 8.3-nm-thick Ag:Al films with an RMS roughness of 0.47 nm, and (c) 7.1-nm-thick Ag:Al films with an RMS roughness of 0.37 nm.

Sheet resistance with the increasing thickness of Ag and Ag:Al films are shown in Fig. 4.28. The Ag films with thickness less than 7 nm behave as insulators, with a high sheet resistance of 10^5 Ω/Sq. In contrast, Ag:Al films of similar thickness show a sheet resistance of several 100 Ω/Sq. The huge drop in sheet resistance in Ag:Al films was due to the enhanced density of heterogeneous nucleation sites, avoiding the formation of isolated islands in the films [46]. The calculated resistivity of the Ag:Al films was comparable to the bulk resistivity of Ag films, confirming the uniform nature of the films.
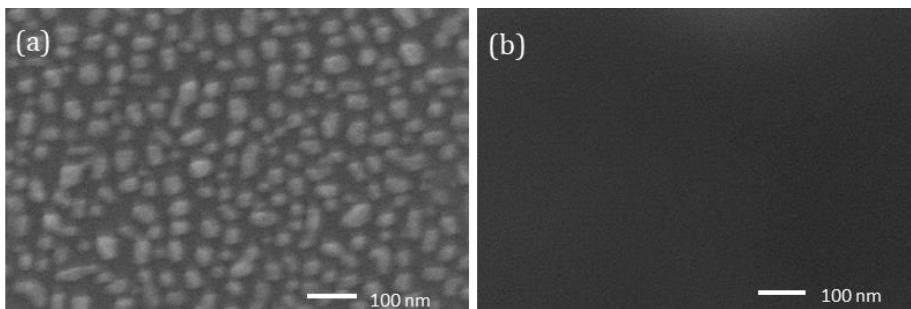
Figure 4.27: Comparison of SEM micrographs corresponding to (a) a Ag film of 6 nm, and (b) a Ag:Al film of 7.1 nm. Al doping reduces the clustering and aids to form more continuous films.
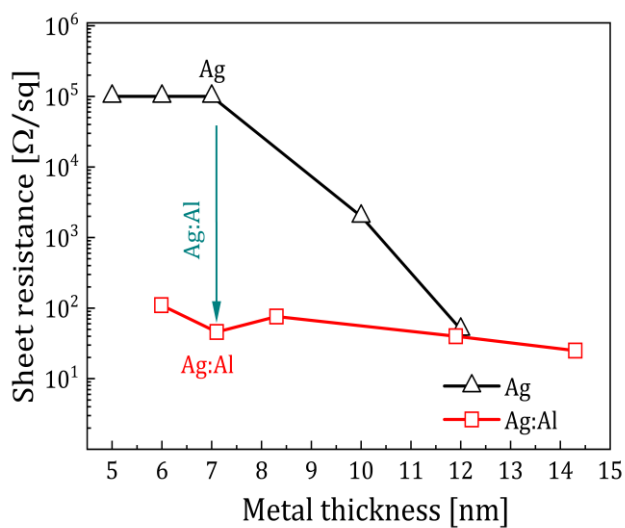
Figure 4.28: Sheet resistance as a function of thickness for Ag and Ag:Al films. The inset compares the resistivity of the Ag and Ag:Al films as a function of thickness.

4.4.4 DMDs (AZO/Ag:Al/AZO)

The influence of the Ag:Al layers on the AZO/Ag:Al/AZO structures was investigated by studying the electrical and optical properties of the multilayers. Fig. 4.29 shows the transmittance spectra for various metal thicknesses, and the inset displays the sheet resistance as a function of metal thickness for AZO/Ag:Al/AZO multilayers.
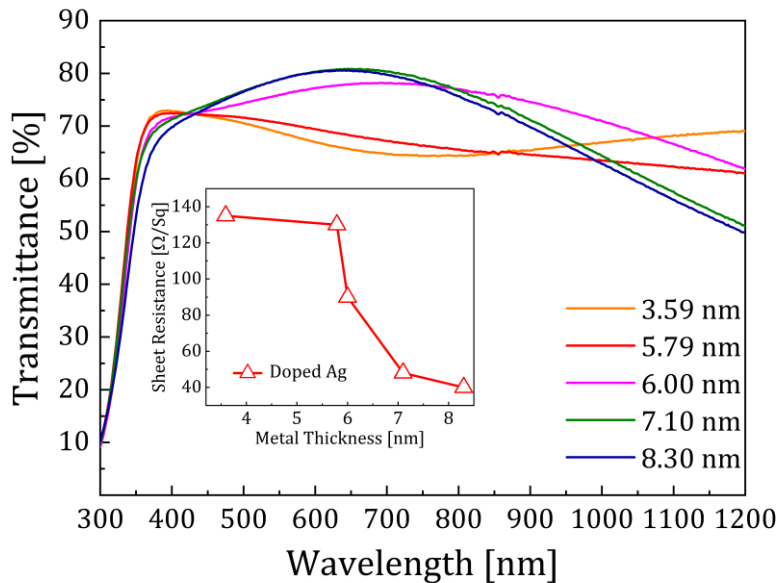
Figure 4.29: Optical transmittance of AZO/Ag:Al/AZO (18 nm/Ag:Al/70 nm) multilayer structure deposited on glass substrate. The inset shows the sheet resistance as a function of the metal thickness.

The thickness of the AZO layers was fixed as 18 nm and 70 nm for the bottom and top layer, respectively. Optimized Ag:Al films sputtered at 138 W with varying thickness from 3 to 8.3 nm were used for the study. As the thickness of the intermediate layer increased, a decrease in sheet resistance and an increase in transmittance was observed in the multilayer structure. The intermediate layer of 7.1 nm showed the best result, with the lowest sheet

resistance of 48 Ω/Sq and the highest transmittance of 80% in the visible region. Considering the final step to fabricate TCO for devices, *FOM* values were calculated for these structures. The *FOM* defined as in Eq. 3.6 was calculated in the 300–1200 nm range for ITO, AZO thin film and multi-layered structure, and the values are given in Table 4.2. The *FOMs* were estimated for reduced AZO films (Ar:H$_2$ atmosphere), at 100 °C and at room temperature (RT), and for non-reduced AZO films (Ar atmosphere) at RT. The multilayer structure attained the highest *FOM* of 1.4 Ω^{-1} compared to other films, which lied between 0.13 and 1.3 Ω^{-1}. This shows the potential of AZO/Ag:Al/AZO multilayer to replace ITO, which could be used as transparent conducting film in various optoelectronic devices such as large-area solar cells, diodes and photodetectors.

Table 4.2: Comparison of *FOM* values for thin films and the multi-layer structure fabricated.

	Temperature (°C)	*FOM* (Ω^{-1})
AZO*	RT	0.13
AZO #	RT	0.9
AZO #	100	1.3
AZO#/Ag:Al*/AZO#	RT	1.4
ITO*	100	1.2

*Deposited in Ar atmosphere. #Deposited in Ar:H$_2$ atmosphere.

4.4.5 Substitute first AZO layer by a TMO to play the double role: HTL and transparent contact for solar cells

In order to implement this electrode in photovoltaic devices, a carrier selective layer must be included. With this aim, further studies were conducted to replace the AZO bottom layer with V$_2$O$_5$, to develop an all-in-one selective contact plus a transparent electrode for silicon-based solar cells. The V$_2$O$_5$ layer is needed to act as a dopant-free hole-selective layer as

described in chapter 2. Even if they have clearly different electronic properties, replacing AZO by V_2O_5 as the bottom layer does not notably modify change the transparency of the stack. The transfer-matrix method (TMM) algorithm developed in a previous work was used to predict the behavior of multilayer thin film structures [13].
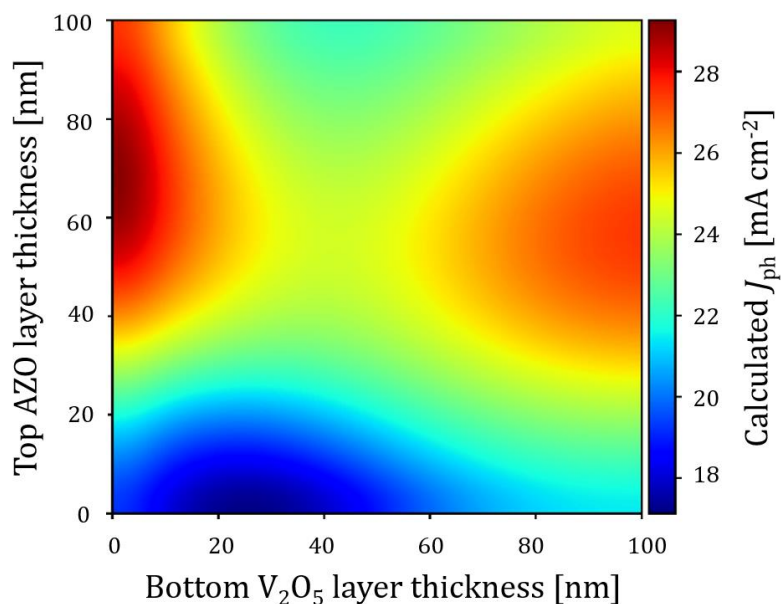
Figure 4.30: Mapping of the photogenerated current J_{ph} under AM 1.5 spectrum irradiance as a function of top AZO and bottom V_2O_5 thicknesses. The Ag:Al intermediate layer thickness was fixed at 7.1 nm.

The TMM algorithm for V_2O_5/Ag:Al/AZO multilayers predicted the optical performance of these structures on c-Si and, by integrating the air-mass 1.5 global irradiance (AM 1.5) spectrum, the total photogenerated current J_{ph} was calculated. Fig. 4.30 shows the expected mapping of the current density for varying thickness of V_2O_5 and AZO with a fixed thickness for the Ag:Al intermediate layer of 7.1 nm. From the simulation, the optimum thickness for the finest optical properties and high photogenerated current for the AZO layer was between 40 and 80 nm. As far as the optimum thickness for V_2O_5 layer is concerned, the best performance could be expected below 20 nm or above 70 nm. However, we have some additional constraints for its

implementation in the solar cell device. On one hand, the thickness of the V_2O_5 layer should not be less than 20 nm to prevent damage at the interface during the sputtering step. On the other hand, it cannot be too thick, such as 100 nm, because of its insulating nature. The same calculation considering the whole AZO/Ag:Al/AZO stack deposited on the V_2O_5 selective layer predicted a reduction in the photogenerated current of about 2–3%. Thus, a direct V_2O_5/Ag:Al/AZO stack on silicon was preferred for device testing. The solar cells were fabricated with a fixed thickness of the AZO layer at 50 nm, and different thicknesses of the V_2O_5 layer from 20 to 50 nm were used as described in Fig. 4.31.
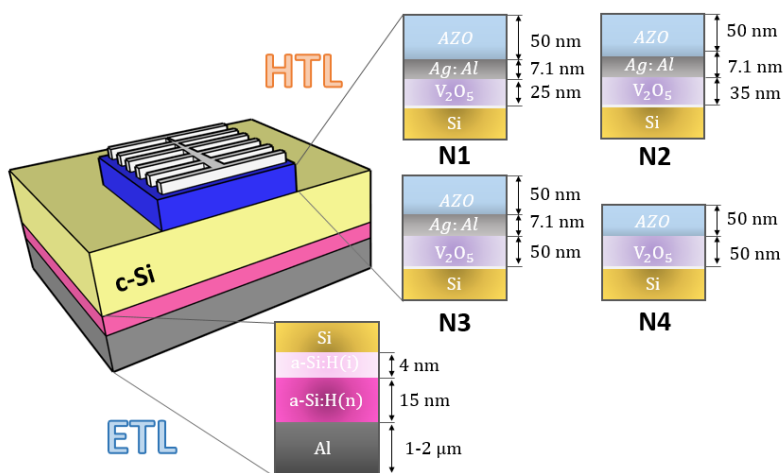
Figure 4.31: Schematic of a solar cell based on *n*-type c-Si, with the different configurations studied. The multi structured layers of V_2O_5/Ag:Al/AZO act as both transparent conducting and hole-selective electrode [49].

Once the multilayer stack was validated via simulation, four different solar cell architectures (N1, N2, N3 and N4) were fabricated using different thicknesses for the V_2O_5 layer (25 nm, 35 nm, 50 nm, and 50 nm, respectively) as the hole-selective contact. Out of these, for N1, N2, and N3 cells V_2O_5/Ag:Al/AZO multilayer acted as hole transport and transparent conducting layer, whereas the N4 cell structure consisted of a AZO/V_2O_5 multilayer, i.e., without the Ag:Al metallic layer. For these studies, the

thickness of the AZO and Ag:Al layer was kept constant at 50 nm and 7.1 nm, respectively. The thickness of the layers was chosen from the electrical, optical, and topographical aforementioned studies on the films of AZO and Ag:Al.
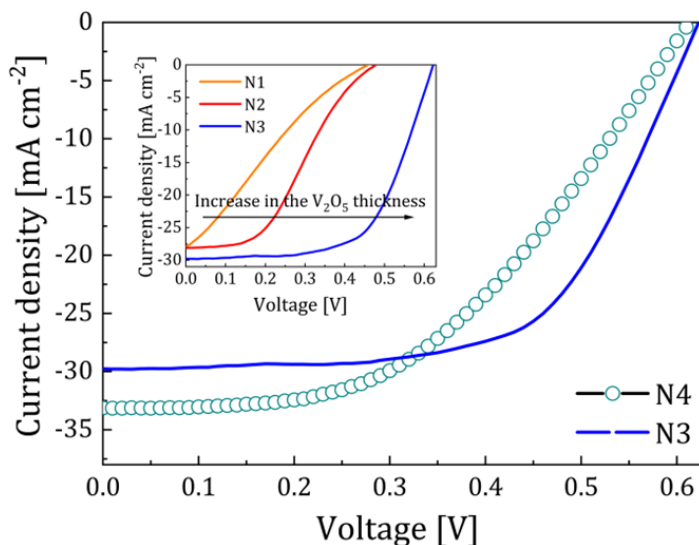
Figure 4.32: *J-V* curve measured under AM 1.5 spectrum irradiance (100 mW/cm²). N1, N2, N3 are the labels corresponding to the devices with V_2O_5 layer thickness of 25 nm, 35 nm, 50 nm, respectively, and N4 for the device without the metallic layer.

Table 4.3: Photovoltaic parameters (V_{oc}, J_{sc}, *FF*, *PCE*) of the solar cells fabricated. N1, N2, and N3 are the cells with V_2O_5 layer thicknesses of 25 nm, 35 nm, and 50 nm, respectively. N4 is the cell without the Ag:Al metallic layer and with a 50-nm-thick V_2O_5 layer.

	N1	**N2**	**N3**	**N4**
V_{oc} (mV)	459	479	631	614
J_{sc} (mA cm⁻²)	28.0	28.1	29.8	33.1
FF (%)	17.5	38.6	61.2	47.5
PCE (%)	2.2	5.2	11.5	9.6

The *J-V* characteristics of the fabricated cells are displayed in Fig. 4.32, whereas Table 4.3 summarizes the resulting photovoltaic parameters. The *J-V* curves corresponding to devices N1, N2 and N3 showed that, as the thickness of the V_2O_5 layer increased, there was a huge increase in the V_{oc} from 459 mV to 631 mV, and in the fill factor (*FF*) from 22 to 61% (inset of Fig. 4.32). This variation could be explained by the formation of defects in the V_2O_5 layer during sputtering because of Ag and Al ion bombardment. As the thickness of the V_2O_5 layer increases, the damaging effect decreases and the inversion layer made by V_2O_5 becomes sufficient to improve the V_{oc} and other parameters of the cell. N4 device was fabricated with 50-nm-thick V_2O_5 layer, hence reducing the bombardment defects and improving the optical parameters. This device without the Ag:Al metallic layer showed a V_{oc} = 614 mV, J_{sc} = 33.1 mA cm^{-2}, *FF* = 47.5%. and a *PCE* = 9.6% (Fig. 4.32). The device N3. with same thickness of V_2O_5, showed V_{oc} = 631 mV, J_{sc} = 29.8 mA cm^{-2}, *FF* = 61.2%, and *PCE* = 11.5%. This enhancement in V_{oc}, *FF* and η in the device N3 could be directly attributed to the presence of the metallic Ag:Al layer, which decreased the sheet resistance. All devices were measured under a simulated AM 1.5 irradiance spectrum of 100 mW/cm^2.

The *EQE* of the N3 solar cell, together with its reflectance spectrum, are plotted in Fig. 4.33. On one hand, the *EQE* dropped at photon energies lower than the Si bandgap (corresponding to wavelengths λ > 1100 nm). On the other hand, at higher photon energies (wavelengths λ < 500 nm) the *EQE* was reduced because of the absorption in the front layers (DMD) and recombination at the front interface. A balance of the current entities calculated by integrating the solar spectrum is computed in the inset of Fig. 4.33, taking into account both optical and internal recombination losses. The maximum photocurrent that could be obtained for photon energies higher than the Si bandgap of 1.1 eV was 42.3 mA cm^{-2}. Reflectance losses of 11.3% on the front surface of the cell reduced the photogenerated current down to 37.5 mA cm^{-2}. The final photogenerated current value limits to 29.8 mA cm^{-2} due to the internal loss of 20.6% in the solar cell.

Photocurrent losses in the c-Si bulk and the rear contact were expected to be very low accounting for the high-quality substrate and the rear surface passivated contact. Thus, the 20.6% internal photocurrent loss could be

explained by the parasitic absorption in the vanadium oxide layer and mainly to the absorption in the Ag:Al metallic layer. The degradation of V_2O_5 during sputtering also increased the internal recombination that eventually led to a reduction in the J_{sc} value. Further optimization in the thickness of the vanadium oxide layer in the V_2O_5/Ag:Al/AZO stack could reduce the damage during sputtering. The fabrication of solar cells on textured wafers assuming the same internal losses could also increase the J_{sc} value up to 2–3 mA cm^{-2}. Finally, controlling the thickness of Ag:Al and AZO layers could lead to further improvement in the photogenerated J_{sc} value.
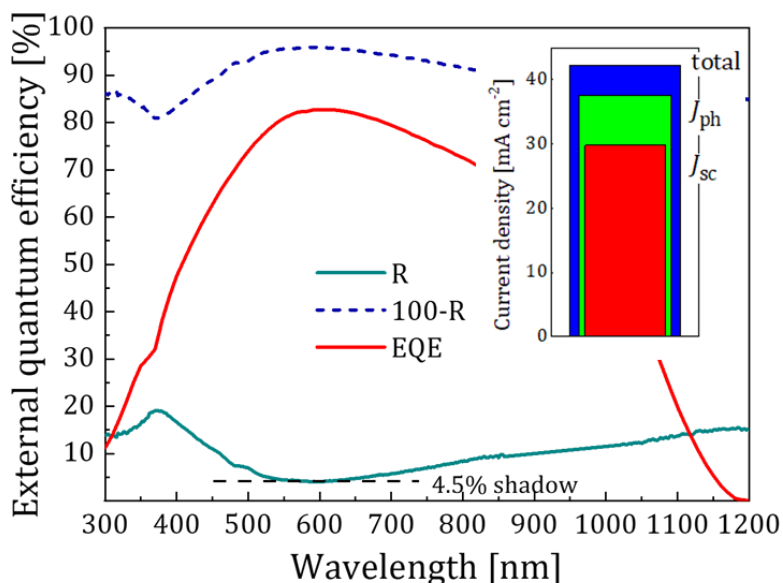
Figure 4.33: *EQE* curve of the fabricated (N3) solar cell together with its front reflectance spectrum. The inset shows the charge-carrier generation and different loss mechanisms balanced for an AM 1.5 spectrum irradiance.

4.5 Conclusions

In the first part of the chapter, the structural, compositional, morphological, electrical, and optical properties of IFO films were investigated in depth

using an industrial approach. The highest mobility of 93 cm^2 V^{-1} s^{-1} at a carrier density of 2.2×10^{20} cm^{-3} was achieved for the films deposited at 3.1% O$_2$ and 2.5% H$_2$. The high-mobility films could then successfully be transferred to monofacial SHJ cells, achieving an efficiency of 22.65%.

In the next part of the chapter, ways to reduce the usage of In were explored due to the high price and scarcity of indium. To address this issue, here we developed the combination of seed layers of high-mobility indium-doped oxides of several nanometers and cheaper indium-free TCOs that are deposited on top of the seed layer, thus achieving high mobility and conductivity of the stack. The highest mobility of 78.3 cm^2 V^{-1} s^{-1} has been achieved in the 45 nm/55 nm IFO/AZO stack. This method can be experimented on other TCO materials, instead of using pure IFO or ITO films. This could help in reducing the usage of indium by 50%, paving the way for future optoelectronic applications.

In the final part of the chapter, the successful In substitution was achieved through the fabrication and optimization of ultra-thin Ag:Al layer as an intermediate layer for the AZO-based DMD structure, namely AZO/Ag:Al/AZO multilayers. The optimized AZO/Ag:Al/AZO multilayer structure showed a sheet resistance of 48 Ω/Sq and 80% transmittance in the visible region of the spectrum. Then, in order to develop a hole-selective layer for the fabrication of solar cells the above TCO multi-structure was reconfigured, i.e., by replacing the bottom AZO layer by V$_2$O$_5$. Hence forming a dopant-free V$_2$O$_5$/Ag:Al/AZO all-in-one TCO and hole-selective contact. Afterwards, solar cells were fabricated using this multilayer with varied thicknesses of the bottom V$_2$O$_5$ layer. The solar cell on n-type c-Si with 50-nm-thickness of V$_2$O$_5$ yielded a *PCE* of 11.5%, with remarkably high V_{oc} of 631 mV and J_{sc} of 29.8 mA cm^{-2}, showing its potential as an excellent TCO as well as a hole-selective contact.

References

[1]   A. Kumar, C. Zhou, The race to replace tin-doped indium oxide: Which material will win?, ACS Nano. 4 (2010) 11–14. https://doi.org/10.1021/nn901903b.

[2]   C.G. Granqvist, Transparent conductors as solar energy materials: A

panoramic review, Sol. Energy Mater. Sol. Cells. 91 (2007) 1529–1598. https://doi.org/10.1016/j.solmat.2007.04.031.

[3]   P.P. Edwards, A. Porch, M.O. Jones, D. V. Morgan, R.M. Perks, Basic materials physics of transparent conducting oxides, Dalt. Trans. (2004) 2995–3002. https://doi.org/10.1039/b408864f.

[4]   L. Barraud, Z.C. Holman, N. Badel, P. Reiss, A. Descoeudres, C. Battaglia, S. De Wolf, C. Ballif, Hydrogen-doped indium oxide/indium tin oxide bilayers for high-efficiency silicon heterojunction solar cells, Sol. Energy Mater. Sol. Cells. 115 (2013) 151–156. https://doi.org/10.1016/j.solmat.2013.03.024.

[5]   C. Han, G. Yang, A. Montes, P. Procel, L. Mazzarella, Y. Zhao, S. Eijt, H. Schut, X. Zhang, M. Zeman, O. Isabella, Realizing the Potential of RF-Sputtered Hydrogenated Fluorine-Doped Indium Oxide as an Electrode Material for Ultrathin SiO_x/Poly-Si Passivating Contacts, ACS Appl. Energy Mater. 3 (2020) 8606–8618. https://doi.org/10.1021/acsaem.0c01206.

[6]   M. Morales-Masis, E. Rucavado, R. Monnard, L. Barraud, J. Holovsky, M. Despeisse, M. Boccard, C. Ballif, Highly Conductive and Broadband Transparent Zr-Doped In_2O_3 as Front Electrode for Solar Cells, IEEE J. Photovoltaics. 8 (2018) 1202–1207. https://doi.org/10.1109/JPHOTOV.2018.2851306.

[7]   T. Koida, H. Fujiwara, M. Kondo, Hydrogen-doped In_2O_3 as high-mobility transparent conductive oxide, Japanese J. Appl. Physics, Part 2 Lett. 46 (2007). https://doi.org/10.1143/JJAP.46.L685.

[8]   D. Erfurt, M.D. Heinemann, S.S. Schmidt, S. Körner, B. Szyszka, R. Klenk, R. Schlatmann, Influence of ZnO-Based Sub-Layers on the Growth of Hydrogen Doped Indium Oxide, ACS Appl. Energy Mater. 1 (2018) 5490–5499. https://doi.org/10.1021/acsaem.8b01039.

[9]   Y. Zhang, M. Kim, L. Wang, P. Verlinden, B. Hallam, Design considerations for multi-terawatt scale manufacturing of existing and future photovoltaic technologies: Challenges and opportunities related to silver, indium and bismuth consumption, Energy Environ. Sci. 14 (2021) 5587–5610. https://doi.org/10.1039/d1ee01814k.

[10]   L. Ciacci, T.T. Werner, I. Vassura, F. Passarini, Backlighting the European Indium Recycling Potentials, J. Ind. Ecol. 23 (2019) 426–437. https://doi.org/10.1111/jiec.12744.

[11]   W. Wu, W. Lin, J. Bao, Z. Liu, B. Liu, K. Qiu, Y. Chen, H. Shen, Dopant-free multilayer back contact silicon solar cells employing V_2O_x/metal/V_2O_x as an emitter, RSC Adv. 7 (2017) 23851–23858. https://doi.org/10.1039/c7ra03368k.

[12]   T. Ma, M. Missous, G. Pinter, X. Zhong, B. Spencer, A.G. Thomas, D.J. Lewis, Sustainable ITO films with reduced indium content deposited by AACVD, J. Mater. Chem. C. 10 (2022) 579–589. https://doi.org/10.1039/d1tc04864c.

[13]   H.T. Nguyen, E. Ros, T. Tom, J. Bertomeu, J.M. Asensi, J. Andreu, I.M. Garcia, P. Ortega, M. Garin, J. Puigdollers, C. Voz, R. Alcubilla, Influence of a Gold Seed in Transparent V_2O_x/Ag/V_2O_x Selective Contacts for Dopant-Free Silicon Solar Cells, IEEE J. Photovoltaics. 9 (2019) 72–77. https://doi.org/10.1109/JPHOTOV.2018.2875876.

[14]   B. MacCo, M.A. Verheijen, L.E. Black, B. Barcones, J. Melskens, W.M.M. Kessels, On the solid phase crystallization of In2O3:H transparent conductive oxide films prepared by atomic layer deposition, J. Appl. Phys. 120 (2016) Art. no. 85314. https://doi.org/10.1063/1.4962008.

[15]   L. Tutsch, H. Sai, T. Matsui, M. Bivour, M. Hermle, T. Koida, The sputter deposition of broadband transparent and highly conductive cerium and hydrogen co-doped indium oxide and its transfer to silicon heterojunction solar cells, Prog. Photovoltaics Res. Appl. (2021) 835–845. https://doi.org/10.1002/pip.3388.

[16]   C. Han, L. Mazzarella, Y. Zhao, G. Yang, P. Procel, M. Tijssen, A. Montes, L. Spitaleri, A. Gulino, X. Zhang, O. Isabella, M. Zeman, High-Mobility Hydrogenated Fluorine-Doped Indium Oxide Film for Passivating Contacts c-Si Solar Cells, ACS Appl. Mater. Interfaces. 11 (2019) 45586–45595. https://doi.org/10.1021/acsami.9b14709.

[17]   T. Koida, M. Kondo, K. Tsutsumi, A. Sakaguchi, M. Suzuki, H. Fujiwara, Hydrogen-doped In_2O_3 transparent conducting oxide films prepared by solid-phase crystallization method, J. Appl. Phys. 107 (2010). https://doi.org/10.1063/1.3284960.

[18]   T. Koida, Y. Ueno, H. Shibata, In_2O_3-Based Transparent Conducting Oxide Films with High Electron Mobility Fabricated at Low Process Temperatures, Phys. Status Solidi Appl. Mater. Sci. 215 (2018) 1–14. https://doi.org/10.1002/pssa.201700506.

[19]   B. Macco, H.C.M. Knoops, W.M.M. Kessels, Electron Scattering and Doping Mechanisms in Solid-Phase-Crystallized In_2O_3:H Prepared by Atomic Layer Deposition, ACS Appl. Mater. Interfaces. 7 (2015) 16723–16729. https://doi.org/10.1021/acsami.5b04420.

[20]   N.L.H. Hoang, Y. Hirose, S. Nakao, T. Hasegawa, Crystallization kinetics of amorphous sputtered Nb-doped TiO_2 thin films, Appl. Phys. Express. 4 (2011) 2–5. https://doi.org/10.1143/APEX.4.105601.

[21]   A. Gulino, Structural and electronic characterization of self-assembled molecular nanoarchitectures by X-ray photoelectron spectroscopy, Anal. Bioanal. Chem. 405 (2013) 1479–1495. https://doi.org/10.1007/s00216-012-6394-8.

[22]   Y. Shigesato, N. Shin, M. Kamei, P.K. Song, I. Yasui, Study on fluorine-doped indium oxide films deposited by rf magnetron sputtering, Japanese J. Appl. Physics, Part 1 Regul. Pap. Short Notes Rev. Pap. 39 (2000) 6422–6426. https://doi.org/10.1143/jjap.39.6422.

[23]   J.S. Seo, J.H. Jeon, Y.H. Hwang, H. Park, M. Ryu, S.H.K. Park, B.S. Bae, Solution-processed flexible fluorine-doped indium zinc oxide thin-film transistors fabricated on plastic film at low temperature, Sci. Rep. 3 (2013) 1–9. https://doi.org/10.1038/srep02085.

[24]   L. Shen, Y. An, D. Cao, Z. Wu, J. Liu, Roomerature Ferromagnetic Enhancement and Crossover of Negative to Positive Magnetoresistance in N-Doped In_2O_3 Films, J. Phys. Chem. C. 121 (2017) 26499–26506. https://doi.org/10.1021/acs.jpcc.7b08732.

[25]   M.M. Can, S. Ismat Shah, M.F. Doty, C.R. Haughn, T. Frat, Electrical and optical properties of point defects in ZnO thin films, J. Phys. D. Appl. Phys. 45 (2012). https://doi.org/10.1088/0022-3727/45/19/195104.

[26]   B. Zhang, Y. Tian, J.X. Zhang, W. Cai, The role of oxygen vacancy in fluorine-doped SnO_2 films, Phys. B Condens. Matter. 406 (2011) 1822–1826. https://doi.org/10.1016/j.physb.2011.02.037.

[27]   N. Juneja, L. Tutsch, F. Feldmann, A. Fischer, M. Bivour, A. Moldovan, M. Hermle, Effect of hydrogen addition on bulk properties of sputtered indium tin oxide thin films, AIP Conf. Proc. 2147 (2019) 1–6. https://doi.org/10.1063/1.5123835.

[28]   S. Talu, S. Kulesza, M. Bramowicz, K. Stepien, D. Dastan, Analysis of the surface microtexture of sputtered indium tin oxide thin films, Arch. Metall. Mater. 66 (2021) 443–450. https://doi.org/10.24425/amm.2021.135877.

[29]   L.H.C. Amorin, L. Da Silva Martins, A. Urbano, Commitment between roughness and crystallite size in the vanadium oxide thin film opto-electrochemical properties, Mater. Res. 22 (2018) 1–6. https://doi.org/10.1590/1980-5373-MR-2018-0245.

[30]   C.S. Prajapati, N. Bhat, Ppb level detection of NO_2 using a WO_3 thin film-based sensor: Material optimization, device fabrication and packaging, RSC Adv. 8 (2018) 6590–6599. https://doi.org/10.1039/c7ra13659e.

[31]   D. Erfurt, M.D. Heinemann, S. Körner, B. Szyszka, R. Klenk, R. Schlatmann, Improved electrical properties of pulsed DC magnetron sputtered hydrogen doped indium oxide after annealing in air, Mater. Sci. Semicond. Process. 89 (2019) 170–175. https://doi.org/10.1016/j.mssp.2018.09.012.

[32]   W. Körner, C. Elsässer, First-principles density functional study of dopant elements at grain boundaries in ZnO, Phys. Rev. B - Condens. Matter Mater. Phys. 81 (2010) 1–12. https://doi.org/10.1103/PhysRevB.81.085324.

[33]   T. Koida, Y. Ueno, Thermal and Damp Heat Stability of High-Mobility In2O3-Based Transparent Conducting Films Fabricated at Low Process Temperatures, Phys. Status Solidi Appl. Mater. Sci. 218 (2021) 27–30. https://doi.org/10.1002/pssa.202000487.

[34]   F. Qu, T. Zhang, H.W. Gu, Q.Q. Qiu, F.Z. Ding, X.Y. Peng, H.Y. Wang, Electrical and optical properties of ZnO:Al films with different hydrogen contents in sputtering gas, Rare Met. 34 (2015) 173–177. https://doi.org/10.1007/s12598-014-0435-8.

[35]   M.A. Sayeed, H.K. Rouf, K. Md Amjad Hussain, Doping and annealing effects on structural, optical and electrical characteristics of Sn-doped ZnS thin film, Mater. Res. Express. 8 (2021). https://doi.org/10.1088/2053-1591/ac1964.

[36]   J.H. Park, C. Buurma, S. Sivananthan, R. Kodama, W. Gao, T.A. Gessert, The effect of post-annealing on Indium Tin Oxide thin films by magnetron sputtering method, Appl. Surf. Sci. 307 (2014) 388–392. https://doi.org/10.1016/j.apsusc.2014.04.042.

[37]   M. Morales-Masis, S. De Wolf, R. Woods-Robinson, J.W. Ager, C. Ballif,

Transparent Electrodes for Efficient Optoelectronics, Adv. Electron. Mater. 3 (2017). https://doi.org/10.1002/aelm.201600529.

[38]   H. Kim, J.S. Horwitz, G. Kushto, A. Pique´, Z.H. Kafafi, C.M. Gilmore, and D.B. Chrisey, Effect of film thickness on the properties of indium tin oxide thin films, J. Appl. Phys. 88 (2000) 1–6.

[39]   E. Rucavado, F. Landucci, M. Döbeli, Q. Jeangros, M. Boccard, A. Hessler-Wyser, C. Ballif, M. Morales-Masis, Zr-doped indium oxide electrodes: Annealing and thickness effects on microstructure and carrier transport, Phys. Rev. Mater. 3 (2019) 1–9. https://doi.org/10.1103/PhysRevMaterials.3.084608.

[40]   T. Kaplas, L. Karvonen, J. Rönn, M.R. Saleem, S. Kujala, S. Honkanen, Y. Svirko, Nonlinear refraction in semitransparent pyrolytic carbon films, Opt. Mater. Express. 2 (2012) 1822. https://doi.org/10.1364/ome.2.001822.

[41]   W.J. Ho, J.C. Lin, J.J. Liu, W. Bin Bai, H.P. Shiao, Electrical and optical characterization of sputtered silicon dioxide, indium tin oxide, and silicon dioxide/indium tin oxide antireflection coating on single-junction GaAs solar cells, Materials (Basel). 10 (2017). https://doi.org/10.3390/ma10070700.

[42]   K. Fleischer, E. Arca, I. V. Shvets, Improving solar cell efficiency with optically optimised TCO layers, Sol. Energy Mater. Sol. Cells. 101 (2012) 262–269. https://doi.org/10.1016/j.solmat.2012.01.037.

[43]   L.Y. Chen, W.H. Chen, J.J. Wang, F.C.N. Hong, Y.K. Su, Hydrogen-doped high conductivity ZnO films deposited by radio-frequency magnetron sputtering, Appl. Phys. Lett. 85 (2004) 5628–5630. https://doi.org/10.1063/1.1835991.

[44]   A. Borgschulte, O. Sambalova, R. Delmelle, S. Jenatsch, R. Hany, F. Nüesch, Hydrogen reduction of molybdenum oxide at room temperature, Sci. Rep. 7 (2017) 1–9. https://doi.org/10.1038/srep40761.

[45]   M. Ohring, Materials Science of Thin Films: Deposition and Structure, Academic Press:Cambridge; MA; USA; 2002, 2002.

[46]   M. Wu, S. Yu, L. He, L. Yang, W. Zhang, High quality transparent conductive Ag-based barium stannate multilayer flexible thin films, Sci. Rep. 7 (2017) 1–9. https://doi.org/10.1038/s41598-017-00178-9.

[47]   Y. Ye, J.Y.Y. Loh, A. Flood, C.Y. Fang, J. Chang, R. Zhao, P. Brodersen, N.P. Kherani, Plasmonics of Diffused Silver Nanoparticles in Silver/Nitride Optical Thin Films, Sci. Rep. 9 (2019) 1–11. https://doi.org/10.1038/s41598-019-56719-x.

[48]   D. Gu, C. Zhang, Y.K. Wu, L.J. Guo, Ultrasmooth and thermally stable silver-based thin films with subnanometer roughness by aluminum doping, ACS Nano. 8 (2014) 10343–10351. https://doi.org/10.1021/nn503577c.

[49]   T. Tom, E. Ros, N. López-Pintó, J. Miguel Asensi, J. Andreu, J. Bertomeu, J. Puigdollers, C. Voz, Influence of Co-Sputtered Ag:Al Ultra-Thin Layers in Transparent V_2O_5/Ag:Al/AZO Hole-Selective Electrodes for Silicon Solar Cells, Materials (Basel). 13 (2020) 4905. https://doi.org/10.3390/ma13214905.

Chapter 5: Hole transport layers

This chapter explores the structural, compositional, optical, and electrical properties of magnetron sputtered MoO$_x$ thin films and its application in silicon solar cells as HTLs.

5.1 Molybdenum oxide as hole transport layer

Recently, the concept of charge-carrier selective contacts has emerged in the field of semiconductor devices, as it has been explained in chapter 2. Layers of appropriate materials can easily transport one charge-carrier type while blocking the other one [1]. In this sense, TMOs demonstrate excellent charge-selective properties on silicon substrates [2][3][4].

Among them, MoO$_x$ has been widely studied in the literature as a hole-selective contact [5][6][7]. In particular, sub-oxidized MoO$_x$ (x<3) films have demonstrated to be required for good charge transport. Cao *et al*. recently demonstrated a power conversion efficiency of 23.83% using MoO$_x$ as HTL in c-Si solar cells [8], when depositing these films via thermal evaporation, which has the advantage of a soft deposition and material qualities that permit good selectivity [9][10]. However, this technique would be less apt for upscaling. Moreover, this thermal evaporation prevents greater control over the metal oxide parameters responsible for the induced c-Si junction, such as optical characteristics, stoichiometry, conductivity, and work function [11].

In this chapter, we explore sputtering as an alternative method to obtain MoO$_x$ films with better control and reliability. Reactive sputtering of a metallic Mo target, and reactive sputtering of a MoO$_3$ target with different atmospheres are studied. The stoichiometry and the optical and electrical properties of the MoO$_x$ can be tuned.

5.2 Reactive sputtering of molybdenum oxide using metallic target

Here, the reduced MoO$_x$ films were obtained by sputtering in a reactive atmosphere of Ar and O$_2$ using a metallic target of Mo. Structural, compositional, optical, and electrical properties of these films were studied. As proof-of-concept silicon solar cells were fabricated using sputtered MoO$_x$ as HTL and compared with the evaporated MoO$_x$ cells.

5.2.1 Experimental method

The MoO$_x$ films were deposited using the RF magnetron sputtering system ATC Orion 8 HV. A metallic target of molybdenum with a purity of 99.99% and 3-inch diameter (7.62 cm) and 6 mm thickness was used. The depositions were done in a reactive atmosphere using Ar:O$_2$ gas mixtures. Prior to each deposition, a base pressure of 2.5×10^{-6} Torr was achieved, and the power density was set at 2.2 W cm^{-2} (100 W); as well, the substrates were left for 3 min (pre-sputtering time) before starting the process. Depositions were made onto an n-type c-Si (100) wafer and Corning 1737F glass. The cleaning of the substrates and characterization techniques were already explained in chapter 3.

N-type (100) c-Si wafers with resistivity of 2 Ωcm, thickness of 280 μm, one-side polished, non-textured were used for the fabrication of solar cells. Different solar cell architectures were developed with modifications in the hole-selective MoO$_x$ layer. Sputtered and thermally evaporated MoO$_x$ was used as the dopant-free hole-selective contact. An intrinsic (i-type) a-Si:H and doped n-type a-Si:H layers were deposited on the rear side by PECVD to provide a reference electron selective contact. The lithographic patterning of 1 cm^2 was defined as the active area and a 2-μm-thick Ag grid (4.5% shadow) was thermally evaporated as the front contact. Finally, the back-contact metallization was accomplished by thermally evaporating Al (1μm thick).

5.2.2 Influence of pressure

The influence of pressure was studied by changing the deposition pressure from 2 mTorr to 32 mTorr under a reactive atmosphere of 3.5% of O_2. No intentional heating of the substrates was applied, and all the depositions were done at room temperature. The deposition time for all films was adjusted to achieve a thickness of $\sim$35 nm.

5.2.2.1 Deposition rate, structure, and composition

The deposition rate of the films decreased from 5.2 nm min^{-1} to 2 nm min^{-1} as the pressure in the chamber increased from 2 mTorr to 32 mTorr. Fig. 5.1 shows the evolution of the deposition rate of MoO_x films with pressure. At higher pressure, the number of collisions between sputtered molecules and gas molecules was enhanced, while reducing the diffusive ability of the molecules [12]. As a consequence, with the increment in deposition pressure, the deposition rate dropped. In addition, the decreased deposition rate can be also caused by the chemical reaction between the sputtering gas O_2 and the target material, which can lead to target poisoning [13].
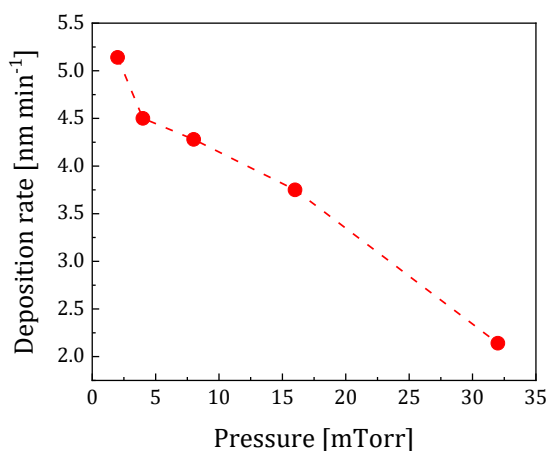
Figure 5.1: The evolution of the deposition rate of MoO_x films with chamber pressure.

Fig. 5.2 shows the X-ray diffraction patterns of the MoO_x films deposited at different deposition pressures (2, 8, and 16 mTorr). The XRD shows a broad peak attributed to (200) reflection of the monoclinic phase of MoO_3, according to PDF reference code no. 01- 84-1360 [14]. This broadness of the peak indicates the amorphous nature of the reactive sputtered MoO_x films. The amorphous character of the films was unchanged as the pressure increased from 2 to 16 mTorr that indicates no dependence on the deposition pressure.
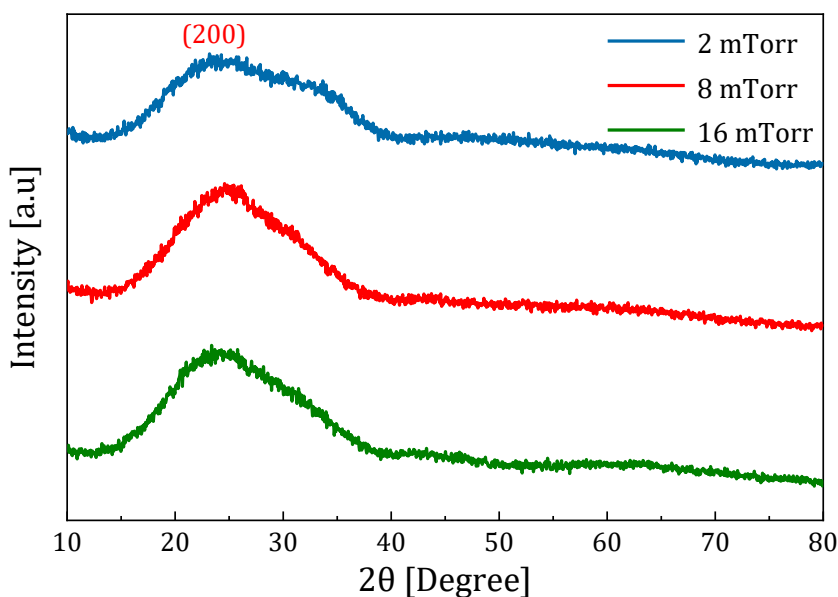
Figure 5.2: XRD diffraction patterns for the MoO_x films deposited at different deposition pressures. All the samples were deposited on Si substrates.

XPS measurements were carried out to investigate the compositional analysis of the MoO_x films sputtered under different pressure. Fig. 5.3 shows the evolution of the different oxidation states over pressure. The Mo3d spectrum was fitted by doublets ($3d_{3/2}$ and $3d_{5/2}$) corresponding to different oxidation states. It was found that the number of doublets in the Mo3d increased at lower deposition pressure.
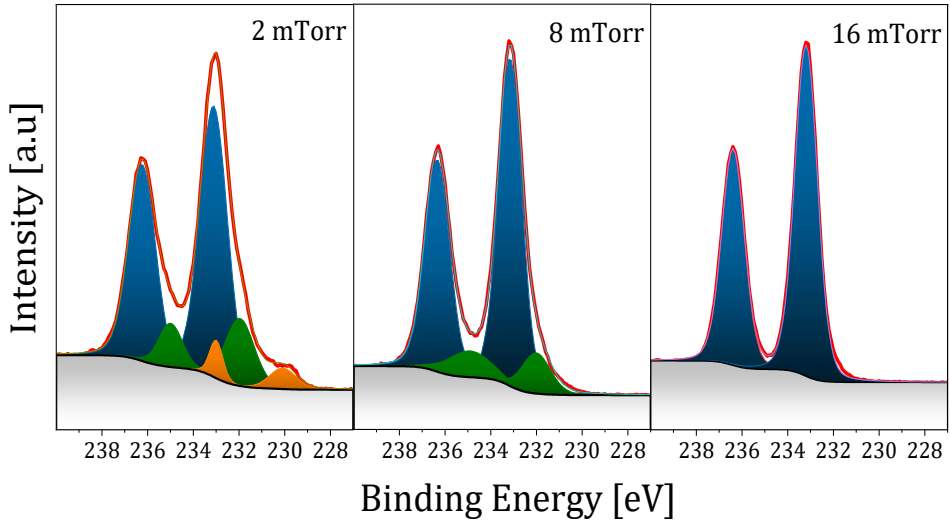
Figure 5.3: XPS Mo3d peaks deconvoluted for films deposited at varying pressure. Blue peaks correspond to Mo^{6+}, green peaks to the Mo^{5+} and orange peaks to Mo^{4+}. The positions of the $3d_{5/2}$ peaks were 233.1, 232.0, and 230.0 eV for Mo^{6+}, Mo^{5+}, and Mo^{4+}, respectively.

For the films deposited at 2 mTorr pressure, Mo3d peak was fitted using 3 doublets. The major contributor peak ($3d_{5/2}$) centered at (233.1 ± 0.2) eV is the 3d doublet peak of Mo^{6+}; the one centered at (232.0 ± 0.3) eV is identified as a 3d doublet of Mo^{5+}; And the minor peak centered at (230.0 ± 0.2) eV corresponds to the Mo^{4+} oxidation state, thus indicating the presence of metallic Mo. The XPS spectrum of the films deposited at 8 mTorr were fitted with two doublets corresponding to the Mo^{6+} and Mo^{5+} oxidation states. Instead, films sputtered at a higher pressure of 16 mTorr showed only Mo^{6+} oxidation state, and their XPS spectra could be simply fitted using a single doublet [15][16][17].

To compute the stoichiometric composition of the films, carbon and oxygen peaks were analyzed. Table 5.1 shows the O/Mo evolution as increase in pressure. As the pressure increased the films became fully stoichiometric, reaching fully stoichiometric MoO_x for the highest pressure of 16 mTorr. This results from the more frequent collision between O and Mo atoms at higher pressure, which ends up in the formation of a completely

stoichiometric MoO_3 film. For films deposited at 2 mTorr and 8 mTorr the O/Mo ratio was 2.7 and 2.9 respectively, indicating the presence of the Mo^{4+} and Mo^{5+} oxidation states. MoO_x films with sub-oxidized stoichiometry between 2.7–2.9 were selected for device fabrication for the sake of comparison with previous works, where the same stoichiometry was reached in evaporated MoO_3 films [18].

Table 5.1: O/Mo ratio of the films deposited at different pressures. The stoichiometry of the samples increased at higher deposition pressure.

Deposition pressure (mTorr)	O/Mo ratio
2	2.7
8	2.9
16	3.0

5.2.2.2 Optical and electrical

Fig. 5.4 shows the optical transmittance of the MoO_x films at different sputtering pressures. The average transmittance of the films was weighted with the Sun's AM1.5 spectra irradiance and is plotted in the inset of the Fig. 5.4. The bandgap was calculated from the transmittance and reflectance measured in the visible and near-infrared parts of the spectrum according to Eq. 2.15.

The films deposited at low pressures (2, 4, and 8 mTorr) exhibited an optical transmittance lower than 50%. This was due to the formation of sub-stoichiometric MoO_3 films, as observed from the XPS measurements. When the deposition pressure increased to 16 and 32 mTorr, the optical transmittance increased to 85% due to the reduced number of oxygen ion vacancies. According to Table 5.1, the O/Mo ratio of the films under these pressures indicates a stoichiometry close to MoO_3 [19].

Fig. 5.5 shows the optical band gap of the films deposited at different pressures with an estimated error less than 5%. The inset shows the Tauc plot used to determine the indirect optical bandgap. For all samples, the corresponding best regression was computed with the method mentioned in chapter 3.
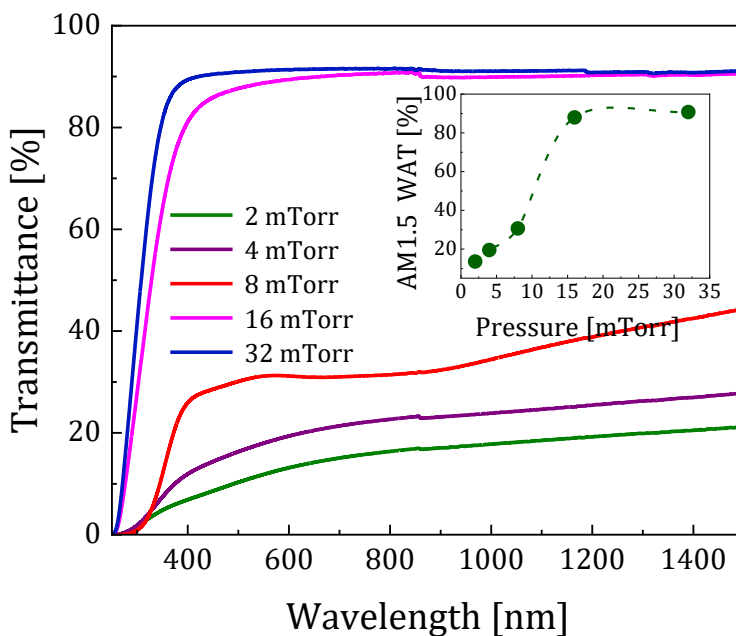
Figure 5.4: Transmittance of the samples deposited at different deposition pressure. The inset shows the weighted average transmittance (WAT) of the MoO_x films with deposition pressure. All samples for optical measurements were deposited on glass.

The optical band gap of the MoO_x films increased as the deposition pressure increased, from 0.7 eV to 3.5 eV for 2 mTorr to 16 mTorr, respectively [20]. On further increase of pressure, the optical band gap remained constant at 3.5 eV [21]. The lower band gap at low deposition pressure was due to the sub-stoichiometric MoO_x and the higher band gap at higher pressure was due to the formation of stoichiometric MoO_x films.
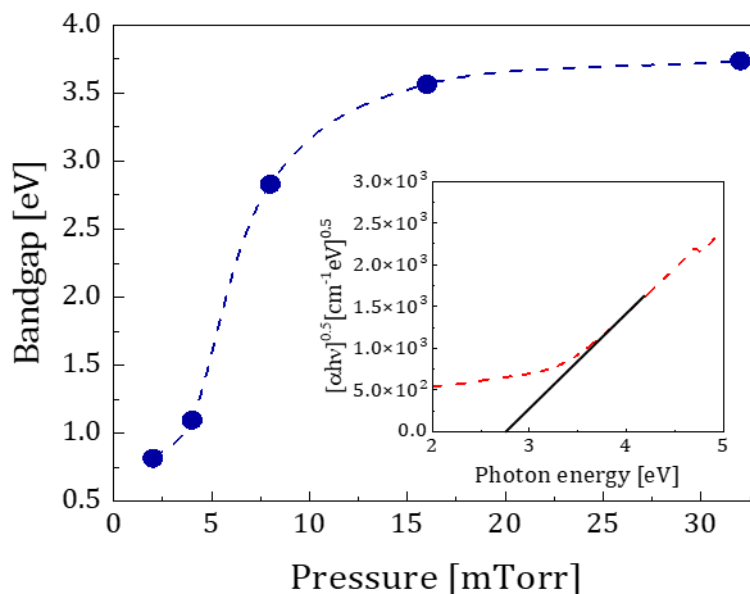
Figure 5.5: The indirect bandgap variation of the MoO$_x$ films with different pressures. The inset shows the example of the Tauc plot used to determine the indirect optical bandgap value for the film deposited under 8 mTorr pressure.

The conductivity of the films was studied employing the TLM method shown in Fig. 5.6. The conductivity dropped from 106 to 1 S m^{-1} as the deposition pressure increased in the chamber. This behavior can be directly attributed to the stoichiometry of the MoO$_3$ films. As the pressure increased, so did the number of Mo collisions with the sputtered gas. Then Mo atoms found enough O$_2$ in the chamber to induce Mo^{6+} oxidation state, as observed from the XPS measurements. In this configuration, MoO$_x$ was expected to be fully stoichiometric (x = 3), the strong localization of the electrons thus yielding low conductivity. The increase in conductivity at reduced pressures (2, 4 mTorr) was due to the presence of the sub-stoichiometric MoO$_x$ with Mo^{4+} and Mo^{5+} oxidation states [22][23][24]. The conductivity values were in accordance with the Mo/O ratio shown in Table 5.1. At low deposition pressure, the films exhibited more metallic nature (MoO$_{2.7}$) due to the absence of oxygen, which was also seen from the transmittance and band gap measurements (decrease in band gap energy).
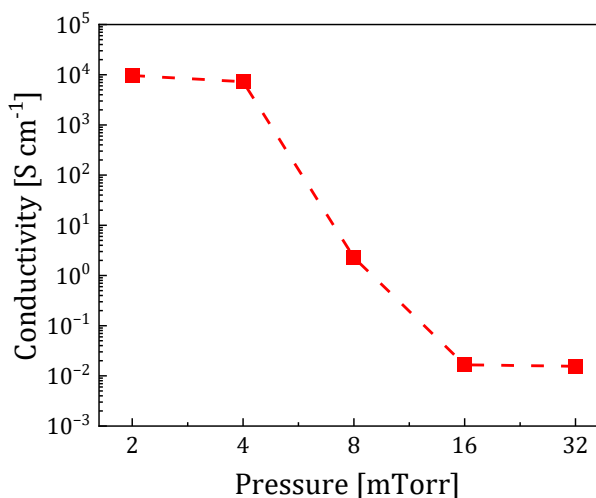
Figure 5.6: Evolution of the conductivity of the MoO$_x$ films, in logarithmic scale, with the deposition pressure. All the samples were deposited on glass substrates.

Aiming at the fabrication of solar cell, a tradeoff must be made between the optical transparency and electrical conductivity of the films. If we select films sputtered at low pressures of 2 or 4 mTorr, the conductivity will be high, but the transparency will be compromised. On the other hand, at higher pressures of 16 and 32 mTorr the films become insulating. Therefore, for the fabrication of cells, we selected an intermediate deposition pressure between 4 and 8 mTorr, which has an average transmittance and conductivity.

5.2.2.3 Effective lifetime

Since the evaporated MoO$_x$/n-Si heterojunctions showed high level of surface passivation and cell performance in our previous studies, we performed a comparative study of both sputtered and evaporated films. MoO$_x$ films were deposited on the front side of the planar n-Si wafers. The silicon wafers with (i/n) a-Si:H on the rear side, with and without the (i) a-Si:H on front side, were used. Intrinsic a-Si:H layer (4 nm) and (i/n) a-Si:H were deposited via PECVD method. The photoconductance was measured in

the QSSPC regime before and after annealing. Afterwards, the annealing was carried at 150 °C for 20 minutes in a forming gas (hydrogen and nitrogen mixture) atmosphere. Table 5.2 shows the effective lifetime (τ_{eff}) of photogenerated carriers at a carrier density of 1.10^{15} cm^{-3}, and the implied open-circuit voltage (iV_{oc}) of the sample having a structure as shown in Fig. 5.7(a). The iV_{oc} can be interpreted as a measure of the maximum theoretical V_{oc} for the MoO$_x$/n-Si heterojunction for illumination of 1 Sun. The effective lifetimes in as-deposited state for all the samples made under different deposition pressure were found to be around 60 μs. However, after annealing the lifetime improved to 400 μs with an iV_{oc} of 640 mV, demonstrating the effect of passivation. The lifetime of the samples showed dependence on pressure, and the highest lifetime of 465 μs with iV_{oc} of 646 mV was observed for films sputtered at 6 mTorr pressure.
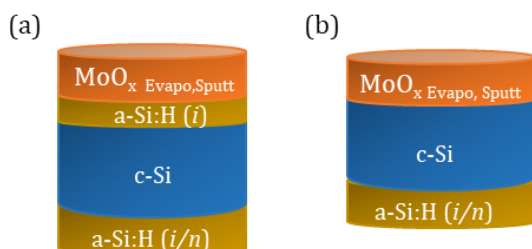
Figure 5.7: The schematic representation of the test structures fabricated to calculate the effective lifetime of the MoO$_x$ films. (a), (b) with and without a-Si:H passivation layer, respectively.

Fig. 5.8 shows the τ_{eff} of photogenerated carriers as a function of carrier density (Δn) before and after annealing. The MoO$_x$ layer sputtered on top of the c-Si, as shown in Fig. 5.7 (b), showed a much lower impact of annealing with a slight improvement in lifetime from 33 μs to 40 μs. In contrast, the films sputtered on a-Si:H layers in as-deposited state showed τ_{eff} of 61 μs. This low surface passivation even after using the a-Si:H was due to the sputtering damage on the surface.

Table 5.2: Passivation qualities of the samples with a-Si:H layers at different deposition pressures: lifetime of photogenerated carriers before and after annealing, and implied V_{oc} after annealing.

Pressure (mTorr)	τ_{eff} after deposition (µs)	τ_{eff} after annealing (µs)	iV_{oc} after annealing (mV)
4.5	58	370	640
5.0	60	375	640
5.5	61	406	642
6.0	62	465	646
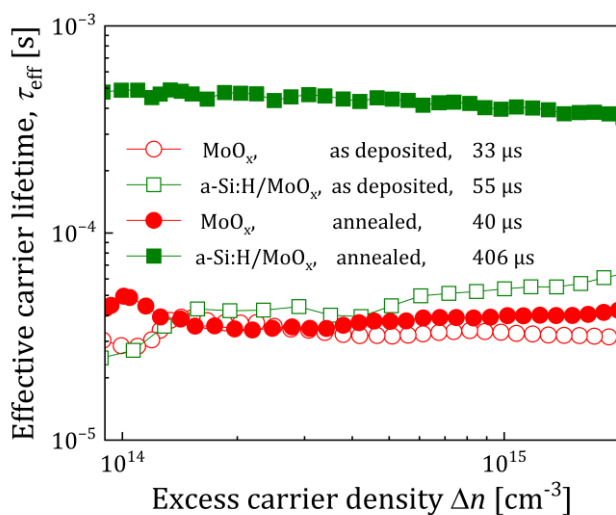
Figure 5.8: Comparison of the effective carrier lifetime of MoO_x films on c-Si sputtered at 5.5 mTorr pressure. The lifetimes with and without the a-Si:H passivation layer before and after annealing are given.

The passivation quality of sputtered MoO_x film was compared with the thermally evaporated MoO_3 films. The highest passivation was achieved for evaporated MoO_3 films deposited on a-Si:H-passivated c-Si with a τ_{eff} of 1740

μs. However, after annealing, lifetime of the evaporated sample decreased to 746 μs (at 655 mV iV_{oc}) unlike the sputtered samples. MoO_3 evaporated on c-Si without a-Si:H passivation layer initially exhibited a significant lifetime of 222 μs but degraded after annealing. Table 5.3 shows the comparison of the lifetime and iV_{oc} of the evaporated and sputtered samples deposited on c-Si without a-Si:H passivation layer.

Table 5.3: Passivation qualities of the evaporated and sputtered (5.5 mTorr) MoO_x films without a-Si:H layers: lifetime of photogenerated carriers before and after annealing, and implied V_{oc} after annealing.

Deposition method	a-Si:H layers	τ_{eff} after deposition (μs)	τ_{eff} after annealing (μs)	iV_{oc} after annealing (mV)
Evaporated	NO	222	175	650
Evaporated	YES	1740	746	655
Sputtered	NO	15	24	582
Sputtered	YES	55.0	406	642

5.2.2.4 Application to solar cells

Finally, solar cells were fabricated to evaluate the performance of sputtered MoO_x implemented as an HTL at the corresponding electrode. Different deposition pressures (4.5, 5, 5.5, and 6 mTorr) were used to deposit MoO_x. The complete heterojunction solar cell structure was ITO/MoO_x/(i)a-Si:H/c-Si/(i/n) a-Si:H/Al with an active area of 1×1 cm². A schematic diagram of this device architecture is given in Fig. 5.9. The solar cells were fabricated on flat c-Si wafers, and thus there is room to increase the current density up to 4 mA cm⁻² when using texturized substrates. On top of the HTL, an ITO layer was sputtered as the front transparent electrode with a sheet resistance of 120 Ω/sq. The top contact was finished with a 1.5-μm-thick metallic grid of silver. As the rear contact, doped (i/n) a-Si:H layers

were used as ETL and covered with an evaporated Al layer of 500 nm. After fabrication, all the cells were annealed at 150 °C in forming gas for 20 min. Fig. 5.10 compares the electrical characteristics under AM1.5 illumination of Si heterojunction solar cells under different deposition pressures. The corresponding photovoltaic parameters of these solar cells are summarized in Table 5.4, and the external quantum efficiency curves are shown in Fig. 5.11.
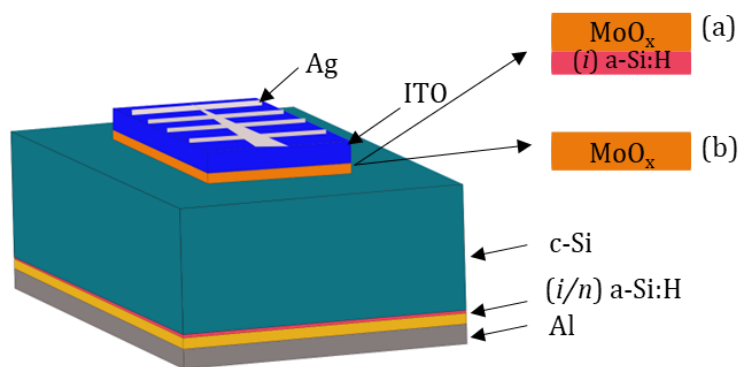
Figure 5.9: Schematic diagram of the fabricated solar cells (a) with and (b) without a thin layer of a-Si:H.

The dependance of solar cell parameters such as V_{oc}, J_{sc} and FF on the deposition pressure was investigated. The V_{oc} of the cells increased with the deposition pressure due to the lower sputtering damage caused to the amorphous silicon layers. Rising the pressure, the number of collisions between sputtered molecules and gas molecules increased, which affected the energy of the particles arriving at the substrate. Thus, at lower pressures, the energetic bombardment of particles on amorphous silicon layers resulted in degradation of passivation, which was reflected in the V_{oc} of the cells. A strong correlation between transparency and conductivity was reflected in the case of the FF and J_{sc} of the cells: as deposition pressure rised, conductivity dropped while transparency increased. In particular, when pressure increased from 4.5 to 5.5 mTorr, the FF and J_{sc} were respectively enhanced from 59.2% to 64.2% and 28.9 to 32.0 mA cm^{-2}. A further increment in pressure to 6 mTor was observed to reduce the FF to 60.8% and J_{sc} to 27.7 mA cm^{-2}.
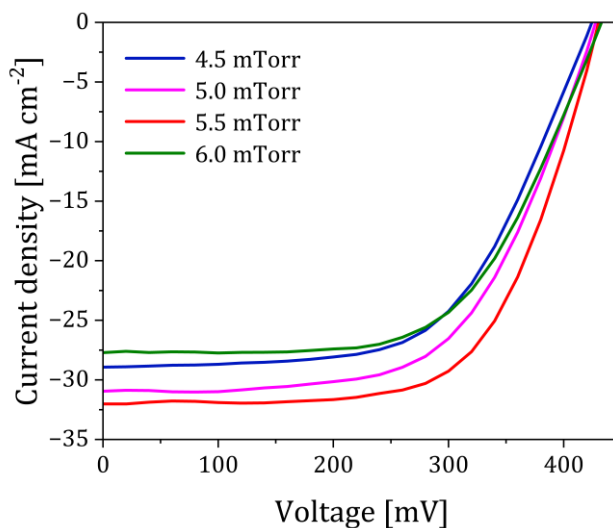
Figure 5.10: Current density-voltage characteristics of the solar cells fabricated at different pressures measured under AM1.5 irradiance. The highest J_{sc} of 32.02 mA cm^{-2} was shown by films sputtered at 5.5 mTorr deposition pressure.

Table 5.4: Photovoltaic parameters of the solar cells fabricated with MoO$_x$ films at different deposition pressure: open-circuit voltage, short-circuit current density, fill factor, and photovoltaic conversion efficiency.

Pressure (mTorr)	V_{oc} (mV)	J_{sc} (mA cm^{-2})	FF (%)	PCE (%)
4.5	424	28.9	59.3	7.3
5.0	427	30.9	60.2	7.9
5.5	430	32.0	64.2	8.8
6.0	432	27.7	60.8	7.3
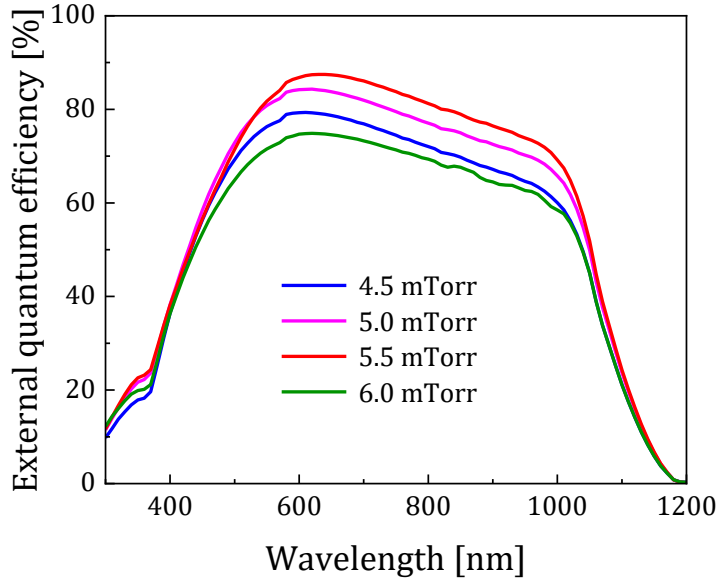
Figure 5.11: *EQE* of the solar cells fabricated with different pressures. The highest *EQE* performance was achieved by cells sputtered at 5.5 mTorr.

The cells with sputtered MoO_x were then compared to the cells with thermally-evaporated MoO_x in the same conditions. The schematic representations of the sputtered and evaporated cells are shown in Fig. 5.9. The cells were fabricated with and without a-Si:H layers. The complete heterojunction solar cell structure were ITO/MoO_x/(*i*)a-Si:H/c-Si/(*i/n*)a-Si:H/Al and ITO/MoO_x/c-Si/(*i/n*)a-Si:H/Al. The cells were annealed before measurements. The comparison of the electrical characteristics of evaporated and sputtered Si heterojunction solar cells under AM1.5 illumination is shown in Fig. 5.12. The corresponding photovoltaic parameters of these solar cells are summarized in Table 5.5, and their external quantum efficiency curves are shown in Fig. 5 .13.
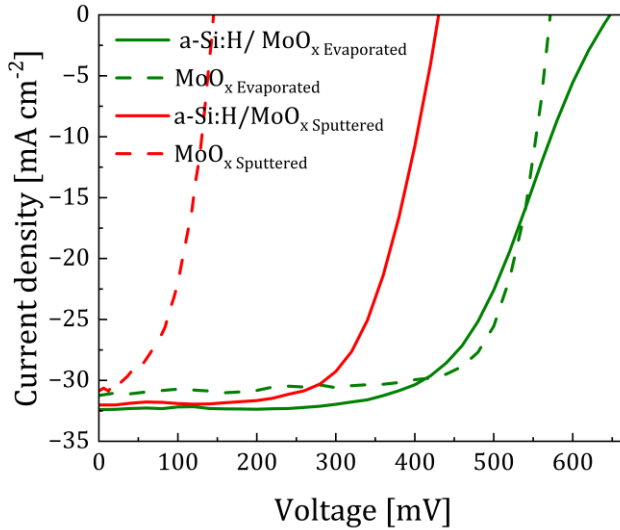
Figure 5.12: *J-V* curves measured under AM1.5 irradiance for solar cells with evaporated and sputtered MoO$_x$. The highest *FF* and *V*$_{oc}$ were obtained for the cells with evaporated MoO$_x$.

The behavior of the *J*$_{sc}$ of the cells with sputtered MoO$_x$ was compared to the one of the cells with evaporated MoO$_x$. The *J*$_{sc}$ of both cells improved after the addition of a passivation layer of a-Si:H that enhances passivation in the cells. The cell with sputtered MoO$_x$ without the a-Si:H layer showed a very low level of surface passivation with an external *V*$_{oc}$ of 145 mV. In contrast, the addition of a passivation layer improved the surface passivation and tripled the external *V*$_{oc}$ to up 430 mV. Nevertheless, even with the passivation layer, cells with sputtered MoO$_x$ were incapable to reach the *V*$_{oc}$ of cells with evaporated MoO$_x$, which was 571 mV without a passivation layer and 647 mV with a passivation layer. Regarding the fill factor, the cells with sputtered MoO$_x$ with a passivation layer showed the highest *FF* of 64.2%, whereas the cells with evaporated MoO$_x$ with passivation layer only showed a *FF* of 59.9% due to an increase in the series resistance of the cells. Instead, the cells with evaporated MoO$_x$ without a passivation layer showed the highest *FF* of 74.5% compared to 49.2% for their sputtered MoO$_x$ counterpart.

Table 5.5: Photovoltaic parameters of the solar cells fabricated with sputtered and evaporated MoO_x films: open-circuit voltage, short-circuit current density, fill factor, and photovoltaic conversion efficiency.

Solar cell MoO_x type	a-Si:H layer	V_{oc} (mV)	J_{sc} (mA cm^{-2})	FF (%)	PCE (%)
Evaporated	NO	571	31.2	74.5	13.3
Evaporated	YES	647	32.4	59.9	12.6
Sputtered	NO	145	30.9	49.2	2.2
Sputtered	YES	430	32.0	64.2	8.8
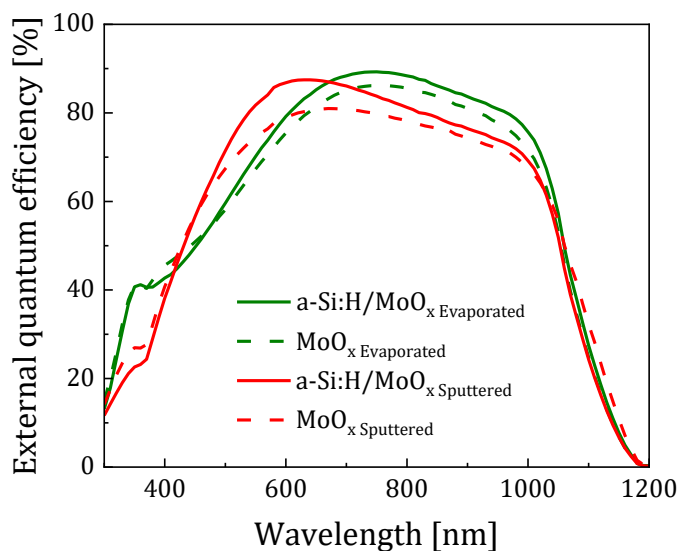
Figure 5.13: Comparison of the *EQE* of solar cells fabricated with sputtered and evaporated MoO_x.

Even if the solar cells fabricated with sputtered MoO_x exhibited a *PCE* of 8.8%, it is not up to the benchmark of solar cell with thermally-evaporated

MoO$_3$, with 13.3%. An evident drop in the *FF* and V_{oc} of the cells was observed for solar cells with sputtered MoO$_x$. The low *FF* was related to the low conductivity of the MoO$_x$ films that did not allow the efficient extraction of the holes, which led to their recombination inside the cell. On the other hand, the V_{oc} was related to the inversion ability of MoO$_x$ and its low work function (below 5 eV), which caused a reduced band bending. Therefore, the inversion on c-Si surface by MoO$_x$ was insufficient to stop electron injection to the electrodes. These factors contributed to the bad performance of the cell. To compare the contact selectivity of the cells (see Fig. 5.14) between evaporated and sputtered MoO$_x$, we have adopted a characterization approach from Bivour *et al.* [9][11][25].
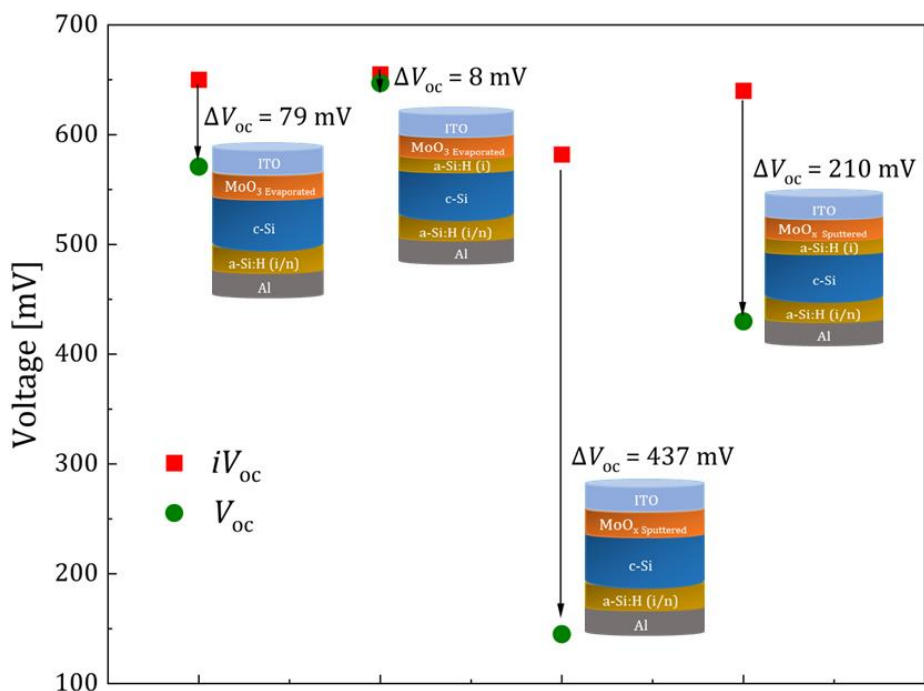
Figure 5.14: Comparison of the variation in the ΔV_{oc} values of the solar cells fabricated using evaporated and sputtered MoO$_x$.

This consists in using ΔV_{oc} as the figure of merit for contact selectivity, $\Delta V_{oc} = iV_{oc} - V_{oc}$, where iV_{oc} is the implied V_{oc} from the surface passivation measurements, and V_{oc} the value corresponding to the fabricated cells. Consequently, $\Delta V_{oc} = iV_{oc} - V_{oc} \gg 0$ eV will show that the contact's characteristics are determined not only by the standard recombination and ohmic shunt and ohmic transport losses, but also by an insufficient selectivity, i.e., a "non-ideal" rectifying behavior. Accordingly, for the solar cells with sputtered MoO_x, with and without a passivation layer, the ΔV_{oc} was > 200 mV. But for solar cells with evaporated MoO_x, the ΔV_{oc} was negligible (see Fig. 5.14). Therefore, compared to the evaporated contacts the performance of the sputtered contacts was constrained by the inability of MoO_x films to extract excess holes from the absorber, or by limited hole selectivity.

In conclusion, it was demonstrated that the reactive sputtering of MoO_x allows for adequate control of its transmittance, conductivity, and stoichiometry. But the low work function of these layers and high ΔV_{oc} blocks the efficient hole collection on silicon. Consequently, reactive sputtering from a metallic target of MoO_x found to make no significant impact. Therefore, as a next step, sputtering from a ceramic target of MoO_3 using a reactive atmosphere was investigated. The next section discusses the properties of MoO_x sputtered from a ceramic target.

5.3 Sputtering of molybdenum oxide using a ceramic target

Here, the reduced molybdenum oxide films were obtained using the ceramic molybdenum trioxide target using different reactive atmospheres. Influence of pressure and temperature on structural, compositional, optical, and electrical properties were studied for these films, X-ray photoelectron spectroscopy revealed reduced states that could be controlled by addition of hydrogen in the sputtering chamber. The effect of slightly increasing the substrate temperature during deposition also lead to the presence of metastable Mo^{4+} states.

5.3.1 Experimental method

The MoO_x films studied were deposited in a RF magnetron sputtering system ATC Orion 8 HV. The depositions were done in different gas mixtures of Ar, H_2 and O_2 to obtain the required film properties. A target of ceramic molybdenum oxide (MoO_3) with a purity of 99.995% and 3-inch diameter (7.62 cm) and 6 mm thickness was used. Prior to each deposition, a base pressure of 2.5×10^{-6} Torr was achieved and the power density was set at $3.3\ W\,cm^{-2}$ (150 W); as well, the substrates were left for 3 min (pre-sputtering time) before starting the process. Depositions were made onto an *n*-type c-Si (100) wafer and Corning 1737F glass. The cleaning of the substrates and characterization techniques was already explained in chapter 3.

5.3.2 Influence of pressure

In order to study the influence of pressure during the deposition this parameter was varied from 3 mTorr to 11 mTorr under different reactive atmospheres. No intentional heating of the substrates was applied, and all the depositions were carried out for 12 min. The gas flow was fixed at full-scale for all atmospheres, oxygen and hydrogen partial flow being 3.5% (e.g., in a total of 20 sccm of gas flow there would be 19.3 sccm of Ar and 0.7 sccm of O_2 or H_2) [26].

5.3.2.1 Deposition rate, structure, and composition

To understand the characteristics of the deposited samples, the deposition rate is one of the foremost parameters to consider. Fig. 5.15 shows the evolution of the deposition rate versus pressure. Depositions in the Ar and Ar:H_2 atmospheres exhibited a similar behavior, the deposition rate showing small difference, whereas the depositions in Ar:O_2 atmosphere showed a very low deposition rate as the pressure increased. The "screening" of activated oxygen particles might be the cause for this decrease, this is, O_2 dissociates into O^0 particles ($O_2 + e^- \rightarrow 2O^0$), which are more chemically reactive and easily absorbed on surfaces, thus "poisoning" them. Those O^0 particles are to be absorbed into the target's surface, consequently reducing the net surface of MoO_3 being bombarded by the plasma, and therefore

screening the sputtering process. In the Ar:H_2 atmosphere, the hydrogen was expected to associate with the sputtered particles to form bronzes once deposited ($H_xMo_x^{5+}Mo_{1-x}^{6+}O_3$) [27]. However, the bronzes are thermodynamically unstable and eventual removal of oxygen and hydrogen to form water should occur, leaving behind a more reduced state of molybdenum (MoO_2). Like this, an oxygen-deficient film grows with co-existing phases in it [27].
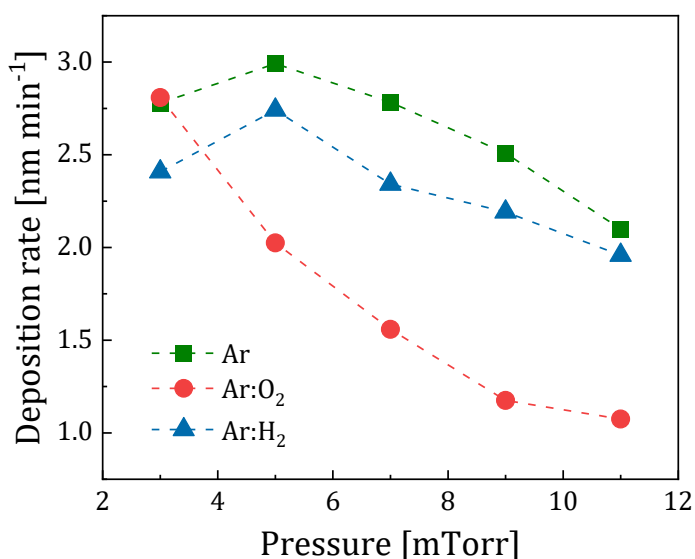
Figure 5.15: Deposition rate of MoO_x thin films deposited with different pressure in atmospheres of Ar, Ar:O_2, and Ar:H_2.

The XRD spectra of the samples grown in different atmospheres and at different pressure are shown in Fig. 5.16. The XRD patterns exhibit a broad peak attributed to (120) reflection of the orthorhombic phase of MoO_3, according to the PDF reference code 00-035-0609 [28]. The diffractogram indicates the amorphous nature of the MoO_x samples deposited at room temperature, and it shows no dependence with the varying pressure or the

atmosphere. This might be due to the low activation energy of the sputtering species at low temperatures [29].
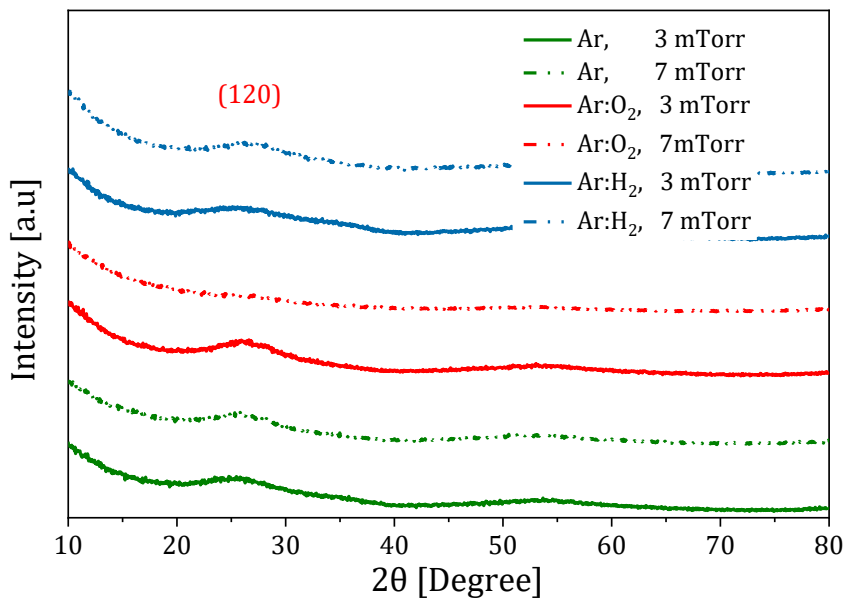
Figure 5.16: XRD patterns of MoO$_x$ thin films deposited at different atmospheres (Ar, Ar:O$_2$, and Ar:H$_2$) and with different pressure) 3 mTorr and 7 mTorr).

The Mo3d core level spectra studied by XPS for different atmospheres are represented in Fig. 5.17, which shows the evolution of the different oxidation states over the increase of pressure. Along with the oxygen core-level spectra, the stoichiometry of the samples was computed. The deconvoluted blue peaks show the Mo^{6+} states, whereas the green peaks show the Mo^{5+} states. For the Mo^{6+} oxidation state, the binding energy value was found at (232.7 ± 0.1) eV, while the peak corresponding to the Mo^{5+} oxidation state was found at (231.6 ± 0.5) eV [30][31]. It should be noted that similar compositional results were obtained for the Ar atmosphere at 3 mTorr and the Ar:H$_2$ atmosphere at 11 mTorr. The oxygen to molybdenum ratio (O/Mo) was computed by dividing the total area of oxygen in the deconvolution by the total deconvoluted area of molybdenum, which leads to stochiometric and sub-stochiometric MoO$_3$ as shown in Fig. 5.18.
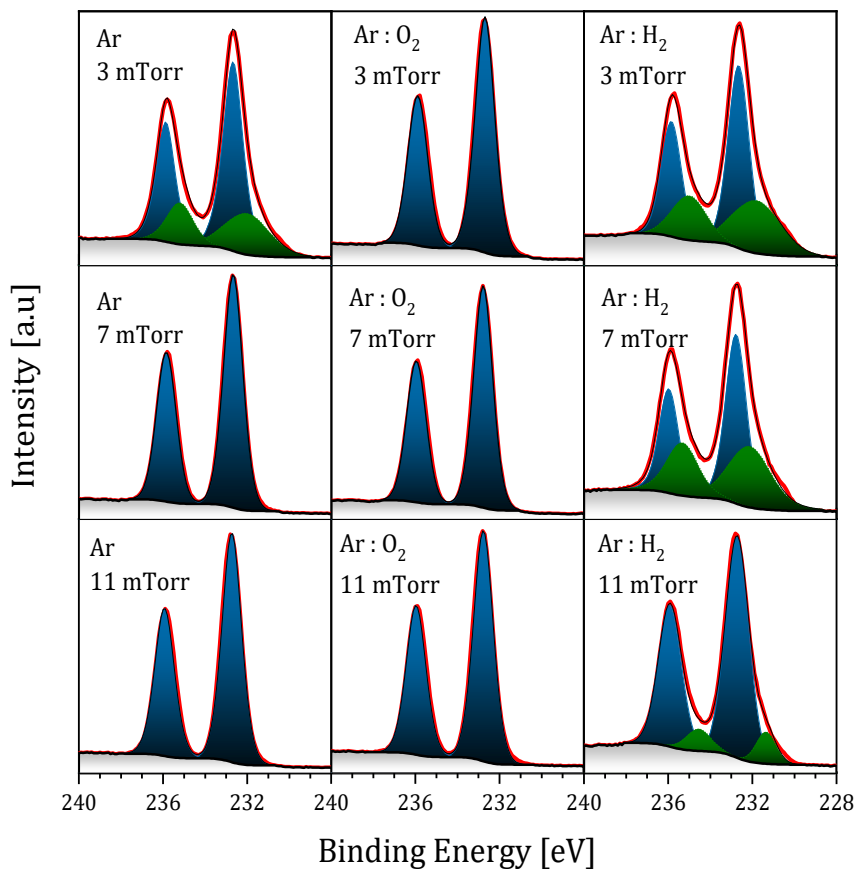
Figure 5.17: XPS-analyzed molybdenum core level spectra peaks for samples deposited under 3, 7, and 11 mTorr and in different atmospheres. Blue and green peaks respectively correspond to the deconvolution of the Mo^{6+} Mo^{5+} peaks. The 3d peaks were centered around 232.7 eV and 232.6 eV for Mo^{6+} and Mo^{5+}, respectively.

The samples prepared in the oxygen atmosphere were nearly stoichiometric, exhibiting higher O/Mo ratios than samples prepared in different atmospheres. In the case of Ar:H_2 atmosphere, the samples were less stoichiometric than in Ar and presented lower O/Mo ratios. The decline

could already be deduced by looking at the XPS results in Fig. 5.17. The Ar:H_2 samples exhibit the Mo^{5+} oxidation state independently of the deposition pressure, whereas the ones in the Ar atmosphere did not (Mo^{5+} states disappear in samples above 7 mTorr). This agrees with the computed stoichiometry values, as displayed in Fig. 5.18, which match the raw observations from the studied Mo3d core level spectra. The reduced oxidation states can be related to oxygen vacancies in the deposited films, indicating that the amount of oxygen deficiency in the film can be controlled either by the deposition pressure or by the applied atmosphere.
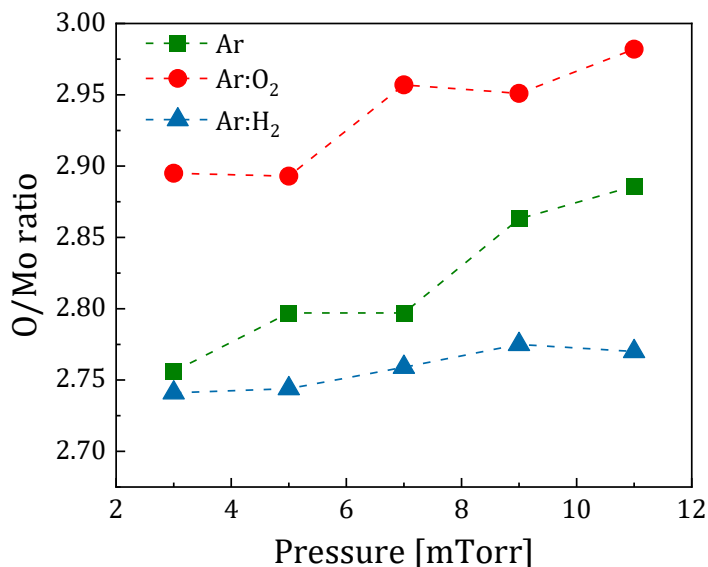
Figure 5.18: O/Mo ratio for different atmospheres computed from the XPS analysis for each deposition pressure. The ratio can be clearly distinguished for ach atmosphere, with increasing ratio values for increasing pressures.

5.3.2.2 Optical and electrical

The optical properties of the films were studied in the visible and near-infrared part of the spectrum to determine the weighted average transmittance of the deposited film [weighted with the Sun's AM1.5

spectrum irradiance using Eq. 3.8] and the bandgap of the samples. Fig. 5.19 plots the absorption coefficient for samples grown in different atmospheres, whereas the inset shows the evolution of the weighted average transmittance (WAT) of the samples as a function of the deposition pressure for each atmosphere.
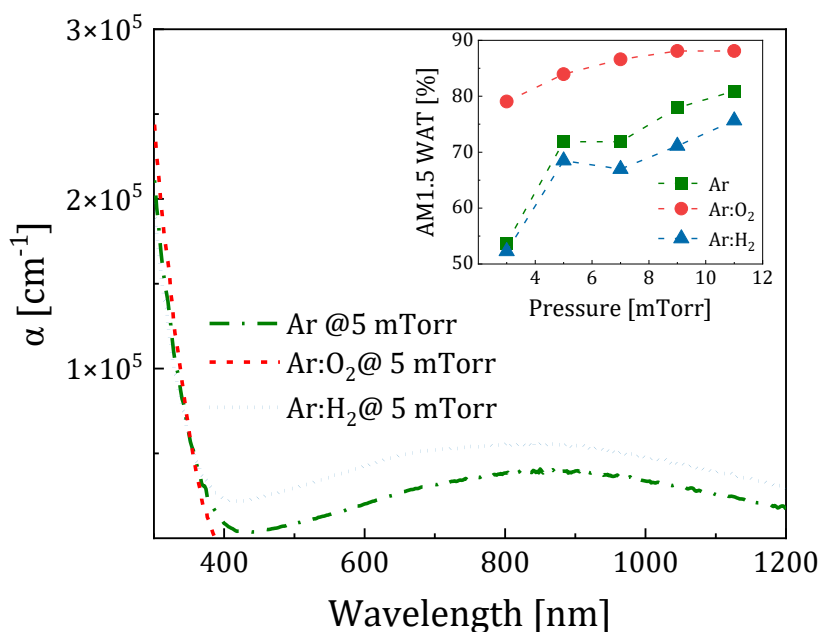
Figure 5.19: The absorption coefficient of the 5mTorr samples for the visible spectra and near-infrared (300 nm to 1200 nm). The dash dot line corresponds to the Ar atmosphere, dashed to Ar:O₂ and dotted to Ar:H₂. The inset shows the variation of the weighted average transmittance (WAT) of for different pressure and atmosphere.

The composition affected the optical behavior of the films, the Ar: H_2 series being the less transparent while the Ar:O₂ ones exhibited the highest transparency. This is due to the sub stochiometric MoO_x with large number of oxygen vacancies in Ar:H₂ series. These oxygen vacancies are evidenced by a sub-bandgap absorption peak centered at ∼850 nm, which is only

present in the Ar and Ar:H$_2$ samples, but not in the more stoichiometric Ar:O$_2$ ones (close to MoO$_3$), as it can be appreciated in Fig. 5.19 by a rise of the absorption coefficient around these wavelengths [32].

Optical bandgap calculations were done using total transmittance and total reflectance spectra shown in Fig. 5.20 Evaluation of the indirect band gap was made as proposed in sub section 3.8. The optical band gap of the films rises as the deposition pressure increases from 3 to 11 mTorr for all atmospheres.
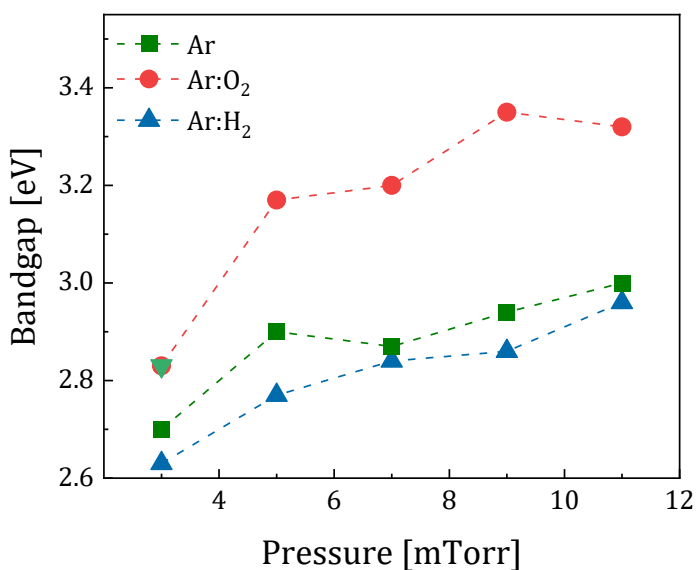
Figure 5.20: Band gap energy as a function of deposition pressure for samples grown in different atmosphere.

A higher band gap (2.8 to 3.4 eV) was obtained for films sputtered in Ar:O$_2$ atmosphere, which is due to the stoichiometry (MoO$_3$) of the films as observed from the XPS measurements. For Ar and Ar:H$_2$ atmospheres, the band gap varies between 2.6 to 2.8 eV due to the sub-stoichiometric MoO$_x$ films. These values are in good agreement with the ones reported in the literature [32][33][34][35][36].
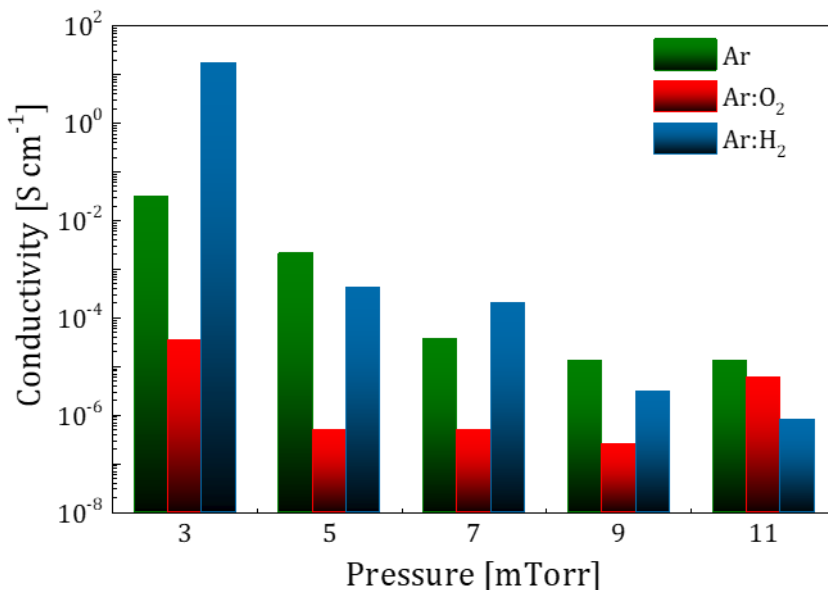
Figure 5.21: Conductivity of the pressure series in a logarithmic scale. For each pressure the conductivity of the Ar, Ar:O_2 and Ar: H_2 atmospheres are shown from left to right respectively. All the measurements were done on films deposited on glass substrates.

The electric characterization of the films was performed through TLM, which consisted in measuring the resistance through the *I-V* curve for each contact distance (see section 3.2.6). The results are displayed in Fig. 5.21. As a general observation for each atmosphere, the samples grown at lower pressure presented a higher conductivity. This difference in the conductivity of the samples could be attributed to their composition: samples deposited at lower pressure were more conductive due to a more reduced stoichiometry (see Fig. 5.18). On the other hand, more stoichiometric samples exhibited a considerably lower conductivity [37]. There are orders of magnitude in difference between the conductivities of samples prepared at 3 mTorr compared to the ones at 9 and 11 mTorr, both for Ar and Ar:H_2 atmospheres. The optical and electric behavior of the films grown in the Ar:H_2 atmosphere can be explained mostly by their stoichiometry. They present a higher amount of Mo^{5+} states (which denotes the presence of

oxygen vacancies) and, for instance, they are more metallic. This composition reduces the transmittance of the films as there is more absorption inside the film. Consequently, they present a lower transmittance as expected for a less stoichiometric metal oxide.

By depositing these films in a different atmosphere, a better understanding of the influence of the Ar:H$_2$ atmosphere was accomplished. Even though samples prepared in the Ar:H$_2$ atmosphere had lower transmittance due to the absence of some oxygen in the films, their behavior was almost the same as in the Ar atmosphere. This happens especially when the deposition pressure increased, thus supporting the idea that hydrogen in the atmosphere may react with the film and the sputtered particles to form bronzes [27]. The resulting film is reduced as it is observed in Fig. 5.18, leading to changes in the conductivity. Improvements in the modulation of the film characteristics, such as higher conductivity (at 3 mTorr) or stoichiometry control (in particular, the existing significant difference at 3 and 5mTorr) through the Ar:H$_2$ atmosphere arouse interest in a more in-depth study of these deposition conditions. Therefore, a temperature series was deposited at 3 mTorr pressure, with substantial differences in the resulting film characteristics.

5.3.3 Influence of temperature

The influence of temperature was studied for samples deposited in an Ar:H$_2$ atmosphere at 3 mTorr, with deposition times ranging from 1.5 to 12 min. The depositions were carried out at room temperature (RT), each one presenting a duplicated sample but deposited at a temperature set point of 100 °C.

5.3.3.1 Deposition rate and composition

The temperature series was aimed at improving the transmittance of the previous MoO$_x$ films by reducing their thickness while being able to maintain the other properties. It was also aimed at being able to further control the sample stoichiometry by making depositions on a slightly hotter substrate (100 °C). For those purposes, deposition time was varied from 1.5 to 12 min

and, for each deposition time, two samples were compared, one at RT and one at 100 °C.

As it can be seen in Fig. 5.22, the deposition rate was not constant; instead, it evolved in a non-linear way. Thinner samples had a higher deposition rate than thicker ones, meaning that the growth rate of the film decreased after the initial layers of the film had already been deposited. For this reason, the sample thickness was hard to predict.
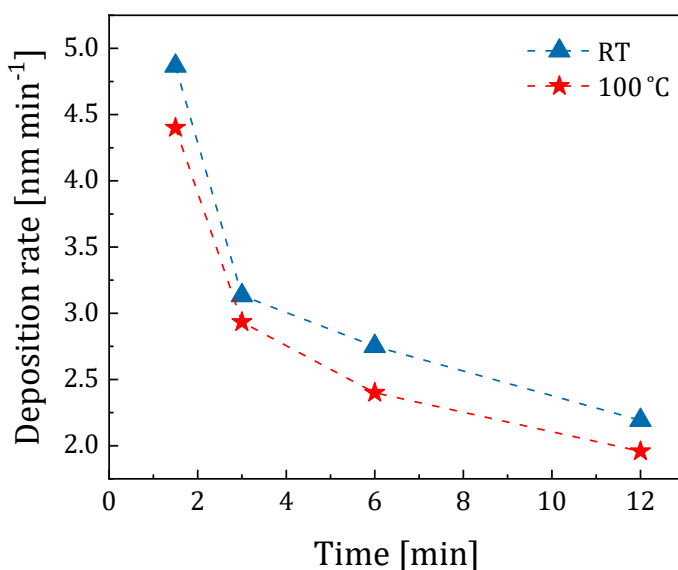
Figure 5.22: Dependence of the deposition rate of MoO_x thin films deposited for different time at room temperature and at 100 °C.

In the case of the series with temperature, the deposition rate of the films was generally slower than at RT [38]. As the sample surface was at a higher temperature, particles were less bound and more propense to leave the surface, especially the lighter ones (i.e., oxygen). Accordingly, samples prepared at 100 °C manifested more metallic than the ones at RT, as is shown by the XPS measurements shown in Fig. 5.23.
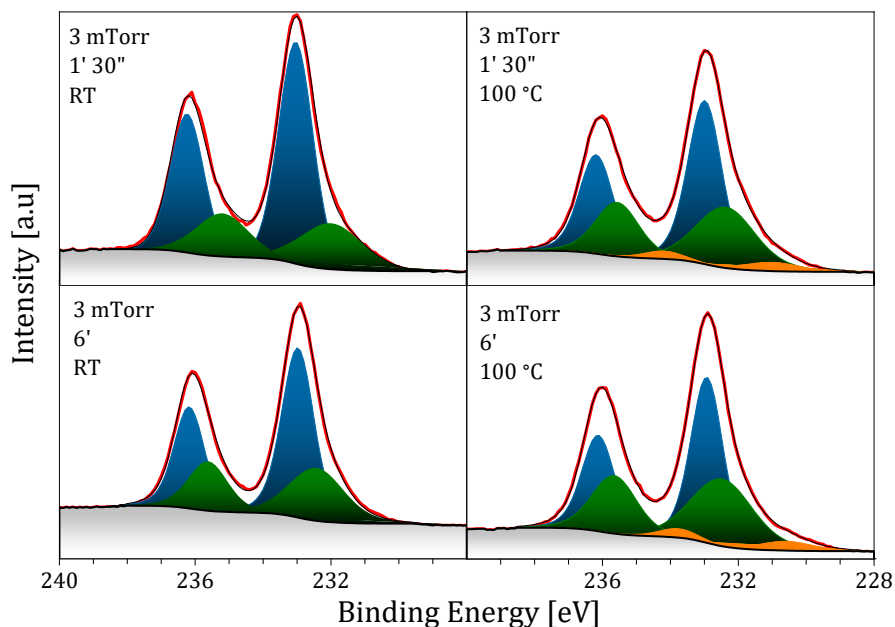
Figure 5.23: XPS molybdenum 3d peaks analyzed for the 1 min 30 s and 6 min samples at RT and at 100 °C. Blue peaks correspond to Mo^{6+} peaks, green peaks to Mo^{5+} deconvolved peaks, and orange peaks to Mo^{4+} deconvolutions. The positions of the 3d peaks were 232.9, 232.0, and 230.6 eV for the Mo^{6+}, Mo^{5+} and Mo^{4+} states, respectively.

XPS was studied to understand the stoichiometry of the samples sputtered at RT and at a set temperature of 100 °C. The primary condition of splitting BE of ~3.2 eV is maintained between the doublet Mo ($3d_{3/2}$ and $3d_{5/2}$) peaks. In this case, Fig. 5.23 shows that the binding energies associated with the lower energy peak were 232.9, 232.0 , and 230.6 eV for the Mo^{6+}, Mo^{5+}, and Mo^{4+} [26] states, respectively. The O/Mo ratio for these samples varied between 2.6 and 2.9, as presented in Fig. 5.24, where differences can be appreciated between 1.5 min and 12 min samples.

The longer the deposition time, the less stoichiometric the films grew. Samples prepared at 100 °C had oxygen deficiency either due to the presence of Mo^{5+} states or the presence of Mo^{4+} states, which would not contribute to generating oxygen vacancies. Note that by increasing the temperature of the substrate and the deposition time, it would be possible to control film stoichiometry in an $Ar:H_2$ atmosphere.
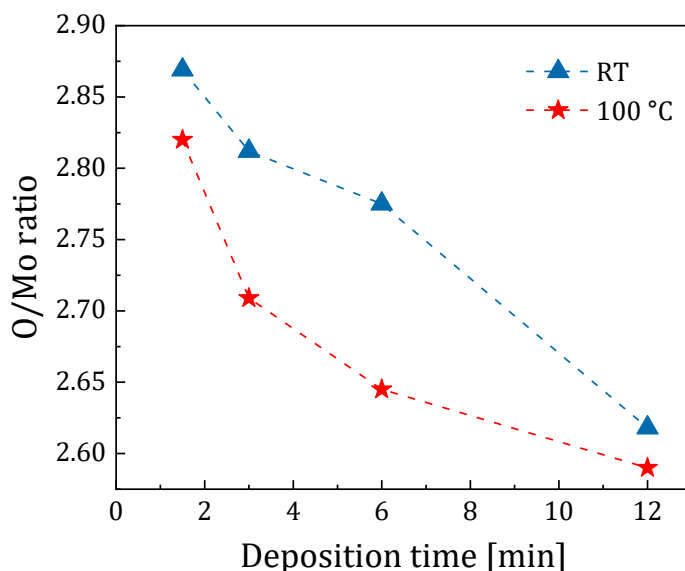
Figure 5.24: Stoichiometry of the films as a function of the deposition time for the samples grown at RT and at 100 °C.

5.3.3.2 Optical and electrical

Regarding to the desired transmittance improvement in samples whose deposition time was 1.5 min (the thinnest ones), they exhibited around 90% average transmittance when weighted with the Sun's AM1.5 spectrum. Samples prepared at 100 °C were moderately less transmitting despite the reduced oxidation states. In Fig. 5.25, it can be appreciated that there was almost no difference between samples prepared at RT and 100 °C, and more importantly that transmittance rapidly decreased with the thickness

(increased deposition time), a difference of less than 20 nm resulting in a decrease on the transmittance of ~45% [39].
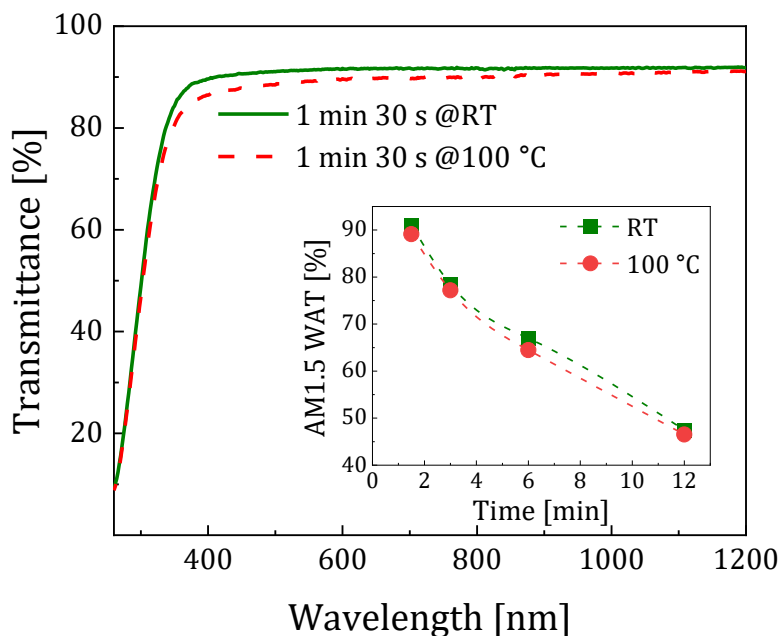
Figure 5.25: Transmittance corresponding to the 1.5 min films for the visible and near-infrared (300–1200 nm) ranges. The straight line corresponds to the RT-deposited samples and dashed lines to the 100 °C-deposited ones. The inset shows the variation of the weighted average transmittance for every deposition time and temperature.

The optical bandgap energy of the computed values, shown in Fig. 5.26, varied from 2.92 to 3.46 eV, which stayed within a similar range as the films deposited in different atmospheres (Fig. 5.20). In the figure, it can be observed a trend in the bandgap energy, which gets narrower as the sample thickness increases. This phenomenon agrees with the XPS results: samples that get their stoichiometry reduced have more defects (e.g., oxygen vacancies).
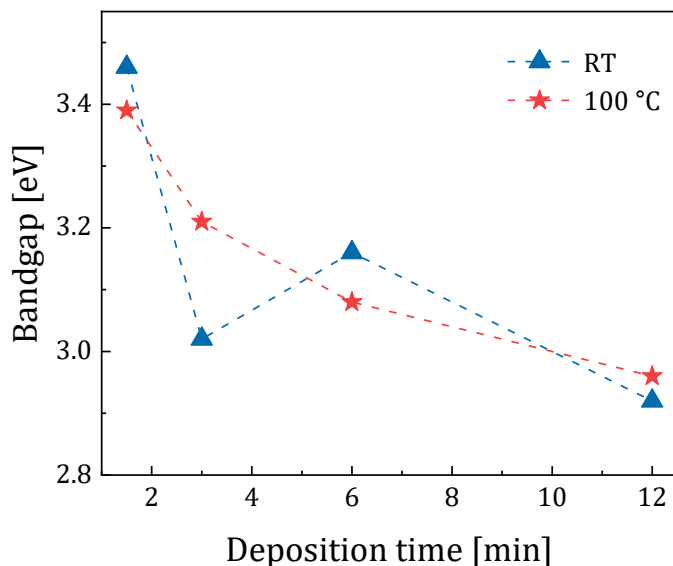
Figure 5.26: Band gap variation of the samples deposited for different times at RT and at 100 °C.

The conductivity of the films, displayed in Fig. 5.27, was measured by TLM, evidencing a notable difference for samples deposited at 100 °C compared to those at RT, in agreement with the reduced oxidation states present in the highest temperature samples [40]. Again, thicker samples were the most conductive due to their stoichiometry being reduced. It must be noted that an anomaly was observed for the sample at 3 min, due to an unknown cause. The deposition with temperature helped in the understanding of the reduction in the film. As the deposition rate was slightly slower when depositing at 100 °C, the oxygen-hydrogen association could be favored as the sputtered particles were reaching the substrate. Supporting this hypothesis was the fact that in the XPS analysis, Mo^{4+} states could be observed, which were related to the presence of MoO_2 metastable configurations in the layer. At RT, this effect was negligible, and only oxygen vacancies were observed. This phenomenon did not influence the transmittance of the films, as seen in Fig. 5.25, but affected the deposition

rate and the conductivity of the samples. As they were more metallic due to the presence of the Mo^{4+} states, they, consequently, were more conducting. Transmittance was mostly affected by the film thickness, whereas the conductivity was predominantly conditioned by the composition of the deposited film. Finally, a great drop in the average transmittance was observed through the samples from the temperature series, but the conductivity increased in a rather smooth behavior.
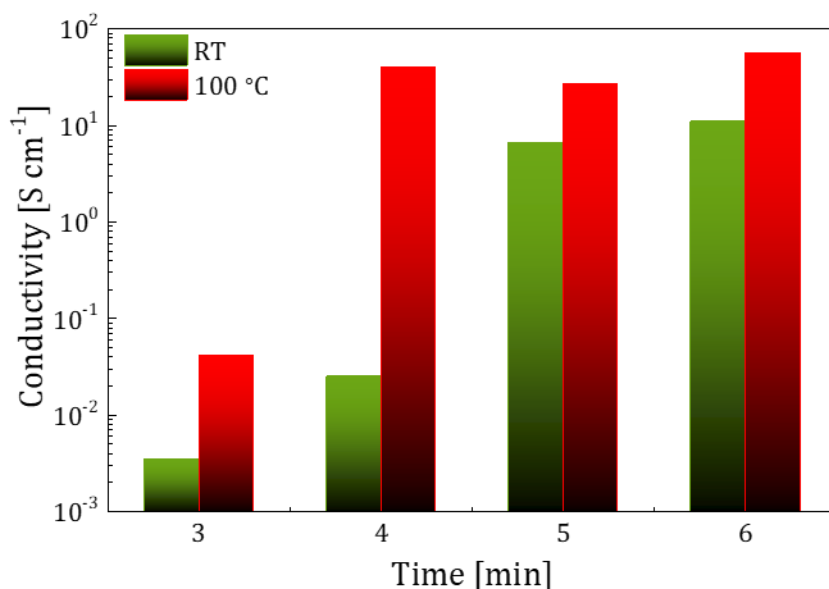
Figure 5.27: Conductivity of the films in a logarithmic scale. For each deposition time the conductivity for samples prepared at RT is displayed on the left (green bars) and the ones at high temperature in the right (red bars).

This study has allowed us determining that variations in the film characteristics arise out of deposition temperature changes, fact that could let us deposit a reduced molybdenum film with the specific characteristic. For a solar cell, the deposition conditions would be sputtering in an $Ar:H_2$ atmosphere with low pressure, at room temperature (unless the vacancies in the film were not enough at RT) and during 3–4 min, in order to have a

highly transparent film with oxygen vacancies to act as a selective HTL contact and with relatively good conductivity.

5.4 Conclusions

In this chapter we have showed various sputtering techniques to replace the thermally-evaporated hole transport layers. At first, reactive sputtering using a metallic target of Mo was studied to adjust the compositional, optical and electrical properties of HTL. The reproducibility of the films and ease of fabrication of these MoO_x films made sputtering more suitable than thermal evaporation for these transition metal oxide contact layers. Unfortunately, when these sputtered films were tested on the HJT solar cells, the performance of the cells were not up to the benchmark of the thermally-evaporated cells. This is due to i) the sputtering damage caused on the a-Si:H layers, ii) the low work function of these layers, iii) and the high ΔV_{oc} that blocks the highly efficient hole connections on silicon.

As the following approach, we sputtered using a ceramic target of MoO_3. This was done in different atmospheres of Ar and reactive atmospheres of $Ar:O_2$ and $Ar:H_2$. Films prepared in the $Ar:H_2$ atmosphere resulted in reduced stoichiometry and improved the conductivity in the films. Nevertheless, changes in the sputtering atmosphere alone were not enough to control every aspect of the deposited film. Therefore, the films were fabricated in varying temperatures, too. The films prepared at higher temperature exhibited Mo^{4+} states and therefore were more conductive. Transmittance, which was highly influenced by film thickness, reached values around 90% in the thinnest films.

References

[1]   P. Gao, Z. Yang, J. He, J. Yu, P. Liu, J. Zhu, Z. Ge, J. Ye, Dopant-Free and Carrier-Selective Heterocontacts for Silicon Solar Cells: Recent Advances and Perspectives, Adv. Sci. 5 (2018). https://doi.org/10.1002/advs.201700547.

[2]   L.G. Gerling, S. Mahato, A. Morales-Vilches, G. Masmitja, P. Ortega, C. Voz, R. Alcubilla, J. Puigdollers, Transition metal oxides as hole-selective contacts in silicon heterojunctions solar cells, Sol. Energy Mater. Sol. Cells. 145 (2016) 109–115. https://doi.org/10.1016/j.solmat.2015.08.028.

[3]   E.R. Costals, G. Masmitjà, E. Almache, B. Pusay, K. Tiwari, E. Saucedo, C.J. Raj, B.C. Kim, J. Puigdollers, I. Martin, C. Voz, P. Ortega, Atomic layer deposition of vanadium oxide films for crystalline silicon solar cells, Mater. Adv. 3 (2022) 337–345. https://doi.org/10.1039/d1ma00812a.

[4]   M. Mews, A. Lemaire, L. Korte, Sputtered Tungsten Oxide as Hole Contact for Silicon Heterojunction Solar Cells, IEEE J. Photovoltaics. 7 (2017) 1209–1215. https://doi.org/10.1109/JPHOTOV.2017.2714193.

[5]   J. Bullock, A. Cuevas, T. Allen, C. Battaglia, Molybdenum oxide MoO_x: A versatile hole contact for silicon solar cells, Appl. Phys. Lett. 105 (2014). https://doi.org/10.1063/1.4903467.

[6]   C. Battaglia, X. Yin, M. Zheng, I.D. Sharp, T. Chen, S. Mcdonnell, A. Azcatl, C. Carraro, B. Ma, R. Maboudian, R.M. Wallace, A. Javey, Hole Selective MoO, NanoLett. 14 (2014) 967–971.

[7]   P. Schulz, J.O. Tiepelt, J.A. Christians, I. Levine, E. Edri, E.M. Sanehira, G. Hodes, D. Cahen, A. Kahn, High-work-function molybdenum oxide hole extraction contacts in hybrid organic-inorganic perovskite solar cells, ACS Appl. Mater. Interfaces.   8   (2016)   31491–31499. https://doi.org/10.1021/acsami.6b10898.

[8]   L. Cao, P. Procel, A. Alcañiz, J. Yan, F. Tichelaar, E. Özkol, Y. Zhao, C. Han, G. Yang, Z. Yao, M. Zeman, R. Santbergen, L. Mazzarella, O. Isabella, Achieving 23.83% conversion efficiency in silicon heterojunction solar cell with ultra-thin MoOx hole collector layer via tailoring (i)a-Si:H/MoO_x interface, Prog. Photovoltaics Res. Appl. (2022) 1–10. https://doi.org/10.1002/pip.3638.

[9]   M. Bivour, J. Temmler, H. Steinkemper, M. Hermle, Molybdenum and tungsten oxide: High work function wide band gap contact materials for hole selective contacts of silicon solar cells, Sol. Energy Mater. Sol. Cells. 142 (2015) 34–41. https://doi.org/10.1016/j.solmat.2015.05.031.

[10]   Z. Zhang, R. Ji, M. Kroll, Y.J. Hofstetter, X. Jia, D. Becker-Koch, F. Paulus, M. Löffler, F. Nehm, K. Leo, Y. Vaynzof, Efficient Thermally Evaporated γ-$CsPbI_3$ Perovskite   Solar   Cells,   Adv.   Energy   Mater.   11   (2021)   1–10. https://doi.org/10.1002/aenm.202100299.

[11]   M. Bivour, F. Zähringer, P. Ndione, M. Hermle, Sputter-deposited WO_x and MoO_x for hole selective contacts, Energy Procedia. 124 (2017) 400–405. https://doi.org/10.1016/j.egypro.2017.09.259.

[12]   E.G. Sheikin, The pressure dependence of the deposition rate in a magnetron sputtering system, Thin Solid Films. 574 (2015) 52–59. https://doi.org/10.1016/j.tsf.2014.11.043.

[13]   D. Depla, R. De Gryse, Target poisoning during reactive magnetron sputtering: Part II: The influence of chemisorption and gettering, Surf. Coatings Technol. 183 (2004) 190–195. https://doi.org/10.1016/j.surfcoat.2003.10.007.

[14]   A. Stoyanova, R. Iordanova, M. Mancheva, Y. Dimitriev, Synthesis and structural characterization of MoO_3 phases obtained from molybdic acid by addition of HNO_3 and H_2O_2, J. Optoelectron. Adv. Mater. 11 (2009) 1127–1131.

[15]   S. Mobtakeri, S. Habashyani, E. Gür, Highly Responsive Pd-Decorated MoO_3 Nanowall H_2 Gas Sensors Obtained from In-Situ-Controlled Thermal Oxidation of Sputtered MoS_2 Films, ACS Appl. Mater. Interfaces. 14 (2022) 25741–25752. https://doi.org/10.1021/acsami.2c04804.

[16]   Y. Liu, P. Liu, Y.L. Men, Y. Li, C. Peng, S. Xi, Y.X. Pan, Incorporating MoO_3 Patches into a Ni Oxyhydroxide Nanosheet Boosts the Electrocatalytic Oxygen Evolution Reaction, ACS Appl. Mater. Interfaces. 13 (2021) 26064–26073. https://doi.org/10.1021/acsami.1c05660.

[17]   E. Vernickaitė, M. Lelis, N. Tsyntsaru, V. Pakštas, H. Cesiulis, XPS studies on the Mo oxide-based coatings electrodeposited from highly saturated acetate bath, Chemija. 31 (2020) 203–209. https://doi.org/10.6001/CHEMIJA.V31I4.4317.

[18]   L.G. Gerling, S. Mahato, A. Morales-Vilches, G. Masmitja, P. Ortega, C. Voz, R. Alcubilla, J. Puigdollers, Transition metal oxides as hole-selective contacts in silicon heterojunctions solar cells, Sol. Energy Mater. Sol. Cells. 145 (2016) 109–115. https://doi.org/10.1016/j.solmat.2015.08.028.

[19]   S. Subbarayudu, V. Madhavi, S. Uthanna, Growth of MoO_3 Films by RF Magnetron Sputtering: Studies on the Structural, Optical, and Electrochromic Properties , ISRN Condens. Matter Phys. 2013 (2013) 1–9. https://doi.org/10.1155/2013/806374.

[20]   O. De Melo, V. Torres-Costa, A. Climent-Font, P. Galán, A. Ruediger, M. Sánchez, C. Calvo-Mola, G. Santana, V. Torres-Costa, Optical and electrical properties of MoO_2 and MoO_3 thin films prepared from the chemically driven

isothermal close space vapor transport technique, J. Phys. Condens. Matter. 31 (2019). https://doi.org/10.1088/1361-648X/ab18e2.

[21]   C. Castillo, G. Buono-Core, C. Manzur, N. Yutronic, R. Sierpe, G. Cabello, B. Chornik, Molybdenum trioxide thin films doped with gold nanoparticles grown by a sequential methodology: Photochemical Metal-Organic Deposition (PMOD) and DC-magnetron sputtering, J. Chil. Chem. Soc. 61 (2016) 2816–2820. https://doi.org/10.4067/S0717-97072016000100014.

[22]   K. Inzani, M. Nematollahi, F. Vullum-Bruer, T. Grande, T.W. Reenaas, S.M. Selbach, Electronic properties of reduced molybdenum oxides, Phys. Chem. Chem. Phys. 19 (2017) 9232–9245. https://doi.org/10.1039/c7cp00644f.

[23]   R. Coquet, D.J. Willock, The (010) surface of a-MoO_3, a DFT + U study, Phys. Chem. Chem. Phys. 7 (2005) 3819–3828. https://doi.org/10.1039/B511044K.

[24]   G.E. Buono-Core, G. Cabello, A.H. Klahn, A. Lucero, M. V. Nuñez, B. Torrejón, C. Castillo, Growth and characterization of molybdenum oxide thin films prepared by photochemical metal-organic deposition (PMOD), Polyhedron. 29 (2010) 1551–1554. https://doi.org/10.1016/j.poly.2010.01.036.

[25]   L. Neusel, M. Bivour, M. Hermle, Selectivity issues of MoO_x based hole contacts, Energy Procedia. 124 (2017) 425–434. https://doi.org/10.1016/j.egypro.2017.09.268.

[26]   N. Lopez-Pinto, T. Tom, J. Bertomeu, J.M. Asensi, E. Ros, P. Ortega, C. Voz, Deposition and characterisation of sputtered molybdenum oxide thin films with hydrogen atmosphere, Appl. Surf. Sci. 563 (2021) 150285. https://doi.org/10.1016/j.apsusc.2021.150285.

[27]   A. Borgschulte, O. Sambalova, R. Delmelle, S. Jenatsch, R. Hany, F. Nüesch, Hydrogen reduction of molybdenum oxide at room temperature, Sci. Rep. 7 (2017) 1–9. https://doi.org/10.1038/srep40761.

[28]   L. Wang, M.C. Li, G.H. Zhang, Z.L. Xue, Morphology evolution and quantitative analysis of β-MoO_3 and α-MoO_3, High Temp. Mater. Process. 39 (2020) 620–626. https://doi.org/10.1515/htmp-2020-0093.

[29]   M. Mazur, A. Lubańska, J. Domaradzki, D. Wojcieszak, Complex Research on Amorphous Vanadium Oxide Thin Films Deposited by Gas Impulse Magnetron Sputtering, Appl. Sci. 12 (2022).

https://doi.org/10.3390/app12188966.

[30]   J. Zou, G.L. Schrader, Multicomponent thin film molybdate catalysts for the selective oxidation of 1,3-butadiene, J. Catal. 161 (1996) 667–686. https://doi.org/10.1006/jcat.1996.0229.

[31]   Z. Yin, M. Tordjman, Y. Lee, A. Vardi, R. Kalish, J.A. Del Alamo, Enhanced transport in transistor by tuning transition-metal oxide electronic states interfaced with diamond, Sci. Adv. 4 (2018). https://doi.org/10.1126/sciadv.aau0480.

[32]   J. Werner, J. Geissbühler, A. Dabirian, S. Nicolay, M. Morales-Masis, S. De Wolf, B. Niesen, C. Ballif, Parasitic Absorption Reduction in Metal Oxide-Based Transparent Electrodes: Application in Perovskite Solar Cells, ACS Appl. Mater. Interfaces. 8 (2016) 17260–17267. https://doi.org/10.1021/acsami.6b04425.

[33]   Y. Wang, Q. Huang, C. Wei, D. Zhang, Y. Zhao, X. Zhang, Improvement of electrical and optical properties of molybdenum doped zinc oxide films by introducing hydrogen, Appl. Surf. Sci. 258 (2012) 8797–8801. https://doi.org/10.1016/j.apsusc.2012.05.093.

[34]   K. Inzani, M. Nematollahi, F. Vullum-Bruer, T. Grande, T.W. Reenaas, S.M. Selbach, Electronic properties of reduced molybdenum oxides, Phys. Chem. Chem. Phys. 19 (2017) 9232–9245. https://doi.org/10.1039/c7cp00644f.

[35]   S.S. Sunu, E. Prabhu, V. Jayaraman, K.I. Gnanasekar, T.K. Seshagiri, T. Gnanasekaran, Electrical conductivity and gas sensing properties of MoO_3, Sensors Actuators, B Chem. 101 (2004) 161–174. https://doi.org/10.1016/j.snb.2004.02.048.

[36]   H. Simchi, B.E. McCandless, T. Meng, J.H. Boyle, W.N. Shafarman, Characterization of reactively sputtered molybdenum oxide films for solar cell application, J. Appl. Phys. 114 (2013). https://doi.org/10.1063/1.4812587.

[37]   H. Ohtsuka, Y. Sakurai, Characterization of MoO_{3-x} Thin Films, Jpn. J. Appl. Phys. 40 (2001) 4680–4683. https://doi.org/10.1143/JJAP.40.4680.

[38]   L. Fang, Y. Jiang, S. Zhu, J. Ding, D. Zhang, A. Yin, P. Chen, Substrate temperature dependent properties of sputtered AlN:Er thin film for in-situ luminescence sensing of Al/AlN multilayer coating health, Materials (Basel).

11 (2018). https://doi.org/10.3390/ma11112196.

[39]   L.S. Pali, J.K. Tiwari, N. Ali, S. Ghosh, K.S. Nalwa, A. Garg, Development of $MoO_3/Au/MoO_3$ Top Transparent Conducting Electrode for Organic Solar Cells on Opaque Substrates, Energy Technol. 10 (2022) 1–8. https://doi.org/10.1002/ente.202100689.

[40]   V. Nirupama, S. Uthanna, Investigations on morphological and electrical studies of sputtered MoO_3 films, J. Mater. Sci. Mater. Electron. 27 (2016) 3668–3674. https://doi.org/10.1007/s10854-015-4206-6.

Chapter 6: Electron transport layers

This chapter explores the possibilities the organic molecules that as an interfacial dipole layer. These films spin-coated onto the crystalline silicon surface, have demonstrated to improve the conversion efficiency in SHJ acting as an electron transport layer.

6.1 Organic molecules as electron transport layer

In recent years, researchers have been trying to replace the heavily-doped hydrogenated amorphous silicon films that are used as carrier selective contacts in SHJ solar cells, due to the complicated fabrication procedure that they require, their parasitic absorption, and their high cost. With this objective in mind, various metal oxides, fluorides, nitrides and organic molecules have been explored [1][2][3][4]. Amongst the latter, solution-processable organic semiconductor molecules have gained more acceptance due to their simple, low-cost, and low-temperature fabrication process, based on the spin coating technique. Carrier selective contacts based on organic molecules have attracted research interest due to their highly adjustable electronic and chemical properties and cheaper fabrication process [5][6]. Interfacial layers based on organic molecules have been shown to modify the ϕ' of metallic electrodes [7]. In this sense, the electric dipole moment of these interlayers has been proven to be capable of shifting the electronic band alignment across the interface and therefore the properties of the metal/semiconductor junction [8].

In this chapter we explore three different organic molecules as the carrier selective contact or as ETL in silicon solar cells. First, we explore the branched polyethylenimine (b-PEI), which is a cationic polyelectrolyte with a large number of amines [9]. Then, in the next section the poly(amidoamine) (PAMAM) dendrimers are used to modify the interface of metal-semiconductor junctions. In the final part of the chapter, the

possibilities of using deoxyribonucleic acid (DNA), which is a naturally-driven biomolecule, is explored as ETL in solar cells [10].

6.2 Branched Polyethylenimine (b-PEI) as ETL

Here, we explore the advantages of b-PEI as an electron-selective contact, and prospect for a deeper explanation of its working principle involving the conduction mechanisms related to dipole layers as well as their specific effect in metal/insulator/semiconductor junctions. Finally, b-PEI was integrated as the ETL in a dopant- free crystalline silicon solar cell test structure with a *PCE* of 13.8%.
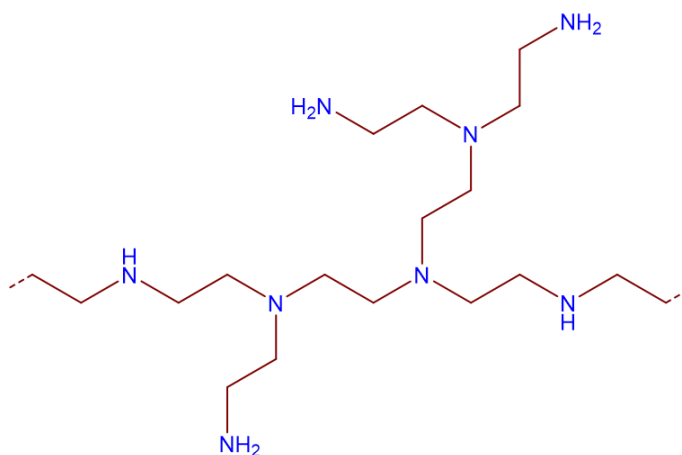
Figure 6.1: Schematic representation of branched polyethylenimine (b-PEI).

6.2.1 Experimental method

The b-PEI solution 50 wt % in H_2O, average M_w = 750,000 by loss spectroscopy, was used as electron-selective contact. Polyethylenimine solutions of different weight percentages from 0.1 to 0.001 wt % were prepared using ethanol as the solvent. One-side polished (FZ) *n*-type c-Si (100) wafers with a thickness of 280 μm and a resistivity of 2 Ω cm were used as the substrates. Spin-coating of PEI solutions was performed on silicon wafers at 5000 rpm for 60 s, and then the films were annealed at a

temperature of 80 °C for 2 min on a hot plate in ambient air. Silicon solar cells with and without the b-PEI at the rear side contact were developed. All these devices were fabricated on non-textured, *n*-type c-Si wafers. The rear side was spin-coated with b-PEI at 5000 rpm for 30 s. Afterwards, on the top of the b-PEI layer, an Al contact was thermally evaporated. On the front side, hole-selective layer of thermally-evaporated V_2O_5, was deposited, whereas the top electrode consisted of sputtered tin-doped indium oxide. Finally, a 2-µm-thick front contact Ag grid was thermally evaporated using a shadow mask.

6.2.2 Film properties

The thickness of the films was studied with varying concentration of the solution. The thickness of the film was 0.3 nm for the least concentrated (0.001 wt %) solution. It steadily increased to 1.0 nm for 0.01 wt % and, finally, to 3.8 nm for the highest 0.1 wt % concentrated solution. The thickness versus concentration plot is as shown in Fig. 6.2.
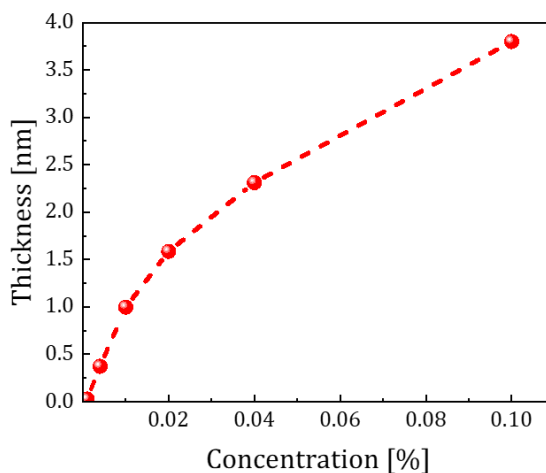
Figure 6.2: Thickness of the films vs. b-PEI concentration. The thickness was measured on films grown on c-Si substrates.

The contact quality for PEI thicknesses ranging from 0.03 to 3.8 nm was studied by the TLM, the results being displayed in Fig. 6.3. The inset shows the *I–V* characteristics of (*n*) c-Si/b-PEI/Al structures with PEI thickness between 0.03 and 3.8 nm.

The linear *I–V* characteristics demonstrate a good ohmic behavior of b-PEI on c-Si. The results plotted in Fig. 6.3 show that there is a minimum in the specific contact resistance for films at 8 mΩ cm^2. The optimum thickness value that minimizes the contact resistance is at 1 nm. On one hand, the rapidly increasing specific contact resistance of the non-passivated sample beyond 1 nm suggests electron tunneling as a dominant conduction mechanism. Such a strong dependence on thickness is also observed in other selective contacts such as alkali salts (e.g., MgF_2 and LiF) [11][12]. On the other hand, the increase in specific contact resistance below 1 nm indicates at least a secondary mechanism arising close to monolayer thickness.
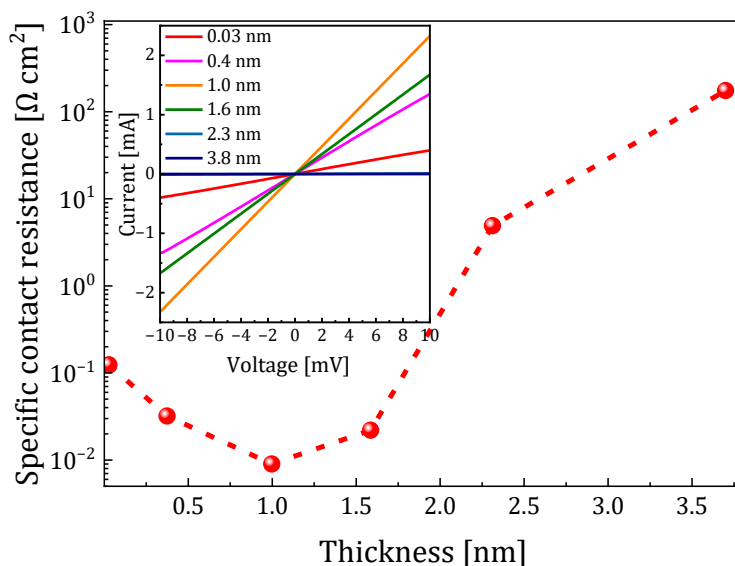
Figure 6.3: Specific contact resistance as a function of b-PEI thickness. All the measurements were performed on samples grown on c-Si.

The surface roughness of 1-nm-thick b-PEI films grown on silicon substrates was studied by AFM, and it is shown in Fig. 6.4. The root mean square (RMS) roughness of the film is estimated to be 0.3 nm.
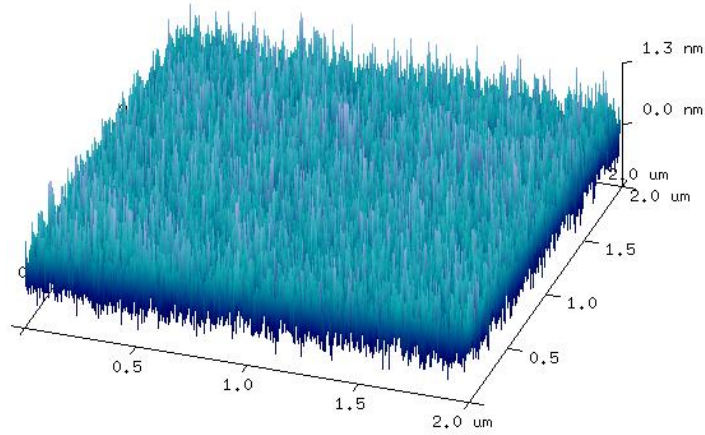
Figure 6.4: AFM image of the 1-nm-thick b-PEI films grown on c-Si substrates.
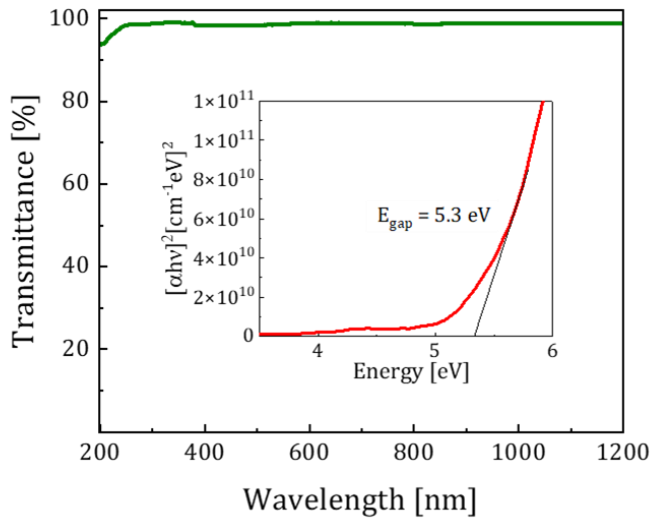
Figure 6.5: Transmittance spectra of the 1-nm-thick b-PEI films grown on sapphire substrate, ranging from 200 nm to 1500 nm. The inset shows the corresponding Tauc plot, showing a direct band gap energy of 5.3 eV.

The low surface roughness and lack of extended sharp peak indicates a good uniformity of the b-PEI films and enhanced wettability over the Si surface. Optical transmittance spectra were acquired from the same films deposited on sapphire substrates. The results corresponding to the 1-nm-thick sample (200–1500 nm range) are shown in Fig. 6.5, exhibiting a high transmittance value, over 95%, throughout the spectrum. The inset shows the corresponding Tauc plot, showing an optical band gap energy of 5.3 eV.
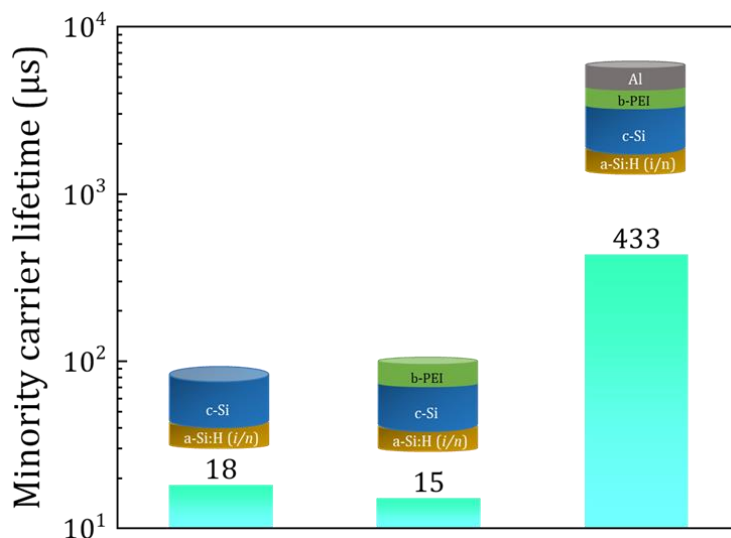
Figure 6.6: Minority carrier lifetime at 10^{15} cm^{-3} injection for bare silicon, silicon with PEI layer, and the previous stack with an additional semitransparent aluminium contact.

The QSSPC study has been performed on different test structures (see Fig. 6.6) for the optimum thickness deduced from TLM measurements. The minority carrier lifetime for both bare and passivated c-Si samples remained practically unchanged after PEI deposition. However, a strong increase by one order of magnitude was observed after depositing a thin semitransparent aluminum capping (i.e., <10 nm). The lifetime values were finally higher than 400 µs.

As it can be seen in Fig. 6.6, the strong lifetime increasing with a semitransparent Al layer indicates an important role of the metallic

electrode to improve surface passivation. These results contrast with the lifetime degradation often observed after depositing metallic electrodes on silicon. Our interpretation of this behavior is the formation of a "metal/dipole/semiconductor" (MDS) junction, a specific variant of classical metal/insulator/semiconductor structures. In particular, the explanation considers PEI monomers behaving as cationic conjugated polyelectrolyte with quaternized amine groups. In this hypothesis, amine groups from the polymer protonate in solution acquiring charge. This could be due to the PEI high Lewis basicity, simultaneously adhering a charged counter-ion from the solution (i.e., counter-ion condensation) [13]. In our case, this would be ethanol, which is known to behave as a weak Brønsted acid forming an ethanolate radical. This leads to a picture where the CP does not have a net charge, but instead forms an interfacial dipole. As a consequence, there is neither an electric field nor any charge transfer to the silicon surface. Therefore, the minority carrier lifetime is not significantly affected after PEI deposition. The situation changes when a thin Al layer is evaporated onto the CP. Since the interface dipole effectively reduces the ϕ of the metal [8], the aluminum layer behaves as an electron reservoir in contact with silicon. Electron doping by charge transfer from the metal would primarily fill interface traps depinning the Fermi level. The leftover charge results in electron accumulation at the semiconductor surface in a similar manner to the creation of ohmic contacts by the use of low ϕ metals.

The UPS spectra of samples with a PEI capping, displayed in Fig. 6.7(a), confirm a decrease in the silicon ϕ associated to the interface dipole. In this case, the measured ϕ value of reference silicon (i.e., 4.2 eV) is 0.9 eV higher than in the c-Si/PEI sample (i.e., 3.3 eV). The observed relative displacement is quite similar to the values reported in the literature for Si/PEI structures ($\Delta\phi \sim 1.2$ eV) [7][14], with slight differences that could be attributed to the different technological procedures. The UPS spectrum for the c-Si/PEI/Al structure indicates an even lower ϕ value of 2.49 eV, which could account for the charge transfer and induced band-bending at the silicon surface. As a consequence of such charge transfer, the internal electric field could further promote dipole orientation in the PEI layer.
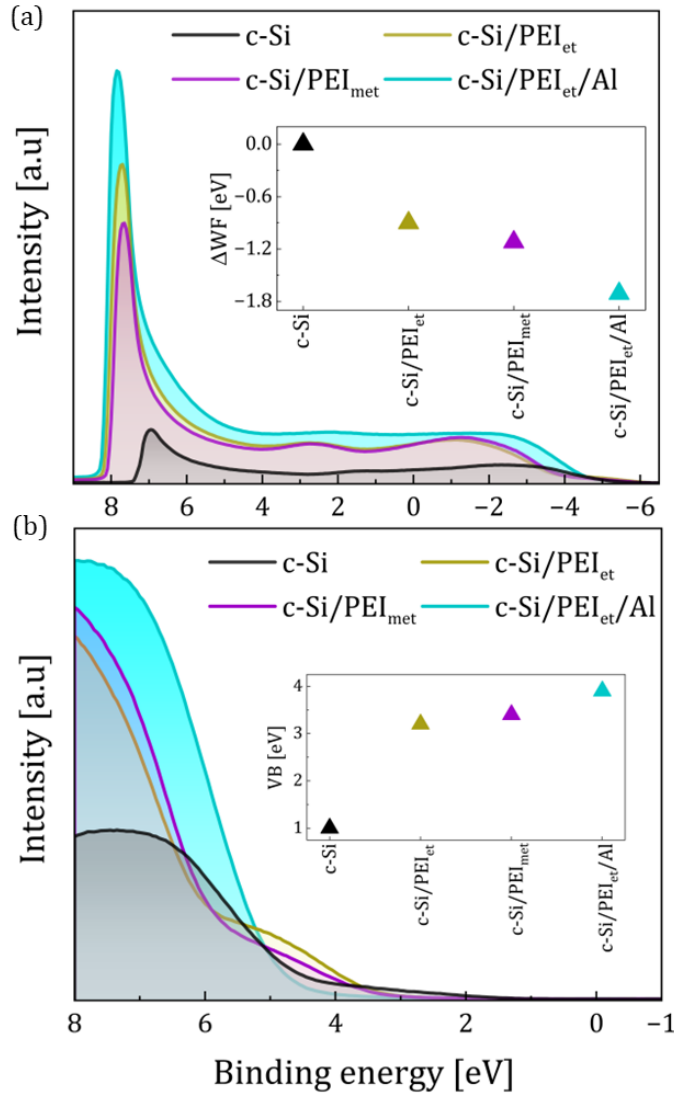
Figure 6.7: Analysis of the UPS spectra for reference c-Si, c-Si/PEI in ethanol solution, c-Si/PEI in methanol solution, and c-Si/PEI/Al in ethanol solution (a) work function and inset shows shift in work function for the different structures. (b) Valence band and inset shows the valence band values of different structures.

This result, along with QSSPC measurements, reinforces the important role of the metal in the final performance of the structure as an electron-selective contact. Finally, the analysis of UPS spectra also reveals an influence from the solvent used in the process. In comparison to the use of ethanol, the solution of PEI in methanol led to an additional 0.15 eV decrease in the ϕ value. Fig. 6.7 (b) shows the valence band edge of the samples from UPS spectra, and the inset shows the VB value of different structures. The valence band edge of the c-Si (reference sample) is approximately 1 eV below the Fermi level, which is typical for *n*-type silicon. The PEI film, on the other hand, has a valence band edge which is 3.20 eV lower than the Fermi level. We may then infer that the film shows an *n*-type character based on an optical gap of 5.3 eV and a valence band edge of 3.20 eV.

Compositional analysis can shed some light on the origin of the dipoles in the PEI layer. With this aim, Fig. 6.8 presents the XPS peaks corresponding to a PEI solution in ethanol, which indicate the presence of sp^3 hybridized nitrogen (N1s) that would correspond to quaternized (i.e., protonated) amino groups.
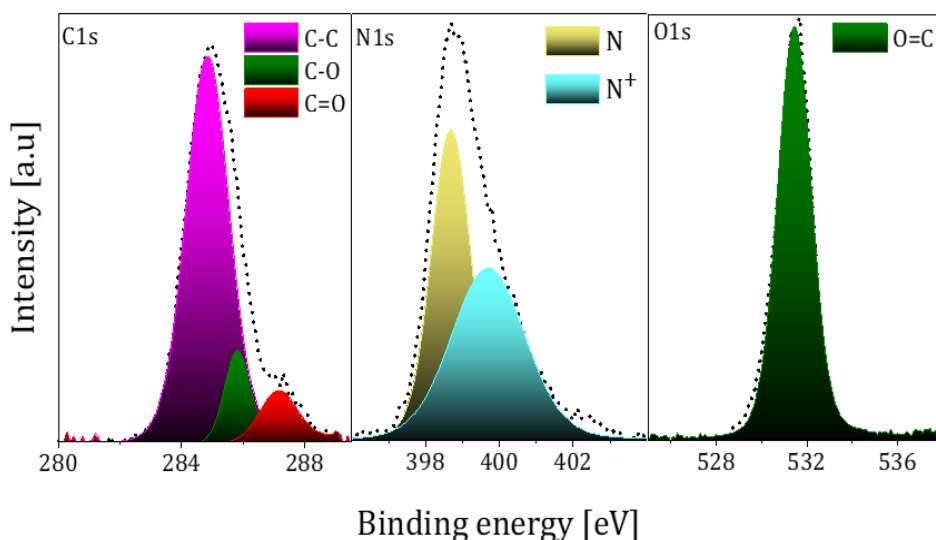
Figure 6.8: Deconvoluted XPS peaks of C1s, N1s and O1s from 1-nm thick b-PEI films. The measurements were performed on films deposited on c-Si substrates.

Carbon–oxygen bonds are also resolved in the C1s and O1s spectrum, which could be related to the presence of leftover solvent (i.e., ethanol) and derivatives. The presence of leftover solvent in a spin-coated film is not an unusual phenomenon [15][16]. The presence of the C–O signal is also consistent with the initial hypothesis of ethanol behaving as a Brønsted acid in the presence of PEI as a Lewis base. The protonated amino groups remain then electrostatically bound to the negative ethanolates, which would be part of the solvent that is not evaporated in the annealing step. The electronegativity of oxygen provides a negative charge density in the –OH group that increases in the ionic ethanolate form.

$$C_2H_5\text{-}OH + NH_2\text{-}R \longrightarrow C_2H_5O + NH_3\text{-}R$$
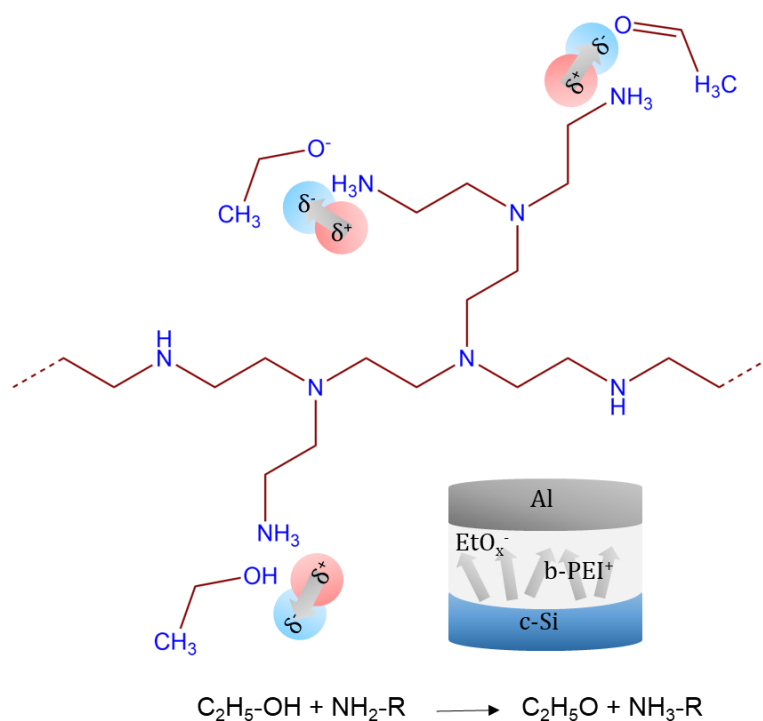
Figure 6.9: Schematic of the b-PEI dipole formation between the c-Si and the Al rear contact [9].

The presence of a double carbon–oxygen bond in the C1s XPS spectrum could be a sign of the alcohol oxidation into the corresponding aldehyde (i.e., ethaldehyde). This would be in line with the idea that ethanol is indeed protonating the amino groups of PEI. As a secondary reaction, some of the resulting ethanolates might thermalize to their aldehyde. Since both ionic groups in PEI^+ and EtO_x^- fulfill the octet rule, they can bind electrostatically to form an array of dipoles along the polymer chain (see Fig. 6.9). Such dipoles consist of quaternized amine groups and their counter-ion, which is a common phenomenon also observed in other CPs [17][18]. In this sense, ethanol has a larger pKa than methanol, i.e., it is a weaker Brønsted acid compared to methanol. Therefore, less protonated amino groups are expected to form in ethanol solutions. Consequently, a less dense dipole layer would explain the 0.15 eV difference in ϕ shift with respect to methanol solvent observed by UPS.

An HRTEM analysis was carried out on the Al/PEI/c-Si samples, as observed in Fig. 6.10. A carbon and oxygen-rich layer with a thickness lower than 1.5 nm could be resolved by energy-dispersive X-ray spectroscopy (EDS) [see Fig. 6.10 (a)], as inferred from the depth profiles corresponding to the C, Si, Al and O signals.

A slightly reduced thickness by approximately 0.5 nm is observed in HRTEM images compared to ellipsometry measurements (1 nm). This difference could be a consequence of using different sides of the silicon wafers (i.e., mechanical, and chemical polishing) for these experiments. The oxygen signal localized in the PEI layer is consistent with the XPS results, and therefore it would confirm the presence of leftover solvent within the layer. XPS results evidenced both single and double carbon–oxygen bonds that we have related to the formation of ethanolate and aldehyde groups after ethanol loses its proton. Fig. 6.10 (b) shows the original scanning HRTEM image of b-PEI between the c-Si substrate and Al. The same figure as well presents the 3D schematic of counterion condensation at PEI branches. The schematic representation of the energy band diagram with b-PEI as the interlayer, proposed on the basis of the determined band gap energy, work function and valence band edge, is shown in Fig. 6.11.

The b-PEI forms a thin dipole intelayer due to the protonated amines, as observed from Fig. 6.8 and Fig. 6.9. In turn, this dipole formation between semiconductor and external electrode leads to the reduction of the apparent metal work function (ϕ'_{Al}) with respect to its non-altered value (ϕ_{Al}) [Fig. 6.7 (b)]. Consequently, a significant charge transfer from Al to Si takes place that avoids Fermi level pinning at the surface.
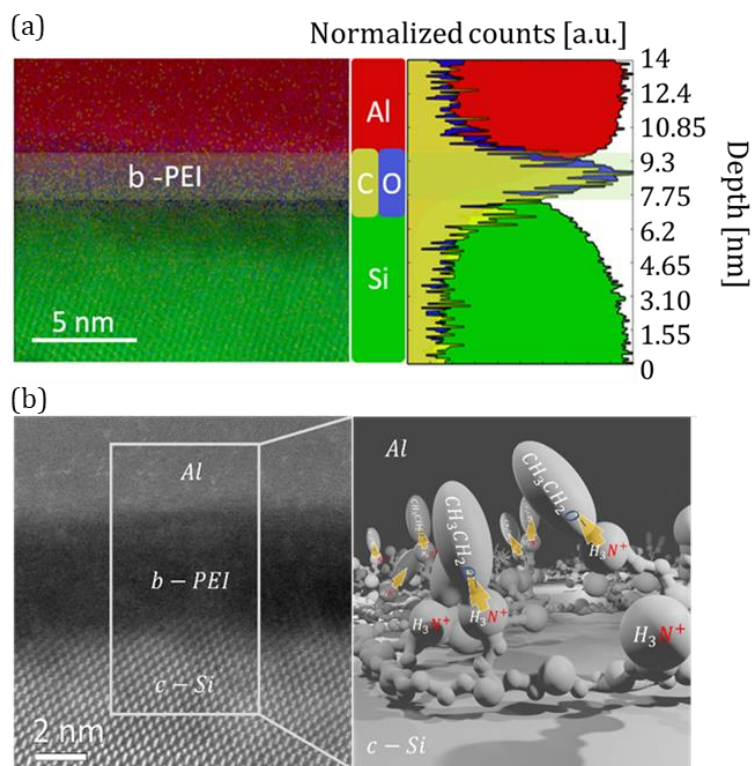
Figure 6.10: (a) HRTEM image superimposed with the EDS signal corresponding to aluminum, silicon, carbon, and oxygen, and depth profiles for each signal along the junction. (b) Original scanning HRTEM image with a 3D schematic of counterion condensation at PEI branches [9].
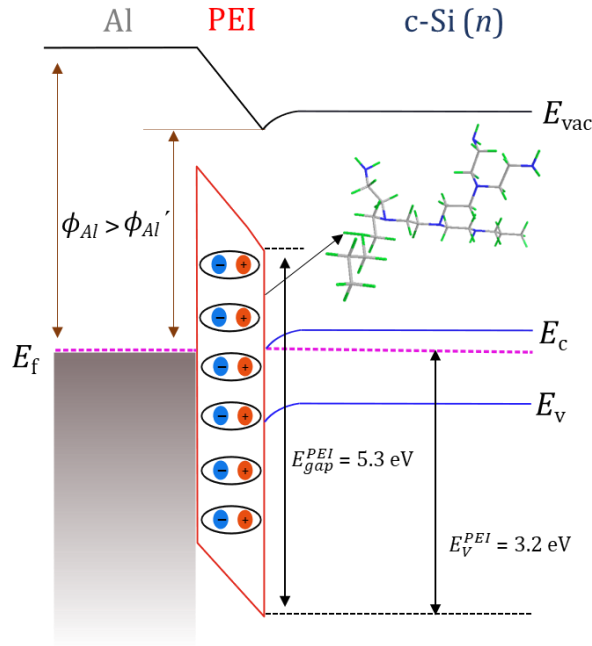
Figure 6.11: Energy band diagram corresponding to the c-Si/b-PEI/Al heterojunction.

6.2.3 Application to solar cells

To check the viability of PEI in a real photovoltaic device, the PEI-modified ETLs were used in a proof-of- concept dopant-free solar cell. The schematic representation of the fabricated device with b-PEI interlayer is shown in Fig. 6.12, whereas Fig. 6.13 shows the *J-V* curves under AM1.5 spectrum illumination of the fabricated devices and their corresponding external quantum efficiency. The obtained PV parameters are summarized in Table 6.1.

The solar cells with an aluminum silicon direct contact show rather low efficiency with a very poor V_{oc}, and low *FF* and J_{sc}. This bad performance can be very likely attributed to the so-called Fermi level pinning at the

semiconductor/metal junction. In contrast, a thin PEI interlayer results in higher FF and J_{sc} values, with an extensive V_{oc} increase of almost 270 mV.

On the one hand, the FF and J_{sc} improvement is consistent with the low contact resistance and passivation effect of PEI evidenced in TLM and QSSPC experiments. On the other hand, the V_{oc} difference could be explained by the passivation and elimination of FLP and interface energy barriers.
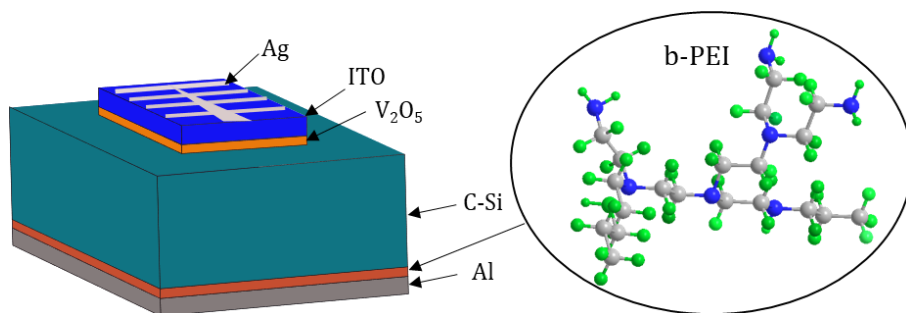
Figure 6.12: Schematic diagram of the fabricated devices containing b-PEI as interlayer. The inset shows the 3D schematic of the b-PEI molecule were grey atoms corresponds to C, blue to the N, and green corresponds to H.
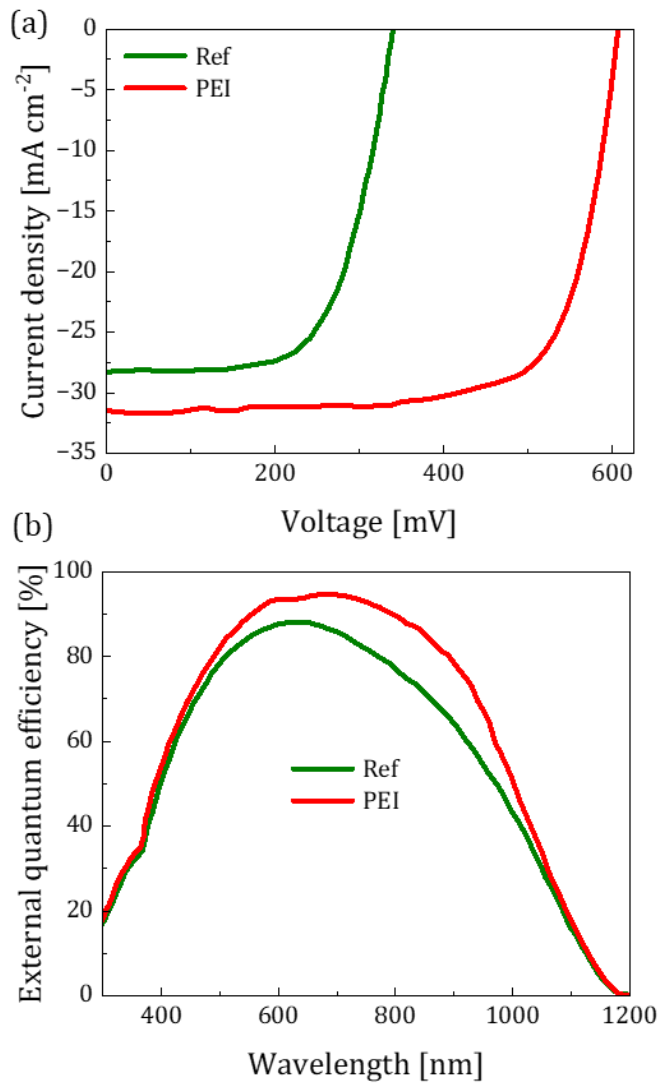
Figure 6.13: (a) *J*–*V* characteristics and (b) external quantum efficiency of the b-PEI based solar cell (in red) and the reference device without b-PEI interlayer (in green).

Table 6.1: *FF*, V_{oc}, J_{sc}, and *PCE* of the fabricated solar cell, as well as the non-containing b-PEI reference.

Structure of cells	*FF* (%)	V_{oc} (mV)	J_{sc} (mA cm^{-2})	*PCE* (%)
ITO/V$_2$O$_5$/c-Si/Al (Ref)	64.4	340	28.3	6.2
ITO/V$_2$O$_5$/ c-Si/b-PEI/Al	72.1	607	31.5	13.8

Overall, a *PCE* up to 13.8% could be achieved in dopant-free silicon solar cells with selective contacts, more than twice the performance of the reference device. In summary, the results hereby reported reveal that the efficiency and overall performance of Si heterojunction-based solar cells can be improved by introducing a dipolar layer based on b-PEI films between the semiconductor and the metal electrode, which promotes photogenerated carrier extraction. Moreover, the b-PEI films are deposited using a rapid and non-toxic approach, and processing this additional interfacial layer has no impact on the fabrication process in terms of time, thermal budget, and cost.

6.3 Poly(amidoamine) (PAMAM) dendrimer as ETL

Here the electrical, optical, morphological, and dipolar characteristics of solution-processed thin films of poly(amidoamine) (PAMAM) generation zero (G0) dendrimer is explored, whose molecular structure is shown in Fig. 6.14.
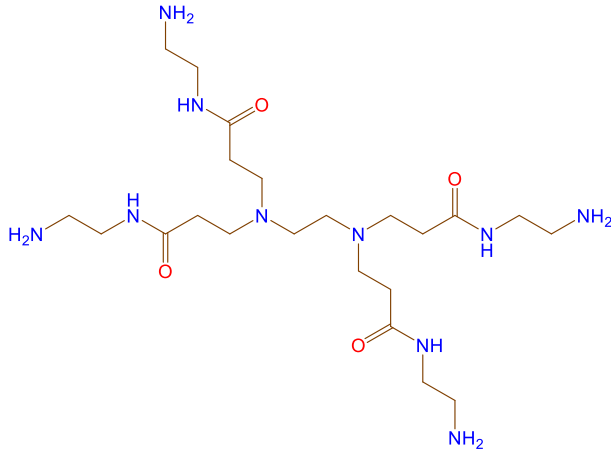
Figure 6.14: Schematic representation of generation 0.0 (G0) PAMAM dendrimer.

As a proof of concept, the PAMAM dendrimer is used as an electron selective contact on dopant-free heterojunction solar cell. The solar cell fabricated using this configuration achieved a *PCE* of 14.5%, which supposes significant enhancement with respect to the reference device without the PAMAM dendrimer interlayer.

6.3.1 Experimental method

PAMAM dendrimer of ethylenediamine core, generation 0.0 (G0), and dissolved in 20% methanol, with a linear formula $NH_2(CH_2)_2NH_2$, was purchased from Sigma Aldrich. Solutions containing different PAMAM dendrimer concentrations, from 0.1 to 0.001 wt %, were prepared using methanol as the solvent. One-side polished (FZ) *n*-type c-Si (100) wafers (thickness of 280 μm, resistivity of 2 Ω cm) and sapphire were used as substrates for various electrical and optical studies. The PAMAM dendrimer

solution was spin coated onto these substrates at 5000 rpm for 30 s and annealed in ambient air on a hot plate for 30 s at 90 °C. For the solar cell fabrication, a PAMAM dendrimer layer was spin coated onto a (non-texturized) *n*-type silicon wafer followed by ambient-air annealing for 30 s. Afterwards, Al was thermally evaporated onto the films as the rear electrode. ALD V_2O_5 was deposited as the front hole selective contact followed by sputtering of ITO layer as the transparent electrode. Finally, Ag was thermally evaporated using a shadow mask as the top grid.

6.3.2 Film properties

Different concentrations of the solution, from 0.001 wt % to 0.1 wt %, were studied, the concentration as a function of thickness being shown in Fig. 6.15. The thickness of the films was found to increase at higher solution concentrations from 0.2 nm to 4.5 nm.
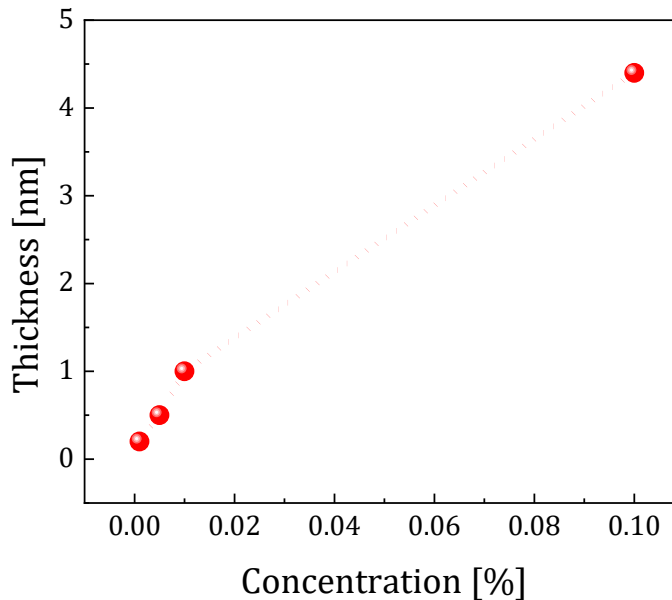
Figure 6.15: Thickness of the films vs. PAMAM concentration plot, the thickness of the films being measured on films grown on c-Si substrates.
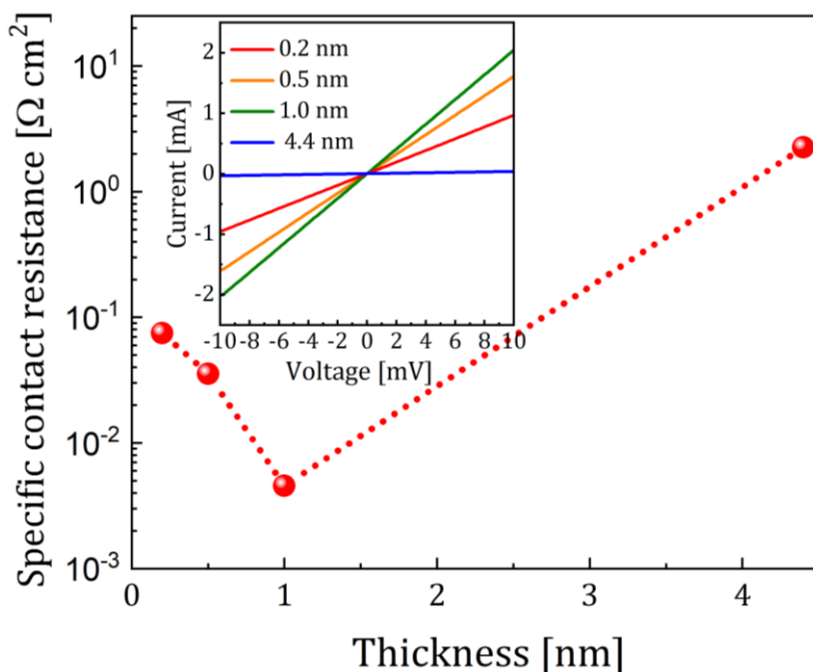
Figure 6.16: Specific contact resistance as a function of PAMAM thickness, as extracted from the TLM measurements. The inset displays the TLM contact schematics for the measurements.

The *I–V* characteristics of the PAMAM dendrimer films spin coated on *n*-type c-Si wafers were studied using the TLM method. The thickness relationship with the contact resistance of the films is plotted in Fig. 6.16, exhibiting an analogous behavior to b-PEI (see Fig. 6.3 in section 6.2.2). The inset shows linear *I–V* characteristics that demonstrate a good ohmic behavior for the films. The optimum contact resistance, of 4.5 mΩ cm², was obtained for the 1-nm-thick film with 0.01 wt % concentration. As in the case of PEI the contact becomes more resistive when increasing the film thickness, suggesting electron tunneling through the PAMAM dendrimer films as the dominating conduction mechanism. On the other hand, the increment in contact resistance below 1 nm indicates at least a secondary mechanism arising close to monolayer thickness. Therefore, the optimum thickness of 1 nm, at a concentration of 0.1 wt %, was chosen for the following studies.

The surface roughness of 1-nm-thick PAMAM dendrimer films on silicon substrates was studied by AFM, shown in Fig. 6.17. The RMS roughness of the film is estimated to be 0.09 nm. The low surface roughness and lack of extended sharp peaks indicates a good uniformity of the PAMAM dendrimer films and enhanced wettability over the Si surface.
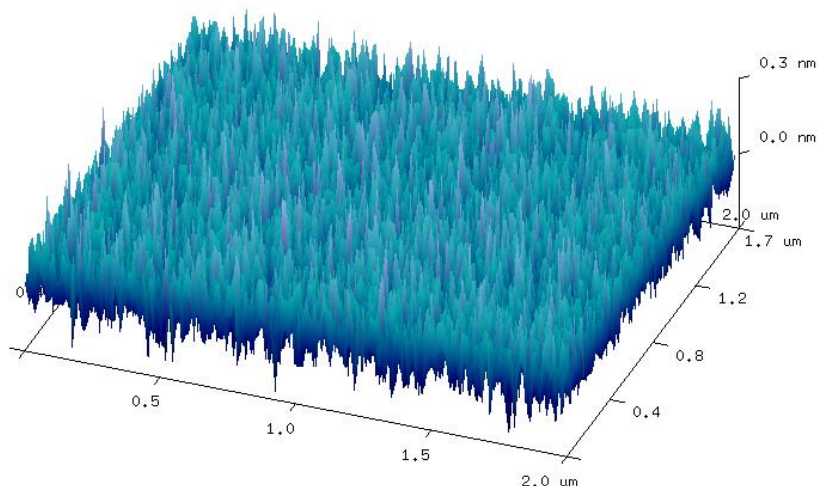
Figure 6.17: AFM image of the 1-nm-thick PAMAM film on c-Si (n) with RMS roughness of 0.09 nm. The measurements were performed on c-Si substrates.

Optical transmittance spectra were acquired from the films deposited on sapphire substrates. The results corresponding to the 1-nm-thick sample (200–1500 nm range) are shown in Fig. 6.18, exhibiting a high transmittance value over 95% throughout the spectrum. The inset shows the Tauc plot obtained from the transmittance data, with a calculated band gap of 4.7 eV. The high transparency and high direct band gap of the films contribute to their low absorption, making them more effective than traditional doped amorphous Si contacts.
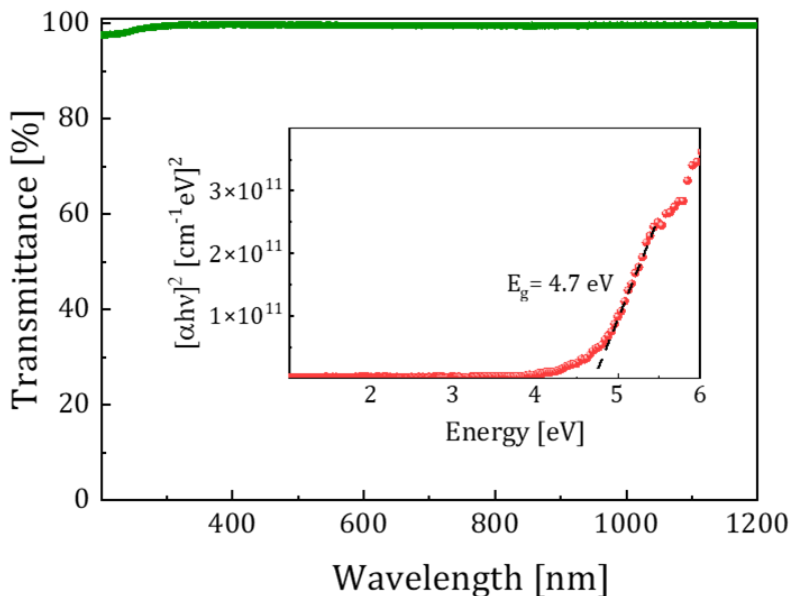
Figure 6.18: Transmittance spectra of the PAMAM films on sapphire substrate, ranging from 200 nm to 1500 nm. The inset shows the corresponding Tauc plot, showing a direct band gap energy of 4.7 eV. The measurements were performed on sapphire substrates.

The chemical analysis of the 1-nm-thick PAMAM dendrimer film on Si substrate was done using XPS. Fig. 6.19 displays the high-resolution C1s, N1s, and O1s XPS spectra. The C1s spectrum is fitted by four peaks at 283.5, 286.1, 287.4, and 289.4 eV. The first peak corresponds to C=C (sp² bonded carbons); the second peak can be assigned to C−C and C−O groups; the third peak is ascribed to acetyl C−O−C moieties and carbon-amide C−NH groups; finally, the fourth peak is attributed to carboxy O−C=O moieties. The O1s spectra could be fitted by two peaks at 532.1 and 533.5 eV, contributions respectively arising from C−O and C=O groups. N1s spectra with peaks fitted at 398.7 and 401.1 eV can be attributed to amines and charged amine moieties. The charged amine moieties represent the positively charged N atoms in the PAMAM dendrimer films with protonated amines occupying 93% of the area in the spectrum [4][7][19][20]. This protonated amine group plays a major role in charge transfer at the Al/PAMAM dendrimer/c-Si

interface. It forms a dipole layer at the interface with protonated nitrogen as the positive, and ethanolate from the counter ion condensation as the negative, counterpart. This occurrence was proved in our previous section 6.2 on polyethilimine.
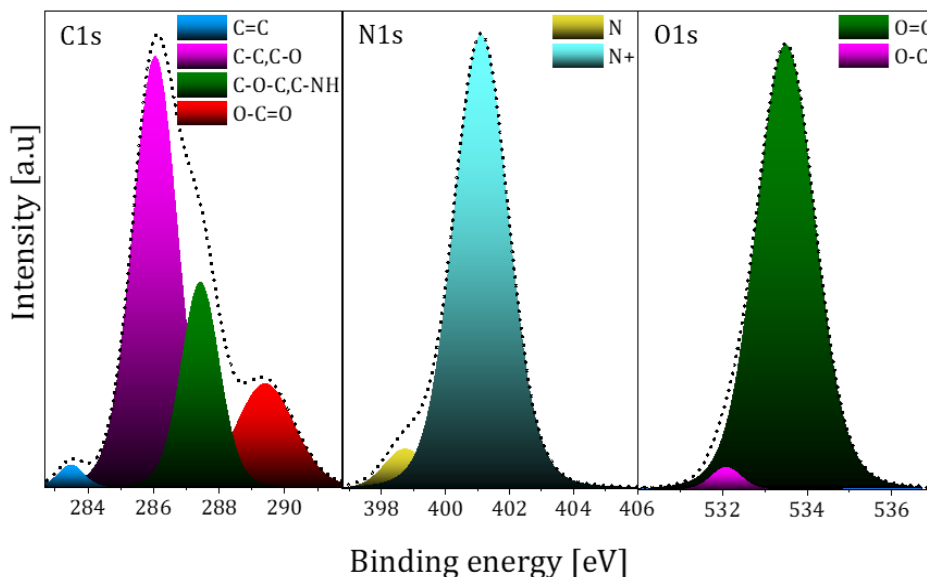
Figure 6.19: Deconvolved high-resolution XPS spectra of C1s, N1s, and O1s bonds, for1-nm-thick PAMAM dendrimer films grown on c-Si.

The ϕ and valence band position of the film were obtained using the UPS measurement shown in Fig. 6.20. The work function is obtained from Eq. 3.15. The thin PAMAM dendrimer film lowers the ϕ from the reference *n*-type silicon (4.28 eV) down to 3.69 eV, in good accordance with the expected value in the literature [21]. This tuning of the apparent work function at the interface explains the formation of an ohmic contact and the resulting low specific contact resistivity. The work function shift also indicates the direction of the dipole formation with negative end pointing towards the electrode, and the positive end pointing towards the silicon substrate.
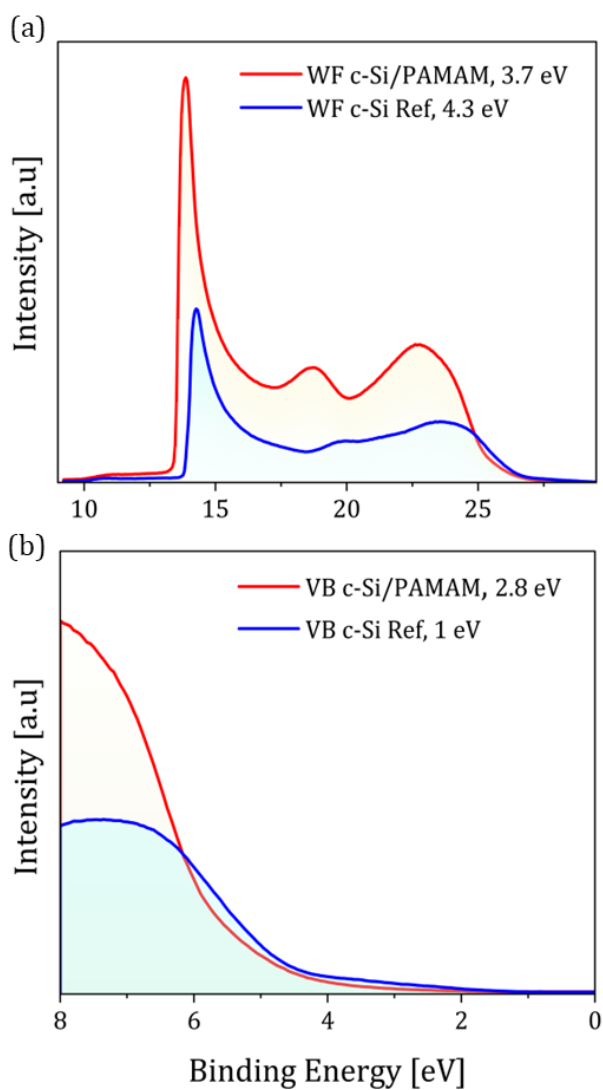
Figure 6.20: Analysis on the UPS spectra of 1-nm-thick PAMAM films carried out to determine a) the work function and b) the valence band from both silicon reference (in blue) and c-Si/PAMAM films (in red).

The valence band edge of the c-Si (reference sample) is approximately 1 eV below the Fermi level, which is typical for *n*-type silicon. The PAMAM dendrimer film, on the other hand, has a valence band edge which is 2.8 eV lower than the Fermi level. We may then infer that the film shows an *n*-type character based on an optical gap of 4.7 eV and a valence band edge of 2.81 eV. Thus, the capability of the PAMAM dendrimer films to form the ohmic contact and the *n*-type character makes it a promising candidate as electron selective contact in heterojunction solar cells. The schematic representation of the energy band diagram with PAMAM dendrimer as the interlayer, proposed on the basis of the determined band gap energy, work function and valence band edge, is shown in Fig. 6.21.
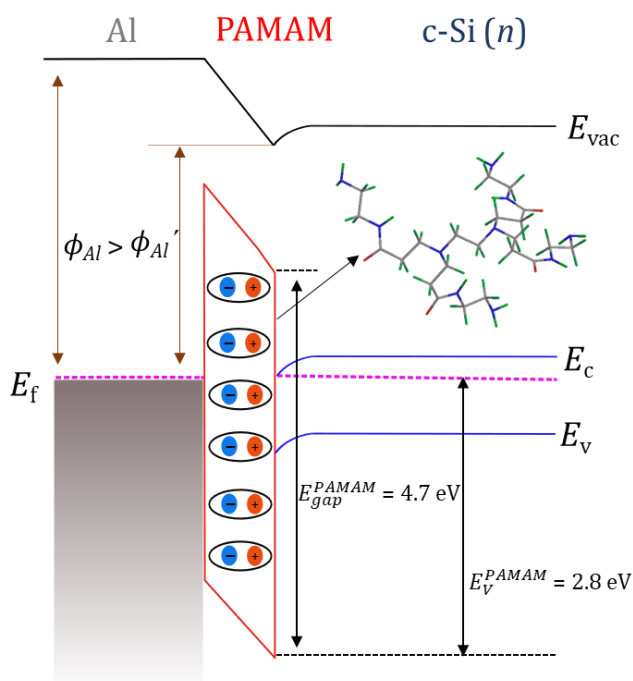
Figure 6.21: Energy band diagram corresponding to the Si/PAMAM dendrimer/Al heterojunction.

The PAMAM dendrimer forms a thin dipole intelayer due to the protonated amines, as observed from the XPS deconvolved spectra (Fig. 6.19). In turn,

this dipole formation between semiconductor and external electrode leads to the reduction of the apparent metal work function (ϕ'_{Al}) with respect to its non-altered value (ϕ_{Al}). Consequently, a significant charge transfer from Al to Si takes place that avoids Fermi level pinning at the surface.

6.3.3 Application to solar cells

Finally, as a proof of concept, a PAMAM dendrimer (1 nm)/Al selective electron contact was integrated into a 1×1 cm^2 doping-free heterojuntion silion solar cell. The schematic of the fabricated device is shown in the Fig. 6.23, with an ITO/V_2O_5/c-Si/PAMAM dendrimer/Al structure. A reference device was also fabricated without the PAMAM dendrimer to show the superior performance of the solar cell incorporating a PAMAM dendrimer dipole interlayer. Fig. 6.24 shows the *J–V* curves of both cells measured under 1 Sun illumination, and an overview of photovoltaic parameters of the solar cells is presented in Table I.
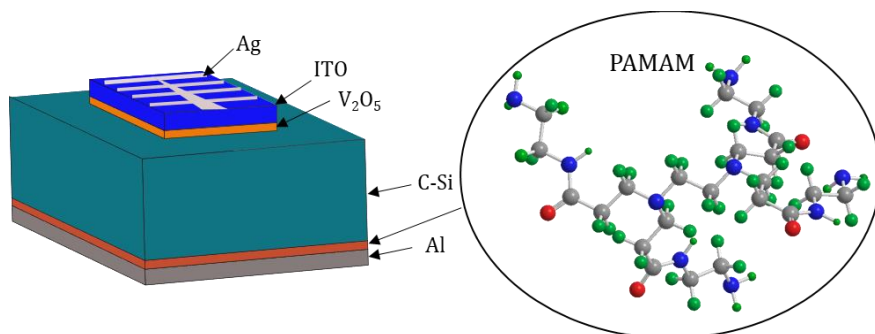
Figure 6.22: Architecture of the employed *n*-type silicon heterojunction cell integrated with a PAMAM dendrimer interlayer as electron selective contact. The inset shows the 3D schematic of the PAMAM dendrimer molecule where grey atoms corresponds to C, blue to the N, red to O, and green corresponds to H.

The massive 260 mV improvement in the V_{oc} of the PAMAM dendrimer-based solar cell compared to the reference one may be attributed to the reduced barrier energy at the interface due to the formation of an ohmic contact. Additionally, the elimination of Fermi level pinning and decrease of contact resistance contribute to increase the *FF*.
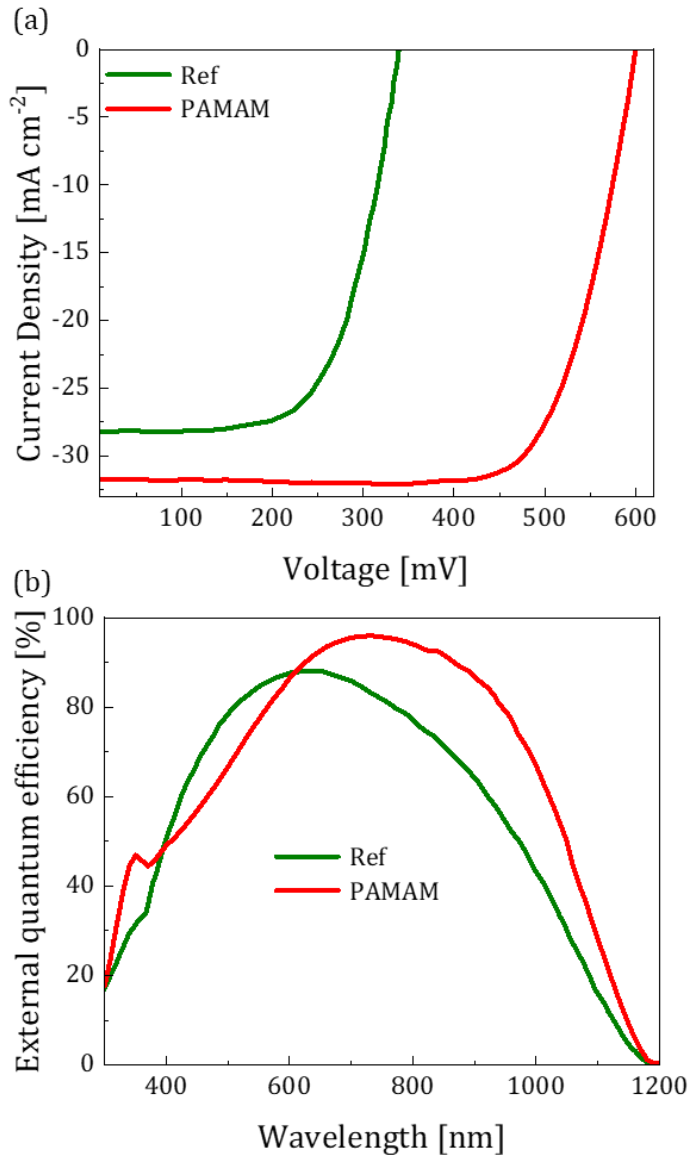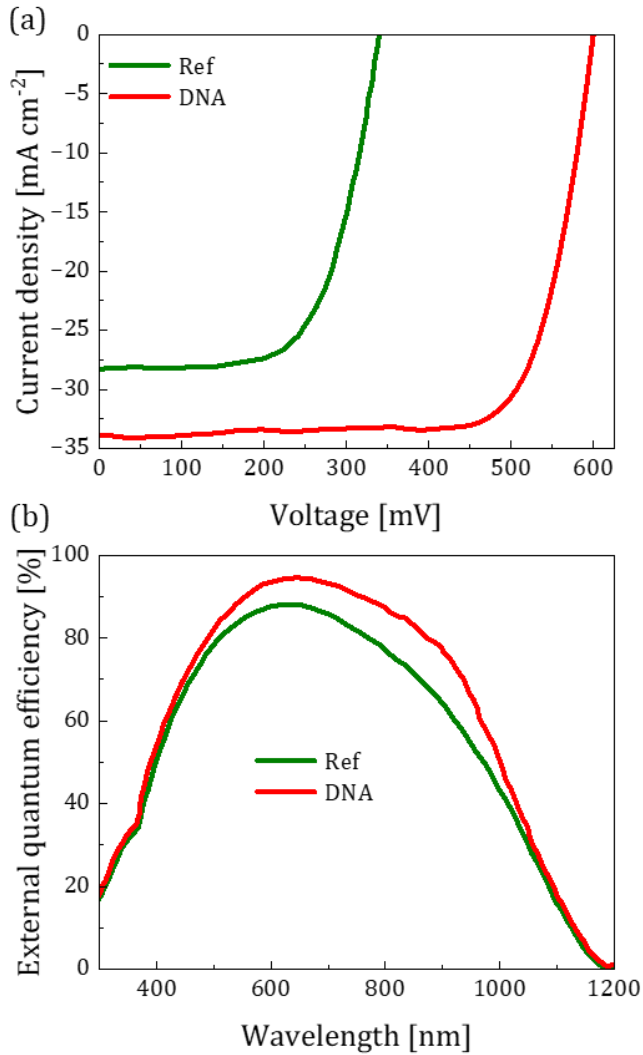
Figure 6.23: (a) *J–V* characteristics and (b) external quantum efficiency of the PAMAM dendrimer-based solar cell (in red) and the reference device without PAMAM dendrimer interlayer (in green).

The PAMAM dendrimer-based solar cells have shown an enhanced *FF* over 76.2%, whereas the reference device exhibits an *FF* of only 64.4%. The 3.4 mA cm^{-2} increase in J_{sc} in PAMAM dendrimer cells could be probably attributed to the Fermi level depinning and hence the improved surface passivation of silicon. Finally, the PAMAM dendrimer-based solar cells have shown a *PCE* of 14.5%, more than twice the performance of the reference device.

Table 6.2: *FF*, V_{oc}, J_{sc}, and *PCE* of the fabricated solar cell, as well as the non-containing PAMAM dendrimer reference.

Structure of cells	*FF* (%)	V_{oc} (mV)	J_{sc} (mA cm^{-2})	*PCE* (%)
ITO/V$_2$O$_5$/c-Si/Al (Ref)	64.4	340	28.3	6.2
ITO/V$_2$O$_5$/ c-Si/PAMAM/Al	76.2	600	31.7	14.5

In conclusion, the obtained results demonstrate that introducing the PAMAM dendrimer as a dipole interlayer between the semiconductor and the metal electrode improves the performance of the solar cell by lowering the metal work function and thereby suppressing the Fermi level pinning. As observed, the solar cell devices under study, containing the PAMAM dendrimer interlayer as the electron selective layer, have doubled the efficiency with respect to the unmodified reference device. Ultimately, this work demonstrates the promising potential of dipole interlayers in optoelectronic devices whose performance (in this case, due to photocarrier extraction) can be improved via interface and energy band engineering.

6.4 Deoxyribonucleic acid (DNA) as ETL

In this section we explore deoxyribonucleic acid (DNA)-based polymer as the ETL in combination with a c-Si absorber. The schematic representation of double helical structure of DNA is shown in Fig. 6.24. A thorough study of the optical, electrical, and compositional properties of the used DNA layers, as well as the electronic effect of these layers on the silicon interface, has been carried out. Finally, the material has been successfully implemented in a non-textured dopant-free solar cell to test the performance of the contact in a finished device, obtaining a *PCE* of 15.6%.
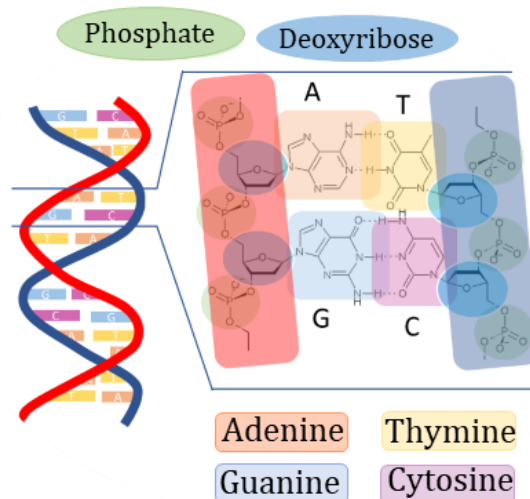
Figure 6.24: Double helical structure of DNA with four types of nitrogen bases: adenine (A), thymine (T), guanine (G), and cytosine (C) [10].

6.4.1 Experimental method

Low-molecular weight DNA biopolymer was used as the electron selective contact for crystalline silicon solar cells. The DNA, which was extracted from the sperm of salmon fish, is soluble in water–methanol solution [28].

DNA solutions of different weight percentages were prepared using 9 mL of anhydrous methanol and 1 mL of deionized water. First, DNA fibers were dissolved in deionized water and the solution was stirred until total transparency. Afterwards, anhydrous methanol was added to the mixture to achieve the required concentration. The solution was stirred overnight and filtered using the sterile disposable Polyvinylidene Fluoride (PVDF) 0.22-μm vacuum filter unit.

These solutions were spin-coated on silicon substrates at 5000 rpm for 30 s to produce films, which were kept overnight in a glove box with nitrogen atmosphere. All the silicon substrates used were non- textured, one-side polished (FZ) n-type c-Si (100) wafers with a thickness of 280 μm and a resistivity of 2 Ω cm.

The proof-of-concept devices were fabricated on n-type FZ c-Si wafers. The 1 wt % of the DNA solution was spin-coated on the rear side of the wafer at 5000 rpm for 30 s, and the wafers were kept in a glove box for overnight drying. Subsequently, the rear Al electrode was thermally evaporated on the back side of the wafer. V_2O_5 hole selective layer was thermally evaporated on the front side of the wafer and the active area was defined by photolithography. Next, an ITO layer was deposited by sputtering. Finally, after insulation of the devices by wet etching, a 2-μm-thick silver grid was thermally evaporated using a shadow mask as the top contact. The reference device was also fabricated using the same process, but without DNA on the rear side electrode.

6.4.2 Film properties

The DNA films used in this study were deposited on n-type c-Si by spin coating using solution concentrations ranging between 0.5 wt % and 2 wt % in 0.5 wt % steps. The thickness of the film was 1.5 nm for the least concentrated 0.5 wt % solution. It steadily increased to 2.5 nm for 1 wt %, 3.3 nm for 1.5 wt % and, finally, 5.1 nm for the highest 2 wt % concentrated solution. The thickness versus concentration plot follows a linear behavior, as shown in the Fig. 6.25.
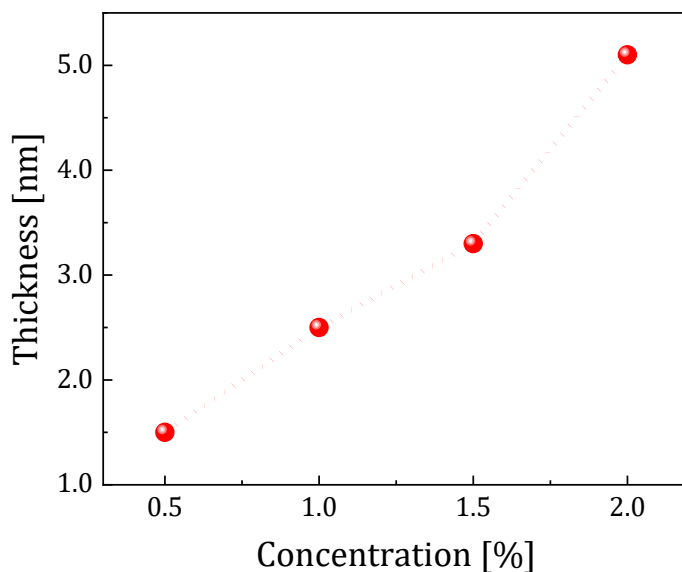
Figure 6.25: Thickness *vs.* concentration plot of the DNA films deposited on silicon.

Subsequently, Al contacts were deposited on the DNA layers to characterize their electrical properties via the TLM method. The inset in Fig. 6.26 shows the *I–V* characteristics of (*n*) c-Si/DNA/Al structures with DNA thickness between 1.5 and 5.1 nm. In the TLM study, the specific contact resistance can be extracted from measurements varying the intercontact distance. These values are shown in Fig. 6.26 for all the DNA films. The linear *I–V* characteristics demonstrate a good ohmic behavior for the DNA films on silicon (see inset in Fig. 6.26). According to these results, an optimal ohmic contact is obtained for the 2.5-nm-thick DNA film with a contact resistance of only 28 mΩ cm^2.

The presence of an optimum contact resistance at an intermediate DNA film thickness suggests that different effects need to be considered. Indeed, increased contact resistance at thicker layers is expected due to a more difficult electron transport through the organic polymer.
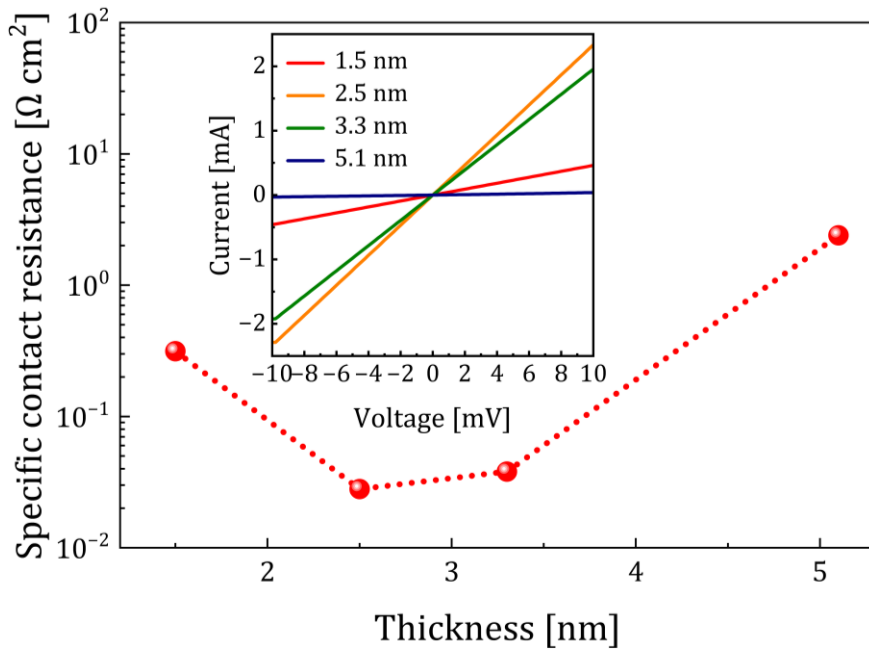
Figure 6.26: Specific contact resistance of c-Si/DNA/Al stack as a function of the DNA film thickness. The inset shows the *I–V* characteristics of the c-Si/DNA/Al stack with DNA film thickness ranging from 1.5 to 5.1 nm.

However, the increase of contact resistance for the thinnest layer indicates that the polymer beneficial effect vanishes. Probably, Fermi level pinning at the silicon surface starts to occur as for direct metal–semiconductor contacts. This V-shaped contact resistance curve with an optimal thickness in electron tunneling range resembles the behavior of other selective contacts using ultra-thin intermediate dielectrics, such as PEI, PAMAM, magnesium oxide (MgO) or magnesium fluoride (MgF$_2$) that also operate in similar thickness ranges [11][22][23].

The topography of the DNA films was studied by AFM. The image corresponding to the sample with 2.5-nm-thick DNA film is displayed in Fig. 6.27. The image shows rather smooth films deposited uniformly. The RMS roughness for the 2.5-nm-thick DNA film was only 0.3 nm. The roughness does not seem to increase much with the thickness, since for the 5.1-nm-

thick film (not shown here) it was 0.4 nm. The quite similar RMS values indicate a similar structure of the films for both thicknesses. The lack of extended sharp peaks is probably associated to the amorphous structure of the film, which is preserved at different thicknesses. The results suggest an excellent wetting of the DNA solutions on the silicon surface, therefore allowing a uniform coverage over the surface.
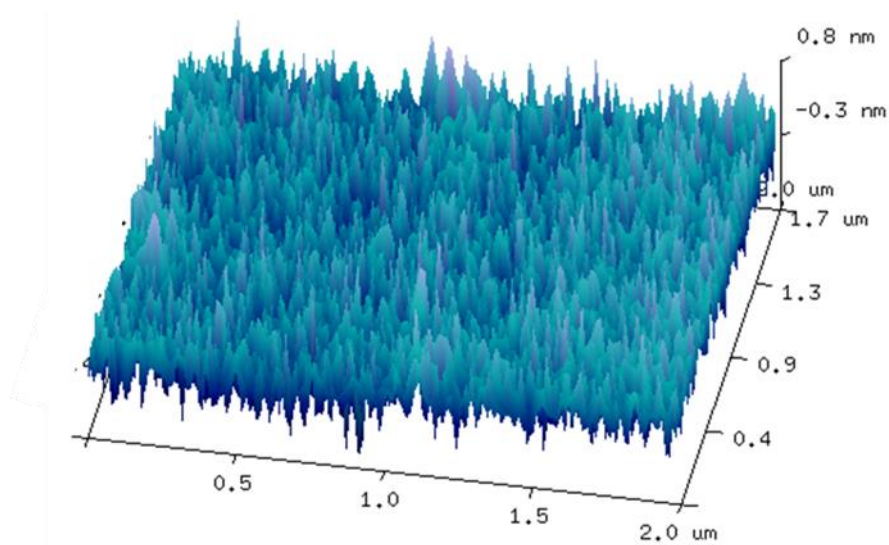
Figure 6.27: AFM image of the 2.5-nm-thick DNA film grown on c-Si substrates.

The study of the DNA optical properties was carried out by means of UV–visible–NIR optical spectroscopy, which in turn gives information concerning the bandgap energy. The transmittance spectrum within the 180–1500 nm range corresponding to the 2.5-nm-thick DNA film (1 wt % solution) can be seen in Fig. 6.28. All the films show more than 95% transmittance throughout the spectral regions other than in UV and visible-blue. The inset in Fig. 6.28 shows the Tauc plot obtained from the transmittance data, with an estimated bandgap of 4.13 eV [24][25]. In this absorption plot, defined peaks at 242 nm (5.12 eV) and 266 nm (4.66 eV) are clearly seen, which have been reported throughout the literature and are generally associated to the nucleic acids and their purity [26][27]. Because

of the large bandgap, the high transparency in the visible and infrared regions makes these films a suitable option also for transparent contacts.
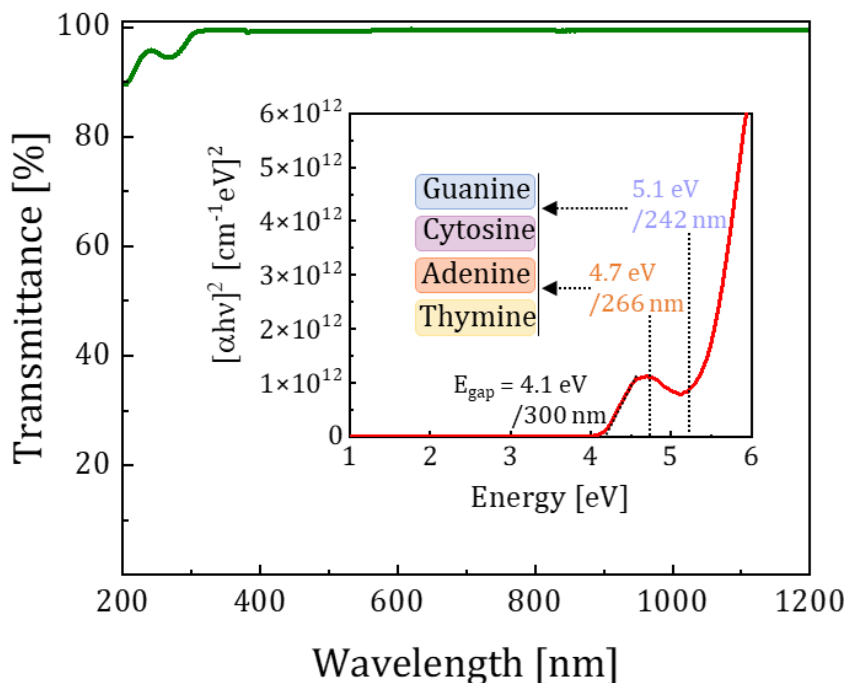
Figure 6.28: Transmittance spectrum corresponding to the sample containing 2.5-nm-thick DNA 1 wt % films. The inset shows the Tauc plot for the same sample, indicating the bandgap energy.

Chemical analysis through XPS allowed for the characterization of the four principal elements (C1s, O1s, N1s, P2p) of DNA, whose spectra corresponding to the thickest sample are presented in Fig. 6.29. The main C1s spectrum shows the characteristics of different nucleobases present in the DNA molecule; peaks at 288.9, 287.9, 286.5, and 284.9 eV correspond to urea, amide, carbon bond to nitrogen, and hydrocarbons, respectively, which represent the main electronic configurations along the double stranded structure. The largest peak of the O1s at 532.5 eV corresponds to the oxygen bond to a phosphate group, whereas peaks at 533.1 and 531.1 eV are ascribed to C=O and metal carbonate peaks, respectively.
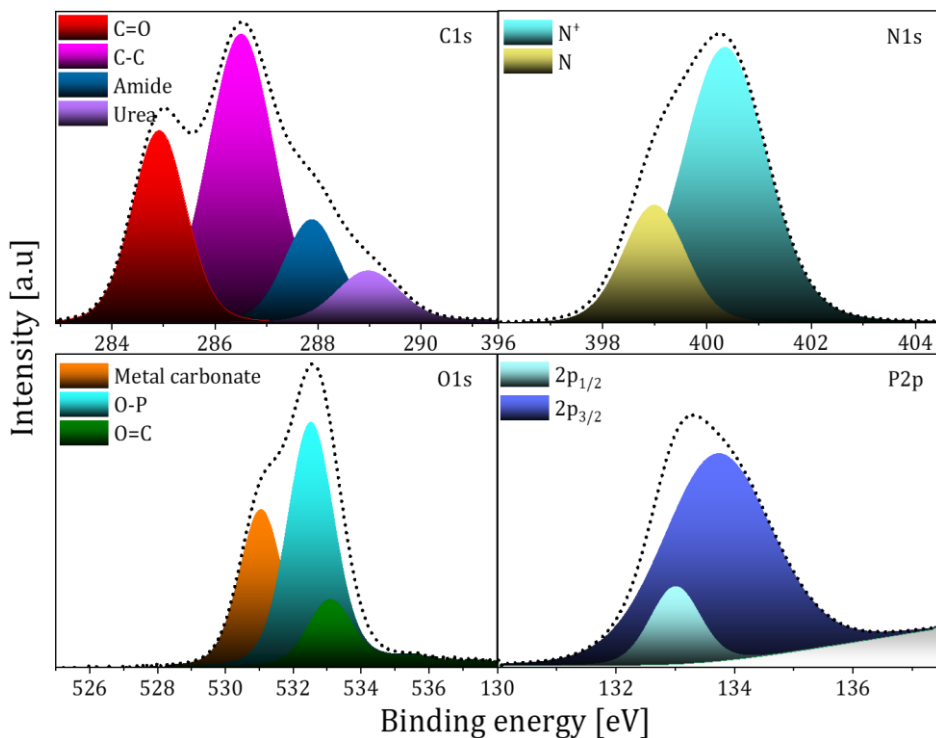
Figure 6.29: High-resolution XPS spectra corresponding to the four main observable elements in 5.1-nm-thick DNA films.

In high concentration of DNA films (5.1 nm) the phosphate peak is highly appreciated and the P2p peak of the phosphate group has been deconvoluted into two subpeaks with the main $2p_{3/2}$ component at 133.7 eV and $2p_{1/2}$ at 133.0 eV, with a splitting value of 0.7 eV. Phosphorus signal indicates the presence of the phosphate groups along the polymer. The principal nitrogen N1s signal has been deconvoluted into two major peaks: one at 399.0 eV, which represents the contribution of N atoms in the double bonds with C (N), and another at 400.3 eV, attributed to the N singly binding with C and H, and the protonated N peaks (N^+). Such positively charged N atoms lead to charge transfer across the interlayers that could explain dipole formation in DNA films [7][28][29].

UPS analysis was also carried out to get a further understanding on the electronic properties of the DNA films on silicon (Fig. 6.30). From the spectra, the ϕ, which is the energy required to extract an electron from the material to the vacuum level (i.e., null potential energy), can be calculated. Whereas the ϕ of the reference n-type silicon is 4.28 eV, in good agreement with the expected value [21], a thin DNA film reduces the calculated ϕ down to 3.28 eV [see Fig. 6.30(a)].

This suggests that DNA is playing a relevant role to tune the apparent interface work function, allowing for a specific charge carrier to be injected or extracted. These interface properties of thin DNA films can be used to explain the low specific contact resistance of the films on silicon obtained by TLM (Fig. 6.26). The DNA films would depin the Fermi level from the Si surface to enhance, in our case, electron injection and extraction from the semiconductor. This property could be used in semiconductor devices as an interface modifier to promote the charge-carrier selectivity at the electrodes. As a preliminary conclusion, DNA films exhibit good potential to be used as an ETL selective contact for silicon heterojunction devices.

On the other hand, UPS allows determining the valence band edge of the material. The valence band energy edge obtained for both silicon reference and DNA films on silicon are represented in Fig. 6.30(b). One can see that the valence band edge of the reference sample is about 1 eV below the Fermi level, as expected for n-type silicon.

On the other hand, the valence band edge is about 3.2 eV below the Fermi level for the DNA film. Considering an optical gap of 4.13 eV with the valence band edge at 3.2 eV, we can deduce some sort of n-type character for the DNA films [30][31]. Such n-type behavior of the DNA films may be beneficial in the heterojunction for electron extraction. However, since the conduction band edge (lowest unoccupied molecular orbital –LUMO–) of the film is still about 0.9 eV higher than the silicon conduction band edge, we do not expect any significant charge transport via thermionic emission at room temperature. Instead, electron extraction could take place via either hopping within the layer or other conduction mechanisms, such as direct or trap-assisted tunneling.
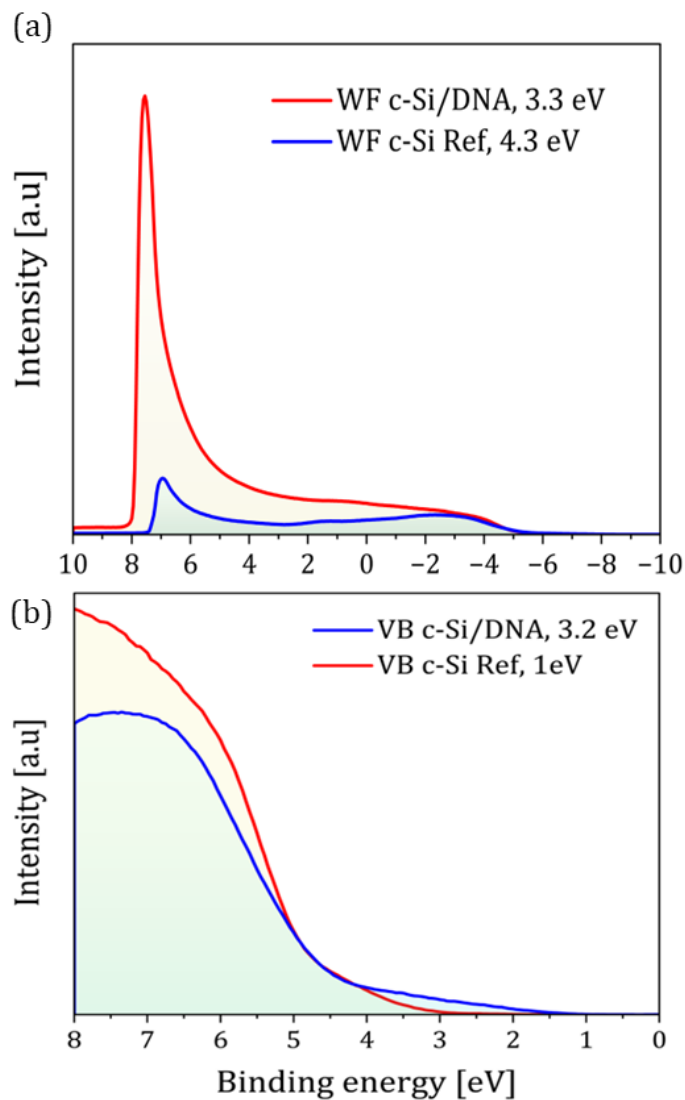
Figure 6.30: Analysis on the UPS spectra carried out to determine a) the work function and b) the valence band corresponding to silicon (in blue) and 2.5 nm DNA films (in red).

In order to visualize these results, we can propose a band diagram on the basis of the work function values and valence band edges estimated from UPS measurements shown in Fig. 6.30. This energy band diagram, displayed in Fig. 6.31, can be used to suggest a possible explanation to the good electron transport of c-Si/DNA/Al heterojunctions.
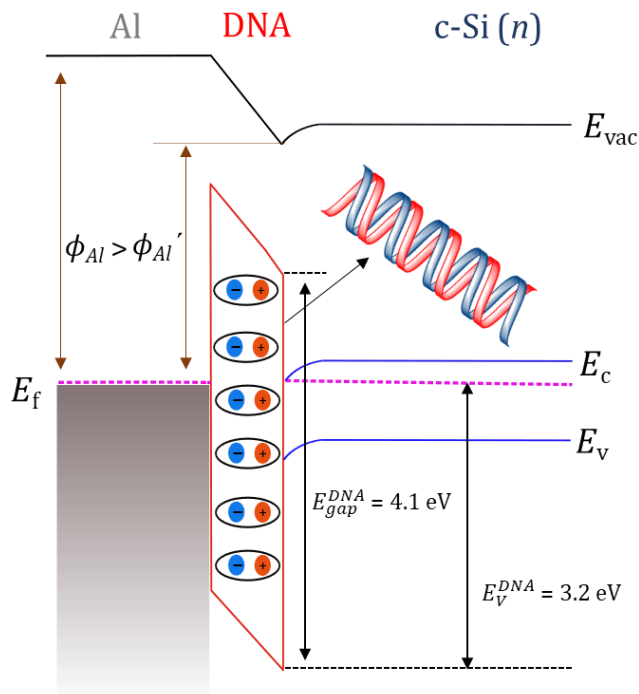
Figure 6.31: Energy band diagram corresponding to the Si/DNA/Al heterojunction under study.

The DNA film would behave as a thin dipolar interlayer, whose origin might be related to the phosphate and amino groups registered in the deconvolution of XPS spectra. The dipole formation between the semiconductor and an external electrode results in a vacuum level shift with an apparent reduction of the metal work function. As a consequence, an important charge transfer from the Al electrode to Si is expected. This effect would counteract Fermi level pinning and result in a region with majority

carrier accumulation [22][32]. This electron doping of the Si surface is in good agreement with the reduction of specific contact resistance observed in TLM measurements (see Fig. 6.26).

On the other hand, the electron extraction through the LUMO level of the DNA film is not possible as there is a roughly 0.7 eV barrier. The most plausible conduction mechanisms through the junction must be either direct or trap-assisted tunneling. This agrees with the need of an extremely thin layer to have a low contact resistance, as seen in the TLM measurements.

6.4.3 Application to solar cells

Finally, a photovoltaic device was fabricated to evaluate the performance of DNA implemented as an ETL at the corresponding electrode. The complete heterojunction solar cell structure was $ITO/V_2O_5/c$-$Si/DNA/Al$ with an active area of 1×1 cm^2. A schematic diagram of this dopant-free device architecture is presented in Fig. 6.32.
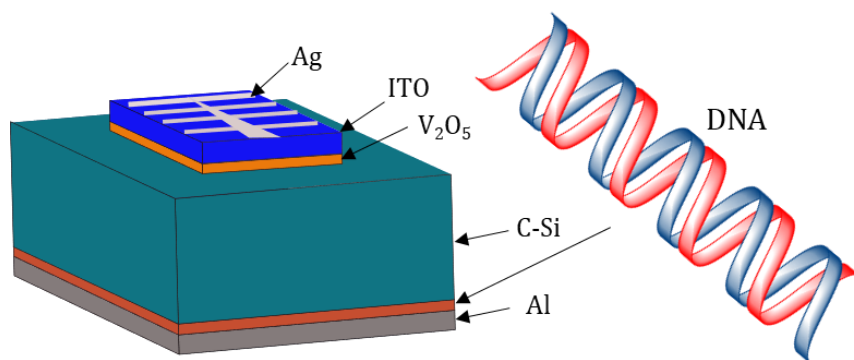
Figure 6.32: 3D sketch of the fabricated device with DNA as ETL.

The solar cell was fabricated on a flat c-Si wafer, thus there is room to increase the current density up to 4 mA cm^{-2} when using texturized substrates. Thermally evaporated V_2O_5 was used as the HTL and neither passivating layers nor doped a-Si:H layers were used in the whole heterojunction device.

On top of the HTL, an ITO layer was sputtered as the front transparent electrode with a sheet resistance of 120 Ω/sq. The top contact was finished with a 1.5-μm-thick Ag metallic grid. As the rear contact, optimized DNA films of 2.5 nm (1 wt % solution) where spin-coated on top of HF-cleaned silicon and covered with an evaporated Al layer of 500 nm.

Fig. 6.33(a) compares the J–V characteristics under AM1.5 illumination of Si heterojunction solar cells with and without the rear DNA layer. The corresponding photovoltaic parameters of these solar cells are summarized in Table 3 and their corresponding external quantum efficiency curves are shown in Fig. 6.33(b).

The solar cell implementing the DNA-based ETL exhibited a remarkable increase in the FF of over 12% with respect to the reference device without such interlayer. The high FF value up to 76.7% could be linked to the elimination of Fermi level pinning as well as a reduced contact resistance by electron accumulation.

Moreover, the V_{oc} is also substantially increased from 340 to 600 mV. The low V_{oc} value of the reference solar cell suggests the presence of an interface energy barrier. Consequently, part of the internal quasi-Fermi level separation would be lost at the rear electrode for electron extraction.

Finally, an increase of about 5 mA cm^{-2} in the J_{sc} has been also observed, probably related to the surface passivation provided by the effect of the DNA layer (carrier recombination time of 275 μs). As a result of all the exposed arguments, the PCE of the DNA-based solar cell exceeded 15%, thus more than doubling that of the reference device.

Figure 6.33: (a) *J–V* characteristics and (b) external quantum efficiency of the DNA-based solar cell (in red) and the reference device without DNA interlayer (in green).

Table 6.3: *FF*, V_{oc}, J_{sc}, and *PCE* of the fabricated solar cell, as well as the non-containing DNA cell as reference.

Structure of cells	*FF* (%)	V_{oc} (mV)	J_{sc} (mA cm^{-2})	*PCE* (%)
ITO/V$_2$O$_5$/c-Si/Al (Ref)	64.4	340	28.3	6.2
ITO/V$_2$O$_5$/ c-Si/DNA/Al	76.8	600	33.8	15.6

In summary, the results hereby reported reveal that the efficiency and overall performance of Si heterojunction-based solar cells can be improved by introducing a dipolar layer based on DNA films between the semiconductor and the metal electrode, which promotes photogenerated carrier extraction. As well, processing of such additional interfacial layer does not affect the fabrication process in terms of time, thermal budget or cost, given that the DNA films deposition is done via a fast and non-toxic technique.

6.5 Conclusions

In the first section, we have used branched polyethylenimine as a polymeric selective contact in crystalline silicon metal/insulator/semiconductor junctions. According to TLM measurements, the contact resistance is optimum for a PEI layer thickness around 1 nm. UPS results evidence that PEI can shift the electrode ϕ by approximately 1 eV. XPS results indicate that the amine groups present in the polymer are partially protonated due to the presence of N$^+$ signal in the nitrogen spectrum. Full dopant-free solar cells with 13.8% efficiency have been demonstrated with PEI modification at the contact. The improved *FF* can be explained by an important reduction of the contact resistance and the elimination of energy barriers from undesired Fermi level pinning.

The next section demonstrates the efficient usage of PAMAM dendrimer as a dipole interlayer that functions as a passivating ETL in heterojunction silicon solar cells. TLM measurements for 1.1-nm-thick PAMAM dendrimer with Al on c-Si substrate showed an exceptionally low specific contact resistance. The XPS study of the films revealed the presence of protonated nitrogen, which contributes to the creation of the interlayer dipole. The UPS measurements demonstrate the *n*-type behavior of the PAMAM dendrimer films. Ultimately, the devices with PAMAM dendrimer layer as the ETL exhibited an efficiency of 14.5%, higher than in the reference device.

In the final section, deposition and characterization of thin DNA films and their use in a metal/semiconductor junction as a buffer layer to provide enhanced electron injection/extraction (ETL) is demonstrated. XPS analysis further proved the presence of all expected organic compounds of DNA in the deposited thin films. The reduction of the electrode work function might be the main working principle of the DNA films, as it promotes electron migration from the metal into silicon. The resulting proof-of-concept solar cell achieved an efficiency higher than 15.6%, with a remarkable improvement in all the photovoltaic parameters.

In conclusion, a significant improvement of electron transport in solar cells fabricated with an organic buffer layers has been confirmed. Furthermore, the possibilities of using thin organic thin films for enhanced electron transport in different electronic devices go far beyond the photovoltaic applications and should be considered as an interesting technology route.

References

[1]   P.H. Liu, C.H. Chuang, Y.L. Zhou, S.H. Wang, R.J. Jeng, S.P. Rwei, W. Bin Liau, L. Wang, Conjugated polyelectrolytes as promising hole transport materials for inverted perovskite solar cells: Effect of ionic groups, J. Mater. Chem. A. 8 (2020) 25173–25177. https://doi.org/10.1039/d0ta09063h.

[2]   Z. Zhang, J.T. Yates, Band bending in semiconductors: Chemical and physical consequences at surfaces and interfaces, Chem. Rev. 112 (2012) 5520–5551. https://doi.org/10.1021/cr3000626.

[3]   T. Tom, E. Ros, N. López-Pintó, J. Miguel Asensi, J. Andreu, J. Bertomeu, J. Puigdollers, C. Voz, Influence of Co-Sputtered Ag:Al Ultra-Thin Layers in Transparent V_2O_5/Ag:Al/AZO Hole-Selective Electrodes for Silicon Solar Cells, Materials (Basel). 13 (2020) 4905. https://doi.org/10.3390/ma13214905.

[4]   B.B. Karakoçak, J. Liang, S. Kavadiya, M.Y. Berezin, P. Biswas, N. Ravi, Optimizing the synthesis of red-emissive nitrogen-doped carbon dots for use in bioimaging, ACS Appl. Nano Mater. 1 (2018) 3682–3692. https://doi.org/10.1021/acsanm.8b00799.

[5]   L. He, C. Jiang, H. Wang, D. Lai, Rusli, High efficiency planar Si/organic heterojunction hybrid solar cells, Appl. Phys. Lett. 100 (2012) 1–4. https://doi.org/10.1063/1.3684872.

[6]   E.L. Ratcliff, B. Zacher, N.R. Armstrong, Selective interlayers and contacts in organic photovoltaic cells, J. Phys. Chem. Lett. 2 (2011) 1337–1350. https://doi.org/10.1021/jz2002259.

[7]   W. Ji, T. Allen, X. Yang, G. Zeng, S. De Wolf, A. Javey, Polymeric Electron-Selective Contact for Crystalline Silicon Solar Cells with an Efficiency Exceeding 19%, ACS Energy Lett. 5 (2020) 897–902. https://doi.org/10.1021/acsenergylett.0c00110.

[8]   L. Chen, Q. Chen, C. Wang, Y. Li, Interfacial dipole in organic and perovskite solar cells, J. Am. Chem. Soc. 142 (2020) 18281–18292. https://doi.org/10.1021/jacs.0c07439.

[9]   E. Ros, T. Tom, D. Rovira, J. Lopez, G. Masmitja, B. Pusay, E. Almache, I. Martin, M. Jimenez, E. Saucedo, E. Tormos, J.M. Asensi, P. Ortega, J. Bertomeu, J. Puigdollers, C. Voz, Expanding the Perspective of Polymeric Selective Contacts in Photovoltaic Devices Using Branched Polyethylenimine, ACS Appl. Energy Mater. 5 (2022) 10702–10709. https://doi.org/10.1021/acsaem.2c01422.

[10]   T. Tom, E. Ros, D. Rovira, J. López-Vidrier, J.M. Asensi, P. Ortega, J. Puigdollers, C. Voz, J. Bertomeu, Deoxyribonucleic Acid-Based Electron Selective Contact for Crystalline Silicon Solar Cells, Adv. Mater. Technol. 8 (2023) 2200936. https://doi.org/10.1002/admt.202200936.

[11]   Y. Wan, C. Samundsett, J. Bullock, T. Allen, M. Hettick, D. Yan, P. Zheng, X. Zhang, J. Cui, J. McKeon, A. Javey, A. Cuevas, Magnesium Fluoride Electron-

Selective Contacts for Crystalline Silicon Solar Cells, ACS Appl. Mater. Interfaces. 8 (2016) 14671–14677. https://doi.org/10.1021/acsami.6b03599.

[12]   J. Bullock, P. Zheng, Q. Jeangros, M. Tosun, M. Hettick, C.M. Sutter-Fella, Y. Wan, T. Allen, D. Yan, D. Macdonald, S. De Wolf, A. Hessler-Wyser, A. Cuevas, A. Javey, Lithium Fluoride Based Electron Contacts for High Efficiency n-Type Crystalline Silicon Solar Cells, Adv. Energy Mater. 6 (2016) 1–7. https://doi.org/10.1002/aenm.201600241.

[13]   G.S. Manning, Limiting laws and counterion condensation in polyelectrolyte solutions. 7. Electrophoretic mobility and conductance, J. Phys. Chem. 85 (1981) 1506–1515. https://doi.org/10.1021/j150611a011.

[14]   X. Yang, Z. Ying, Z. Yang, J.R. Xu, W. Wang, J. Wang, Z. Wang, L. Yao, B. Yan, J. Ye, Light-Promoted Electrostatic Adsorption of High-Density Lewis Base Monolayers as Passivating Electron-Selective Contacts, Adv. Sci. 2003245 (2021) 1–13. https://doi.org/10.1002/advs.202003245.

[15]   J. Perlich, V. Körstgens, E. Metwalli, L. Schulz, R. Georgii, P. Müller-Buschbaum, Solvent content in thin spin-coated polystyrene homopolymer films, Macromolecules. 42 (2009) 337–344. https://doi.org/10.1021/ma801878j.

[16]   J. García-Turiel, B. Jérôme, Solvent retention in thin polymer films studied by gas chromatography, Colloid Polym. Sci. 285 (2007) 1617–1623. https://doi.org/10.1007/s00396-007-1733-6.

[17]   E. Ros, Z. Barquera, P.R. Ortega, L.G. Gerling, G. Masmitjà, I. Martín, R. Alcubilla, J. Puigdollers, C. Voz, Improved Electron Selectivity in Silicon Solar Cells by Cathode Modification with a Dipolar Conjugated Polyelectrolyte Interlayer, ACS Appl. Energy Mater. 2 (2019) 5954–5959. https://doi.org/10.1021/acsaem.9b01055.

[18]   C. Wang, Y. Luo, J. Zheng, L. Liu, Z. Xie, F. Huang, B. Yang, Y. Ma, Spontaneous Interfacial Dipole Orientation Effect of Acetic Acid Solubilized PFN, ACS Appl. Mater. Interfaces. 10 (2018) 10270–10279. https://doi.org/10.1021/acsami.8b00975.

[19]   H. Viltres, O.F. Odio, M.C. Biesinger, G. Montiel, R. Borja, E. Reguera, Preparation of Amine- and Disulfide-Containing PAMAM-Based Dendrons for the Functionalization of Hydroxylated Surfaces: XPS as Structural Sensor,

ChemistrySelect. 5 (2020) 4875–4884. https://doi.org/10.1002/slct.202000432.

[20] S. Demirci, F.B. Emre, F. Ekiz, F. Oguzkaya, S. Timur, C. Tanyeli, L. Toppare, Functionalization of poly-SNS-anchored carboxylic acid with Lys and PAMAM: Surface modifications for biomolecule immobilization/stabilization and bio-sensing applications, Analyst. 137 (2012) 4254–4261. https://doi.org/10.1039/c2an35472a.

[21] D. Menzel, M. Mews, B. Rech, L. Korte, Electronic structure of indium-tungsten-oxide alloys and their energy band alignment at the heterojunction to crystalline silicon, Appl. Phys. Lett. 112 (2018). https://doi.org/10.1063/1.5010278.

[22] C. Reichel, U. Würfel, J.H. Hack, K. Winkler, C.A. Messmer, H.F. Schleiermacher, M. Kohlstädt, M. Hermle, S.W. Glunz, Effect of Thermal Annealing on the Charge Carrier Selectivity of Ultra-Thin Organic Interface Dipoles in Silicon Organic Heterojunction Solar Cells, Sol. RRL. 5 (2021) 25–30. https://doi.org/10.1002/solr.202100466.

[23] Y. Wan, C. Samundsett, J. Bullock, M. Hettick, T. Allen, D. Yan, J. Peng, Y. Wu, J. Cui, A. Javey, A. Cuevas, Conductive and Stable Magnesium Oxide Electron-Selective Contacts for Efficient Silicon Solar Cells, Adv. Energy Mater. 7 (2017). https://doi.org/10.1002/aenm.201601863.

[24] F.F. Maia, V.N. Freire, E.W.S. Caetano, D.L. Azevedo, F.A.M. Sales, E.L. Albuquerque, Anhydrous crystals of DNA bases are wide gap semiconductors, J. Chem. Phys. 134 (2011). https://doi.org/10.1063/1.3584680.

[25] K. Iguchi, Semiconductivity and band gap of a double strand of DNA, J. Phys. Soc. Japan. 70 (2001) 593–597. https://doi.org/10.1143/JPSJ.70.593.

[26] A.E. Gasperini, S. Sanchez, A.L. Doiron, M. Lyles, G.K. German, Non-ionising UV light increases the optical density of hygroscopic self assembled DNA crystal films, Sci. Rep. 7 (2017) 1–10. https://doi.org/10.1038/s41598-017-06884-8.

[27] J. Richter, M. Nnaji, H. Park, Solvent effect to the uniformity of surfactant-free salmon-DNA thin films, Polymers (Basel). 13 (2021). https://doi.org/10.3390/polym13101606.

[28]   S. Ptasińska, A. Stypczyńska, T. Nixon, N.J. Mason, D. V. Klyachko, L. Sanche, X-ray induced damage in DNA monitored by X-ray photoelectron spectroscopy, J. Chem. Phys. 129 (2008). https://doi.org/10.1063/1.2961027.

[29]   D.Y. Petrovykh, H. Kimura-Suda, L.J. Whitman, M.J. Tarlov, Quantitative analysis and characterization of DNA immobilized on gold, J. Am. Chem. Soc. 125 (2003) 5219–5226. https://doi.org/10.1021/ja029450c.

[30]   A.M. Shing, Y. Tolstova, N.S. Lewis, H.A. Atwater, Effects of surface condition on the work function and valence-band position of $ZnSnN_2$, Appl. Phys. A Mater. Sci. Process. 123 (2017) 1–9. https://doi.org/10.1007/s00339-017-1341-3.

[31]   M. Tsai, S. Su, J. Chang, D. Tsai, C. Chen, C. Wu, L. Li, L. Chen, J. He, M. Science, E. Engineering, M. Sciences, M. Sciences, S. Arabia, Monolayer MoS 2 Heterojunction Solar, ACS Nano. 8 (2014) 8317–8322.

[32]   C. Reichel, U. Würfel, K. Winkler, H.F. Schleiermacher, M. Kohlstädt, M. Unmüssig, C.A. Messmer, M. Hermle, S.W. Glunz, Electron-selective contacts via ultra-thin organic interface dipoles for silicon organic heterojunction solar cells, J. Appl. Phys. 123 (2018). https://doi.org/10.1063/1.5010937.

Chapter 7: Conclusions

This chapter summarizes the main results and conclusions of this thesis, as a result of development of transparent conductors and development of HTL and ETL selective contacts for SHJ solar cells.

The main objectives of this thesis were to reduce or replace the indium usage in silicon heterojunction silicon solar cells, and to fabricate a non-doped SHJ by replacing the doped layers by either carrier selective contact films or organic dipole interlayers using a broad variety of techniques. In the following, the main achievements reached in the different parts of the thesis are summarized.

The **chapter 4 of the thesis** addresses the high mobility TCOs and the indium reduction.

❖ Section 4.2 was focused in developing the high mobility TCO layers to reduce the near-IR free carrier absorption.

    ➢ The XRD measurements revealed that substantial amount of H_2 doping is needed to achieve the required film properties and solid phase crystallization in the films.

    ➢ The annealed films exhibited less defects and high mobility due to incorporation of singly-charged donors (hydrogen, fluorine), and also due to a reduction of doubly-charged oxygen vacancies.

    ➢ The highest mobility of 93 $cm^2V^{-1}s^{-1}$ at a carrier density of 2.2×10^{20} cm^{-3} was achieved for the films deposited at 3.1% O_2 and 2.5% H_2.

    ➢ The high-mobility films could then be successfully transferred to monofacial SHJ cells. This resulted in increased J_{sc} in the cells, with an increase in the mobility of the films. The highest mobility film achieved the highest efficiency of 22.6%.

❖ Section 4.3 was focused in reducing the usage of In due its high price and scarcity. Here, we developed a combination of several nanometers-thick

seed layers of high-mobility indium-doped oxides and cheaper indium-free TCOs (AZO) deposited on top, resulting in a stack with high mobility and conductivity.

- ➤ The structural investigations by XRD showed an increase in grain size of the films as the thickness increases.
- ➤ The 5-nm-thick films exhibited an electron mobility of 78.8 $cm^2V^{-1}s^{-1}$, which increased up to 93 $cm^2V^{-1}s^{-1}$ for 100-nm-thick films.
- ➤ Mobility of 44 $cm^2V^{-1}s^{-1}$ was achieved for 5 nm/95 nm (IFO/AZO) films, a considerably higher value compared to the pure 100-nm-thick AZO film with mobility of 17.4 $cm^2V^{-1}s^{-1}$.
- ➤ The highest mobility of 78.3 $cm^2V^{-1}s^{-1}$ has been achieved in 45 nm/55 nm IFO/AZO stack, which could help in reducing the usage of indium by 50 %.

- ❖ Section 4.4 was devoted to develop an all-in-one transparent conductor and hole-selective contact layer of V_2O_5/Ag:Al/AZO. This substitutes traditional TCOs and henceforth reduces the need for more expensive standard ITO electrodes.
  - ➤ Al doping in Ag layer helped to obtain ultra-thin smooth metallic films of higher transmittance and lower sheet resistance.
  - ➤ The optimized AZO/Ag:Al/AZO multilayer structure showed a sheet resistance of 48 Ω/Sq and 80% transmittance in the visible region of the spectrum.
  - ➤ Then, to develop a hole-selective layer for the fabrication of solar cells the above TCO multi-structure was reconfigured, i.e., by replacing the bottom AZO layer by V_2O_5.
  - ➤ The solar cell on *n*-type c-Si with 50-nm-thick V_2O_5 yielded a *PCE* of 11.5%, with remarkably high V_{oc} of 631 mV and a J_{sc} of 29.8 mA cm^{-2}, showing its potential as both an excellent TCO and a hole-selective contact.

The **chapter 5 of the thesis** dealt with HTL development by sputtering for SHJ solar cells.

- ❖ Section 5.2 aimed at optimizing HTL contact by reactive sputtering of Mo to obtain MoO_x films in an $Ar:O_2$ atmosphere. The technique of sputtering was chosen to replace the thermally-evaporated HTLs.
  - ➢ Sub-oxidized stoichiometry of the films was proved by XPS measurements indicating the presence of Mo^{4+}, Mo^{5+} and Mo^{6+} peaks.
  - ➢ The optical transmittance of the films increased to 85% due to the reduced number of oxygen ion vacancies at higher deposition pressures.
  - ➢ The conductivity of the films dropped from 106 to 1 S m^{-1} as the deposition pressure increased in the chamber, attributing this behavior to the stoichiometry of the MoO_3 films.
  - ➢ Afterwards, the sputtered films were tested on the SHJ solar cells, with a highest *PCE* of 8.8%. However, the performance of the cells was not up to the benchmark of the thermally-evaporated cells, with a *PCE* of 13.3%.

- ❖ Section 5.3 was devoted to introduce sputtering from a ceramic target of MoO_3 using different atmospheres of Ar, $Ar:O_2$ and $Ar:H_2$. This procedure was selected due to the reactive sputtering from a metallic target not making a significant impact in the *PCE* of solar cells.
  - ➢ The XRD patterns indicated the amorphous nature of the films, whereas XPS demonstrated that films prepared in the $Ar:H_2$ atmosphere were more sub-stoichiometric.
  - ➢ Higher band gap was obtained for films sputtered in $Ar:O_2$ atmosphere, whereas Ar and $Ar:H_2$ atmospheres induced a reduced band gap due to the sub-stoichiometric MoO_x films.
  - ➢ TLM measurements showed higher conductivity for the films sputtered in $Ar:H_2$ atmosphere.
  - ➢ The films sputtered at higher temperatures showed more sub-stochiometric MoO_x films with oxygen to molybdenum ratios from 2.6 to 2.9, the films being more conductive.

The **chapter 6 of the thesis** concentrates in ETLs, using organic molecules as dipole interlayers.

- ❖ In section 6.2, branched polyethylenimine is explored as a polymeric electron selective contact in crystalline silicon solar cells.
  - ➢ The optimum contact resistance for a PEI layer thickness was found around 1 nm.
  - ➢ QSSPC measurements for that optimized thickness show that the passivation of crystalline silicon improves after the metal is deposited.
  - ➢ UPS results demonstrated that PEI could shift the electrode work function by approximately 1 eV.
  - ➢ The amine groups present in the polymer were partially protonated, as seen from the XPS spectrum.
  - ➢ Finally, solar cell structures have been fabricated to test the use of PEI in electron selective contacts. Full dopant-free solar cells with 13.8% efficiency have been demonstrated with PEI modification at the contact.

- ❖ Section 6.3 demonstrates the efficient usage of PAMAM as a dipole interlayer that functions as a passivating ETL in SHJ solar cells.
  - ➢ TLM measurements of 1-nm-thick PAMAM dendrimer with Al on c-Si substrate revealed an exceptionally low specific contact resistance of 4.5 mΩ cm^2.
  - ➢ Transmittance measurements showed an exceptional optical transparency with a band gap of 4.6 eV.
  - ➢ The XPS study of the films demonstrated the presence of protonated nitrogen, which contributed to the creation of the interlayer dipole.
  - ➢ The UPS measurements were used to calculate the work function shift and valence band level, revealing the formation of ohmic contact at the junction and the *n*-type behavior of the PAMAM dendrimer films.
  - ➢ Ultimately, the devices with PAMAM dendrimer layer as the ETL exhibited an efficiency of 14.5%, higher than the reference device, demonstrating the promising potential of the dipole interlayer.

- ❖ Finally, section 6.4 reports the fabrication and characterization of thin DNA films, and their use in a metal/semiconductor junction as a buffer

layer to provide enhanced electron injection/extraction (i.e., acting as the ETL).

➢ Specific contact resistance values extracted from TLM measurements proved a clear reduction for a DNA thin layer around 2 nm.

➢ Tauc plots obtained from optical transmittance from the DNA films showed the presence of nucleic bases through the peaks at 4.7 eV and 5.1 eV, and an optical gap of 4.1 eV was determined.

➢ UPS analysis of DNA allowed locating the valence band of 3.2 eV below the Fermi level, which suggests a possible *n*-type doping of the film.

➢ The resulting proof-of-concept solar cell achieved an efficiency higher than 15.6%, with a remarkable improvement in all the photovoltaic parameters.

➢ This effect could be attributed to the elimination of Fermi level pinning, as well as to a better surface passivation and charge-carrier extraction due to electron accumulation at the silicon surface.

Overall, the present thesis has shown important advances in the field of selective layers and transparent electrodes for SHJ solar cells, from the point of view of reduction in scarce critical-raw-material usage as well as of cost-effective and scalable fabrication techniques. Indeed, this work paves the way for the research in new materials (or material combination) aiming at improving charge selectivity and its extraction in Si-based solar cells. In this sense, some of the unexplored works that could be addressed in the future are:

➢ Development of solar cells using the IFO/AZO stacks, understanding the behavior of J_{sc} with the mobility of the stacks.

➢ Replacing the dielectric layers in the DMDs for better optical properties, thus improving the *PCE* of the cells.

➢ Development of HTL layers using the high work function organic contacts. The most interesting HTL layer that should be explored is self-assembled monolayer (3-Aminopropyl)triethoxysilane

(APTES), which shows interesting specific contact resistance characteristics and a higher work function.

➢ Development of non-doped silicon solar cell using organic contacts as both ETL (e.g., DNA) and HTL [e.g., DNA-cetyltrimethylammonium chloride (DNA-CTMA)].

List of figures

List of tables

List of symbols

Latin alphabet

Δ	Phase difference
Δn	Photogenerated excess electrons
$\degree C$	Degree Celsius
A	Absorptance
$A_{weighted}$	Weighted absorptance
Ac	Effective contact area
B	Constant parameter
B_z	Magnetic field
C	Speed of light
D	Crystalline size
d	Distance, width
d_{hkl}	Interplanar spacing between (hkl) lattice planes
E, E_c, E_v	Energy of the state or level, Energy at conduction band and valence band edge
E_0	Secondary electron cut-off energy
EA	Electron affinity
E_c	Conduction band edge
E_f	Fermi level energy
E_{FC}	Quasi-Fermi energy level within the CB
E_{FV}	Quasi-Fermi energy level within the VB
E_g	Band Gap Energy
E_{vac}	Energy at the vacuum level
$f(E)$	Fermi-Dirac distribution function
g	ideality factor
$h\nu$	Photon energy
I	Current

I_{light}	Intensity of light
IE	Ionization energy
iV_{oc}	Implied open circuit voltage
I_y	Applied current
J_0	Recombination prefactor
J_{0c}	Recombination current density
J_{mp}	Current density at maximum power point
J_{ph}	Photogenerated current
J_{sc}	short-circuit current density
$J\text{-}V$	Current Density-Voltage
k	Shape factor
k_B	Boltzmann constant
L	Contact separation
L_T	Transfer length
m	Integer
mp	Maximum power density
n	Electron concentration
Ne	Free-carrier concentration
n_i	Intrinsic carrier density
p	Hole concentration
$\vec{p}$	Electric dipole moment
$P, P_{\text{in}}, P_{\text{out}}$	Power, incident power, output power
q	elementary charge
R	Reflectance
ref	Reference
R_M	Resistance of metal film
R_O	Resistance of dielectric film
R_p	Shunt resistance
R_q	Root mean square roughness
R_s	Series resistance

R_sh	Sheet resistance
R_T	Total resistance
S_front	Front surface recombination
S_rear	Rear surface recombination
t	Thickness of the film
T	Absolute temperature
TT	Transmittance
V	External voltage
V_H	Hall voltage
V_mp	Voltage at maximum power point
V_oc	Open-circuit voltage
W	Absorber layer thickness

Greek alphabet

ρ	Complex reflectance ratio
ψ	Amplitude ratio
$\Delta\sigma$	Change in photoconductance
μ, μ'	Electron mobility, Hole mobility
μ_g	Mobility (Scattering at grain boundaries)
μ_i	Mobility (Ionized impurity scattering)
μ_l	Mobility (Lattice vibration scattering)
μ_n	Mobility (Neutral impurity scattering)
α	Absorption coefficient
β	FWHM
Δ	Shift
θ	Angle
λ	Wavelength
ρ	Resistivity
ρ^2	Linear regression coefficient
ρ_c	Specific contact resistance
$\sigma, \sigma_n, \sigma_p$	Conductivity, Electron conductivity, Hole conductivity

τ, τ_{eff}	Carrier lifetime, Effective carrier lifetime
φ	Potential
ϕ'	Apparent work function
ϕ, WF	Work function
Φ	Spectral photon flow
G	photogeneration rate of the excess carriers

List of acronyms

A	Absorptance
AFM	Atomic Force Microscopy
ALD	Atomic Layer Deposition
AM 1.5	Air Mass 1.5
ARC	Anti Reflection Coating
BE	Binding Energy
BSF	Back Surface Field
CB	Conduction Band
CCiT-UB	Centres Científics i Tecnològics de la Universitat de Barcelona
CP	Conjugated Polyelectrolyte
CVD	Chemical Vapor Deposition
DC	Direct Current
DMD	Dielectric Metal Dielectric
EB	Extension Buffer
EC	Extension Chamber
EDS	Energy Dispersive X-ray Spectroscopy
EELS	Electron Energy Loss Spectroscopy
EQE	External Quantum Efficiency
ETL	Electron Transport Layer
FCA	Free Carrier Absorption
FF	Fill Factor
F-ISE	Fraunhofer Institute for Solar Energy
FLP	Fermi Level Pinning
FOM	Figure of Merit
FWHM	Full Width at Half Maximum
FZ	Float Zone
HAADS	High-Angle Annular Dark-Field imaging

HIT	Heterojunction with Intrinsic Thin layer
HRTEM	High Resolution Transmission Electron Microscopy
HTL	Hole Transport Layer
ICDD	International Centre for Diffraction Data
ICN2	Institut Català de Nanociència i Nanotecnologia
IQE	Internal Quantum Efficiency
KE	Kinetic Energy
LED	Light Emitting Diode
LL	Load Lock
LMA-INA	Laboratorio de Microscopias Avanzadas of Zaragoza
LUMO	Lowest Unoccupied Molecular Orbit
MDS	Metal-Dipole-Semiconductor
MTCE	Multi Tunneling Capture and Emission
PCD	Photo Conductance Decay
PCE	Power Conversion Efficiency
PECVD	Plasma Enhanced Chemical Vapor Deposition
PERC	Passivated Emitter Rear Cell
PV	Photovoltaic
PVD	Physical Vapor Deposition
QSSPCD	Quasi-Steady State Photo Conductance Decay
RCA	Radio Cooperation of America
RF	Radio Frequency
RMS	Root Mean Square
RT	Room Temperature
SEM	Scanning Electron Microscopy
SHJ	Silicon Heterojunction
SP	Screen Printing
SRH	Shockley Read Hall
STEM	Scanning Transmission Electron Microscope
TCO	Transparent Conducting Oxides
TEM	Transmission Electron Microscopy
TLM	Transfer Length Method

TMM	Transfer Matrix Method
TMO	Transition Metal Oxide
TR	Total Reflectance
TT	Total Transmittance
UB	Universitat de Barcelona
UPC	Universitat Politècnica de Catalunya
UPS	Ultraviolet Photoelectron Spectroscopy
UV	Ultra Violet
VB	Valence Band
WAT	Weighted Average Transmittance
WF	Work Function
XPS	X-Ray Photoelectron Spectroscopy
XRD	X-Ray Diffraction

List of chemical species

APTES	(3-Aminopropyl)triethoxysilane
a-Si:H	Hydrogenated amorphous silicon
Al	Aluminum
Ar	Argon
ATO	Antimony doped tin oxide
AZO	Aluminum doped zinc oxide
Au	Gold
b-PEI	Branched Polyethylenimine
C	Carbon
CdTe	Cadmium telluride
Ce	Cerium
Cr	Chromium
c-Si	Crystalline silicon
CTMA	Cetyltrimethylammonium chloride
DNA	Deoxyribonucleic acid
Ge	Germanium
H_2	Hydrogen
HCl	Hydrochloric acid
HF	Hydrofluoric acid
Hf	Hafnium
IFO	Fluorine doped indium oxide
In_2O_3	Indium oxide
InGaAs	Indium gallium arsenide
ITO	Tin doped indium oxide
LiF	Lithium fluoride
MgF_2	Magnesium fluoride
MgO_x	Magnesium oxide

Mo	Molybdenum
MoO$_x$	Molybdenum oxide
N$_2$	Nitrogen
O$_2$	Oxygen
P	Phosphorous
PAMAM	Polyamidoamine
PH$_3$	Phosphine
PVDF	Polyvinylidene fluoride
Si	Silicon
SiH$_4$	silane
SiO$_x$	Silicon oxide
Ta	Tantalum
Ti	Titanium
TiO$_x$	Titanium oxide
TMAH	Tetramethyl ammonium hydroxide
TMB	Trimethylborane
V	Vanadium
V$_2$*O*$_x$	Vanadium oxide
W	Tungsten
WO$_x$	Tungsten oxide
Zn	Zinc
Zr	Zirconium

List of abbreviations

at. %	Atomic percent
Eq.	Equation
et al.	From latin, *et alii* (and others)
Fig.	Figure
i.e.	From latin, *id est* (*that is*)
min	Minute
wt %	Weight percent

Curriculum vitae

Thomas Tom

thomastomphysics@gmail.com

Academic background

2018-2023	Physics Ph.D. (Solar Energy Group, Universitat de Barcelona): *Selective contacts for crystalline silicon solar cells.* Directed by Joan Bertomeu i Balagueró and Julian Vidrier López.
2014-2016	Master of Science in Physics (National Institute of Technology, Tiruchirappalli, India): Master thesis on *Hybrid Magnetic Nanofluids For Anti-Corrosive Coating In Metallic Tubes.* Supervised by J.Hemalatha.
2010-2013	Bachelor of Science in Physics (St. Berchmans College Mahatma Gandhi University, Chaganacherry, India)

Professional background

2021-2022	Internship at Fraunhofer Institute for Solar Energy Systems ISE, Heidenhofstr.2,

Freiburg, Germany. *High-mobility sputtered Indium oxide doped films and its transfer to silicon solar cells.* Supervised by Martin Bivour.

2014-2015   Internship at Raja Ramanna Centre for Advanced Technology, Indore, India.
Orientation course on Accelerators, Lasers and related Science and Technology.

Experimental skills

- Vacuum Technology: Working experience with High Vacuum thin film deposition equipment in Clean Room environment (Lab-scale and industrial sputtering, thermal evaporation, PECVD) and also spin coating.

- Optical, Compositional and Structural: UV-Vis-NIR Spectrophotometer, XPS, SEM, TEM, XRD, EDS, AFM, XPS, UPS, EPMA.

- Electrical Characterization: Hall effect measurements, Four-point probe, TLM, solar cells characterization.

Language skills

- Malayalam: Native language
- English: Fluent
- Tamil: Basics
- Spanish: Basics

Scientific publications

First author publications

[1] **T. Tom**, E. Ros, N. López-Pintó, J. Miguel Asensi, J. Andreu, J. Bertomeu, J. Puigdollers, C. Voz, Influence of Co-Sputtered Ag:Al Ultra-Thin Layers in Transparent V_2O_5/Ag:Al/AZO Hole-Selective Electrodes for Silicon Solar Cells, Materials (Basel) 13 (2020) 4905. https://doi.org/10.3390/ma13214905.

[2] E. Ros*, **T. Tom***, D. Rovira, J. Lopez, G. Masmitja, B. Pusay, E. Almache, I. Martin, M. Jimenez, E. Saucedo, E. Tormos, J.M. Asensi, P. Ortega, J. Bertomeu, J. Puigdollers, C. Voz, Expanding the Perspective of Polymeric Selective Contacts in Photovoltaic Devices Using Branched Polyethylenimine, ACS Appl. Energy Mater. 5 (2022) 10702–10709. https://doi.org/10.1021/acsaem.2c01422.

[3] **T. Tom***, E. Ros*, D. Rovira, J. López-Vidrier, J.M. Asensi, P. Ortega, J. Puigdollers, C. Voz, J. Bertomeu, Deoxyribonucleic Acid-Based Electron Selective Contact for Crystalline Silicon Solar Cells, Adv. Mater. Technol. 8 (2023) 2200936. https://doi.org/10.1002/admt.2 02200936.

[4] **T. Tom***, E. Ros*, J. López-vidrier, J.M. Asensi, P. Ortega, J. Puigdollers, J. Bertomeu, C. Voz, Modification in Crystalline Silicon Solar Cells Poly (amidoamine) Dendrimer as an Interfacial Dipole, J. Phys. Chem. Lett. (2023). https://doi.org/10.1021/acs.jpclett.3c00643.

[5] E. Ros*, **T. Tom***, P. Rafael Ortega, I. Martin, E. Maggi, J.M. Asensi, J. Lopez, E.Saucedo, J.Bertomeu, J.Puigdollers, C.Voz, Elimination of interface energy barriers polyelectrolytes with fractal geometry using dendrimer, ACS Appl. Mater. Interfaces (2023) *Submitted*.

[6] **T. Tom**, L. Tutsch, M. Hermle, J. M. Asensi, J. López-Vidrier, J. Bertomeu, M. Bivour, High-mobility sputtered fluorine-doped indium oxide and its transfer to the heterojunction silicon solar cells. *Under preparation*.

[7]   **T. Tom**, L. Tutsch, M. Hermle, J. M. Asensi, J. López-Vidrier, J. Bertomeu, M. Bivour, Reducing the usage of Indium in transparent conducting electrodes by AZO films with high-mobility fluorine-doped indium oxide as seed layers. *Under preparation*.

Co - author publications

[8]   H.T. Nguyen*, E. Ros*, **T. Tom**, J. Bertomeu, J.M. Asensi, J. Andreu, I.M. Garcia, P. Ortega, M. Garin, J. Puigdollers, C. Voz, R. Alcubilla, Influence of a Gold Seed in Transparent V_2O_x/Ag/V_2O_x Selective Contacts for Dopant-Free Silicon Solar Cells, IEEE J. Photovoltaics 9 (2019) 72–77. https://doi.org/10.1109/JPHOTOV.2018.2875876.

[9]   N. Lopez-Pinto, **T. Tom**, J. Bertomeu, J.M. Asensi, E. Ros, P. Ortega, C. Voz, Deposition and characterisation of sputtered molybdenum oxide thin films with hydrogen atmosphere, Appl. Surf. Sci. 563 (2021) 150285. https://doi.org/10.1016/j.apsusc.2021.150285.

[10]   D. Rovira, E. Ros, **T. Tom**, M. Jiménez, J. Miguel Asensi, C. Voz, J. López, J. Puigdollers, J. Bertomeu, E. Saucedo, Polymeric Interlayer in CdS-Free Electron Selective Contact for Sb_2Se_3 Thin Film Solar Cells, Int. J. Mol. Sci. 24 (2023). https://doi.org/10.3390/ijms24043088.

Conference publications

[11]   **T. Tom**, L. Tutsch, M. Hermle, J. M. Asensi, J. López-Vidrier, J. Bertomeu, M. Bivour, High-mobility Flourine Doped Induim Oxide Films for High Efficiency Silicon Solar Cells, 8th World Conf. Photovolt. Energy Conversion, Milan, Italy. (2022) 128–132. https://doi.org/10.4229/WCPEC-82022-1CV.2.39.

[12]   E. Ros, **T. Tom**, G. Masmitja, B. Pusay, E. Almache, M. Jimenez, J. Lopez, E. Saucedo, P. Ortega, J. Bertomeu, J. Puigdollers, C. Voz, Polyethienimine interface dipole tuning for electron selective contacts, Conf. Rec. IEEE Photovolt. Spec. Conf. 2022-June (2022) 1363–1365. https://doi.org/10.1109/PVSC48317.2022.9938825.

Presentations at conferences

[1]   12th Spanish Conference on Electron Devices: CDE 2018, Universidad de Salamanca, Spain. Poster presentation: **T. Tom**, E. Ros, P. Ortega, C. Voz, J. Miguel Asensi, J. Andreu, J. Bertomeu, C. Voz. Molybdenum oxide hole-selective contacts by reactive sputtering for *n*-type silicon heterojunction devices (2018).

[2]   21st International Vacuum Congress, Malmö, Sweden. Poster presentation: **T. Tom**, E. Ros, P. Ortega, C. Voz, J. Miguel Asensi, J. Andreu, J. Bertomeu, C. Voz. Reactive Magnetron Sputtering of ZnO:Al and application to ZnO:Al/Ag:Al/ZnO:Al structures (2019).

[3]   E-MRS 2019 Fall Meeting in Warsaw, Poland. Poster presentation: **T. Tom**, E. Ros, P. Ortega, C. Voz, J. Miguel Asensi, J. Andreu, J. Bertomeu, C. Voz. ITO free silicon solar cells using reactive sputtered ZnO:Al (2019).

[4]   Latsis Symposium on Earth-Abundant Materials for Future Photovoltaics, École Polytechnique Fédérale de Lausanne (EPFL) Lausanne, Switzerland. Oral presentation: **T. Tom**, E. Ros, E. Tormos, J.M. Asensi, J. Puigdollers, C. Voz, J. López-Vidrier, J. Bertomeu. Polymeric carrier selective contacts for crystalline silicon solar cells (2022).

[5]   8th World Conference on Photovoltaic Energy Conversion, Milan, Italy. Poster presentation: **T. Tom**, L. Tutsch, M. Hermle, J. M. Asensi, J. López-Vidrier, J. Bertomeu, M. Bivour. High-mobility Flourine Doped Induim Oxide Films for High Efficiency Silicon Solar Cells (2022).

* Co-first authors